Illuminating the highly dynamic on-cell target search of bacteriophage and phage-like particles

Dreesens, L.L.

Publication date
2021

Document Version
Final published version

Citation (APA)
Dreesens, L. L. (2021). *Illuminating the highly dynamic on-cell target search of bacteriophage and phage-like particles*. [Dissertation (TU Delft), Delft University of Technology].

Illuminating the highly dynamic on-cell target search of bacteriophage and phage-like particles

Illuminating the highly dynamic on-cell target search of bacteriophage and phage-like particles

Proefschrift

ter verkrijging van de graad van doctor
aan de Technische Universiteit Delft,
op gezag van de Rector Magnificus Prof.dr.ir. T.H.J.J. van der Hagen,
voorzitter van het College voor Promoties,
in het openbaar te verdedigen op
maandag 14 Juni 2021 om 12.30 uur

door

Lisa Laura DREESENS

Master of Science in Biomolecular Sciences,
Vrije Universiteit Amsterdam, Nederland,
geboren te Venray, Nederland.

Dit proefschrift is goedgekeurd door de promotor en copromoter.

Samenstelling promotiecommissie bestaat uit:

Rector magnificus,	voorzitter
Dr. ME. Aubin-Tam	Technische Universiteit Delft, promotor
Dr. H.J.E. Beaumont	Technische Universiteit Delft, copromotor

Onafhankelijke leden:

Prof.dr. B. Rieger,	Technische Universiteit Delft
Prof.dr. A. Briegel,	Universiteit Leiden
Prof.dr. A. Aertsen,	Katholieke Universiteit Leuven, België
Prof.dr. N.H. Dekker,	Technische Universiteit Delft
Dr.ir. S.S.J. Brouns,	Technische Universiteit Delft

This research project was funded by the Netherlands Organisation for Scientific Research (NWO) as part of the NanoFront programme.

Keywords: phage, phage-like particle, single-particle, fluorescence microscopy

Printed by: IPSKAMP printing

Cover by: D.C. Dreesens

Casimir PhD Series, Delft-Leiden 2021-06

ISBN: 978-90-8593-472-1

An electronic copy of this dissertation is available at http://repository.tudelft.nl/

Voor mijn ouders

Summary

Phages are tiny nanomachines that are composed of a protein coat encapsulating a genome. Since they are metabolically inert, they depend on a bacterial host for replication. They are abundantly present in all kinds of environments, patiently awaiting their target. The nanoscopic mechanical details of how phages find the correct target and commit to infect remains unresolved. Traditionally bulk methods have been used to investigate the molecular properties of phages and phage-host interaction dynamics, which does not provide the required detailed information to understand how a phage moves on the cell prior to the decision to commit to infecting it. More detailed insights on this process have been gained by single-particle EM studies, providing information on main structural configurations near atomic level that occur during the initial binding process (i.e. interaction between tail-fibers and host) up till commitment (i.e. sheath contraction followed by penetration of the cell membrane and DNA ejection). These static EM snapshots imply that the phage might use their tail-fibers to walk over the cell surface. However, any dynamical information is lacking. Direct visualization of labeled phage lambda using fluorescence microscopy confirmed the presence of on-cell movement with interactions that are governed based on the binding between phage and host receptor. However, they did not reveal the mechanism behind the observed movement. Within this thesis we optimized a method based on fluorescence microscopy to study the fast dynamics of the on-cell motion and decision-making process of phages at single-particle level with high temporal resolution and implemented a control for detecting possible artefacts due to cell-movement.

Chapter 1 starts with a general introduction into the biology of phages, including their ecology, life cycle, structure and taxonomy. In particular, we highlight the currently known details behind the mechanism of host recognition for phage T4, which is the model phage that was studied within this thesis. We also introduce so-called phage-like particles, which are protein structures that are evolutionarily related to phages and, among others, are stochastically secreted by multiple bacterial species as a kind of defense mechanism to kill closely related strains and species. These phage-like particles have evolved repeatedly in disparate lineages of phages suggesting that these structures have diverged from a single common ancestor. However, their function is different to that of phages, lacking a genome they have evolved to kill a cell by dissipation of the membrane potential.

In **chapter 2** we describe the optimization of a method, based on fluorescence microscopy, that can study the target-search mechanism of phage/phage-like particles in more detail. The optimization of this method consisted of three parts: i) Optimization of a flowcell-design to adhere and immobilize host cells to a glass slide in order to increase the chances of observing phage-host interactions. Here, we assessed the concentration of the adherence co-factor, effect of flowrate, adherence time and initial cell concentration on the number and fraction of immobilized cells. Based on these findings we established a protocol, involving coating of the flowcell with poly-L-lysine

and concentrating the cells suspensions, followed by an incubation period of the cells in the flowcell and a subsequent washing step at specific flow rate. This yielded flow cells containing a sufficient number of firmly fixed cells. Part ii) focused on fluorescently labelling of phage and phage-like particles to allow visualization by fluorescence microscopy. Results showed that phages and phage-like particles labeled with 10 mM of the nonspecific dye Alexa647-NHS have a good signal-to-noise ratio ensuring tracking of the particles at any given location at the cell and over a sufficiently long time-period at continuous excitation. Part iii) describes the development of a semi-automatic data analysis framework to extract phage/phage-like particle positions on the cell surface that can be used to study the phage/phage-like particle-host binding distributions and interaction dynamics at nanoscale resolution.

Chapter 3 provides results on the irreversible binding distribution of labeled T4 phage on *Escherichia coli* B using fluorescent microscopy. Further, we investigated whether there is an effect of a shift in medium composition, from LB to M9, or change in host receptor, from LPS (host *E. coli* B) to OmpC in combination with a more branched version of LPS (host *E. coli* K-12), on the binding distribution. The former experiment, effect of shift in medium composition, was primarily tested to observe whether this medium could be used to track dynamics without effecting the binding distribution as an alternative to the highly autofluorescent LB medium. Results show that, like many other phages, the binding distribution of T4 phage on *E. coli* B was non-uniform, with a bias towards the cellular poles. We detected no effect of medium composition on the binding distribution, making M9 medium a good alternative to obtain trajectories of bacteriophages by means of fluorescence microscopy opposed to the autofluorescent LB medium. Contrastingly, we found a significant effect of a change in receptor spectrum on the binding distribution, which showed a change in the strength of polar binding when comparing our data with a previously reported distribution of T4 on *E. coli* K-12. These results provide a first step towards the understanding of the search and commitment mechanism and identification of key-factors playing a role in this process.

Chapter 4 reveals, for the first time, the detailed interaction dynamics between labeled bacteriophage T4 and host *E. coli* B. We show that this method is capable of discriminating different motion regimes corresponding to the different search states of the phage. Most importantly we provide direct evidence of step-wise near/on-cell motion. We believe this discrete near/on-cell motion is facilitated by either a tethered-walk through binding and subsequent unbinding of individual LTFs with host cell receptors and/or hopping through repeated brief attach and detachment of the phage to host receptors. Together, these findings provide the first step towards an in-depth understanding of the mechanism behind the target-finding and decision-making process.

In **chapter 5** we provide first insights in the binding distribution and dynamics of R2-type pyocins and *Pseudomonas aeruginosa* 13s. Here we show that the binding distribution and search process of single-R2-type pyocins resemble those observed for phage T4. Within this chapter we also developed a method to study the killing process of R2-type pyocins. Here we optimized the concentration of the membrane-potential sensitive dye $DiSC_3(5)$ and showed that we could use this method to track depolarization of the 13s cells upon exposure to pyocins. With further development,

this method has the potential to monitor the 'killing' process of pyocins in real-time and at single-cell level in a quantitative manner.

Finally, in **chapter 6** we explore how the extension of the existing body knowledge with the insights presented in this thesis bring a new level of understanding of the mechanism behind the dynamical interaction between phage/phage-like particles and host occurring at nanoscale level and how this could contribute to the development of new applications.

Samenvatting

Fagen zijn kleine nanomachines die zijn samengesteld uit een eiwitmantel met een ingekapseld genoom. Ze zijn metabolisch inert en daarvoor afhankelijk van replicatie in een bacteriële gastheer. Ze zijn in groten getale in allerlei omgevingen aanwezig, in afwachting om de juiste gastheer te treffen. De nanoscopische details omtrent het mechanisme waarmee fagen het juiste doelwit vinden en beslissen om deze te infecteren zijn nog grotendeels onbekend. Tot op heden is voornamelijk gebruik gemaakt van bulkmethoden om de moleculaire eigenschappen van fagen en de interactiedynamiek tussen faag en gastheer te onderzoeken, maar deze methodes verschaffen niet de vereiste gedetailleerde informatie om te begrijpen hoe een faag zich op de cel beweegt voorafgaand aan de beslissing om deze te infecteren. Een aantal van deze details zijn verkregen door onderzoek dat gebruik maakt van een elektronenmicroscoop. Hiermee is men in staat om, op nabij atomair niveau, de belangrijkste structurele configuraties van een faag partikel te onderzoeken die optreden tijdens het initiële bindingsproces (de interactie tussen receptoren van de faag en gastheer) tot en met de beslissing om de gastheercel te infecteren (het moment waarop de binding van de faag onomkeerbaar wordt door structurele configuraties die plaatsvinden in de eiwitstructuur). De verkregen statische afbeeldingen uit deze momentopnames suggereren dat de fagen hun staartfilamenten zouden kunnen gebruiken om over het celoppervlak te lopen. Echter, informatie omtrent deze dynamiek ontbreekt. Een ander onderzoek dat gebruik maakt van fluorescent gelabelde fagen heeft met behulp van fluorescentiemicroscopie bevestigd dat de fagen kunnen voortbewegen op de gastheer door middel van specifieke interactie tussen de staartfilamenten en de gastheerreceptoren. Echter hebben ze niet het mechanisme achter de waargenomen beweging onthuld. Binnen dit proefschrift hebben we een methode geoptimaliseerd op basis van fluorescentiemicroscopie om de snelle dynamiek van deze voortbeweging op de cel en het besluitvormingsproces van fagen op het niveau van een enkel faag partikel te bestuderen met een hoge temporele resolutie en controle op mogelijke artefacten als gevolg van beweging van de gastheercel.

Hoofdstuk 1 begint met een algemene inleiding in de biologie van fagen, inclusief hun ecologie, levenscyclus, structuur en taxonomie. In het bijzonder belichten we de momenteel bekende details achter het mechanisme van gastheerherkenning voor faag T4, de modelfaag die in dit proefschrift wordt bestudeerd. We introduceren ook zogenaamde faagachtige deeltjes, eiwitstructuren zonder genetisch materiaal, die evolutionair verwant zijn aan fagen en onder andere stochastisch worden uitgescheiden door meerdere bacteriesoorten als een soort afweermechanisme om nauw verwante stammen en soorten te doden. Deze faagachtige deeltjes zijn herhaaldelijk geëvolueerd in fagen van verschillende afkomst, wat suggereert dat deze structuren van een enkele gemeenschappelijke voorouder afstammen. Hun functie is

echter anders dan die van fagen. Ze hebben zich ontwikkeld om een cel te doden door dissipatie van de membraanpotentiaal.

In **hoofdstuk 2** beschrijven we de optimalisatie van een methode, gebaseerd op fluorescentiemicroscopie, die het zoekmechanisme van faag/faagachtige deeltjes in meer detail kan bestuderen. De optimalisatie van deze methode bestaat uit drie delen: i) Optimalisatie van een *flowcell* ontwerp om gastheercellen te hechten en te immobiliseren aan een objectglaasje waardoor de kans op waarneming van faag-gastheerinteracties vergroot kan worden. Hier hebben we het effect van de concentratie van de co-factor die aanhechting verzorgt, de wassnelheid van de flowcell, de incubatietijd van gastheercellen aan de flowcell en de insertie van de initiële gastheercelconcentratie in de flowcell beoordeeld op het aantal en de fractie van geïmmobiliseerde cellen aan het glasoppervlak. Op basis van deze bevindingen hebben we een protocol opgesteld, waarbij we de flowcell coaten met poly-L-lysine en de cel suspensies concentreren, gevolgd door een incubatieperiode van de cellen in de flowcell en een daaropvolgende wasstap met een specifieke snelheid. Dit levert een flowcell op met daarin voldoende aantal gefixeerde cellen. Deel ii) concentreert zich op het fluorescent labelen van faag/faagachtige partikels om visualisatie door fluorescentiemicroscopie mogelijk te maken. De resultaten tonen aan dat fagen/faagachtige deeltjes die gelabeld zijn met 10 mM van de niet-specifieke label Alexa647-NHS een goed signaal-achtergrondruisverhouding hebben, waardoor de faag-partikels op de cel op elke gegeven locatie en gedurende een voldoende lange tijdsperiode onder continue excitatie gevolgd kunnen worden. Deel iii) beschrijft de ontwikkeling van een semiautomatische analysemethode voor het analyseren van de genomen beelden met de fluorescentie microscoop. Hiermee kan de positie van faag/faagachtige deeltjes op het celoppervlak geëxtraheerd worden om vervolgens bindingsverdelingen en interactiedynamiek tussen faag en gastheer op nanoschaalresolutie te kunnen bestuderen.

Hoofdstuk 3 presenteert resultaten over de bindingsverdeling van gelabelde T4-faag op gastheercel *Escherichia coli* B. De resultaten tonen aan dat, net als voor veel andere fagen, de bindingsverdeling van T4-faag op *E. coli* B niet uniform is en een voorkeur heeft om te binden aan de cellulaire polen. Verder onderzoeken we of er een effect is van een verschuiving in mediumsamenstelling, van LB naar M9, of verandering in gastheerreceptor, van LPS (gastheer *E. coli* B) naar OmpC in combinatie met een meer vertakte versie van LPS (gastheer *E. coli* K-12), op de bindingsverdeling. Het eerste experiment, effect van verschuiving in mediumsamenstelling, wordt primair getest als alternatief voor het sterk autofluorescerende LB-medium. Hier wordt onderzocht of M9-medium kan worden gebruikt voor het volgen van de bindingsdynamiek zonder de huidige bindingsverdeling, geobserveerd in LB-medium, te beïnvloeden. We ontdekken geen effect van mediumsamenstelling op de bindingsverdeling, waardoor M9-medium een goed alternatief is voor het hoog autofluorescerende LB-medium om de positie van bacteriofagen over tijd te volgen met behulp van fluorescentiemicroscopie. Daarentegen constateerden wij, bij het vergelijken van onze resultaten met een eerder gerapporteerde verdeling van T4 faag op *E. coli* K-12, een significant effect van een verandering in receptorspectrum op de bindingsverdeling. Hier constateren wij dat er een shift in de mate van polaire binding plaatsvindt. Deze resultaten vormen een eerste

stap op weg naar het begrijpen van het zoek- en beslissingsmechanisme en het identificeren van sleutelfactoren die een rol spelen in dit proces.

Hoofdstuk 4 onthult voor het eerst de gedetailleerde interactiedynamiek tussen gelabelde bacteriofaag T4 en gastheercel *E. coli* B. We laten zien dat deze methode in staat is om verschillende bewegingsregimes te onderscheiden die overeenkomen met de verschillende stadia van zoekacties van de faag. Meest belangrijk, we leveren direct bewijs van stapsgewijze beweging van de faag op/nabij de cel. Wij geloven dat deze discrete op/nabij-cel beweging tot stand komt door ofwel een wandeling van de faag middels binding en daaropvolgende ontbinding van individuele faagreceptoren met gastheercelreceptoren en/of "hoppen" doormiddel van herhaalde korte periodes van hechting en loslating van de faag aan gastheerreceptoren. Samen vormen deze bevindingen de eerste stap naar een diepgaander begrip van het mechanisme achter het proces van het vinden van een geschikte gastheercel en het nemen van de beslissing om deze te infecteren.

In **hoofdstuk 5** geven we eerste inzichten in de bindingsverdeling en dynamica van R2-type pyocines met *Pseudomonas aeruginosa* 13s. Hier laten we zien dat de bindingsverdeling en het zoekproces van individuele R2-type pyocines lijken op die waargenomen voor faag T4. Binnen dit hoofdstuk hebben we ook een methode ontwikkeld voor het volgen van cel depolarisatie. Hiervoor hebben we de concentratie van de membraanpotentiaalgevoelige fluorescente kleurstof $DiSC_3(5)$ geoptimaliseerd en aangetoond dat we deze methode kunnen gebruiken om de dissipatie van de membraanpotentiaal van 13s-gastheercellen te volgen bij blootstelling aan pyocines. Met verdere ontwikkeling beschikt deze methode het vermogen om het 'doden' van pyocines live en op een enkel-gastheercelniveau op een kwantitatieve manier te onderzoeken.

Ten slotte onderzoeken we in **hoofdstuk 6** hoe de uitbreiding van de bestaande kennis met de in dit proefschrift gepresenteerde inzichten een nieuw niveau van begrip brengt van het mechanisme achter de dynamische interactie tussen faag/faagachtige deeltjes en gastheer op nanoschaalniveau en hoe dit zou kunnen bijdragen aan de ontwikkeling van nieuwe toepassingen.

Table of contents

1

General introduction: Ancient warfare at nanoscale

Lisa L. Dreesens, Marie-Eve Aubin-Tam, Hubertus J. E. Beaumont

Bacteriophages are abundantly present on our planet, with estimated numbers of 10^{31} they outnumber bacteria in 10-fold. They are obligate parasites, and rely solely on the infection of bacteria in order to produce progeny. Infection starts with the specific attachment of the phage to its host. Here the phage uses its receptor binding proteins to bind to the host, followed by DNA injection. These interactions between phage and host have led to the so far never-ending warfare playing at the smallest scale, driving evolution in both phage and bacteria. Studying the biology of phages and their obligate relationship with their host will not only lead to understanding of their important role in shaping and maintaining microbial communities affecting our biosphere, but also aid development of advanced genetic and diagnostic tools, and enable the use of phages and related protein complexes as novel therapeutic agents. Here we provide an overview of the basic structure and function of phages and related phage-tail like particles and introduce the main questions addressed by the research described in this thesis.

*Part of this chapter served as basis for the following publication: Nobrega, F. L., Vlot, M., de Jonge, P. A., **Dreesens, L. L**., Beaumont, H. J. E., Lavigne, R., Dutilh, B. E., & Brouns, S. J. J. (2018). Targeting mechanisms of tailed bacteriophages. *Nature Reviews Microbiology*, *16*, 760–773. https://doi.org/10.1038/s41579-018-0070-8

1

1.1 Introduction

We live in a world that relies on, and is driven by, microbial ecosystems. Bacteria (and archaea) have been in a war with phages, for most likely over a billion years, dominating life on earth from the early beginnings. Bacteriophages, or phages, are the most abundant quasi-autonomous replicating biological entities on earth. With estimated numbers of 10^{31} particles they outnumber bacteria by 10-fold [1]. They act as obligate parasites, lacking their own metabolism, and depend therefore on the infection of a bacterial host for their replication. This never ending co-evolutionary arms-race at nanoscale has driven and evolved endless bacterial defense systems [2, 3], such as restriction-modification, CRISPR-Cas and the abortive infection system. However, phages have on their turn evolved many counter-adaptations to circumvent these bacterial phage defense mechanisms. Due to the constant attack and high number of phage particles in the environment, there is an enormous evolutionary pressure on bacteria to evade phages. Recent evidence indicated that viral numbers found within the ocean reach the level of saturation, with up to 10^7 virus-like-particles (VLPs) per milliliter [1, 4-6]. With these enormous numbers is has been predicted that on daily basis phages kill about 4-50% of the oceans bacterial population [7]. This would suggest that the result of this warfare occurring at nanoscale has a significant impact on global scale. This has been shown to play an important role in the exchange of nitrogen and carbon between organisms and the environment, affecting the climate by influencing biogeochemical and ecological process [1, 4], and drive evolution of the biosphere by influencing the composition of communities and shuttling genetic information between organisms [8], resulting among others in the evolution of virulence within human pathogens [9]. Besides this warfare between bacteria and phages, bacteria may also, in some occurrences, benefit of the infection by a phage when they carry and transfer beneficial genes from one organism to the other. Phage facilitated transmission of such genes between host strains has played an important role in microbial evolution over all those years [10]. An intriguing example are instances of so-called evolutionary co-option [11] — the use of an existing biological structure to accomplish a new function by mutation and selection — that has led among others to a range of bacteriophage-tail like particles that perform new functions inside cells. These phage-like structures lack their own genome and are expressed and used by bacteria as a bacterial defense system to outcompete bacterial rival strains.

Even after an extended period of research, the fundamental insights about the target-finding process, DNA ejection, replication and propagation, as well as, host selectivity and adaptability are still not fully understood. New innovative techniques available today, i.e. advanced and high-throughput sequence technologies, new and improved techniques to study single-phage-host behavior in real-time and in its native environments i.e. fluorescent and electron microscopy, AFM and optical tweezers, can help to shed light on some of the answers of these questions. Understanding of the dynamical interactions between microorganism and phage (co-evolution processes) is key to comprehend not only their mechanism but also their relationship into viral emergence and the never-ending battle between phages and bacteria. In addition, it will most likely aid the development of new biotechnological tools and novel therapeutic agents to fight bacterial pathogens.

1.2 History

Even though we know about bacterial existence since the 1670's, bacteriophages were only discovered about a hundred years ago. First observations of bacteriophages were documented by the British pathologist Frederick William Twort in 1915, who described the presence of a transmissible agent causing bacterial death. Two years later, Felix d'Herelle, a French-Canadian, independently described a similar sighting of clearing zones that were present on bacterial lawns of Shigella cultures. He referred to this agent as 'bacteriophage', which translates to bacteria-eater and refers to the bactericidal property of this agent [12]. Once discovered, phage research was followed by many others during the 1920s and 1930s who realized that these biological entities could kill bacteria and had the potential to be used as a therapeutic agent for treating bacterial infections. However, the discovery of penicillin in 1928 led to the pre-era of antibiotics. The ease and broad spectrum of antibiotics lead to the abandonment of bacteriophage research in most western countries. In Eastern countries, research and practice of using bacteriophage did continue, and is today still successfully used to treat certain bacterial infections [13].

Nevertheless, phage biology has brought us lots of insight and provided us with new tools that we still use today in modern biotech industry, e.g. polymerases, restriction and ligase enzymes, gene-expression systems, site-specific recombination, phage display, and the newly discovered gene editing tool CRISPR [14, 15].

The last decade, phage biology has regained interest for use to treat bacterial infections. This recent renaissance seen in phage biology is triggered by the rise of multi drug resistant (MDR) bacterial strains and the need for novel therapeutic agents and development of new tools. In addition, the awareness and rapidly growing majority of newly discovered phages across all kinds of environments triggers research to elucidate the prominent and profound role of phages in shaping microbial communities in all ecosystems, including that of our own biome [16].

1.3 Phage life cycles

All viruses, including phages, are obligate parasites and are therefore incapable of reproducing on themselves. For replication, they are entirely dependent on infecting bacterial cells. The first stage in the phage live cycle starts with adsorption - recognition and binding of the phage to the bacterial host cell surface. This adsorption process relies on phage binding proteins that recognize receptors present on the outer bacterial surface. This recognition process is very specific and in turn defines the host range – the bacterial strains to which the phage can adsorb and infect. In some cases, the cell receptors are obscured by the host membrane. Certain phages are capable of degrading the membrane with enzymes to reach the receptors and facilitate binding. After binding to the host, the next step is to surpass the cell membrane and eject the genomic material within the host. In some occasions, this cell penetration process is supported by lysozymes, enzymes capable of forming pores in the peptidoglycan layer of bacteria, providing the necessary access to reach the cytoplasm. Once the DNA has been delivered into the bacterial cell, different phage life cycle strategies can be adopted, depending on the type of phage (virulent or temperate) and metabolic state of the host.

In case of a virulent phage, the phage will go into a lytic cycle (Figure ***1.1***), acting as a typical virus, hijacking its host cell and using the host cell machinery to produce new progeny viruses. After replication and assembly of progeny, lysozymes are produced that result in the lysis (burst) of the host cell releasing progeny to the environment. This latter process kills the host cell. These new phages can then, on their turn, infect a host and start the cycle again. Since this life cycle involves killing the host cell, it heavily aids the bacterial population dynamics and therefore plays an important role in shaping and maintaining microbial communities.

This is in contrast with a temperate phage, which follows a lysogenic cycle (Figure ***1.1***), where the phage integrates its genome into the bacterial chromosome, or exists as plasmids within the host cell, becoming a so-called prophage. This 'dormant' state allows the phage to reproduce and being maintained without killing its host. Here the DNA of the phage is replicated alongside that of the bacterium and passed to each daughter cell. It stays within this 'dormant' state until a cue (i.e. specific stimuli), such as DNA damage, triggers a switch in the life cycle of the prophage and activates the lytic cycle. This lysogenic cycle can hold-up for thousands of bacterial division cycles.

Lastly, other known and most likely less used life cycle strategies are the pseudolysogeny route and the chronic infection (Figure ***1.1***). Pseudolysogeny can occur when the phage enters a host that remains in a unfavorable growth condition (e.g.

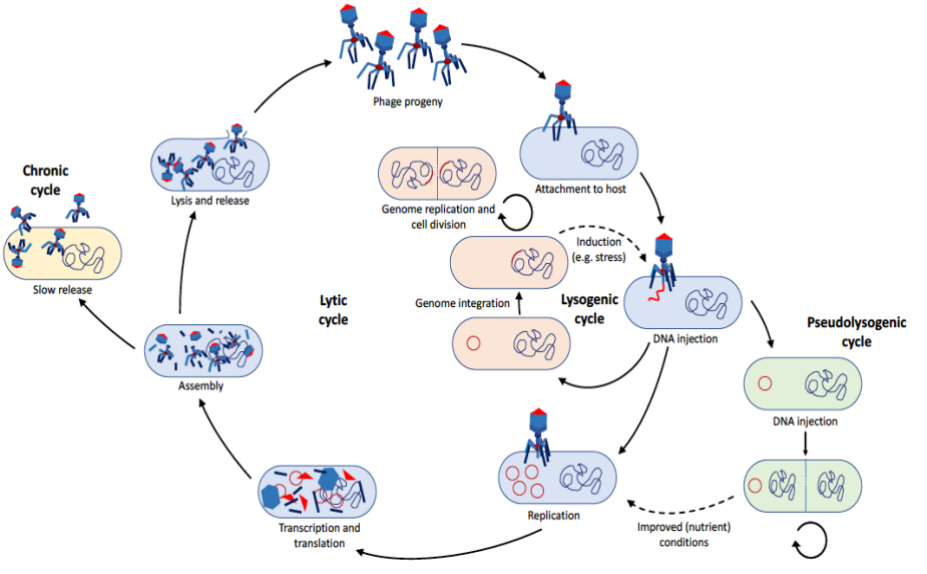

Figure 1.1: Various life cycles of a bacteriophage. Virulent phages go through a lytic life cycle (blue cells). After binding and DNA injection the phage hijacks the bacterial machinery for replication, transcription and translation to assemble new virions and release them into the environment by lysing the host cell. Alternatively, temperate phages have a lysogenic life cycle (orange cells), ensuring insertion of the phage genome into the genome of the host, resulting in replication of the phage genome in synchrony with that of the host cell. Less common/studied life cycles are the pseudolysogenic cycle (green cells), where host growth conditions are unfavorable and the phage genome neither replicates nor integrates awaiting better conditions to initiate either the lytic or lysogenic cycle, and the chronic cycle (yellow cell), where phage replication and release runs at a slow pace, preventing killing of the host cell.

starvation). Here the phage replication cycle is stalled till host conditions improve, where after either the lytic or lysogenic cycle will be initialized. During the chronic infection cycle, phage infection results in a slow pace production and subsequent release of new progeny ensuring the survival of the host cell.

1.4 Ecology

Tailed phages are believed to roam the earth for approximately 3.5 million years, and most likely already existed prior to the development of the more complex life forms like eubacteria and euryarchaeota [17]. Since phages lack any form of metabolism they solely rely on a bacterial host for replication, linking their abundance and distribution to that of their host. Bacteria are found in all kinds of environments and this has hold true for phages as well. First insights, based on culturing techniques, led to the belief that phages were scares and therefore played an irrelevant role in shaping microbial environments [19]. But recent modern techniques, like for example epi-fluorescence microscopy and sequencing, revealed that phages outnumber bacteria greatly, making them the most abundant biological entity found on our planet [1, 4-6]. High phage concentrations were found among others in soils, the ocean, and even within our own digestion track [18, 20].

Experiments involving chemostats have shown a close relationship between the abundance and diversity of phage and host populations, showing that these cannot endlessly grow due to the cost to phage resistance and *vice versa*. Therefore, this relationship has not only a substantial effect on the maintenance of the density of bacterial communities, but also drives diversification by changes in the bacterial competitors and transfer of genes among closely related strains, via horizontal gene transfer by insertion, deletions, inversions, or other rearrangements of gene segments on the bacterial genome. Some of these led to the encoding of useful or beneficial genes, i.e. toxins and anti-phage defense systems. However, the opposite holds true as well. Since phages are dependent on the presence of its host, their killing activity cannot become unrestrained, as the host would subsequently diminish and with that, the capacity of phages to replicate. Therefore, phages have developed sophisticated mechanisms for sensing the host abundance. One such mechanism is to produce peptides during the last stage of the phage life cycle. These are released during the burst of a cell and serve as a signal for the phage progeny to switch to the lysogenic cycle [21]. Another mechanism involves the hypervariable area on the RBPs that is prone to mutation allowing a switch in the recognition of receptor or host. This warfare that occurs on the smallest scale, influences not only the bacterial communities around them, but on its turn, has an (in)direct impact on our biosphere by affecting biochemical and ecological processes on global scale [1, 4].

With the development of metagenomics tools, new phages are found and identified at a rapid rate and in high numbers in all kinds of environments. All these pieces of information gained by these enumeration and identification methods slowly unfold and merge together, improving our understanding of their abundance and diversity, and their profound impact on the ecology. Continuing research with these new tools will help closing the remaining gaps within our understanding of phage evolution and phage-host interaction, and in turn lead to a better understanding of their behavior and

their impact on the environment, as well as, aid the developments of tools that can be used in the pharmaceutical and biotech industry.

1.5 Structure and taxonomy of phages

After the discovery of several kinds of phages and describing their morphology for the first time using negative staining EM in the 1940s [22], Lwoff *et al*. provided in 1962 the first recognized phage classification system [23]. Over the years, iterations and new discoveries were added [24, 25] leading to the taxonomic classification system that we use today. This is established and maintained by the International Committee on Taxonomy of Viruses (ICTV). Today it contains more than 8000 documented bacteriophages that are capable of infecting over 140 bacterial genera [29]. Within the ICTV these phages have been further distinguished and divided into 13 families and 30 genera [17, 26-29].

All these classified phages are composed of a protein coat (capsid) that encapsulates the genetic material. Up till today phages are being classified according to their genomic and morphological information. Genome typing includes classification based on size and type, which might be either RNA or DNA, and single (ss) or double-stranded (ds). In addition, classification is based on the morphology of the capsid. The capsid has a polyhedral (often icosahedral) structure, either with or without an attached tail, or presents itself in a filamentous or pleomorphic form. Lastly, a diversification is made based on the presence or absence of a lipid envelope. This divides phages in the following families, Myo-, Sipho-, Podo-, Ino-, Micro-, Tecti-, Cortivo-, Plasma-, Cysto-, Levi-, one unclassified, and the recently added family Ackermann- and Herrelleviridae (Figure ***1.2***) [30, 31]. These families are divided further at the genus and subgenus level from criteria based on host range and genome organization, among others.

So far, thousands of phages have been classified today and every day new phages are being discovered. However due to the high rate of diversification and exchange of genes that has taken place over all these years, phage genomes became like a 'mosaic', resulting in homology in both structure, genome and morphology, lacking the presence of distinct markers to classify phages within their own phylogenetic affinity via the traditional hierarchical system. This results in a large group of phages that cannot be classified within an order. To circumvent this problem and to create some structure in the system, a "polythetic species concept" was created and mostly applies to define the phage genera. Here species are defined by a set of characteristic properties that are present among members of the same group [32, 33]. With the rapid developments in the field of metagenomics, numerous new phages genomes are being discovered. However, standard culturing or morphological assessment is lacking, overwhelming the system with new information that cannot be used for classification of phages according to the traditional guidelines. For this reason, the ICTV classification system needs to be updated, providing new guidelines for phages that are being discovered by genomic-based methods and assigning them accordingly. Others accept the fact that genomes and structures are to scrabbled, and therefore cannot be accurately traced back anymore and propose other ways of classification over the currently used hierarchical tree, e.g. a network that presents relationships to classify and group [18, 30, 34].

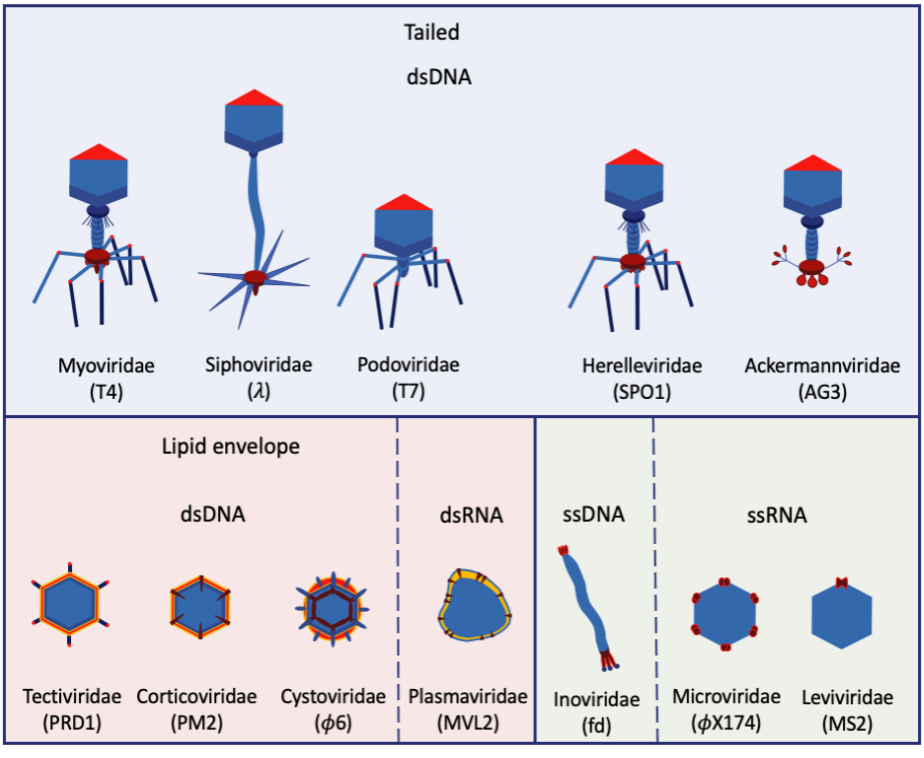

Figure 1.2: Classification of bacteriophages according to the ICTV. Phages are classified according their morphology, genome type and size, presence of a tail or lipid envelope, and having either double or single stranded DNA or RNA. Model phages of each family can be found within the brackets.

1.6 Phage-tail like particles

During scanning of bacterial genomes, protein complexes homologous to phage tail-like components were found. These phage tail-like components are believed to be phage remnants co-opted by bacteria, which have evolved over time to become fundamental components of the bacterial machineries, with individual parts adapted to each perform a different biological function other than the biological function of phages. They are produced by bacteria to outcompete other related strains. Analyses of phylogenetic relationships among phages and homologous protein structures indicated a wide diversity of protein complexes with a conserved protein fold and assembly mechanism. Interestingly, these phage-derived complexes, from here on referred to as phage-tail like particles, evolved repeatedly in disparate phage lineages (Figure ***1.3***). This reveals the creative potential of exaptation. Comparing all the phages and phage-tail like particles known today reveals a diversity that points to the fact that all of these structures have diverged from a single common ancestor. Such an ancestor must have consisted of at least the few simple structural components found within all the present structures. However, the fast turn-over and evolution among them over all these years make it hard to trace things back to their origin.

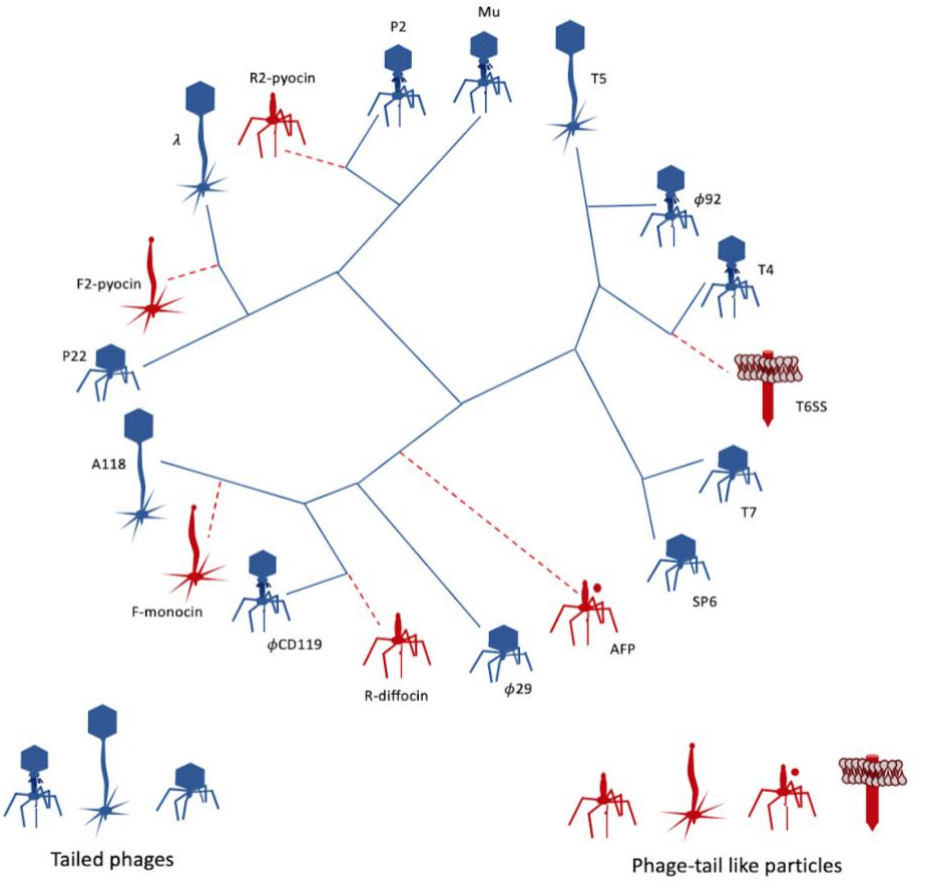

Figure 1.3: Evolutionary relationships of a subset of tailed bacteriophages and phage-tail like particles. Radial cladogram of phages (blue) and phage-tail like particles (red) generated with the Viral Proteomic Tree Server (http://www.genome.jp/viptree/), which clusters phages on the basis of protein sequence diversity and proteome composition [35]. The branch lengths represent mutational distances using the distance measure of the Viral Proteomic Tree Server. The various branches from which phage-tail like particles evolved (lengths were not quantitative) were constructed based on the following references [36-40] and give an indication of the phylogenetic relations. Consistent with other phylogenetic analyses, phage-tail like particles appear to have evolved repeatedly in disparate linages of phages [36, 41, 42]. Comparing all the phages and phage-tail like particles complexes known today reveals a diversity that points to the fact that all of these structures have diverged from a single common ancestor. Such an ancestor must have consisted of at least the few simple structural components found within all the present structures.

1.6.1 Structure of phage-tail like particles

Nowadays we know that the genes encoding functional proteins are conserved among phages, allowing us to identify the function of genes in unknown phages or phage-tail like particles [43]. During the last decade, the genomic sequencing of bacterial genomes has enabled the addition of a substantial and still growing body of gene sequences to the database. Some of these gene orders were found to be similar to those of phages, showing resemblance in genetic clusters of tail structural modules (i.e. assembly proteins or chaperones, regulatory genes and often a lysis cassette), but are lacking a

few of the essential genes (i.e. capsid and DNA-packaging and replication modules), making them a distinctively different class with so-far mostly unknown functions. These phage-tail like particles are composed of at least three groups, namely tailocins, Bacterial Secretion Systems (BSSs), and Phage-like Protein-Translocation Systems (PLTSs) (Figure ***1.4***). These are easily morphologically distinguished from phages by the lack of a capsid and genetic material. Phage-tail like particles share a conserved protein core with strong homology to phages, but with individual parts that are adapted to each perform a different biological function. All phage-tail like particles contain a tail-tube, spike and baseplate, and, with the exception of BSSs, RBPs [38].

The best described phage-tail like particles in literature are the tailocins, first observed by Jacob in 1952 as high molecular weight bactericidal protein complexes induced by *Pseudomonas aeruginosa* [44] and later described in more molecular detail by Kageyama and Egami in 1962 [45]. Based on their morphology they can be divided into two subgroups, rod-like (R)-type tailocins with a contractile tail resembling phages from the *Myoviridae* class and flexuous rod-like (F)-type tailocins with a long flexible tail tube resembling phages of the *Siphovirdae* class [39]. Tailocins are found in high numbers across the genomes of different species, targeting both gram-negative and gram-positive bacteria [91].

Type VI Secretion system (T6SS) found in different bacterial species, is the only system within the BSS that shows to be evolutionarily related to *myoviridae* phages [37]. Unlike phages and tailocins, T6SS does not hold RBPs and is lacking two of the five core baseplate proteins as well as the tape measure protein found in phages and tailocins. In addition, it is the only subgroup that is not secreted by the producer strain. It remains intracellularly, where it is anchored within the cell membrane [46]. Upon contraction, it punctures through its own cell membrane as well as that of the target bacteria located nearby. Interestingly, the tail-tube is neutrally charged holding one or multiple effectors that are, upon assembly, incorporated in the tail-tube or positioned on the side of the tail-spike [47-49]. They are released, upon disassembly of the tail-tube, targeting both pro- and eukaryotic cells. The producing strain is insensitive to their own effectors. Further, it is the only contractile system currently known that contains a recycle function. After disassembly, it re-uses subunits for a new round of assembly, reducing energy required for *de novo* synthesis of proteins. Single genomes can encode multiple T6SS that seem not to be co-regulated, and might have distinct purposes [50]. Their ecological function is not fully understood, but evidence is suggesting that they play at least a role in virulence and symbiosis [51]. It has recently been shown in *Serratina marcescens* that RcsB regulates the expression of T6SS. This expression only exceeds basal level upon damage due to exposure of effectors of a competing strain [52].

PLTS resemble phages of the *Myoviridae* class and include at least the antifeeding prophage (Afp) identified in *Serratia entomophila* [53] and its homologue Photorhabdus virulence cassettes (PVCs) induced by *Photorhabdus luminescencens* and *Photorhabdus asymbiotic*a [54]. These PLTS have a similar morphology as tailocins but share common molecular features with T6SSs [55]. Namely, PLTS encodes for PAAR repeat proteins, AAA+ ATPase, effectors and is believed to be involved in translocation. So far, no lysis system has been found, but PLTS does seem to be secreted into the medium. Interestingly, both Afp and PVCs are not bactericidal but insecticidal [54], showing that

targeting has evolved beyond that of bacteria. Their ecological implications remain to be elucidated.

Other tail-like structures with so-far unknown functions were found by genome analysis. An example of such recently found phage-tail like particle was the Metamorphosis-associated contractile structure (Mac) (MacT1 and MacT2) encoded and secreted by *Pseudoalteromonas luteoviolacea* [56]. Mac's are large clustered arrays of contractile tail-tubes. Ten to hundreds are connected on one side, with TFs and baseplates extending outward (Figure ***1.4***). Further, the TFs seem to be interconnected with each other forming a hexagonal net. Apart from the fact that Mac's trigger metamorphosis of *H. elegans*, their ecological function remains unknown. Similar hexameric arrays have also been described for *Streptomycetes endus* [57].

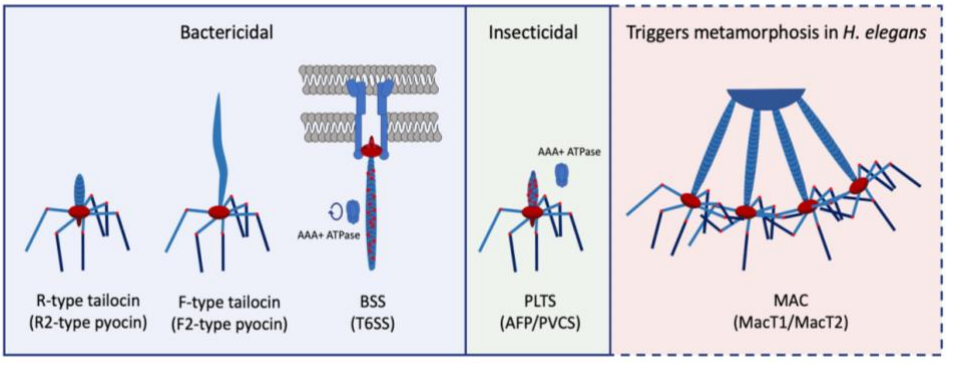

Figure 1.4: Schematic representation of phage-tail like particles that are produced by bacteria. All phage-tail like particles are homologs of contractile phage tails, with the exception of F-type tailocins which resemble flexible (non-contractile) phage tails, that target and puncture bacterial related strains (blue square). T6SS is exceptional because this structure is membrane bound and it is the only PBLT for which the tail is recycled after being used. So far, no TFs have been detected and therefore its triggering mechanism is unknown. PLTS are similar in structure to the R-type tailocins, but also show homology with T6SS containing effector molecules and having AAA+ ATPase. However, they are distinct from the bactericidal phage-tail like particles as they seem to be insecticidal (green square). Lastly, there are large clustered arrays comprising about 100 contractile tail-like structures (red square). These arrays are organized, with the LTFs and baseplate facing outward. It seems that these structures are held together by a hexagonal net that connect one to another. The ecological function of these structures is not well studied, but they seem to play an important role in triggering the metamorphosis of *H. eligans*. Examples of the phage-tail like particles of each family are indicated in brackets.

1.7 Mechanisms of host recognition, adsorption and DNA ejection

Currently the public genome database is mainly comprised (85%) with tailed bacteriophages from the order *Caudovirales.* These phages contain a double-stranded genome and an icosahedral head with a tailed morphology. The families within this order are *Sipho*- with a long non-contractile tail (compromises 56% of tailed phages), *Myo*- (compromises 17% of tailed phages) with a long-contractile tail, *Podo*- with a short non-contractile tail (compromises 12% of tailed phages), and the more recently discovered *Herelle*- and *Ackermannviridae* (compromises <3% of tailed phages) also with a long-contractile tail [18, 28, 58]. The use of a tail for the infection process is evolutionarily advantageous over other strategies of viral infection and therefore may explain that the *Caudovirales* are largest found order within the phage classification

system. The end of the tail contains RBP's, i.e. TF, tail spikes and tail tips, that are capable of recognizing bacterial host receptors, i.e. porins, lipopolyschariде (LPS), and teichoic acids. The tail and RBPs determine the host specificity and the process by which the phage penetrates the cell to eject the genome and therefore play an important role in the first stage of the phage infection process.

Myoviridae, are a family of phages belonging to the *Caudovirales* order with a long contractile tail (Figure ***1.2***). A well-studied model-phage within this family is T4 phage. This is also the phage that we will study within the scope of this thesis. T4 phage contains more subcomponents than most other phages within this family, making its mechanism more complex. Phages within this family can be easily morphologically distinguished based on the presence of a contractile tail. The tail of these phages, located between the capsid and baseplate, consist out of an inner tube and a contractile outer sheath (Figure ***1.5***). Attached to the baseplate are the receptor binding proteins (RBPs), which are the tail fibers (TFs), tail spikes and the central tail spike, which each can interact with host-receptors present on the outer membrane surface of bacteria. T4 specifically, has besides the six long tail fibers (LTFs) also an additional set of six short tail fibers (STF). These LTFs alternate between folded and extended conformation, and are the ones interacting with the host receptor, i.e. LPS or outer membrane protein C (OmpC), ensuring docking of the phage to the cell surface [59, 60]. Based on static cryo-EM images, it is believed that once T4 has docked to the cell surface with at least one of the LTFs, the phage moves over the host cell surface by subsequent binding and unbinding of individual LTFs, allowing the phage to 'explore' the cell surface in a reversible manner (Figure ***1.6***) [59, 61]. Recent structural studies, involving X-ray crystallography and cryo-EM together with powerful 3D reconstruction, have revealed new insights on the structural rearrangement and led to an atomic mechanistic model of the initial stages of the phage infection process [59]. Once enough of these LTFs are bound (estimated to be at least three out of six LTFs [59, 62]), a signal is transmitted to the baseplate, leading to conformational changes that release the STFs. These can interact with the host cell receptor LPS (Figure ***1.6***). Binding of these STFs orients the phage perpendicular to the bacterial membrane, bringing the baseplate closer to the surface [61]. Binding of the STFs results in further expansion of the baseplate triggering conformational changes that unlock the stored energy in the sheath. Acting like a powered spring, the sheath contracts up to roughly 37% of its original length [62-67], subsequently piercing the inner tail tube like a needle through the cell wall of the host. The tip of the inner tail tube contains three lysozymes that ensure degradation of the peptidoglycan layer [61, 68], allowing the tube to reach the cytoplasmic membrane. Once the passage is created, DNA can be ejected in the host cell's cytosol (Figure ***1.6***). This latter process can occur in some cases in less than a minute [69, 70].

Interestingly, several of the steps within the phage infection process have shown to respond to environmental factors, i.e. ion concentration, temperature, pH, and organic co-factors [71-74]. For example, binding of the co-factor molecule L-tryptophan to the LTFs of phage T4 has shown to result in their extension [75], while the molecule indole inhibits this process by forcing the LTFs to remain in the retracted position against the phage body [75]. This has shown to affect the binding kinetics (i.e. binding rate and efficiency [76, 77]). The concentration of these molecules within the environment have been shown to change with respect to the growth phase of cells [78]. It could be that

phage T4 uses these molecules as sensor for the presence of a metabolically active host and enhance the facilitation between TF-receptor interaction.

Siphophages have a long, flexible, non-contractile tail (Figure ***1.2***). The cues and series of triggering events that occur after irreversible binding to a cell remain poorly understood. The best studied model phage within this family is phage λ, which uses its tail to dock to the bacterial maltose pore LamB through which it delivers its genome into the cell interior [79, 80].

Lastly there are podophages, which have a short, non-contractile tail (Figure ***1.2***). These tails are marked by the presence of an adaptor protein that ensures the attachment of the tail to the capsid. Lacking a baseplate, the other side contains a nozzle to which six or twelve TFs or tail spikes are attached that can recognize and bind to host cell receptors [81]. One of the model phages studied within this family is T7, which uses its TFs to interact with the host cell receptor LPS. Interaction between the two arranges the phage in the correct orientation. Once this position is reached, initiation of protein and DNA ejection is triggered. These proteins ensure the DNA can translocate to the cell cytoplasm, starting the second stage of the phage infection process, replication [82].

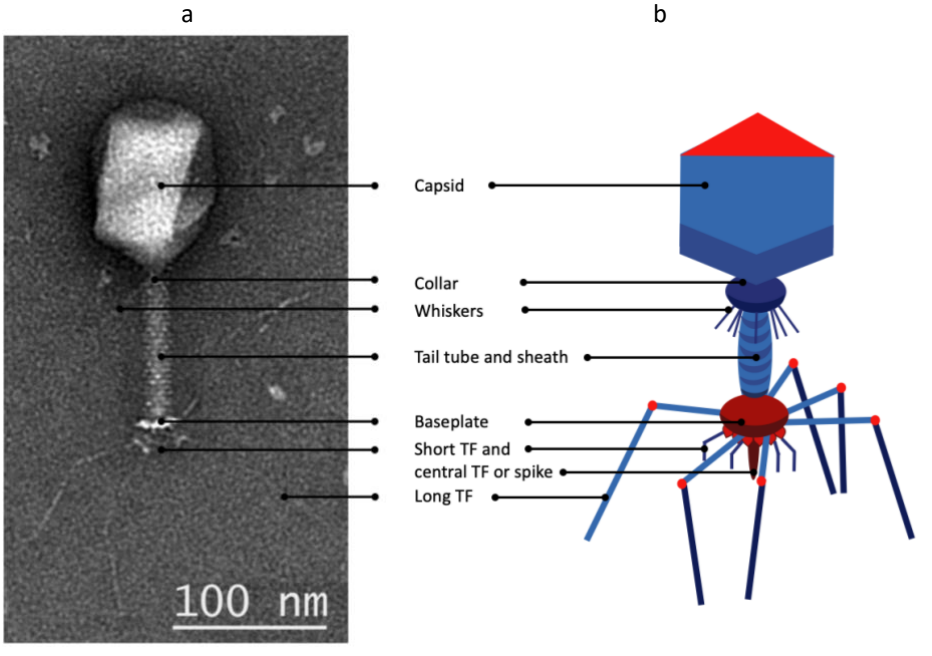

Figure 1.5: Representative structure of myoviridae phage T4. a, Negative stain electron micrograph of T4 phage, from the family *Myoviridae*. **b,** A schematic image of the model phage T4, indicating all structural components.

Now, let us consider host-cell interaction mechanisms of phage-tail like particles. Among these, R-type pyocins of the tailocins class are the best studied structures. Within this group there are five subgroups (R1 - R5) showing all a conserved N-terminus

but diverged C-terminus [83] allowing for recognition of different hosts by binding to different moieties of the host cell receptor LPS [84]. The host range of R-type pyocins, as well as several other tailocins, have been modified via engineering. Here the C-terminal part of the TFs of pyocins was swapped with those of other tailocins, as well as, with those of phages [83, 85, 86]. As these "reprogrammed" tailocins remained active and structural homology between the sheath and baseplate proteins was found [87], their mechanism of transmitting the signal of contraction upon host cell recognition can be assumed similar, if not the same, as that of phages. This points towards a universal mechanism of contraction that might hold true for all contractile systems. Energy stored in the sheath protein during assembly is released upon contraction and results in the inner tube of phage tail being pushed through the membrane [88]. Interestingly, the length (and therefore also the stored energy) of these contractile structures differs among these systems. With tailocins having the shortest tail-tube and T6SS the longest. This might be coupled to their function (transportation of protons and ions for tailocins and effectors for T6SS). T6SS is the only complex for which, so far, no TFs were found. What triggers the contraction of these systems remains an open question. However, given that for the other systems the cue for sheath contraction originates from conformation changes within the baseplate, T6SS might operate similarly. It has been proposed that TssM and TssL, located within the outer membrane, might act in a comparable way as the baseplate of phages by

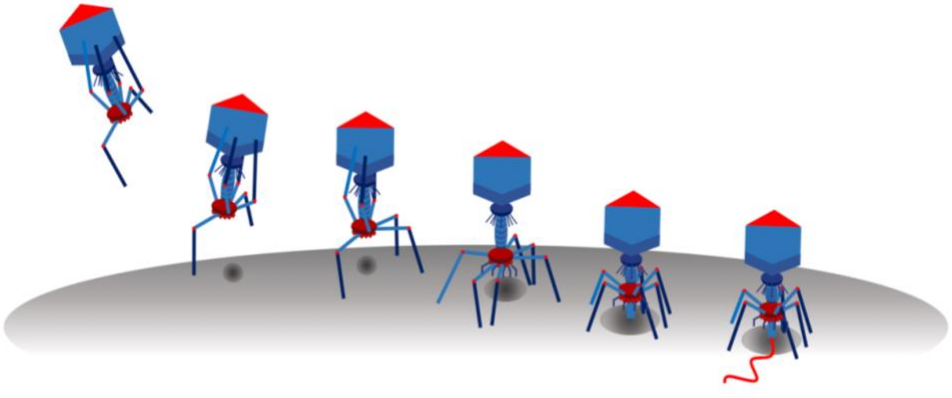

Figure 1.6: Schematic representation of T4 adsorption process over time. There is a so-called two-step binding process. From left to right: Phages are freely diffusing in their environmental surrounding, with most of their LTF in the retracted position. Once a phage collides with a potential host one of the extended LTFs can interact and bind specifically, but reversible, to a host receptor. While keeping the phage docked at the surface, other LTFs have the time to interact with nearby host cell receptors. This happens in a transient manner, allowing the phage to move over the cell surface by subsequent alternation of attach- and detachments of the individual LTFs. Eventually this leads either to: detachment of the phage - not enough LTFs are bound to the host, or permanent attachment (irreversible binding). The latter state is reached once at least three out of six LTFs are bound. Irreversible binding triggers a series of conformational changes within the baseplate. First, the STFs are released that can now interact with the host cell surface, orientating the phage perpendicular and pulling it closer to the cell surface. This triggers a second conformational change in the baseplate, allowing the sheath to contract. This results in subsequent penetration of the inner tube through the cell membrane, where after the DNA can be ejected.

undergoing conformational changes triggering sheath contraction [89, 90]. How PLTS structures recognize the host remains unknown, but their TFs have shown to resemble those of the *Adenoviridae* phages (non- tailed class of phages) [53] and might therefore be different as observed for other tailed phages, allowing them to target insect cells.

The vast majority of this information was obtained by experiments in bulk and through analysis of static EM images, which allow us to observe with high resolution the phage structure during the initial main stages of the infection process, giving valuable mechanistic insights. However, these methods do not allow us to gather any dynamic information between phage and host at the single particle level, which is needed to understand how the functions of phages and phage-tail like particles emerge at the nanoscale. Some related questions are for example; how does a phage search its target and decides to infect a cell? Is there a universal process employed by all phages and/or phage-like particles, or are there key-strategies found within classes or families? Does binding always lead to infection, and what is the chance of failing in one of these steps along the way? Does cell structure and receptor organization, as well as the current growth state of the cell, play a role in the binding dynamics and decision making process of a phage? And is this process affected by environmental conditions, i.e. temperature, pH, salinity, or certain co-factors?

Throughout this thesis, we describe a framework and method that makes use of fluorescence microscopy, that can be used to study the dynamics and binding kinetics around the target-finding process of phages (and tailocins) in real-time at high spatial and temporal resolution. This sheds the first light on this still unknown territory and answers questions regarding the effect of receptor and environmental components on the binding distribution and explores the fundamental mechanism behind the dynamics of phage T4 and pyocin R2 on-cell motion.

1.8 Thesis outline

Chapter 2 on page 23: “Establishing methods to study bacteriophage/pyocin-host interactions at the single-particle level”.

In chapter 2 we describe a method to follow and analyze single-particle trajectories using fluorescent microscopy. We first describe how the flow cell used for analysis is built-up and how cell adherence and cell density to the coverslip are optimized. Secondly, we describe the optimization process of fluorescent labeling of T4 phages, and show that this labeling procedure can be extended to pyocin R2. Lastly, we provide a description of a workflow and semi-automatic detection method that can be used to analyze the images and movies obtained from fluorescent microscopy in order to determine the binding distribution of phages and/or pyocins to its host, as well as, to track and study the dynamic interactions of single-phage or pyocin particles with their host cell.

Chapter 3 on page 95: "Irreversible binding distribution of phage T4 on *Escherichia coli* B is targeted towards the cellular poles".

In chapter 3 we investigate the binding distribution of fluorescently labeled T4 phage to its host *E. coli* B using single-particle fluorescence microscopy. We find that T4 presents a non-uniform binding distribution on *E. coli* B, with a bias of binding towards the cellular poles of a cell. We compare our data with a previously reported distribution of T4 on *E. coli* K-12 to investigate whether a change in target host-receptor influences the binding distribution. We report that a change in receptor spectrum affects the strength of polar binding significantly. Lastly, we investigate whether environmental factors, i.e. medium components, have an influence on the irreversible binding distribution. Our study reveals no detectable difference in distribution between irreversibly bound T4 phages and *E. coli* B in LB or M9 medium.

Chapter 4 on page 117: "Long-range discrete near/on-cell motion of labeled bacteriophage T4".

In chapter 4 we investigate the dynamical interactions between fluorescently labeled T4 phage and its host *E. coli* B using single-particle fluorescent microscopy in HILO mode. We show that there are three modes of motion: free in diffusion, subdiffusive on-cell motility, and constrained motion - bound. During this reversible process of on-cell motion, we find discrete step-like behavior, which we believe is to be facilitated by either the binding and subsequent unbinding of individual LTFs or repeated brief attach and detachment of the phage to the host, allowing the phage to explore the cell-surface for an area fit for binding. Here, our study reveals for the first time the dynamical interactions between T4 and its host *E. coli* B, leading us to a more detailed understanding of the mechanism behind the target-finding process.

Chapter 5 on page 161: "Single-particle dynamics of R2-type Pyocins".

In chapter 5 we demonstrate, as a proof-of-concept, that the method described in chapter 2 can also be used for studying pyocin-R2 behavior at the single-particle level in real-time. This indicates that this method has a promising prospect to be used for studying a variety of different phage- and PTLB-host interactions at single-particle level. Moreover, our results revealed the first observations of the binding distribution and search process of single-pyocins, which seems to show resemblance with that observed for phages. In addition, we investigate the membrane-potential sensitive dye $DiSC_3(5)$ as an indicator to track depolarization of the cell upon exposure to pyocins. We found that the fluorescent intensity of the cells was correlated to the bacterial activity of pyocins and has the potential to be used in a quantitative manner to study the 'killing' process of pyocins in real-time and at single-cell level.

Chapter 6 on page 193: “Final remarks & Outlook: From the past to the future: Impact of phage research on society”.

In Chapter 6 we recapture the perspective of our research and phage research in general and how this new information aids genetic engineering as well as its prospects towards new applications.

References

[1] C.A. Suttle, Viruses in the sea, Nature 437(7057) (2005) 356-61.
[2] A. Stern, R. Sorek, The phage-host arms race: shaping the evolution of microbes, Bioessays 33(1) (2011) 43-51.
[3] S.J. Labrie, J.E. Samson, S. Moineau, Bacteriophage resistance mechanisms, Nat Rev Microbiol 8(5) (2010) 317-27.
[4] J.A. Fuhrman, Marine viruses and their biogeochemical and ecological effects, Nature 399(6736) (1999) 541-8.
[5] C.H. Wigington, D. Sonderegger, C.P. Brussaard, A. Buchan, J.F. Finke, J.A. Fuhrman, J.T. Lennon, M. Middelboe, C.A. Suttle, C. Stock, W.H. Wilson, K.E. Wommack, S.W. Wilhelm, J.S. Weitz, Re-examination of the relationship between marine virus and microbial cell abundances, Nat Microbiol 1 (2016) 15024.
[6] N.R. Fuhrman JA, Viruses and protists cause similar bacterial mortality seawater. , Limnol Oceanogr 40(7) (1995) 1236-1242.
[7] M. schaechter, Encyclopedia of microbiology, 3th edition. , Academic Press2009.
[8] A.M. Comeau, H.M. Krisch, War is peace--dispatches from the bacterial and phage killing fields, Curr Opin Microbiol 8(4) (2005) 488-94.
[9] H. Brussow, C. Canchaya, W.D. Hardt, Phages and the evolution of bacterial pathogens: from genomic rearrangements to lysogenic conversion, Microbiol Mol Biol Rev 68(3) (2004) 560-602, table of contents.
[10] H.T. Williams, Phage-induced diversification improves host evolvability, BMC Evol Biol 13 (2013) 17.
[11] J. Brosius, S.J. Gould, On "genomenclature": a comprehensive (and respectful) taxonomy for pseudogenes and other "junk DNA", Proc Natl Acad Sci U S A 89(22) (1992) 10706-10.
[12] H.-W. Ackermann, Félix d'Hérelle—découvreur des bactériophages, Med. Sci. 8 (1997) 4.
[13] S.T. Abedon, S.J. Kuhl, B.G. Blasdel, E.M. Kutter, Phage treatment of human infections, Bacteriophage 1(2) (2011) 66-85.
[14] G. Ofir, R. Sorek, Contemporary Phage Biology: From Classic Models to New Insights, Cell 172(6) (2018) 1260-1270.
[15] G.P. Salmond, P.C. Fineran, A century of the phage: past, present and future, Nat Rev Microbiol 13(12) (2015) 777-86.
[16] R. Sausset, M.A. Petit, V. Gaboriau-Routhiau, M. De Paepe, New insights into intestinal phages, Mucosal Immunol 13(2) (2020) 205-215.
[17] H.W. Ackermann, Tailed bacteriophages: the order caudovirales, Adv Virus Res 51 (1998) 135-201.
[18] M.B. Dion, F. Oechslin, S. Moineau, Phage diversity, genomics and phylogeny, Nat Rev Microbiol 18(3) (2020) 125-138.
[19] F. Torrella, R.Y. Morita, Evidence by electron micrographs for a high incidence of bacteriophage particles in the waters of Yaquina Bay, oregon: ecological and taxonomical implications, Appl Environ Microbiol 37(4) (1979) 774-8.
[20] W.B. Whitman, D.C. Coleman, W.J. Wiebe, Prokaryotes: the unseen majority, Proc Natl Acad Sci U S A 95(12) (1998) 6578-83.

[21] Z. Erez, I. Steinberger-Levy, M. Shamir, S. Doron, A. Stokar-Avihail, Y. Peleg, S. Melamed, A. Leavitt, A. Savidor, S. Albeck, G. Amitai, R. Sorek, Communication between viruses guides lysis-lysogeny decisions, Nature 541(7638) (2017) 488-493.
[22] H. Ruska, B.v. Borries, E. Ruska, Die Bedeutung der Übermikroskopie für die Virusforschung, Archiv f Virusforschung 1 (1939) 155-169.
[23] A. Lwoff, R. Horne, P. Tournier, A system of viruses, Cold Spring Harb Symp Quant Biol 27 (1962) 51-5.
[24] D.E. Bradley, Ultrastructure of bacteriophage and bacteriocins, Bacteriol Rev 31(4) (1967) 230-314.
[25] P. Wildy, Classification and Nomenclature of Viruses: First Report of the International Committee on Nomenclature of Viruses Monographs in virology, S. Karger1971, p. 81.
[26] J. Maniloff, H.W. Ackermann, Taxonomy of bacterial viruses: establishment of tailed virus genera and the order Caudovirales, Arch Virol 143(10) (1998) 2051-63.
[27] M.H.V. van Regenmortel, C.M. Fauquet, D.H.L. Bishop, E.B. Carstens, M.K. Estes, S.M. Lemon, J. Maniloff, D.J. McGeoch, C.R. Pringle, R.B. Wickner, Virus Taxonomy: Seventh Report of the International Committee on Taxonomy of Viruses, 1st ed., Academic Press, San diego, 2000.
[28] H.W. Ackermann, Bacteriophage observations and evolution, Res Microbiol 154(4) (2003) 245-51.
[29] M.J. Adams, E.J. Lefkowitz, A.M. King, B. Harrach, R.L. Harrison, N.J. Knowles, A.M. Kropinski, M. Krupovic, J.H. Kuhn, A.R. Mushegian, M.L. Nibert, S. Sabanadzovic, H. Sanfacon, S.G. Siddell, P. Simmonds, A. Varsani, F.M. Zerbini, R.J. Orton, D.B. Smith, A.E. Gorbalenya, A.J. Davison, 50 years of the International Committee on Taxonomy of Viruses: progress and prospects, Arch Virol 162(5) (2017) 1441-1446.
[30] J. Barylski, F. Enault, B.E. Dutilh, M.B. Schuller, R.A. Edwards, A. Gillis, J. Klumpp, P. Knezevic, M. Krupovic, J.H. Kuhn, R. Lavigne, H.M. Oksanen, M.B. Sullivan, H.B. Jang, P. Simmonds, P. Aiewsakun, J. Wittmann, I. Tolstoy, J.R. Brister, A.M. Kropinski, E.M. Adriaenssens, Analysis of Spounaviruses as a Case Study for the Overdue Reclassification of Tailed Phages, Syst Biol 69(1) (2020) 110-123.
[31] E.M. Adriaenssens, H.W. Ackermann, H. Anany, B. Blasdel, I.F. Connerton, D. Goulding, M.W. Griffiths, S.P. Hooton, E.M. Kutter, A.M. Kropinski, J.H. Lee, M. Maes, D. Pickard, S. Ryu, Z. Sepehrizadeh, S.S. Shahrbabak, A.L. Toribio, R. Lavigne, A suggested new bacteriophage genus: "Viunalikevirus", Arch Virol 157(10) (2012) 2035-46.
[32] M.H. Van Regenmortel, Virus species, a much overlooked but essential concept in virus classification, Intervirology 31(5) (1990) 241-54.
[33] H.W. Ackermann, M.S. DuBow, A.W. Jarvis, L.A. Jones, V.N. Krylov, J. Maniloff, J. Rocourt, R.S. Safferman, J. Schneider, L. Seldin, et al., The species concept and its application to tailed phages, Arch Virol 124(1-2) (1992) 69-82.
[34] B. Bolduc, H.B. Jang, G. Doulcier, Z.Q. You, S. Roux, M.B. Sullivan, vConTACT: an iVirus tool to classify double-stranded DNA viruses that infect Archaea and Bacteria, PeerJ 5 (2017) e3243.
[35] F. Rohwer, R. Edwards, The Phage Proteomic Tree: a genome-based taxonomy for phage, J Bacteriol 184(16) (2002) 4529-35.

[36] M.G.K. Ghequire, R. De Mot, The Tailocin Tale: Peeling off Phage Tails, Trends Microbiol 23(10) (2015) 587-590.
[37] P.G. Leiman, M. Basler, U.A. Ramagopal, J.B. Bonanno, J.M. Sauder, S. Pukatzki, S.K. Burley, S.C. Almo, J.J. Mekalanos, Type VI secretion apparatus and phage tail-associated protein complexes share a common evolutionary origin, Proc Natl Acad Sci U S A 106(11) (2009) 4154-9.
[38] S. Kube, P. Wendler, Structural comparison of contractile nanomachines, AIMS Biophysics 2(2) (2015) 88-115.
[39] K. Nakayama, K. Takashima, H. Ishihara, T. Shinomiya, M. Kageyama, S. Kanaya, M. Ohnishi, T. Murata, H. Mori, T. Hayashi, The R-type pyocin of Pseudomonas aeruginosa is related to P2 phage, and the F-type is related to lambda phage, Mol Microbiol 38(2) (2000) 213-31.
[40] G. Lee, U. Chakraborty, D. Gebhart, G.R. Govoni, Z.H. Zhou, D. Scholl, F-Type Bacteriocins of Listeria monocytogenes: a New Class of Phage Tail-Like Structures Reveals Broad Parallel Coevolution between Tailed Bacteriophages and High-Molecular-Weight Bacteriocins, J Bacteriol 198(20) (2016) 2784-93.
[41] F. Boyer, G. Fichant, J. Berthod, Y. Vandenbrouck, I. Attree, Dissecting the bacterial type VI secretion system by a genome wide in silico analysis: what can be learned from available microbial genomic resources?, BMC Genomics 10 (2009) 104.
[42] P.F. Sarris, E.D. Ladoukakis, N.J. Panopoulos, E.V. Scoulica, A phage tail-derived element with wide distribution among both prokaryotic domains: a comparative genomic and phylogenetic study, Genome Biol Evol 6(7) (2014) 1739-47.
[43] D. Veesler, C. Cambillau, A common evolutionary origin for tailed-bacteriophage functional modules and bacterial machineries, Microbiol Mol Biol Rev 75(3) (2011) 423-33, first page of table of contents.
[44] F. Jacob, [Induced biosynthesis and mode of action of a pyocine, antibiotic produced by Pseudomonas aeruginosa], Ann Inst Pasteur (Paris) 86(2) (1954) 149-60.
[45] M. Kageyama, F. Egami, On the purification and some properties of a pyocin, a bacteriocin produced by Pseudomonas aeruginosa, Life Sci (1962) 1 (1962) 471-6.
[46] E. Durand, V.S. Nguyen, A. Zoued, L. Logger, G. Pehau-Arnaudet, M.S. Aschtgen, S. Spinelli, A. Desmyter, B. Bardiaux, A. Dujeancourt, A. Roussel, C. Cambillau, E. Cascales, R. Fronzes, Biogenesis and structure of a type VI secretion membrane core complex, Nature 523(7562) (2015) 555-60.
[47] B.T. Ho, T.G. Dong, J.J. Mekalanos, A view to a kill: the bacterial type VI secretion system, 15(1) (2014) 9-21.
[48] S. Pukatzki, A.T. Ma, D. Sturtevant, B. Krastins, D. Sarracino, W.C. Nelson, J.F. Heidelberg, J.J. Mekalanos, Identification of a conserved bacterial protein secretion system in Vibrio cholerae using the Dictyostelium host model system, Proc Natl Acad Sci U S A 103(5) (2006) 1528-33.
[49] S. Pukatzki, A.T. Ma, A.T. Revel, D. Sturtevant, J.J. Mekalanos, Type VI secretion system translocates a phage tail spike-like protein into target cells where it cross-links actin, Proc Natl Acad Sci U S A 104(39) (2007) 15508-13.
[50] J.D. Mougous, M.E. Cuff, S. Raunser, A. Shen, M. Zhou, C.A. Gifford, A.L. Goodman, G. Joachimiak, C.L. Ordonez, S. Lory, T. Walz, A. Joachimiak, J.J. Mekalanos, A virulence locus of Pseudomonas aeruginosa encodes a protein secretion apparatus, Science 312(5779) (2006) 1526-30.

[51] A.R. Records, The type VI secretion system: a multipurpose delivery system with a phage-like machinery, Mol Plant Microbe Interact 24(7) (2011) 751-7.
[52] M. Lazzaro, M.F. Feldman, E. Garcia Vescovi, A Transcriptional Regulatory Mechanism Finely Tunes the Firing of Type VI Secretion System in Response to Bacterial Enemies, mBio 8(4) (2017).
[53] M.R. Hurst, S.S. Beard, T.A. Jackson, S.M. Jones, Isolation and characterization of the Serratia entomophila antifeeding prophage, FEMS Microbiol Lett 270(1) (2007) 42-8.
[54] G. Yang, A.J. Dowling, U. Gerike, R.H. ffrench-Constant, N.R. Waterfield, Photorhabdus virulence cassettes confer injectable insecticidal activity against the wax moth, J Bacteriol 188(6) (2006) 2254-61.
[55] J.B. Heymann, J.D. Bartho, D. Rybakova, H.P. Venugopal, D.C. Winkler, A. Sen, M.R. Hurst, A.K. Mitra, Three-dimensional structure of the toxin-delivery particle antifeeding prophage of Serratia entomophila, J Biol Chem 288(35) (2013) 25276-84.
[56] N.J. Shikuma, M. Pilhofer, G.L. Weiss, M.G. Hadfield, G.J. Jensen, D.K. Newman, Marine tubeworm metamorphosis induced by arrays of bacterial phage tail-like structures, Science 343(6170) (2014) 529-33.
[57] S. Ogata, H. Suenaga, S. Hayashida, Pock Formation of Streptomycetes endus with Production of Phage Taillike Particles, Appl Environ Microbiol 43(5) (1982) 1182-7.
[58] S. Roux, S.J. Hallam, T. Woyke, M.B. Sullivan, Viral dark matter and virus-host interactions resolved from publicly available microbial genomes, Elife 4 (2015).
[59] B. Hu, W. Margolin, I.J. Molineux, J. Liu, Structural remodeling of bacteriophage T4 and host membranes during infection initiation, Proc Natl Acad Sci U S A 112(35) (2015) E4919-28.
[60] A. Washizaki, T. Yonesaki, Y. Otsuka, Characterization of the interactions between Escherichia coli receptors, LPS and OmpC, and bacteriophage T4 long tail fibers, Microbiologyopen 5(6) (2016) 1003-1015.
[61] P.G. Leiman, P.R. Chipman, V.A. Kostyuchenko, V.V. Mesyanzhinov, M.G. Rossmann, Three-dimensional rearrangement of proteins in the tail of bacteriophage T4 on infection of its host, Cell 118(4) (2004) 419-29.
[62] L.D. Simon, T.F. Anderson, The infection of Escherichia coli by T2 and T4 bacteriophages as seen in the electron microscope. I. Attachment and penetration, Virology 32(2) (1967) 279-97.
[63] N.M. Taylor, N.S. Prokhorov, R.C. Guerrero-Ferreira, M.M. Shneider, C. Browning, K.N. Goldie, H. Stahlberg, P.G. Leiman, Structure of the T4 baseplate and its function in triggering sheath contraction, Nature 533(7603) (2016) 346-52.
[64] V.A. Kostyuchenko, P.R. Chipman, P.G. Leiman, F. Arisaka, V.V. Mesyanzhinov, M.G. Rossmann, The tail structure of bacteriophage T4 and its mechanism of contraction, Nat Struct Mol Biol 12(9) (2005) 810-3.
[65] M.G. Rossmann, V.V. Mesyanzhinov, F. Arisaka, P.G. Leiman, The bacteriophage T4 DNA injection machine, Curr Opin Struct Biol 14(2) (2004) 171-80.
[66] M.F. Moody, Structure of the sheath of bacteriophage T4. I. Structure of the contracted sheath and polysheath, J Mol Biol 25(2) (1967) 167-200.
[67] L.D. Simon, T.F. Anderson, The infection of Escherichia coli by T2 and T4 bacteriophages as seen in the electron microscope. II. Structure and function of the baseplate, Virology 32(2) (1967) 298-305.

[68] S. Kanamaru, P.G. Leiman, V.A. Kostyuchenko, P.R. Chipman, V.V. Mesyanzhinov, F. Arisaka, M.G. Rossmann, Structure of the cell-puncturing device of bacteriophage T4, Nature 415(6871) (2002) 553-7.
[69] L. Letellier, P. Boulanger, M. de Frutos, P. Jacquot, Channeling phage DNA through membranes: from in vivo to in vitro, Res Microbiol 154(4) (2003) 283-7.
[70] D. Van Valen, D. Wu, Y.J. Chen, H. Tuson, P. Wiggins, R. Phillips, A single-molecule Hershey-Chase experiment, Curr Biol 22(14) (2012) 1339-43.
[71] T.T. Puck, A. Garen, J. Cline, The mechanism of virus attachment to host cells. I. The role of ions in the primary reaction, J Exp Med 93(1) (1951) 65-88.
[72] A.D. Hershey, G.M. Kalmanson, J. Bronfenbrenner, Coordinate Effects of Electrolyte and Antibody on the Infectivity of Bacteriophage, J Immunol 48(4) (1944) 221-239.
[73] P. Horacek, V. Zarybnicky, J. Roubal, J. Turkova, M. Dobisova, Influence of NaCl, KCl and MgSO4 concentration on total and irreversible adsorption of T2r phage on isolated cell walls, Folia Microbiol (Praha) 15(4) (1970) 282-7.
[74] R. Moldovan, E. Chapman-McQuiston, X.L. Wu, On kinetics of phage adsorption, Biophys J 93(1) (2007) 303-15.
[75] E. Kellenberger, A. Bolle, E. Boydelatour, R.H. Epstein, N.C. Franklin, N.K. Jerne, A. Reale Scafati, J. Sechaud, Functions and Properties Related to the Tail Fibers of Bacteriophage T4, Virology 26 (1965) 419-40.
[76] Z.J. Storms, E. Arsenault, D. Sauvageau, D.G. Cooper, Bacteriophage adsorption efficiency and its effect on amplification, Bioprocess Biosyst Eng 33(7) (2010) 823-31.
[77] T.F. Anderson, Cold Spring Harbor Symp. Quant. Biol. 11 (1945) 1-13.
[78] H. Gaimster, D. Summers, Regulation of Indole Signalling during the Transition of E. coli from Exponential to Stationary Phase, PLoS One 10(9) (2015) e0136691.
[79] J. Wang, M. Hofnung, A. Charbit, The C-terminal portion of the tail fiber protein of bacteriophage lambda is responsible for binding to LamB, its receptor at the surface of Escherichia coli K-12, J Bacteriol 182(2) (2000) 508-12.
[80] J. Wang, V. Michel, M. Hofnung, A. Charbit, Cloning of the J gene of bacteriophage lambda, expression and solubilization of the J protein: first in vitro studies on the interactions between J and LamB, its cell surface receptor, Res Microbiol 149(9) (1998) 611-24.
[81] A. Cuervo, M. Pulido-Cid, M. Chagoyen, R. Arranz, V.A. Gonzalez-Garcia, C. Garcia-Doval, J.R. Caston, J.M. Valpuesta, M.J. van Raaij, J. Martin-Benito, J.L. Carrascosa, Structural characterization of the bacteriophage T7 tail machinery, J Biol Chem 288(36) (2013) 26290-9.
[82] V.A. Gonzalez-Garcia, M. Pulido-Cid, C. Garcia-Doval, R. Bocanegra, M.J. van Raaij, J. Martin-Benito, A. Cuervo, J.L. Carrascosa, Conformational changes leading to T7 DNA delivery upon interaction with the bacterial receptor, J Biol Chem 290(16) (2015) 10038-44.
[83] S.R. Williams, D. Gebhart, D.W. Martin, D. Scholl, Retargeting R-type pyocins to generate novel bactericidal protein complexes, Appl Environ Microbiol 74(12) (2008) 3868-76.
[84] T. Kohler, V. Donner, C. van Delden, Lipopolysaccharide as shield and receptor for R-pyocin-mediated killing in Pseudomonas aeruginosa, J Bacteriol 192(7) (2010) 1921-8.

[85] D. Gebhart, S. Lok, S. Clare, M. Tomas, M. Stares, D. Scholl, C.J. Donskey, T.D. Lawley, G.R. Govoni, A modified R-type bacteriocin specifically targeting Clostridium difficile prevents colonization of mice without affecting gut microbiota diversity, mBio 6(2) (2015).
[86] D. Scholl, M. Cooley, S.R. Williams, D. Gebhart, D. Martin, A. Bates, R. Mandrell, An engineered R-type pyocin is a highly specific and sensitive bactericidal agent for the food-borne pathogen Escherichia coli O157:H7, Antimicrob Agents Chemother 53(7) (2009) 3074-80.
[87] M. Brackmann, S. Nazarov, J. Wang, M. Basler, Using Force to Punch Holes: Mechanics of Contractile Nanomachines, Trends Cell Biol 27(9) (2017) 623-632.
[88] P. Ge, D. Scholl, P.G. Leiman, X. Yu, J.F. Miller, Z.H. Zhou, Atomic structures of a bactericidal contractile nanotube in its pre- and postcontraction states, Nat Struct Mol Biol 22(5) (2015) 377-82.
[89] G. English, O. Byron, F.R. Cianfanelli, A.R. Prescott, S.J. Coulthurst, Biochemical analysis of TssK, a core component of the bacterial Type VI secretion system, reveals distinct oligomeric states of TssK and identifies a TssK-TssFG subcomplex, Biochem J 461(2) (2014) 291-304.
[90] A. Zoued, E. Durand, C. Bebeacua, Y.R. Brunet, B. Douzi, C. Cambillau, E. Cascales, L. Journet, TssK is a trimeric cytoplasmic protein interacting with components of both phage-like and membrane anchoring complexes of the type VI secretion system, J Biol Chem 288(38) (2013) 27031-41.
[91] D. Scholl, Phage Tail-Like Bacteriocins, Annu Rev Virol 4(1) (2017) 453-467.

2

Establishing methods to study bacteriophage/pyocin-host interactions at the single-particle level

Lisa L. Dreesens, Wouter Liefting, Igor Rutka, Kyriakos Nikolaou, Thomas Wisse, Cleo Bagchus, Lars Houtman, Marie-Eve Aubin-Tam, Hubertus J. E. Beaumont

In this chapter, we describe the development and implementation of experimental methods and a semi-automatic framework that allow the study and characterization of phage- and pyocin-host interactions at the single particle level in real-time with high spatial and temporal resolution. To capture these interactions, several parameters of an existing flow-cell design were optimized, including the concentration of the adhesion molecule to immobilize cells at the substrate, the number of input cells and their time to adhere to the substrate for an optimal number of cells per field of view, and the flow rate at which the flow cell was washed to remove free and moving cells from the flow cell. Further, we describe how phages (and pyocins) can be labeled with a non-specific fluorescent organic dye and its effects on adsorption. The concentration of the label was optimized to ensure tracking of their position over time using fluorescent microscopy in HILO mode. Lastly, data analysis methods were developed to extract information on the position of phages on cells that can be used to study the irreversible binding distribution, as well as, the dynamical interactions. The results gathered with these methods were in good agreement with expected phage and pyocin behaviors and enable investigations into the nanobiology of bacteriophages and pyocins.

2.1 Introduction

Bacteriophages are abundantly present in all kinds of environments around us playing an important role in maintaining bacterial numbers and diversity. However, there is limited information on the fundamental mechanism at single-particle level with which these phages operate leading to infection of a cell. The research described in this thesis set out to study the first crucial step of the infection process: target-finding and adsorption to the host. In addition, we aimed to examine the adsorption of phage-like particle R2-type pyocin with their target cells. Phages and pyocins are not only capable of adsorbing to bacterial cells; as they interact with the cell surface, they discriminate between suitable and non-suitable hosts and, in some cases, 'decide' whether or not to commit to sheath contraction. The nanoscopic details of how these fitness-enhancing dynamics emerge from mechanisms at the nanoscale remain largely unknown. Addressing this requires techniques that allow us to resolve the dynamic interactions between individual phage or pyocin particles and their hosts with high temporal and spatial resolution. One technique capable of achieving this is fluorescence microscopy. Due to their small nature, phages fall below the detection limit of the standard light microscopes. However, individual phages can be made visible by tagging them with a fluorescent label. This has previously been done by Rothenberg *et al.,* who genetically engineered phage λ to express EYFP on its capsid [1]. They used a simple flow cell design in which they coated the glass slide with an adhesion molecule to immobilize host cells. Once they added the phages to the flow cell they used fluorescence microscopy to track the phage particles over time. These results gave a first glimpse of the dynamics of the phage target-finding process, revealing the presence of some sort of on-cell motion. However, many unresolved questions remain. Most importantly, limitations on the temporal resolution (frame rate not exceeding 30 Hertz) prohibit resolving the detailed mechanism behind the observed on-cell motion.

In this chapter, we describe the establishment of experimental and data analysis methods that afford a higher spatial and temporal resolution. This involved i) optimizing the immobilization and density of cells to the flow cell to increase the throughput of usable data, ii) optimizing the labeling concentration of small organic dyes that bind non-specifically and can therefore be used to label any phage or phage-like particle, iii) implementation of a fluorescent microscope with highly inclined and laminated optical sheet (HILO) illumination capable of a higher temporal resolution (50-200 Hertz), and iv) developing a data analysis pipeline to analyze phage trajectories and extract positions on the cell surface that can be used to study the phage-host binding distributions and phage-host interaction dynamics at nanoscale resolution. The developed methods provide the opportunity to gain in-depth knowledge, among others, on the fundamental search mechanism behind the target finding process, allowing for characterization of interaction dynamics in terms of binding kinetics, dwell time, dwell area, regime of motion, and directionality of motion that can lead to a model that could explain the mechanism behind phage-host exploration and decision making process – commitment to infection. Further, the behavior among competing phage strains, and the effect of environmental factors (e.g. pH, temperature, ions, metals, co-factors, etc.) or host-cell receptor modifications (i.e. leading to resistance) on binding dynamics could be studied in more detail.

Part I – Flow cell

2.2 Results

2.2.1 Flow cell design

To enable dynamic detection of the interaction between phage and host at the single particle level by fluorescence microscopy, we used a flow-cell design that was modified from Rothenberg *et al.* [1]. This flow cell contained in- and outlet ports to introduce cells and phages, and to enable the exchange of buffers during an experiment. Cells can be fixed to the glass slides using an adhesion co-factor to allow observations to be made. As such, the system in principle allows for the real-time study of phage-host interactions.

The final design of the flow cell used in the research described in this thesis is shown in Figure **2.1**. The top and bottom layer of the flow cell consist of a standard microscope slide and a coverslip, respectively. These are separated by a 100 μm transparent spacer of double-sided adhesive tape. Three separated chambers of 3.3 cm x 0.2 cm, holding a volume of 10 μl each, are excised using a laser cutter. Each chamber has its own inlet and outlet ports, created by pre-drilled holes in the microscope slide. A connector is placed on each in- and outlet, allowing for introduction of cells and phages in the flow cell using a pipette. Cells were fixed to the coverslip, which was pre-coated with the nonspecific poly-cationic adherence co-factor poly-L-lysine. This polymer has previously been used to facilitate attachment of all kinds of cell types to a range of different substrates [2]. Here the polymer works as mediator between the negatively charged glass surface and cell membrane. Under controlled pressure, the flow cell can be washed to remove unattached cells or realize exchange of buffers using a syringe-

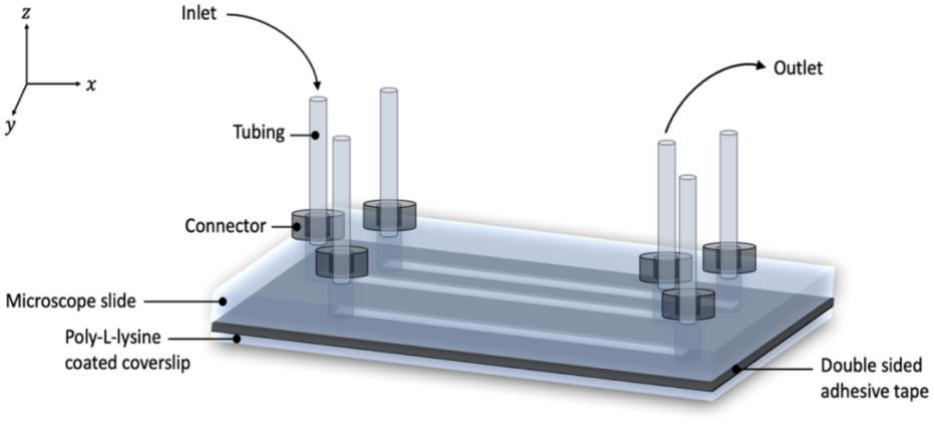

Figure 2.1: Flow cell design. The flow cell contains three chambers. Cells can be introduced in the appurtenant inlet port of each chamber, where they can attach to the coverslip pre-coated with the adherence co-factor poly-L-lysine. Using the same inlet port, the flow cell can be washed to remove unbound cells, buffers can be exchanged, or phages can be introduced.

driven dispenser connected with tubing to the inlet connector. To ensure safety, e.g. when working with ML2 classified bacteria, the system is closed by a reservoir that is connected with tubing to the outlet. Any spill-over is collected in the reservoir.

Once we had constructed and tested the basic functionalities of our flow cell, we experimentally explored how to increase the chance of observing phage-cell interactions in the flow cell. This involved varying a number of variables that potentially affect the number and fraction of immobilized single cells. Below, we report and discuss the results of experiments in which the following parameters were varied: i) the concentration of the adherence co-factor poly-L-lysine, ii) the flow rate at which the flow chamber was washed, iii) the time the cells are allowed to adhere to the slide (adherence time), and iv) the initial cell concentration in the flow cell.

For optimization of these parameters within the design of this flow cell, *E. coli* B cells were used. This strain is well studied and often used as model organism for scientific research within the field of molecular biology, and it is known as an important marker of water contamination caused by humans. In addition, we chose this strain as a host to study the target finding process of the model phage Escherichia virus T4 [3]. Characterized by its long contractile tail, T4 belongs to the family of *Myoviridae* in the order of *Caudovirales*, tailed-phages, and infects *Escherichia coli* strains. This model phage is one of the 'T-even' phages that has been well studied since the late 1930s. Its genome sequence and gene structuration/organization are known [4]. Further, a near-atomic structural model is present [5-8], as well as, its molecular and serological properties are defined including identification of the host receptors, LPS and OmpC [9]. Even though new technologies using three-dimensional reconstruction utilizing electron microscopy have revealed some of the key intermediates of T4 infection process, giving insight in the mechanism behind the mechanism of adsorption till cell penetration [5], the dynamical details regarding the target-finding process and decision making are still lacking. With the development and optimization of this method we can study the phage T4 target-finding process in more detail, bridging the remaining gap in understanding of the T4 infection process. In addition, many aspects of the mechanism behind the T4 infection process might apply for other phages within this family. This might even extend to phage-like complexes using similar structural components (i.e. contractile-sheath and RBPs) or to some degree to other families within the order of tailed-phages.

2.2.1.1 Adherence co-factor poly-L-lysine

First, we wanted to ensure that cells attached to the coverslip in sufficient numbers to capture phage-host interactions. To establish which concentration of the adherence co-factor poly-L-lysine ensures a sufficient number of fixed cells to the substrate, we investigated two different concentrations of poly-l-lysine, 0.01 and 0.1% respectively, which have previously been used in studies requiring cell fixation [1, 2, 10]. A layer of poly-L-lysine to which cells could attach was deposited on slides by incubating them in a poly-L-lysine solution. Cell fixation to the substrate takes place once the cells contact the coated surface via adhesion between the anionic cell surface and the poly-cationic layer created by the polymer poly-L-lysine [2]. Qualitative inspection revealed that the

highest percentage of poly-L-lysine resulted in more adhered bacteria Figure **2.2**. High concentration of poly-L-lysine has been previously found to result in some degree of cell deformation or even shearing of the membrane due to the increased membrane tension [2]. As coating the slide surface using a 0.1% poly-L-lysine solution yielded a sufficient number fixed cells, we did not examine the effects of higher concentrations and decided to conduct our experiments with 0.1% poly-L-lysine.

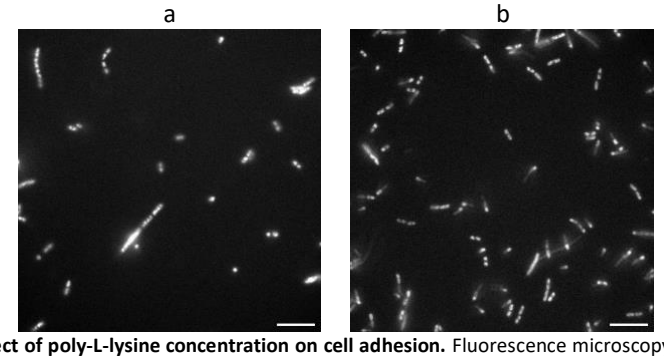

Figure 2.2: Effect of poly-L-lysine concentration on cell adhesion. Fluorescence microscopy images of cells stained with the nucleic acid stain DAPI that are incubated in a flow cell coated with different concentrations of poly-L-lysine. **a**, 0.01%. **b**, 0.1 %. Scale bar represents 10 µm.

2.2.1.2 Flow rate

Even after prolonged incubation, a substantial fraction of the cells introduced into the flow cell did not attach firmly to the slide. The presence of freely diffusing cells increases background noise, reduces the sensitivity of phage detection and interferes with particle tracking. In addition, a considerable fraction of attached cells still moved. This could be resolved by washing of the flow cell with a buffer or medium of interest. However, washing could also remove firmly attached cells, reducing the number of usable cells per field of view. In order to establish the optimal washing flow rate, we first measured the effect of flow on the fraction and total number of immobilized cells.

The effect of washing on the fraction and number of firmly attached cells was quantified using an image analysis algorithm that was developed as part of the project described in this thesis (see section 2.6.4.4). Briefly, this algorithm converted the phase contrast image, using a thresholding method, into a binary image. The binary objects (cells) of every frame taken over time were overlaid. A color marking is used to easily identify if cell movement has taken place. This marking method is based on the fraction of overlapping binary pixels. Green indicates the presence of the binary pixels present within all frames (fraction of 1). Any deviation, caused by cell motion, results in a summed fraction <1 and is marked with the color red. This is an indication of cell movement, and in addition, shows the extent of its motion. This method indicates cell movement up to a single pixel level, i.e. 80 nm (depending on the resolution of the microscope).

We tested if there was an effect of washing on the fraction of attached cells that did not show motion (i.e. immobilized cells) by comparing the fraction of immobile cells

before and after washing of the flow cell. This was realized by taking at least 10 images of different positions within one or multiple flow cells per tested rate before washing and its appurtenant position after washing. The fraction of immobilized cells before and after washing was determined by counting the total number, with a minimum number of 10 cells per field of view, and the corresponding number of immobile cells per field of view using the algorithm described above. This showed that, independent of the flow rate tested, the fraction of immobilized bacteria was significantly greater after washing the flow cell than before (Bonferroni corrected Wilcoxon signed-rank test; $N > 10$, $p < 0.01$; Figure **2.4**a). Washing the flow cell resulted in at least a 2.7-fold increase of the fraction of immobilized cells, showing that washing is an effective procedure to selectively remove poorly attached cells.

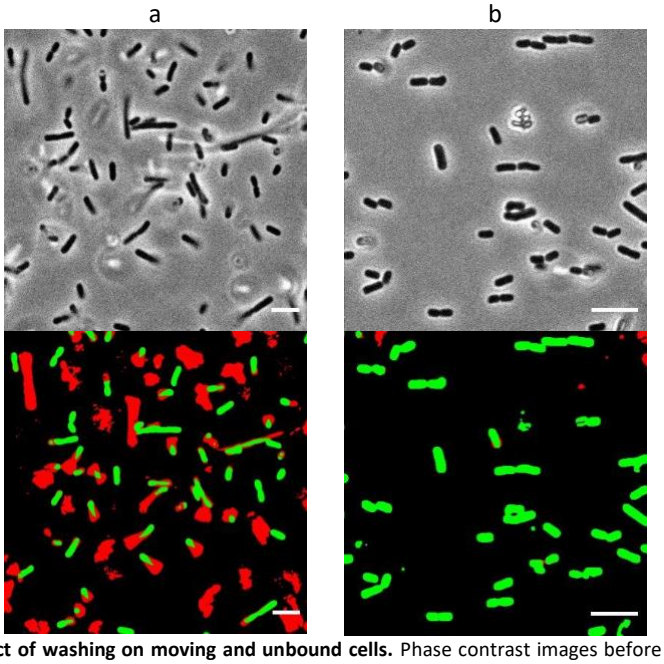

Figure 2.3: Effect of washing on moving and unbound cells. Phase contrast images before (top) and after (bottom) image analysis to detect moving cells. **a,** Before washing. **b,** After washing. Green shows the initial cell position and red marks movement of the cell over time by indicating the non-overlapping area of the same cell. Scale bar represents 5 μm.

The flowrate at which the flow cell is washed might affect the fraction of immobilized cells to the surface. It is also likely that a minimal rate might be required to remove the poorly attached cells. On the other hand, there might be a maximum rate beyond which cells that are immobile are also removed from the substrate. Thus, there might be a trade-off between increasing the fraction of immobile cells and maximizing the total number of immobile cells per field of view. We examined this by measuring the effect of the flowrate on the fraction and total number of immobilized cells. We tested flowrates ranging from 35 to 525 μl/min. Increasing the flow rate from 35 to 175 μl/min resulted in a significant increase of the total fraction of immobilized cells (Bonferroni corrected Mann Whitney U test; $N = 46$, $p < 0.001$; Figure **2.4**a); however, further

increase of the flowrate did not reveal a detectable effect on the fraction of immobilized bacteria (Figure **2.4**a). Based on these findings, we conclude that the fraction of immobilized cells is optimal after washing at a flowrate of 175 µl/min and is not increased substantially by higher flow rates. Since we were interested in a high fraction of immobilized cells but also wished to optimize the number of fixed cells per field of view, we also investigated the effect of washing flowrate on this variable. We used the Spearman's rho correlation coefficient to assess whether there is a relationship between the flow rate and the number of immobilized cells (Figure **2.4**b). This revealed a significant negative correlation, demonstrating that immobile cells were being removed at high flow rates (Bonferroni corrected Spearman's rho correlation; r_s = -0.45, N = 125, p < 0.0001; Figure **2.4**b). Taken together, these observations led us to conclude that a washing flow rate of 175 µl/min is optimal for our purposes.

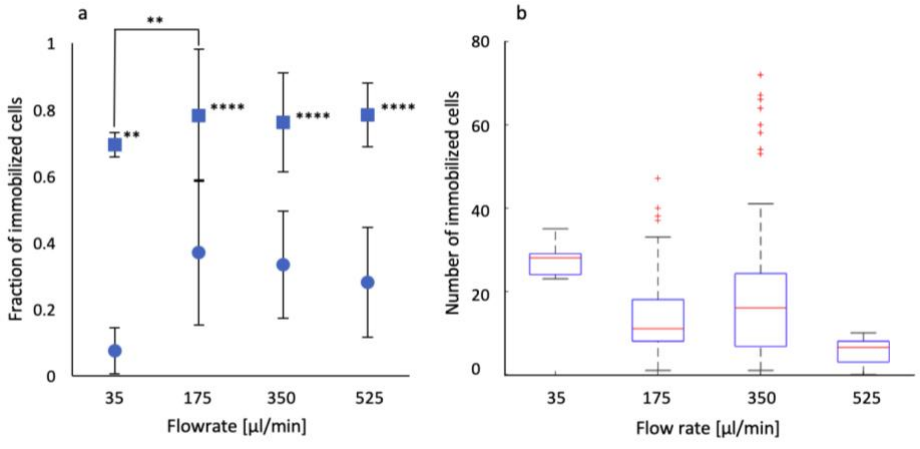

Figure 2.4: Effect of washing flow rate on fraction and number of immobilized cells. a, Fractions of immobilized cells per field of view before (circles) and after (squares) washing at different flow rates. Asterisks next to squares indicate significance of effect of washing and asterisks above brackets indicate significance of effect of the flow rate (**: p < 0.01; ****: p < 0.001; see text for statistical analysis). **b**, Number of immobilized cells per field of view after washing the flow cell at different rates. Boxes indicate the 25th and 75th percentile, the whiskers extend to the most extreme data points not considered outliers, line in box indicates median, red crosses (+) are outliers.

The effects of washing might differ between bacterial species and strains. We examined this for a different species by performing washing experiments on *Pseudomonas aeruginosa* 13s. This species and strain was chosen based on the fact that it is a host indicator strain of R2-type pyocins and will be used within this thesis to study single-particle pyocin-cell interactions. The same washing procedure and variation of the flow rate were examined as for *E. coli* B. This revealed that the washing of the flow cell has a similar positive effect on the fraction of immobilized cells (data not shown). Surprisingly, in contrast to *E. coli* B cells, the highest fraction of immobilized 13s cells was reached with a washing rate of 35 µl/min. An increase in rate, led to a reduced fraction and a reduced total number of immobilized cells. The difference in optimal washing flow rate between the two bacterial strains might stem from the different cell sizes.

In addition to the beneficial effect of washing on the fraction of immobilized cells, it also increased signal-to-background ratio. This allows for a more accurate detection of phages and cells in the data analysis. Washing the flow cell, independent of the flow rate used, resulted on average in an 14% increase in signal-to-background ratio (Bonferroni corrected Mann Whitney U test; $N \geq 157$ cells, $p < 0.001$; Supplementary figure **2.1**). The increased signal-to-background ratio was a result of removing unbound bacteria in the background that emit light due to auto fluorescence and by removing any residue of growth media containing auto fluorescent components that might have been left behind during the step of pelleting cells and resuspension in interaction media.

2.2.1.3 Adherence time

Washing the flow cell was shown to be an effective means to remove unbound and moving cells, resulting in approximately 15 immobile *E. coli* B cells per field of view. A higher number of immobile cells per field of view would increase the chance of observing a phage-host interaction. Therefore, we tested if extending the time during which cells were allowed to adhere to the poly-L-lysine coated slide had a positive effect on the number of immobilized cells after washing while maintaining a high fraction of immobilized cells. We investigated two incubation times: 10 and 30 minutes in an experimental design that resembled the previous analysis of the effect of washing. Per condition, we imaged at least 10 different fields of views per flow cell before and its corresponding fields after washing. Using the cell movement algorithm, the number of immobilized cells and the total number of cells were counted. First, we analyzed the effect of incubation time on the number of immobile cells before washing the flow cell. This showed that the number of immobilized cells became significantly greater with a prolonged incubation time (Bonferroni corrected Mann Whitney U test; $N = 50$, $p < 0.001$; Figure **2.5**a). Secondly, we tested if this positive effect of time on the number of immobilized cells was still present after washing the flow cell. Results showed the same positive effect of incubation time on the number of immobilized cells after washing the flow cell, with significantly more cells after a longer incubation time (Bonferroni corrected Mann Whitney U test; $N = 50$, $p < 0.01$; Figure **2.5**a). Prolonged incubation did not affect the fraction of immobilized cells (Figure **2.5**b). Taken together, these results demonstrated that increasing the incubation time had a positive effect on the number of immobilized cells. However, implementation of a longer incubation time has a negative impact on the preparation time and therefore a reduced throughput and would only be considered when sample material is limited.

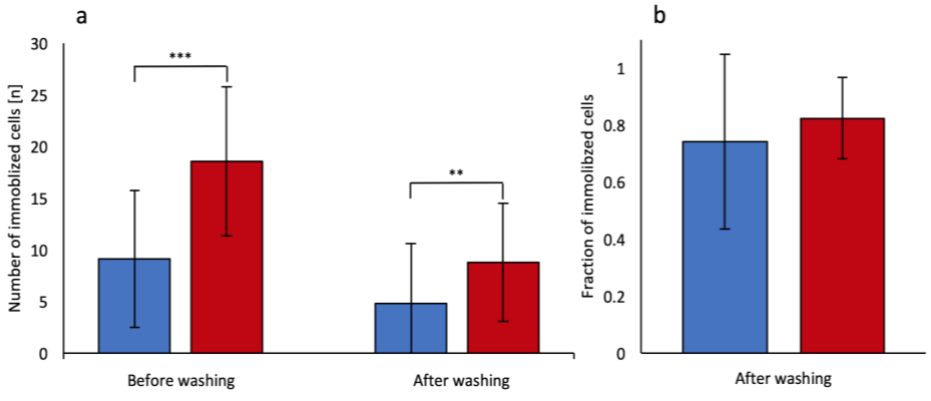

Figure 2.5: Effect of incubation time on cell adhesion before and after washing. a, Effect of incubation time on the number of immobilized cells per field of view before and after washing. **b**, Effect of incubation time on the fraction of immobilized cells after washing the flow cell. Blue and red bars represent 10 and 30 minutes' incubation time for cells to adhere to the substrate, respectively. Error bars indicate standard deviation. Asterisks above brackets indicate statistical significance (**: $p < 0.01$; ***: $p < 0.001$; see text for statistical analysis).

2.2.1.4 Cell concentration

Another variable that had the potential to increase the chance of observing a phage-host interaction was the initial cell concentration within the flow cell. A higher cell concentration could lead to a higher number of immobilized cells at the substrate. We tested, in an experimental design that resembled the previous analysis, whether the initial cell concentration influenced the number of cells immobilized to the substrate. Therefore, we varied the initial cell concentration by growing cells in LB to the exponential phase (OD_{600} of 0.3), where after cells were either diluted or concentrated in the interaction medium to create the following cell concentrations: OD_{600} equal to approximately 0.05 (~$5 \cdot 10^6$ cells/ml), 0.5 (~$5 \cdot 10^7$ cells/ml), or 1.0 (~10^8 cells/ml). Per condition, we imaged 30 fields of views, obtained from three flow chambers, before washing, and its corresponding position after washing. Using the cell movement algorithm, the number of immobilized cells and the total number of cells were counted.

First, we tested whether there was an effect of the initial cell concentration on the number of cells fixed to the substrate before washing the flow cell. This indicated that a ten-fold increase in the initial cell concentration, from an OD_{600} equal to 0.05 to 0.5, led to a significant increase in the number of immobilized cells (Bonferroni corrected Mann-Whitney test; $N = 45$, $p < 0.001$; Figure **2.6**a), while a 5-fold increase in cell concentration, from an OD_{600} equal to 0.5 to 1.0, showed no detectable increase in number of immobilized cells.

Secondly, we tested whether this effect of initial cell concentration on the number of immobilized cells was still present after washing the flow cell. In alignment with the results before washing, we detected a significant increase in immobilized numbers with a ten-fold increase (Bonferroni corrected Mann-Whitney U test; $N = 45$, $p < 0.001$; Figure **2.6**a), but not for the five-fold increase in initial cell concentration. Varying the initial cell concentration did not affect the fraction of immobilized cells. However, the variance among the groups does get significantly smaller with a higher

concentration of input cells (Bonferroni corrected Levene's test; N = 75, p < 0.001; Figure **2.6**b). Overall, these results demonstrated that a 10-fold increase in cell concentration had a positive effect on the number of immobilized cells. Also, a higher cell concentration produced less variation/a more controlled output in immobilized fraction. Based on these results we decided that concentrating our cells before the start of the experiment, over the earlier described extended incubation time, would benefit the number of immobilized cells. For further experiments described within this thesis, we implemented the 10-fold increase in initial cell concentration, with an OD_{600} equal to 3.0, to increase our chances of observing phage-host interactions.

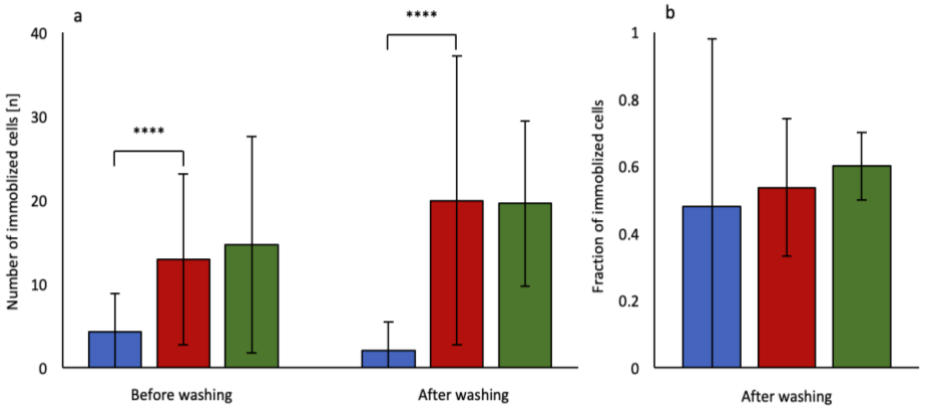

Figure 2.6: Effect of initial cell concentration on cell adhesion before and after washing. a, Effect of initial cell concentration on the number of immobilized cells per field of view before and after washing the flow cell. **b**, Effect of initial cell concentration on the fraction of immobilized cells after washing the flow cell. Blue, red, and green bars represent the used initial cell concentration with an OD_{600} equal to 0.05, 0.5, and 1.0, respectively. Error bars indicate standard deviation. Asterisks above brackets indicate statistical significance (****: p < 0.0001; see text for statistical analysis).

2.2.1.5 Orientation of cells in flow cell

The orientation of the in-flow direction could cause a bias in the orientation in which the cells adhere to the substrate, as the flow could impose a dragging force on the adhered cells. The alignment of cells in one direction might have an effect on data interpretation. For example, the initial point of contact with the cell will be biased towards the pole when phages move in direction of the flow. To investigate whether that washing of the flow cell had an effect on the orientation of cells adhered to the substrate, we analyzed 772 cells that were acquired using images from multiple flow cells (n > 3) obtained over three days. Each detected cell was made binary, by using a thresholding method on pixel intensity and the orientation of the long-axis (X_L) of each cell was compared to the direction of the flow. Testing the null hypothesis that the flow direction did not influenced the orientation of immobilized cells in the flow cell revealed a significant bias in the orientation of the cells in the direction of the flow (Kolmogorov-Smirnov test; N = 772, p < 0.001; Figure **2.7**), indicating that the flow imposes a force large enough to cause the cells to align predominantly in the direction of the flow. This cell alignment should be taken into account when studying properties that are prone or affected by cell orientation, e.g. the initial binding distribution studied in Chapter 4.

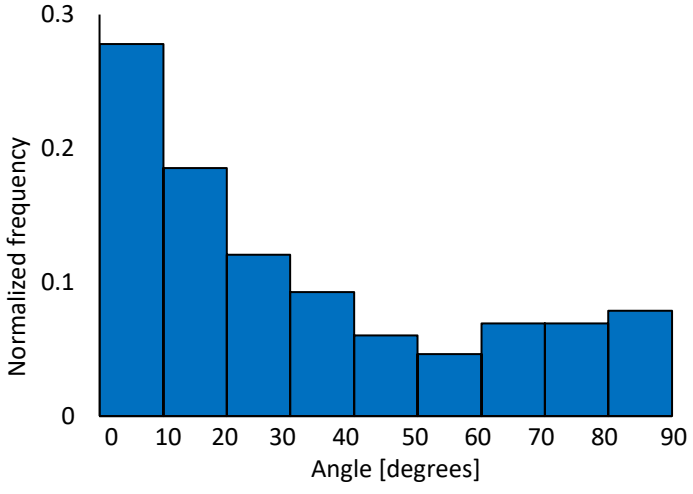

Figure 2.7: Orientation of cells in flow cell. Effect of flow on the orientation of cells after washing the flow cell. X-axis shows the angle of the absolute orientation of the long axis (X_L) of the cell relative to the direction of the flow.

2.3 Discussion and conclusion

We performed experiments to establish a suitable flow cell design and cell attachment procedures to allow dynamic tracking of phages as they interact with bacterial cells. We found that a modified version of the flow cell design published by Rothenberg *et al*. [1] met our needs. A poly-L-lysine concentration of 0.1% provided an attachment layer that resulted in a sufficiently large number of firmly fixed cells per field of view. Washing of the flow cell at 175 μl/min was shown to strike the optimal balance between removal of cells that were attached but still displayed motion and achieving an optimal fraction of firmly fixed cells per field of view. Lastly, the optimal number of firmly fixed cells was reached by either a longer attachment incubation time of 30 minutes or by a 10-fold increase in initial cell concentration. Based on these findings, we can establish a protocol that yielded flow cells containing a sufficient number of firmly fixed cells that allowed detection of the interaction of phages or pyocins with their target cells. An unexpected additional finding was that the optimal flow rate differed between the two tested strains.

Although a higher concentration of poly-L-lysine resulted in a larger number of well-attached cells, stronger adhesion can also affect the physiology and viability of the cells, which could affect the phage-cell interaction. While poly-L-lysine is generally used to immobilize bacterial cells to a substrate, high concentrations have previously been shown to increase the membrane tension, affecting the physiology of bacterial cells. This has been shown to have direct consequences on the proton motive force gradient, as high membrane tension can trigger partial dissipation of membrane potential, that on its turn has been shown to subsequently affect diverse process of protein localization patterns [11-13]. Possible changes in cell surface properties (e.g.

receptor distribution and accessibility) and physiological parameters (e.g. due to disruption of the membrane/cell envelope integrity) might affect the interactions of phages and phage-like particles with cells. However, previous studies have shown that irreversible phage adsorption was not dependent on cell curvature [10] and that adsorption readily occurs on cell envelope fragments that contain the receptor [14]. Moreover, two experiments described in section 2.2.2.2 of this chapter and in section 5.2.2. of Chapter 5, which used a fluorescent dye that can only enter cells with a damaged membrane and stain cells on the basis of membrane potential, respectively, showed no evidence of cell envelope damage. Taken together, this indicates that the poly-L-lysine concentration that we used is highly unlikely to have large effects on the phage-cell interactions that are the focus of the research described in this thesis. That said, it would be of future interest to examine the possibility that surface geometry has subtle effects on phage adsorption in a quantitative manner.

Washing of the flow cell was shown to be an effective method to remove free and poorly attached cells. A point of notice was the low fraction of immobilized cells before washing the flow cell at a rate of 35 μl/min. We expected to obtain a value that was similar to those obtained for the other tested flow rates, as all other parameters were kept the same. Only one flow cell was used within this data set, in contrast to a minimum of four used to examine the other flow rates. The low fraction of immobilized cells for 35 μl/min is likely due to small experimental variations between flow cells that were not averaged out owing to the limited replication. In spite of this quantitative deviation, our main conclusion regarding the positive effect of washing on the fraction of firmly attached cells is nonetheless supported by the effect of washing at 35 μl/min.

Immobilized cells aligned with the direction of the flow. Depending on the interplay between the flow and diffusion dynamics of the phages after their introduction to the flow cell, the orientation of the cells relative to the phage movement might have implications on the location of the initial phage-host interaction. As such, the flow-induced bias in cell orientation could result in a bias toward first phage-cell contact at the polar regions of a cell. This can be further examined by interpreting the results on the positioning of first phage-host encounters. The observed flow-alignment bias in cell orientation does not impact analyses of the motion of phage particles on the cell surface after the first interaction with a cell surface, as no flow was applied during phage tracking.

The overall goal of the experiments described in this section was to formulate and optimize a protocol for cell immobilization to increase the chances of observing phage-host interactions and allow their study with high precision at single-phage level. This required a high fraction and number of single immobilized cells. Previously described methods that study parts of the phage infection process by means of fluorescent microscopy involved either immobilization of cells with agarose [10, 15-17], or via cell adhesion using poly-L-lysine coated slides without or with very limited washing of the flow cell, using a one-time manual flush with a pipette [1, 10, 15]. The first method, involving immobilization of cells with agarose, lacked the ability to study binding dynamics at single-phage level in an environment that is similar to the bulk liquid conditions under which phage adsorption has predominantly been examined. The latter method, involving immobilization of cells with poly-L-lysine coated slides without or with limited washing of the flow cells, did not allow long term tracking with

high spatial and temporal resolution in an efficient way, either due to a high fraction of poorly adhered cells or large experimental variations between flow cells. Taken together, our findings allowed us to formulate a protocol of cell immobilization that circumvents these and other issues and is used in the experiments described in the remaining chapters of this thesis to shed light on the single-particle binding distribution (chapter 3) and on-cell dynamics of phage T4 on *E. coli* B cells (chapter 4) and the on-cell dynamics of pyocin R2 on its bacterial target 13s (chapter 5).

Part II – Fluorescent labeling

2.4 Results

2.4.1 Fluorescent labeling

To enable dynamic detection of the interaction between phage or pyocin particles and their host at the single particle level by means of fluorescence microscopy, they had to be fluorescently tagged. Our approach was to select and optimize a labeling strategy for phages and subsequently apply this to pyocins. Phages of the class *myoviridae* consist of proteins and DNA, which can both be tagged using a variety of labeling methods that have been previously successfully used to visualize phages (Figure **2.8**) [1, 15-25]. For our purposes, we required a labeling method that does not rely on prior knowledge of the structure and genetics making it easily applicable to any phage. Next to this, we needed the possibility to use a variety of fluorophores that are compatible with our microscope systems, have a bright fluorescence and exhibit limited photobleaching to allow prolonged imaging of the dynamics. Lastly, the dye molecule should be as small as possible with only a single binding site to limit the potential impact of cross-binding and drag on the natural behavior of the phage/pyocin and potentially obstruct its functional properties.

Since pyocins lack a genome, we decided to use the nonspecific protein labeling method, as this method can be used to label both phages and pyocins, and can be performed using a broad range of small dyes. First, we optimized the dye concentration for visualization, and tested whether this labeling concentration sufficed for tracking over a period of one minute. Secondly, to explore the possibility to obtain functional information, i.e. DNA ejection, while tracking phage position, we also tested an alternative nonspecific staining method for phages based on labeling the DNA. Here, we also optimized the dye concentration and assessed its compatibility with tracking on a 1-minute timescale.

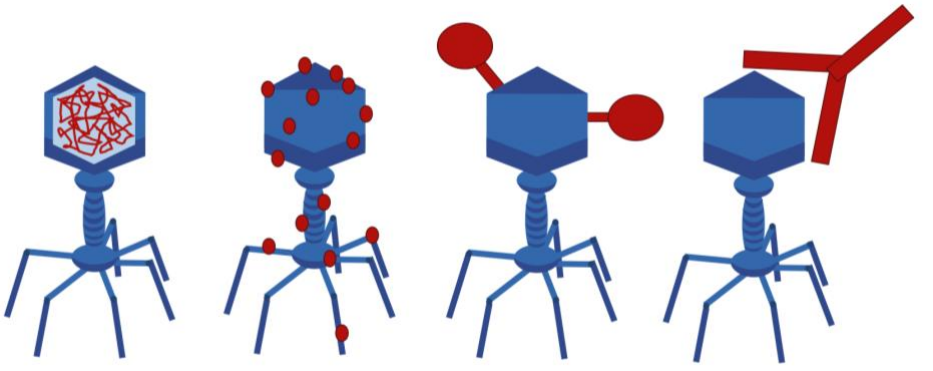

Figure 2.8: Fluorescent labeling strategies. Phages can be fluorescently labeled using several methods. **a,** Genome stain, where the dye intercalating between the DNA bases, binds to the minor or major grooves, or binds externally to the DNA. These dyes are often not specific, with little to no sequence preference. **b,** Protein labeling via chemical conjugation, where several surface exposed amino acids can be targeted for chemical conjugation with corresponding reactive groups. These reactive groups are coupled to a variety of different dyes, e.g. from Quantum dots to small organic dyes. **c,** Expression of tag via genetic engineering, where either a fluorescent protein, e.g. GFP, or a binding site, e.g. biotin that can be non-covalently coupled to streptavidin coated dyes, can be encoded on the genome and expressed with a high precision in both location and quantity, e.g. expression of a tag fused to non-essential capsomers. **d**, Fluorescently tagged antibodies, which can bind with high specificity and affinity to targeted protein regions. Schematics of phages (blue) and label (red) are not to scale.

2.4.1 Nonspecific fluorescent-dye based protein labeling

Nonspecific protein labeling is a non-invasive method of fluorescently labeling proteins that requires no prior genetic and structural knowledge. The dye is attached to surface exposed amino acids via chemical conjugation. There are several groups that can be tagged via chemical conjugation, i.e. primary amines, carboxyls, sulfhydryls and carbonyls. Of these specific groups, primary amines are often abundantly available and, due to their positive charge at physiological pH, mainly found at the outer surface of a protein, making them readily accessible for conjugation of reactive groups. Furthermore, they are nucleophilic, making them an easy target for coupling of reactive groups. These primary amines can be found in N-termini and in the side chain of lysine residues which are abundantly present on T4 phage (Figure **2.9**), making it a highly efficient target for chemical conjugation.

A reactive group capable of chemically conjugating a dye molecule to these primary amines is N-hydroxysuccinimide (NHS)-ester (Figure **2.10**). This reactive group has been used before to couple linkers or dyes to phages [17, 20, 26]. There are several fluorophores with this reactive group commercially available. Alexa Fluor™ 647 NHS-ester is a small but bright and photostable water soluble far-red dye, which does not show significant self-quenching when used at high molar ratios, and that has compatible excitation and emission properties with the laser and filter set of our microscope, ensuring high sensitivity of tracking over longer periods of time within our experimental conditions of interest.

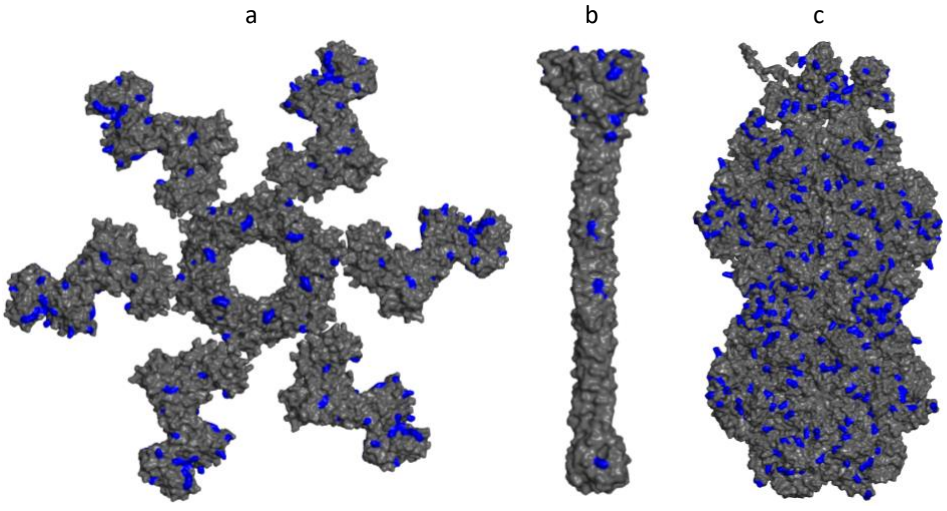

Figure 2.9: Locations of exposed lysine residues in bacteriophage T4. Presence of exposed lysine residues (blue) on **a,** the sheath (top view), **b,** the distal end of the LTF (side view), and **c**. a single capsomer (side view) consisting of gp24 pentamer and gp23 hexamer, that provide potential labeling sites for chemical conjugation with dyes containing an NHS-ester group.

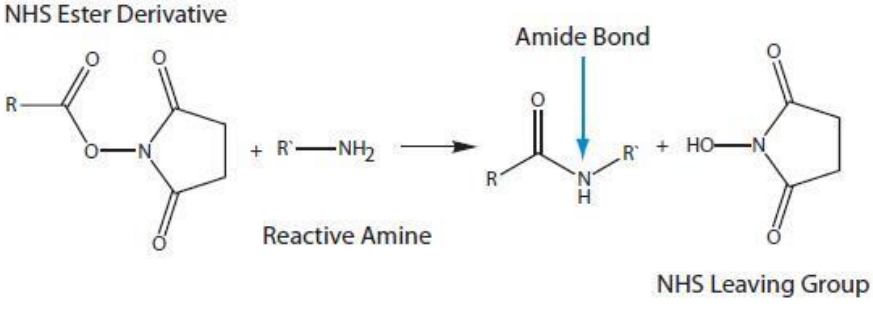

Figure 2.10: NHS ester reaction scheme for chemical conjugation. Dye molecule (R) containing a NHS ester reacts with a primary amine group or N-terminus that is exposed on the outside of a protein (R'). A stable amine bond is formed between the dye and the protein molecule, leaving a NHS group as a byproduct. Image obtained from [27].

We required labeled phages to be distinguishable from the background (high signal-to-background ratio) and the ability to track them on a minute time-scale in order to allow us to analyze the phage-host interactions. To avoid background fluorescence from labeled non-phage proteins present in phage preparations produced by the lysis method, we applied a generally used method of phage purification [78]. After T4 phages were amplified in a liquid *E. coli* B culture, we isolated phages by PEG-precipitation and obtained selectivity by CsCl density gradient. We confirmed activity and concentration with a spot assay, which examines the overall presence of active phage and provides a rough estimate of their titer. Purity of phage suspension was assessed visually for protein debris (non-phage proteins) using negative staining transmission electron microscopy (TEM). Overall, we observed no large contamination of other proteins or debris (Figure **2.11**a). In addition, the majority of the phage fraction was intact (Figure

2.11b), with only occasional observations of inactivated phage (contracted sheath and in some cases, empty capsids) (Figure **2.11**c). Phage activity was detected using a spot assay, showing a concentration of 10^{11} PFU ml^{-1} after purification.

We used a commercially available dye, Alexa Fluor™ 647 NHS-ester, which has previously been used to label cells and protein complexes [28, 29], but to our knowledge has not yet been applied specifically on phages. In order to establish which concentration of this dye ensured a sufficient signal-to-background ratio for detection and tracking of the phage on a minute timescale, we examined a range of dye concentrations. Secondly, we investigated if this dye concentration allowed for detection of particles across the entire image depth (i.e. z-axis defined as shown in Figure **2.1**) of a cell, ensuring detection of phage-host interaction at any given position on the cell. Lastly, we tested whether this dye concentration was not limited to labeling T4 phage and suitable for R2-type pyocin visualization.

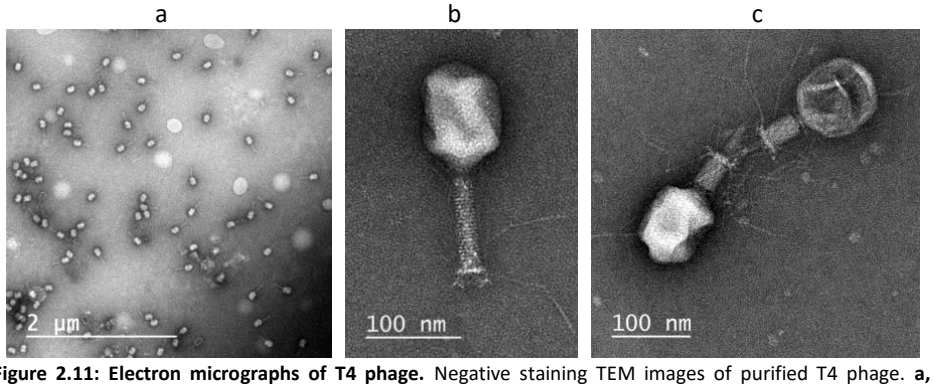

Figure 2.11: Electron micrographs of T4 phage. Negative staining TEM images of purified T4 phage. **a,** Overview of purified T4 phage preparation. **b,** Intact T4 phage. **c,** Two contracted T4 phages, of which one has ejected its genome.

We investigated four different concentrations of Alexa647 NHS-ester, ranging from 100 µM to 100 mM, and assessed the signal-to-background ratio. This was accomplished by incubating phages with Alexa647 NHS-ester dye following the manufacturer's instructions and removal of remaining dye from the solution using a filter column with a size excluded cut-off. Labeled phages were loaded into a flow cell containing immobilized *E. coli* B cells. Per tested condition we captured 10 images and qualitatively assessed to signal-to-background ratio using an intensity plot. These results revealed that the maximal tested initial dye concentration resulted in the highest signal-to-background ratio (Figure **2.12**). As high concentrations of dye might negatively affect the functional properties of the phage, e.g. obstruct binding to the host cell receptor, we decided that a 10 mM labeling concentration showed a signal-to-background ratio sufficient for our experimental conditions to detect single T4 phages.

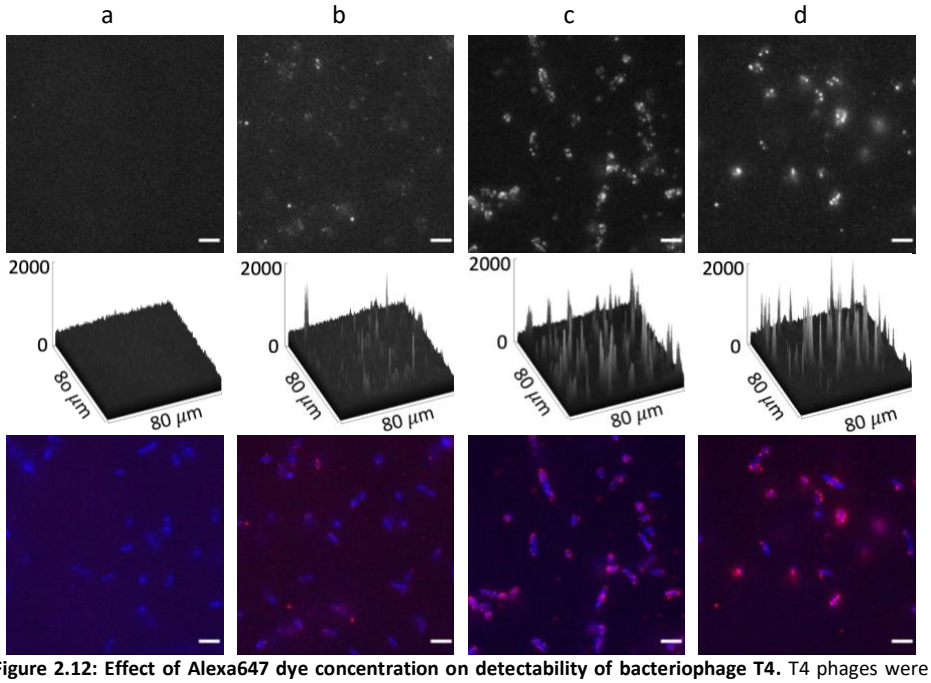

Figure 2.12: Effect of Alexa647 dye concentration on detectability of bacteriophage T4. T4 phages were incubated with four different concentrations of Alexa647 dye containing a reactive NHS-ester that binds to exposed lysines and N-termini, with **a,** 100 µM, **b,** 1 mM, **c,** 10 mM, **d,** 100 mM. Fluorescent images (top), their intensity profile (middle), and an overlay (bottom) of T4 (red) with *E. coli* B (blue, stained with the DNA stain DAPI). Exposure time and laser intensity differed between images of the first and last two labeling concentrations, with 150 ms and 551 µW versus 100 ms and 424 µW. Scale bar represents 5 µM.

To study phage-host interactions, we required our method to observe all phage collisions at any given position on the z-axis of the host cell. To test the range of detectability of labeled phages above and below the focal plane and assess whether this was sufficient to allow us to detect all phage-host interactions within our field of view, we investigated the z-axis range over which these fluorescently labeled phages where detectable across the focal image plane. To this end, we took images at different focal distances from the slide to which the cells were attached (z-stack, or focus stacking). We started at the bottom of the slide and ended at the top-end of the bacterium, using 200 nm increments. We found that labeling with 10 mM dye allowed for detection of phages across the entire desired z-axis range depth. Labeled phages bound to glass and on top of the cell where detected within each focal plane. This encompassed the complete height of the cell, providing an indication that detection of phages was possible up to at least 1.5 µm from the focal plane (Figure **2.13**). These results indicate that labeling phages with 10 mM is sufficient for detection of particles at all z-axis locations on the cell.

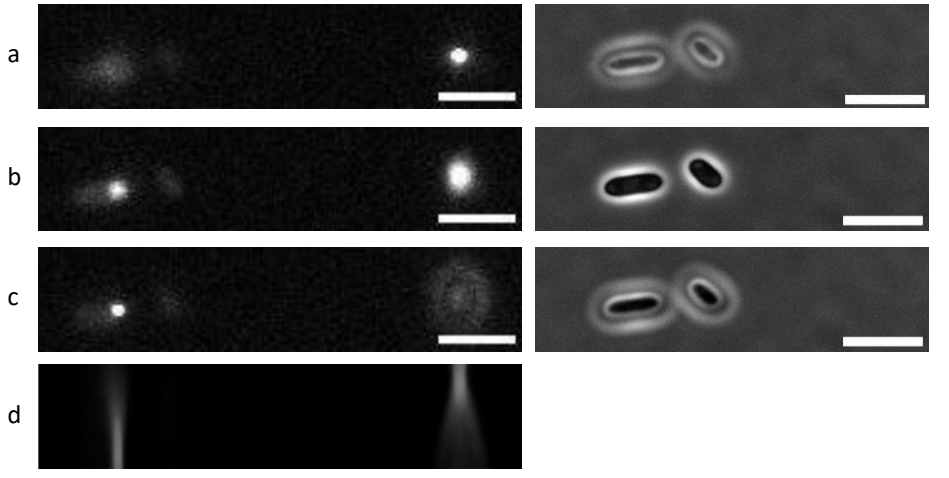

Figure 2.13: Phage detection outside the focal plane. Z-stack of the fluorescent channel (left) and corresponding phase contrast channel (right). Focus shifts from **a,** glass slide, **b,** mid-cell, **c,** top of cell. **d,** Intensity profile of fluorescent channel in z-direction showing a visual detection depth from the glass slide (attached phage to glass surface) up to at least 1.5 µm above the focal plane height (bound phage on top of cell). Scale bar represents 5 µM.

In addition to detecting the position of phages in static images, we were also interested in tracking phages over time. In order to test if labeling phages with 10 mM Alexa647 was sufficient for tracking phages over a longer period of time, we took images of bound phages (N = 3) throughout a period of 100 seconds while the sample was continuously excited (Figure **2.14**a). We delineated the fluorescent foci (phage) as a ROI and followed its mean intensity over time. We found that, during this time, the signal-to-background ratio of the fluorescent foci was sufficient to allow detection of the particle's position. The lowest observed ratio was 2.5 and was easily distinguished from background. However, bleaching of the fluorescent phage was observed, showing a loss of up to 50% in fluorescent intensity over a 100 second time period (Figure **2.14**b). We observed no single step bleaching event, indicating that the number of dye molecules present per phage was high. This indirectly led us to conclude that the chance of observing a phage that has not been labeled was low.

Overall, these results showed that labeling T4 with 10 mM of dye molecules allowed for a sufficient signal-to-background ratio ensuring detection of the phage across the entire focal plane of a cell, as well as, throughout a time period of at least a minute. Hence, the fact that phage detection was not limited to the cell surface, but also included the detection of phages to the substrate, should be taken into account during further data analysis and interpretation. We decided that this concentration of labeling T4 satisfied our requirements to detect phage-host interactions with our experimental set-up and used this concentration throughout further experimentation.

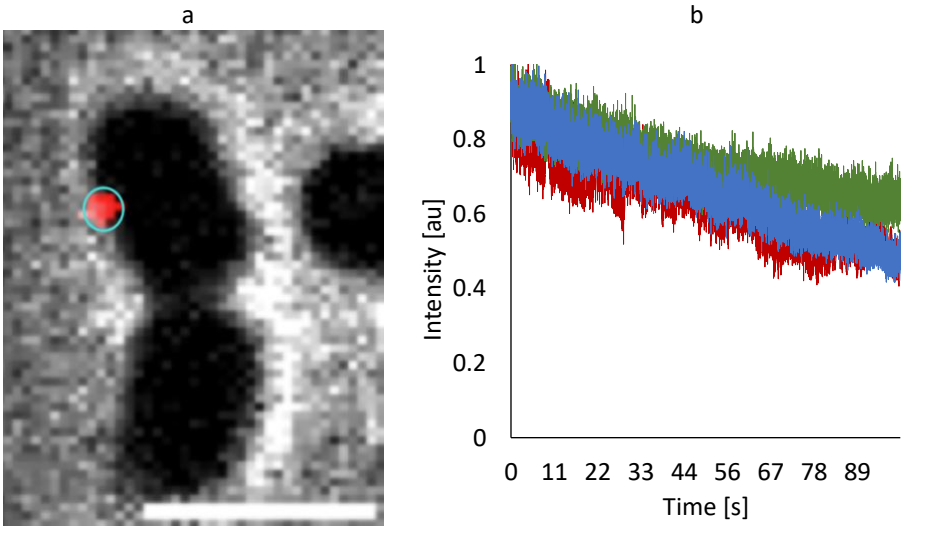

Figure 2.14: Alexa647 NHS-ester labeled T4 signal stability over time. Detection of fluorescent foci over time under continuous dye excitation. **a,** Phase contrast image of a cell overlaid with the corresponding fluorescence channel image showing a labeled bound phage (red). The foci for analysis were defined by circular ROIs (cyan) **b,** Normalized intensity profile of three single fluorescent phages (ROIs) over time. Scale bar represents 2 µM.

2.4.2. Nonspecific fluorescent-dye based protein labeling of pyocins

Next to studying phage-host interactions, we were also interested in following the search process of R2-type pyocins. In order to track them at single particle level, they needed to be fluorescently labeled. Pyocins are made out protein which can be fluorescently tagged. The nonspecific fluorescent-dye based protein labeling method applied on phages, described in the previous section, only required the presence of exposed primary amines. We tested whether this method and the Alexa647-dye concentration used to tag T4 phage could be extended to label R2-type pyocins. Therefore, we first obtained pyocins and assessed their purity and activity. This was

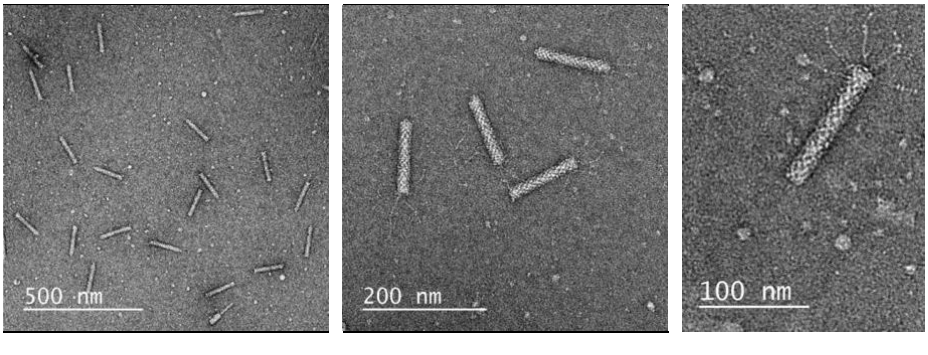

Figure 2.15: Electron micrographs of isolated R2-type pyocins. Negative stained EM images of isolated R2-type pyocins showing limited impurity of non-pyocin proteins or other contaminants. The vast majority of pyocins was non-contracted (left), and tail fibers were visible and intact (middle and right).

followed by labeling of the pyocins with 10 mM Alexa647 and a subsequent qualitative assessment on their detection, the degree to which the staining resulted in detectable single pyocin particles using fluorescent microscopy in a similar fashion as described above. Lastly, we assessed the visibility of single labeled pyocin particles over time.

R2-type pyocins were obtained from *P. aeruginosa* PAO1 strain, which produces these phage-tail like particles. Pyocins were isolated from cell lysate by ammonium precipitation followed by sedimentation via ultracentrifugation, as described by Williams *et al.* [30]. We confirmed the presence of R2-type pyocin particles and assessed their purity by visual inspection of negatively stained TEM images, and we tested their activity with a bactericidal droplet assay. Overall, we observed no contamination of other proteins or debris with a comparable size to pyocins. Further, the majority of pyocin fraction was non-contracted and intact (Figure **2.15**). The bactericidal droplet assay showed clearing zones of the bacterial lawn at a dilution >1:3125 (Figure **2.16**) indicating a concentration well above 10^6 pyocins per ml lysate.

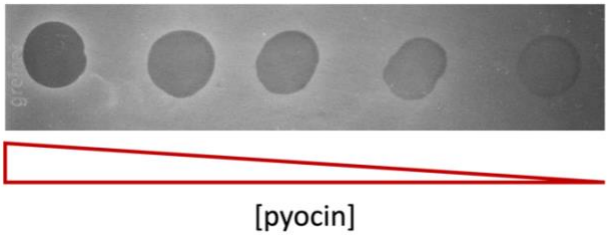

Figure 2.16: Bactericidal activity of R2 type pyocins. Bactericidal droplet assay showing the bactericidal activity of R2 pyocins in five-fold serial dilution on the target indicator strain *P. aeruginosa* 13S. Clearing of the bacterial lawn (dark areas) indicated cell death. Intensity of the droplet area indicated the degree to which indicator strain cells were able to grow.

Next, we labeled pyocins with 10 mM Alexa647 NHS-ester and tested their detection across the focal plane of a cell. Therefore, we inserted labeled pyocins in a flow cell containing immobilized 13s cells. After a short incubation period, we obtained images and assessed their visibility within the focal plane. Results showed fluorescent foci with a detectable signal-to-background signal. Similar as was observed for phages, labeled pyocins bound to glass were still visible with a focal plane at mid cell as out-of-focus foci, indicating that at this focal plane, pyocins can be detected across the entire z-axis of a cell (Figure **2.17**a). In addition, we tested whether labeling pyocins with 10 mM Alexa647 was sufficient for tracking pyocins over a longer period of time. Therefore, we observed fluorescent foci (cell bound pyocins) for at least a time period of a minute and measured its mean intensity over time (Figure **2.17** b). In alignment with fluorescent T4 phage, we observed an effect of bleaching over time. In spite of this, under the imaging conditions used (50 fps with an excitation time of 4 ms), we could distinguish pyocins easily from the background during a time period of a minute, with the lowest signal-to-background

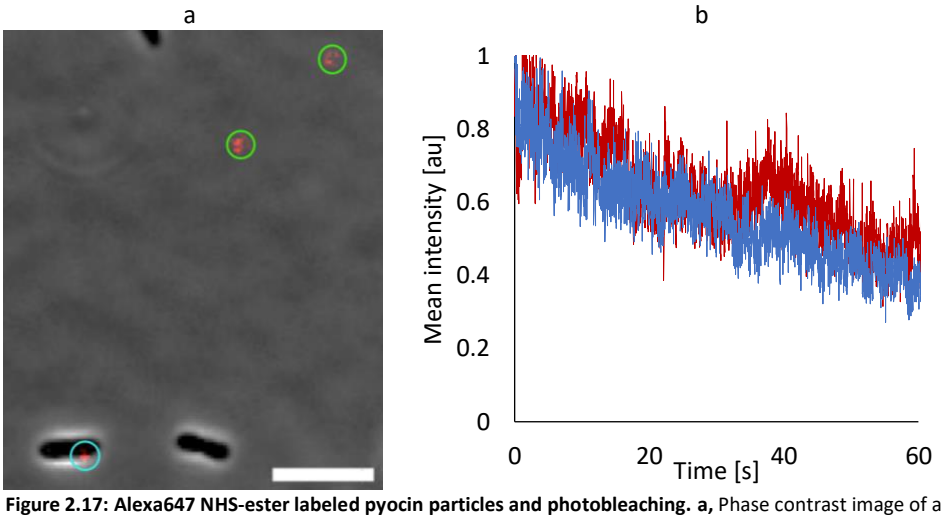

Figure 2.17: Alexa647 NHS-ester labeled pyocin particles and photobleaching. a, Phase contrast image of a cell overlaid with the corresponding fluorescence channel image showing labeled pyocins (red foci). Labeled pyocins were detectable both bound to the cell (cyan circle), as well as, bound to the glass slide (green circle). **b,** Intensity of two single fluorescently labeled pyocins bound to a cell over time. Scale bar represents 2 μM. ratio being >1000 (*n* = 2). This indicated that this dye and concentration is not only suitable for T4 phages, but can also be used to detect and track R2-type pyocins-host interactions. This result also suggests that a staining concentration of 10 mM Alexa647 is likely to be suitable for use with a broad range of bacteriophages and phage-like-particles.

2.4.3 Fluorescent labeling the genome

At the onset of this PhD project, we envisioned that we might reach a point at which we could combine phage tracking with detection of DNA injection. To this end, we explored the possibility to combine the nonspecific protein staining with DNA staining, to follow both processes while maintaining accurate detection of particle position. Many dyes have successfully been used to fluorescently label the genome of phages to facilitate visualization using fluorescent microscopy [15, 22, 31]. However, most dyes are not compatible with visualization of the DNA ejection process, as this process is obstructed by the dye binding properties. A high-affinity nucleic acid stain that gains over a 500-fold fluorescent enhancement when intercalated between the major grooves of DNA [32], referred to as SYTOX dye, has been shown to be capable of tracking the DNA ejection process of phage λ in real-time [15]. When used to label the DNA of phages, this dye has been shown to suffer a rapid decrease of fluorescent intensity over a timescale of seconds during exchange of buffer. This was documented to be caused by the fact that the dye diffuses back into the buffer, where changing the buffer leads to loss of dye molecules [15]. If required, this loss in intensity can be circumvented by resupplying an appropriate amount of dye to the buffer. We investigated whether SYTOX green was compatible with Alexa647 dye to ensure visualization of both the adsorption and DNA ejection process. Compatibility was checked in terms of overlap between their respective excitation and emission spectra and the filter requirements, followed by a qualitative assessment. We selected this dye, because it has previously been shown to be impermeable to intact cells [33, 34], therefore no signal would be detected without being infected by a phage or sustaining

a compromised membrane. Also, this dye had excitation and emission spectra compatible in terms of their respective excitation and emission spectra and filter requirements needed to obtain separate images.

We first tested the required concentration of SYTOX green needed to detect T4 phages, before assessing whether double labeling was possible. This involved qualitative examination of the degree to which SYTOX green concentrations, ranging from 50 nM to 50 μM, resulted in detectable particles. Phages were obtained and purified as described in section 2.2.2.1. Next, phages were labeled with the appropriate SYTOX green concentration and washed using a filter column with a molecular weight cut-off. The resulting phages were examined by obtaining 10 fluorescent microscopy images per tested dye concentration and the signal-to-background ratio was assessed qualitatively on the basis of intensity plots. These results revealed the same trend as was observed for nonspecific fluorescent protein labeling, with the best signal-to-background ratio obtained at the highest initial dye concentration (Figure **2.18**). Any concentration above 5 μM resulted in a detectable signal-to-background ratio after our standard procedure of exchanging buffers using a filter column. These results indicated that labeling phages with 50 μM dye yielded a sufficiently high signal-to-background ratio to be easily detected by fluorescence microscopy.

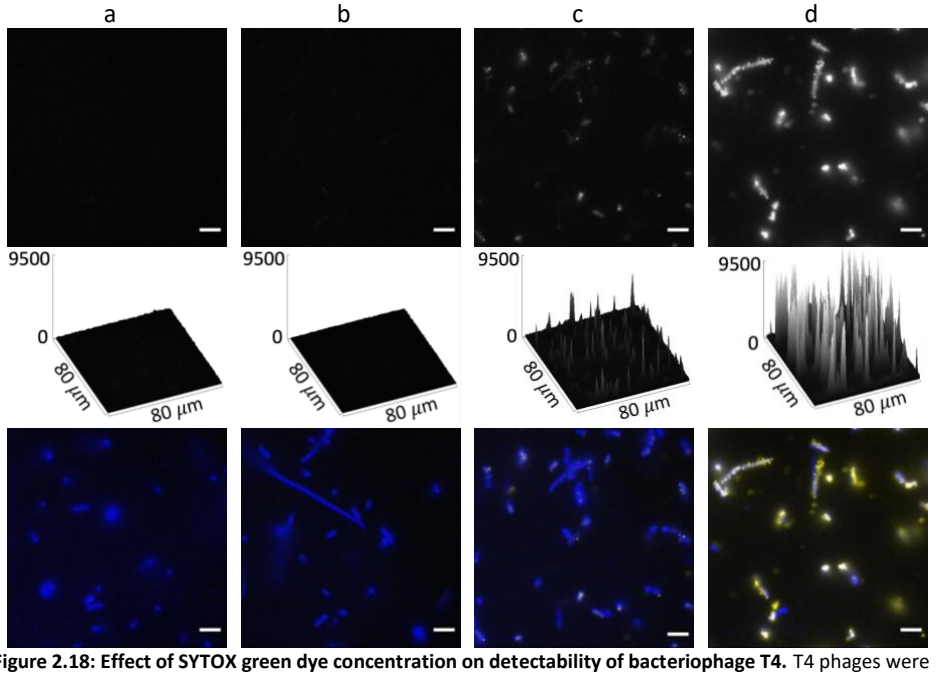

Figure 2.18: Effect of SYTOX green dye concentration on detectability of bacteriophage T4. T4 phages were incubated with four different concentrations of the DNA stain SYTOX Green. **a**, 50 nM. **b**, 500 nM. **c**, 5 μM. **d,** 50 μM. Fluorescent images (top), intensity profiles (middle), and an overlay (bottom) of T4 (yellow) with *E. coli* B (blue, stained with the DNA stain DAPI). Laser intensity differed between images obtained for the first three and last labeling concentrations, 346 and 242 μW, respectively. Scale bar represents 5 μM.

Next, we tested whether labeling of T4 phage with the nonspecific protein dye Alexa647 and DNA staining with SYTOX green could be combined. We first labeled protein using

10 mM Alexa647 NHS-ester, as described in section 2.2.2.1, followed by staining the DNA using 50 μM SYTOX green. The resulting doubly labeled phages were loaded into a flow cell containing immobilized *E. coli* B cells. The detection of both labels was assessed qualitatively by analysis of the respective fluorescent foci and the degree of spatial co-localization. Perfect co-localization of fluorescent foci was observed between the SYTOX green and Alexa647 signal. We occasionally observed a difference in the fluorescent intensity of SYTOX green between cell-bound phages. Freely diffusing- and phages bound to glass showed both signals. In some cases, cell-bound phages showed only a visible signal that originated from Alexa647 dye (Figure **2.19**). The latter observation most likely represents cell-bound phages that had ejected their genome. Overall, the results showed that it is possible to simultaneously detect the position of the phage and DNA ejection in real-time with dedicated fluorescent labels. Tracking of the binding dynamics could be realized by first exciting Alexa647 and imaging at high frame rate, followed by alternated excitation of SYTOX green and Alexa647 and imaging at low frame rate to observe subsequent DNA ejection while maintaining detection of the phage position.

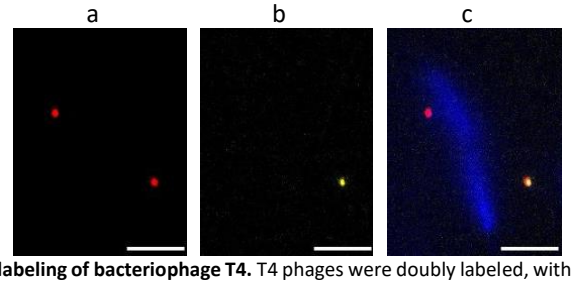

Figure 2.19: Double labeling of bacteriophage T4. T4 phages were doubly labeled, with **a,** 10 mM nonspecific protein dye Alexa647 NHS-ester and **b,** 50 μM DNA stain Sytox Green. **c,** Overlay of doubly labeled phage and *E. coli* B cells (blue, stained with the DNA stain DAPI) indicating the presence of two phages, one attached to the glass surface, and the other bound to a cell. Note that the bound phage lacks the DNA stain and has most likely already ejected its DNA into the host. Scale bar represents 5 μM.

2.4.4 Effect of labeling on activity and binding kinetics

Fluorescent labeling of phages by tagging viral DNA or protein, or by expression via genetic engineering has previously been shown to affect the phages biological function. These effects include, among others, a shift in mobility diameter [23], a decreased binding rate (the collision frequency of a single phage with a cell per volume unit during a given time interval) [17], and obstruction of DNA ejection [22]. Labeling T4 with the nonspecific protein label Alexa647 NHS-ester could, for instance, affect the functionality of the phage through steric hindrance of the interaction between LTF and host-receptor when one or several dyes bind to exposed lysines present on the distal-end of the LTF (Figure **2.9**b). Since, we were interested in studying the target-finding process of T4 phage by means of fluorescent microscopy, we investigated whether labeling with 10 mM Alexa647 altered the adsorption kinetics in bulk. To achieve this, we first examined the effect of labeling on the ability of phages to infect cells and replicate by means of a spot assay. Similarly, we also investigated the effect of labeling on the bactericidal activity of pyocin R2. Next, we investigated whether the dye had an effect on the size and/or shape of the phages by measuring its effect on the

hydrodynamic radius (R_h) with dynamic light scattering (DLS). Lastly, we analyzed the effect of labeling on the binding efficiency (i.e. fraction of phage particles in solution that adsorb irreversibly to the host) and binding rate, using a bulk adsorption assay. These results will provide insights in if and how labeling might affect these binding kinetics that should be accounted for when studying their behavior at single-phage level with microscopy.

The effects of labeling on the capacity of phages to infect cells, replicate and infect new cells was assessed by comparing the plaque counts using a spot assay. Labeling with Alexa647 was performed as described in section 2.2.2.1. Samples of labeled T4 phages and unlabeled T4 phages that had undergone the labeling treatment in the absence of the dye were serially diluted and spotted on an actively growing lawn of host indicator strain *E. coli* B. Infection was scored by visual inspection of clearance zones in the bacterial lawn, which at high dilutions allowed detection of plaques initiated by individual phage particles. The latter allowed determination of the active phage titer by counting individual plaques visible at lower dilution factors. These results revealed clearing zones of the bacterial lawn for both T4 and labeled T4 phage, indicating that the T4 phages were still capable of infection and propagation after labeling (Figure **2.20**). Statistical comparison of the number of plaques at lower dilution factors showed no significant difference in the active phage titer between labeled and unlabeled phages (n = 6).

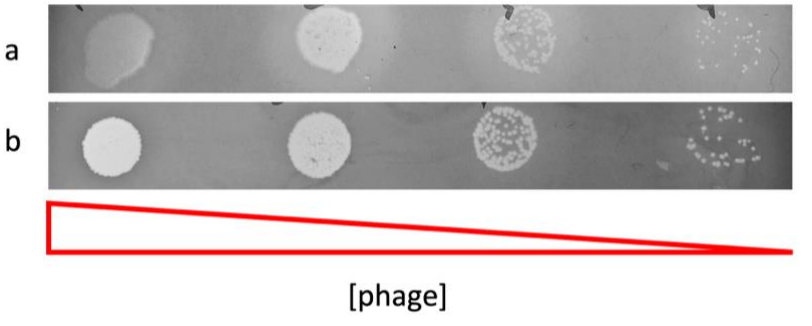

Figure 2.20: Effect of labeling on the active titer of T4 phages. Spot assays of increasingly diluted unlabeled (**a**) and Alexa647 labeled (**b**) T4 on *E. coli* B. Small clearance zones in bacterial lawn represent plaques formed by individual particles.

In a similar fashion, we also examined the effect of labeling on the capacity of pyocin R2 to kill cells of the host indicator strain *Pseudomonas aeruginosa* 13s. Comparison of the active pyocin R2 titer on the basis of the highest dilution that still caused clearing, indicate no substantial effect of the dye (Figure **2.21**).

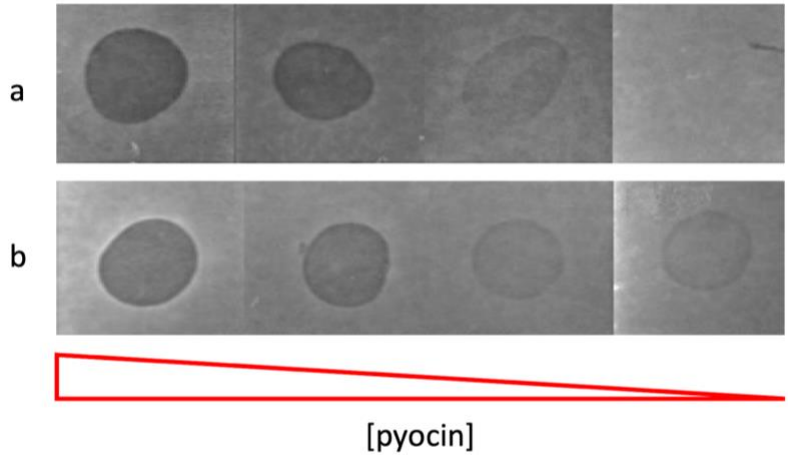

Figure 2.21: Effect of labeling on the bactericidal activity of pyocin R2. Bactericidal droplet assay of 5-fold increasingly diluted unlabeled (**a**) and Alexa647 labeled (**b**) R2 pyocins on 13s. Intensity of the droplet areas indicated the degree to which indicator strain cells were able to grow.

We also measured how the hydrodynamic radius (R_h) of T4 was affected by fluorescent labeling with Alexa647. This is related to the diffusion coefficient, and therefore, might affect the obtained fluorescence microscopy observed displacement of T4 through the medium studied in chapter 4. This might impact the obtained values gained within our experimental set-up. In addition, the hydrodynamic radius also provided information regarding the structural integrity, LTF deployment, and aggregation of T4 particles, that could affect the interaction with the host. The fluorescent label was relatively small (R_h of 7.52 Å and MW of 1250 Da) compared to T4 phage. Therefore, the effect of the label on the MW and size of T4 was expected to be small. We characterized the hydrodynamic radius by dynamic light scattering (DLS) in M9 medium at room temperature. First, we measured the size of unlabeled T4, which yielded a R_h of 67.83 ± 0.35 nm (mean ± SD), with a polydispersity percentage of 8.50 ± 2.49 indicating the sample to be monodisperse and showing no form of aggregation. The measured hydrodynamic radius differed significantly from a previously reported value (137.9 ± 1.06 nm) [35] (Bonferroni corrected t-test; n = 6, p < 0.0001). This was most likely a result from the calibration settings, i.e. our set-up was calibrated with spherical particles. Secondly, we measured the size of Alexa647-labeled T4 and compared its size to unlabeled T4. Labeled T4 phages had a R_h of 78.70 ± 0.80 nm. The measured size distribution showed a narrow peak (Supplementary figure **2.2** and Supplementary figure **2.3**), with a polydispersity of 17.43 ± 3.39 %, indicating the integrity of the phage lysate after labeling, and no form of aggregation of phage particles. This relatively large increase in size was significant (Bonferroni corrected t-test; n = 6, p < 0.0001; Figure **2.22**). However, the increase in volume and/or mass of the attached fluorescent labels was likely not by itself able to explain the mean increase of 11 nm in size. Rather, it might be a consequence of extension of the LTFs, as result of the presence of fluorescent labels. LTF deployment has previously been shown to increase the drag coefficient of the phage particle [36]. We investigated whether LTF extension and retraction could indeed alter the R_h by measuring the size of T4 in the presence of a

saturating amount of L-tryptophan with respect to phage particles (> 6 molecules per phage), known to act as co-factor in LTF deployment (i.e. unbinding from the sheath) [36, 37], and indole, known to inhibit LTF deployment [38]. Here the latter served as a control. In M9 medium, T4 phage was known to have 1 to 2 of their LTFs in the extended state. Phages in M9 + L-tryptophan were expected to have the remaining LTFs in extended state, which was, with a shift in position of 4-5 LTFs, expected to result in a relatively large increase in hydrodynamic size. This in contrast with phages in the presence of indole, which should result with the retraction of all LTFs – shift in position of 1-2 LTFs, in only a small decrease in hydrodynamic size. Results showed that L-tryptophan significantly increased the R_h of T4 (Bonferroni corrected t-test; $n = 6$, $p < 0.001$; Figure **2.22**), indicating that LTF extension/retraction could alter the R_h. To assess whether the positive effect of the dye on the size of T4 could be explained by the LTF-mediated effects of L-tryptophan, we compared the size of T4 in M9 + L-tryptophan with the size of labeled T4 in M9. We found that labeled T4 had a significantly larger R_h then T4 with L-tryptophan induced deployed LTFs (Bonferroni corrected t-test; $n = 6$, $p < 0.001$; Figure **2.22**). This indicated that, even when there was enough dye that resulted in full LTF deployment, as was observed for phages M9 + L-tryptophan, it would only explain a part of the observed increase in R_h. However, a combination thereof, where labeling results in both LTF deployment and an increase in size and drag of these deployed LTF, which together – the sum of their effects, are larger than the effect of the individual components together, might be able to explain the measured R_h. Whether LTF deployment was indeed an underlying cause of the increase in R_h could be confirmed by examining the R_h of labeled phages in the presence of L-tryptophan. If there is no measurable difference in R_h than the presence of dye does effect LTF deployment.

Overall, we established that there was a detectable effect of dye on the R_h which meant that there was also a direct effect on the value of the measured diffusion coefficient. This should be taken into account when comparing the obtained value with values of unlabeled phages in literature.

Lastly, we tested whether the dye had an effect on the adsorption kinetics. This was accomplished by examining the binding efficiency (ε) and binding rate constant (k) by means of an adsorption assay. To achieve this, we wanted to create an environment with near ideal binding conditions, in which we could measure the effect with maximal resolution. As mentioned in the previous section, certain molecules have been shown to affect the LTF deployment state of T4 phages, which subsequently affect binding to the cell. L-tryptophan has been shown to remodel T4 phages [37, 39-43], by causing a conformational change in the phage tail structure, resulting into a configuration in which all six tail fibers are extended downward from their tail plate, [36, 37] that increases the chance of binding to the cell – maximal binding likelihood. Conversely, indole has been shown to 'deactivate' T4 phage by preventing LTF deployment, causing them to remain in a retracted position along the phage body [38], decreasing the chance of binding – minimal binding likelihood. Therefore, the state of LTF deployment in the presence of these molecules can serve as an indicator of the fraction binders of phages. In other words, the different tested media – different states of LTF deployment, can serve as a proxy for the fraction binders, i.e. provides a measure of the infectivity

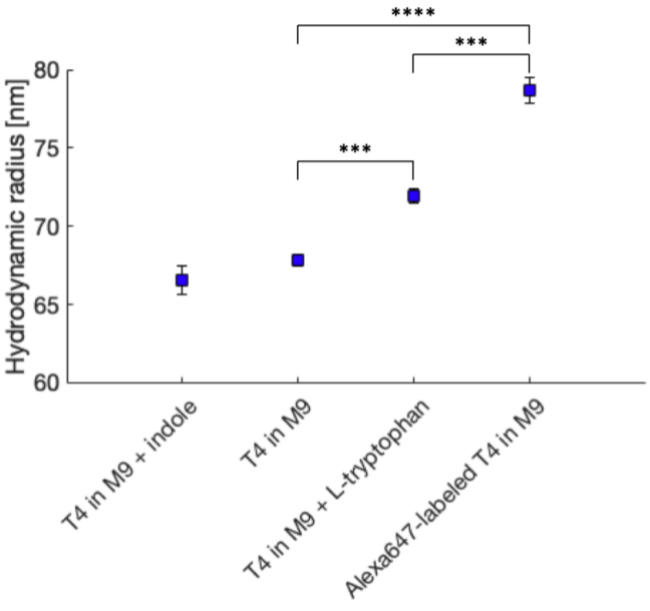

Figure 2.22: Effect of dye and medium components on hydrodynamic radius of T4 phage. The hydrodynamic radius of purified T4 phage measured with DLS in the presence of different medium components. Error bars indicate standard deviation. Asterisks above brackets indicate statistical significance (***: $p < 0.001$, ****: $p < 0.0001$; see text for statistical analysis).

of a phage on population level. This in turn can be related to establish the extent of the effect of labeling, assuming the phages are within an ideal environment for binding. We first confirmed whether adsorption of our T4 phage stock was, under our experimental conditions, sensitive to the indole and L-tryptophan molecules by investigating the effect of adsorption efficiency of phage T4 to its host in the presence and absence of these molecules. Afterwards, we established for each of these conditions the maximal fraction of binding that could take place, allowing us to establish the most ideal medium composition, i.e. the medium composition that relatively gives the highest fraction of binders. Next, this medium was used to test the effect of labeling on the adsorption kinetics, by comparing the adsorption rate and efficiency of labeled vs unlabeled T4 phages. First, we examined the fraction T4 phages in the population that bound irreversibly to the cells in the three media compositions: M9, M9 supplemented with L-tryptophan, and M9 supplemented with indole. Both of these compounds were added in concentrations that were saturating with respect to their effects on LTF deployment state [44, 45]. Phages were incubated with *E. coli* B for 15 minutes, whereafter the free and bound phages were separated using a filter with a size cut-off. The fraction of bound phages was determined by measuring the change in the concentration of free phages, which was quantified by counting individual plaques using a spot assay. The concentration of irreversibly bound phage was normalized by dividing it by the initial phage concentration to obtain the fraction of irreversibly bound phages. A significant decrease in the fraction of irreversibly bound phage was found in the presence of indole

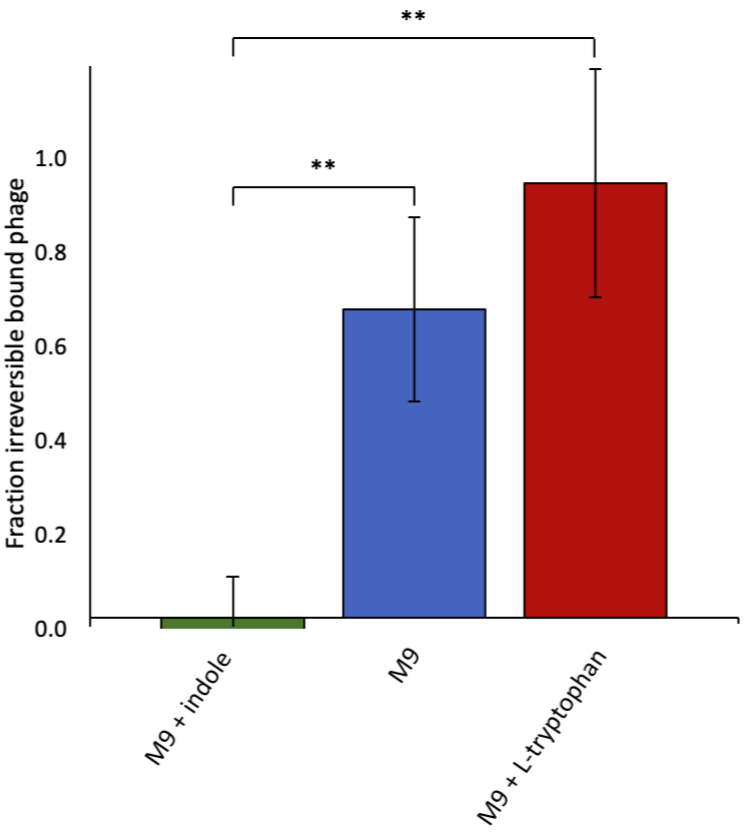

Figure 2.23: Effect of LTF deployment on fraction irreversibly adsorbed T4. Normalized fraction of irreversibly bound T4 phage after 15-minute incubation with *E. coli* B. Values were normalized relative to the initial stock concentration. Error bars indicate standard deviation. Asterisks above brackets indicate statistical significance (**: $p < 0.01$; see text for statistical analysis).

compared to M9 and M9 with L-tryptophan (Bonferroni corrected t-test; $N = 6$, $p < 0.01$; Figure **2.23**). This indicated that within these experimental conditions our T4 phage stock was sensitive, with respect to binding efficiency, towards the presence of these molecules. However, there was no significant effect found between the T4 binding fraction in M9 and M9 + L-tryptophan, making it impossible to determine the most ideal medium composition for binding. However, the priori power analysis showed a low value (0.13 for one-sided student t-test with equal variance), most likely due to the large standardized effect size (d = 1.22), which may therefore not have rejected an incorrect H_0 hypothesis. As the highest binding fraction was found for T4 in M9 + L-tryptophan, with a mean fraction of 0.93 ± 0.24 closest to a 100% binding fraction, we decided to test the effect of the dye on the binding kinetics within this medium composition.

After establishing the most optimal medium for binding, we addressed the question whether there was an effect of the dye on the adsorption kinetics. This was assessed by examining the adsorption efficiency and rate of unlabeled- and Alexa647-labeled T4

phages. We obtained these binding properties via an adsorption assay with *E. coli* B cells in M9 medium + L-tryptophan. The fraction of irreversible binders was measured as a function of time and obtained as described in the previous section. Due to the unknown initial phage concentration for labeled T4 phage, these labeled samples were normalized using the initial phage concentration of a previous experiment that made use of the same labeled stock. Here we assumed that, given the fact that these phages were from the same batch, and decay of phages was negligible during a week of storage at 4 °C (data not shown), that concentrations were the same and therefore should not affect the interpretation of the outcome. The following model that describes the adsorption kinetics of T4 phage to *Escherichia coli* system as a function of time was used [43]:

$$\frac{C_p(t)}{C_{p0}} = 1 - \varepsilon(1 - e^{-kC_{h0}t}), \qquad \text{Equation 2.1}$$

where $C_p(t)$ is the free phage concentration at time point t, C_{p0} the initial phage concentration, C_{h0} the initial host concentration, ε the adsorption efficiency, and k the rate constant, was fitted to the experimentally obtained results to extract the binding efficiency ε and rate constant k. This model was proposed by Storms *et al.* [43] to better describe the observed data than the widely accepted older two-step adsorption model

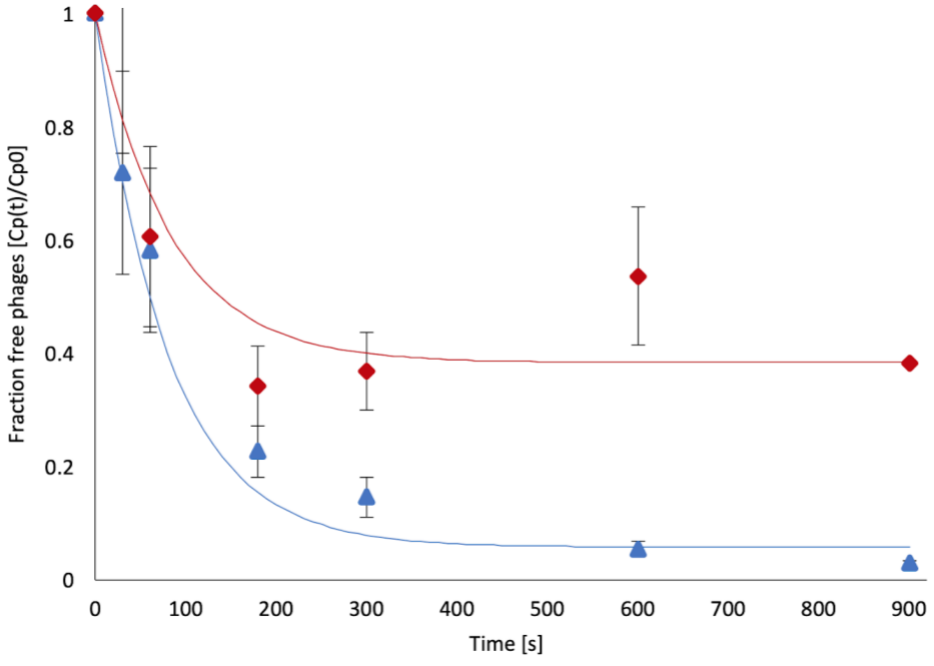

Figure 2.24: Effect of labeling on adsorption kinetics of bacteriophage T4. Adsorption assay of T4 (blue triangle, N = 3) and Alexa647-labeled T4 (red diamond, N = 2) to *E. coli* B in M9 medium supplemented with 1 g/L L-tryptophan. Error bars present the standard deviation. Experimental data is fitted to the proposed adsorption model described by Storms *et al.* [43] and presented as a line (blue and red for T4 and Alexa647-labeled T4 phage, respectively).

described by Stent and Wollman [44]. Using this model, results of labeled and unlabeled T4 were shown to exhibit the same trend: an initial rapid decay in the fraction free phage, followed by a period of little to no further adsorption (Figure **2.24**). Based on the results shown in Figure **2.23**, we expected that, in presence of enough L-tryptophan, T4 phages bind with a high binding efficiency (i.e. near 100%) to *E. coli* B. The obtained results showed a binding efficiency of 0.95 ± 0.04 and a rate of 3.73e-10 ± 2.79e-10 mL s^{-1} (mean ± SD) for unlabeled phages. These averages were found not to deviate significantly from the adsorption efficiency and rate values previously obtained by Storms *et al*. (fraction of 0.99 ± 0.09 and 6.8e-10 ± 3.5e-11 mL s^{-1}) for T4 phage in MSM + L-tryptophan buffer [43]. This confirmed our previous observation that binding conditions within this medium were close to optimal in the presence of high amounts of L-tryptophan. This allowed us to study the effect of labeling on binding kinetics. Labeling of T4 resulted in a significant decrease in binding efficiency, with a fraction of irreversibly bound particles of 0.64 ± 0.02 (Bonferroni corrected t-test; $N = 5$, $p < 0.01$; Figure **2.25**a), and a small decrease in rate to 4.45e-10 ± 3.75e-10 mL s^{-1}, which was found not to deviate significantly from unlabeled phage (Figure **2.25**b). Overall, these results demonstrate that, although the rate was not measurably affected, a large fraction of the phage population experienced steric hindrance during the adsorption process as a consequence of labeling.

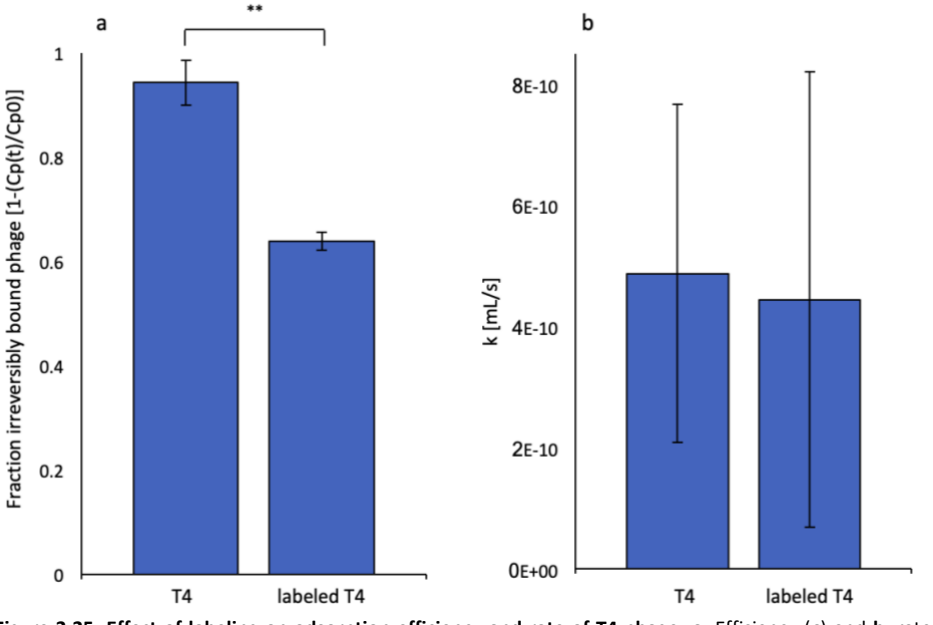

Figure 2.25: Effect of labeling on adsorption efficiency and rate of T4 phage. a, Efficiency (ε) and **b,** rate constants (k) of T4 and Alexa647-labeled T4 phage stock to *E. coli* B were extracted using the model described by Storms *et al.* [43]. Error bars present standard deviation. Asterisks above brackets indicate statistical significance (**: $p < 0.01$; see text for statistical analysis).

2.5 Discussion and conclusion

We performed experiments to establish a suitable dye concentration to label phage T4 and pyocin R2 to study dynamical interactions between single-phage/pyocin and host using fluorescent microscopy. We found that a nonspecific fluorescent dye-based protein labeling method that made use of chemical conjugation with an NHS-ester, previously described to successfully couple linkers or dye molecules to phages [17, 20, 26], met our requirements. A labeling concentration of 10 mM Alexa647 NHS-ester provided a sufficient signal to detect single T4 phages and R2-type pyocins at all sites on a cell and for a time sufficient to track interactions with host cells. In addition, the genome stain SYTOX green was shown to be compatible with Alexa647-labeled T4 phage, at a concentration of 50 μM, potentially easing the process with which the initial cell contact till DNA ejection can be studied at single-phage level. Based on these findings, we established a protocol that yielded fluorescently labeled phages and pyocins that could be tracked at single-particle level to study interactions with their host. As with all labeling methods, some adverse effects of labeling were found. In particular, labeling T4 with Alexa647 increased the hydrodynamic radius and reduced the binding efficiency of particles within a liquid environment.

Phages contained an abundant number of fluorescent labels, making it possible to track phages across the entire cell body. Even though the point spread function (PSF) of the fluorescent foci gives a rough idea of the position of the phage particle relative to the focus of the image plane at mid-cell position (i.e. PSF increases relative to the distance from the focal plane), it does not provide information on the direction within *z* (i.e. substrate or top of cell body). On top of that, this information gets lost during the generation of trajectory paths (described in section 2.6.4.1) that only makes use of *xy* coordinates. As phage particles were detected across the whole cell body, this resulted in the generation of phage trajectories that would also have occurred at the substrate, next to those at the cell. The fact that these obtained phage trajectories were not necessarily present at the cell surface should be taken into account during analysis and interpretation of those given trajectories. One could consider using an intensity cut-off for spherical foci with a set diameter, preventing detection of 'out-off focus' phage trajectories that were present at the substrate. However, these actions would also result in a reduced length, and therefore information, of the obtained trajectories, due to the effect of bleaching and/or potential *z*-directional movement of the phage particle across the cell body.

The measured hydrodynamic radius of T4 phage did not match the results described by Szermer-Olearnik *et al.* [35]. In addition, the values were also smaller than the sizes obtained by EM. A likely explanation could be the difference in calibration of the set-up. Within our set-up the size was obtained assuming that phages were spherical particles. Despite this difference, our main conclusion regarding the effect of dye on the hydrodynamic radius was still valid. Even though this effect was larger than we can explain on account of dye-induced LTF deployment, a combination of additional factors could have added to this effect. For example, labeling of the dye will increase the surface area slightly by approximately 1.43 nm [46]. Future investigations could test whether the dye was a source contributing to the hydrodynamic radius of the labeled T4 phage, by measuring its size in M9 + L-tryptophan. If labeling of the phage with this

dye results in LTF deployment, the hydrodynamic radius of labeled phages should not be affected by the presence of L-tryptophan.

Although no effect of dye was found on the fraction of infective phages and the size and morphology of plaques in top-agar plates, the binding efficiency in liquid was strongly reduced. It is not known whether this was caused by non-functional phages or by compromised phages that exhibited slower binding kinetics due to dye-induced steric hindrance of the LTF-receptor interaction. The latter seems most likely, as the unbound fraction (i.e. free phage fraction at each given time point within the adsorption assay) was still capable of infection and replication on agar plates. This point towards the fact that a large fraction of phages has extremely slow binding kinetics on the timescale beyond that of 15 minutes. This could be tested by repetitively adding the remaining free phage fraction after each 15-minute incubation period to a new batch of bacteria and measuring the concentration over time. A decrease in the free phage fraction provides evidence of these slow binding kinetics. Assuming the latter, that they were still capable of infection, their numbers were with .34 of the trajectories considerable and could have direct implications with regard to studying single phage-host interactions in our experimental set-up, e.g. these phages could still interact reversibly with host cells during the short timescale period in which we imaged. However, assuming these phages exhibited extremely slow binding kinetics due to the dye-induced steric hindrance of the LTF-receptor interaction, we would expect these interactions to occur less often and to be shorter in duration compared to the 'normal' fraction, i.e. fraction of phages that binds within a 15-minute time window. If and how the interaction dynamics of these presumably slow-binders presented themselves could be examined by imaging phage trajectories of such an isolated fraction. Given the fact that these phages were most likely still capable of some sort of interaction, albeit at a lower rate, should be taken into account when interpreting trajectory dynamics.

Even though no statistically significant difference was found in the adsorption rate of labeled and unlabeled T4, the variation among samples was large. As a result, the power of the test to detect relatively small differences was low. To improve the test power, either the sample size needs to be increased or the standard deviation be decreased. The latter could be accomplished by for example increasing the volume in which phage-host interaction takes place.

Based on the findings, we conclude that tracking of phages on a short timescale or single images of bound phages can best be made using phage DNA staining as this does not hinder the phage-host interactions. However, this method cannot be used to label and track pyocins, nor is it known if it could be used under experimental conditions to track phages at high temporal resolution and over longer time periods. The latter depends on the bleaching rate of the dye molecules that are intercalated within the DNA and the rate with which these bleached molecules get exchanged with new ones that could be added to the medium. Even though we have not investigated this experimentally, it would be a good recommendation to explore for future directions. Another class of dye that could label the protein and which was compatible with the technique currently tested, were Qdots. The use of Qdots over organic dyes, could reduce the number of labels extensively, as Qdots are known for their good signal-to-background ratio with a signal that could be tracked for hours without substantial photobleaching, requiring only one or two labels per phage. However, such

a low number of Qdots, has been shown to result in a fraction of unlabeled phages [21]. In addition, labeled phages with such low numbers of Qdots suffer from blinking states, disrupting tracking of the phage particle. Moreover, as Qdots are relatively large compared to organic dyes (10-20 nm depending on the coating), labeling phages with Qdots have been shown to results in a shift in mobility diameter [23], and a substantial decrease in adsorption rate [17]. Furthermore, as the labels were substantially larger, they potentially could cause a more severe effect on steric hindrance when bound on an unfavorable place, even though this chance reduces when the number of labels are decreased.

Taken together, our finding allowed us to formulate a protocol of phage/pyocin labeling that is used in the experiments described in the remaining chapters of this thesis to shed light on the single-particle binding distribution and on-cell dynamics of phage T4 on *E. coli* B cells and the on-cell dynamics of pyocin R2 and its bacterial target 13s.

Part III - Data analysis

2.6 Results

2.6.1 Experimental set-up

In the two previous parts of this chapter, we optimized a flow cell (part I) to which we can insert fluorescently labeled T4 phages or R2-type pyocins (part II) that can interact with the immobilized target cells attached to a poly-L-lysine coated coverslip. The last part of this chapter (part III) will cover the data analysis workflow. To obtain data that can be analyzed, the position and dynamical interactions with the cell can be observed using fluorescent microscopy. The major technical challenge of single-particle tracking (SPT) is that the signal to background noise ratio (SNR) tends to decrease rapidly over time due to bleaching of fluorescent dye molecules. Our goal was to track fluorescent single-phage particles over time and their interaction with their host. We achieved this by using a mode of microscopy referred to as a highly inclined and laminated optical sheet (HILO) illumination. This mode has almost eight times higher SNR over conventional epifluorescent microscopy [47]. This reduces the required output of the laser intensity, and therefore, increases accurate tracking over longer periods of time. Essentially, HILO is a mode of imaging between Total Internal Reflection Fluorescence (TIRF) and epifluorescence, were the laser is directed at an angle just beyond TRIF, resulting in a thin light sheet with an imaging illumination depth of up to 10 μm. In contrast to TIRF, this mode allowed for visualization beyond the surface area, allowing visualization of the phage along the entire height of the bacterial cell with only a minor loss in SNR. This mode has been used before to visualize and quantify molecular dynamics, kinetics and interactions in biological systems for tissues, nuclei or other cell material that are not within reach using TIRF [47]. In addition, this method has been previously used to observe the first phage-host interaction of phage λ belonging to the family of S*iphoviridae* [1]. Here we applied this mode of microscopy for SPT of another family of phages, namely T4 of the *Myoviridae*. In addition, we also used it to study the

phage-like particle R2-type pyocins. An overview of our experimental set-up is shown in Figure **2.26**.

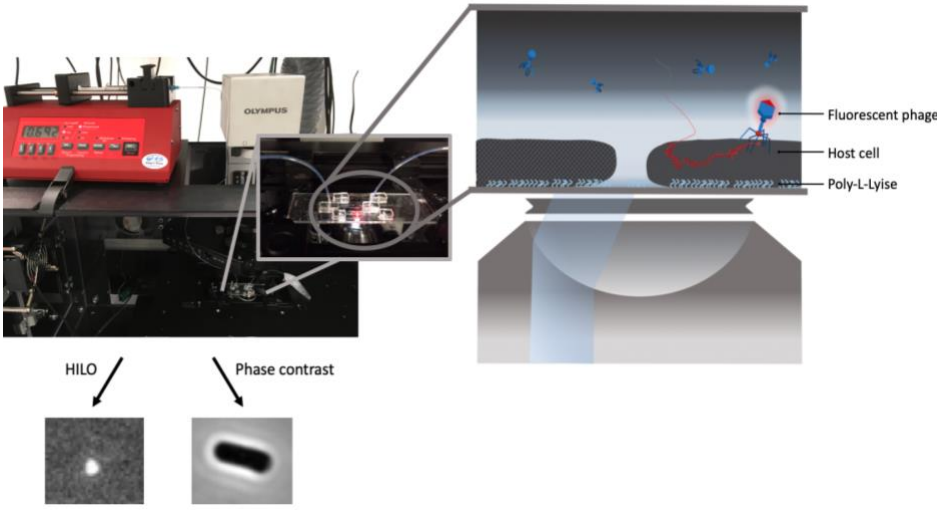

Figure 2.26: Experimental set-up for SPT of phage-host interactions. a, Photo of experimental set-up, with an enlargement on the area containing the loaded flow cell that is placed on top of the microscope objective. Imaging of fluorescent phages was performed with fluorescent microscopy in HILO mode with an imaging illumination depth of at least 3 µm, while cells were imaged with phase contrast microscopy. **b,** Schematic representation of experimental set-up, visualizing a cross-section of the microscope in HILO mode, with the beam positioned to propagate near the objective edge creating a thin laminated sheet. On top of the objective a cross-section of a flow cell can be found, containing fluorescent phages freely diffusing within the medium. These phages can interact with host cells immobilized to the poly-L-lysine coated flow cell. Once phages are within the reach of the illuminated sheet, the position can be tracked over time, as indicated by the illustrative trajectory.

2.6.2 Overview of the data processing workflow

The data obtained from the microscope within our set-up were fluorescent and phase contrast images containing information about phage and bacterium position. In order to extract data-containing information on the phage's position relative to bacterial host cells, we developed a framework, involving a number of steps, in which these images were being processed. The processed data can be used to study phage-host interactions, including the reversible and irreversible binding distribution, binding dynamics, and detailed on-cell motion of phages. Here we elaborate this framework. The workflow was split in two branches, one for obtaining and studying the binding distribution (single-image analysis) and another to study dynamical interaction between phage and cell (multiple-image analysis). The workflow for both single- and multiple-image analysis was outlined in Figure **2.27** and described in detail in the sections below.

Briefly, to study the binding distribution, single-image analysis started with determining the contour of bacterial cells using a thresholding method in ImageJ, followed by cell selection in Matlab. In parallel, the center position of individual phages was localized by detecting the center position of intensity of each fluorescent focal point. Next, phages attached to cells were selected and the corresponding coordinates

were transformed to a normalized bacterial coordinate representation that could be used for studying the binding distribution.

For the study of binding dynamics, a multiple-image analysis framework was developed. Here, cell contours were obtained, similar to single-image analysis, and subsequently examined for cell movement, followed by a cell selection procedure in Matlab. In parallel, trajectories of phages were obtained using TrackMate, a plugin of Fiji, and imported into Matlab. When two different cameras were used in the microscope set-up (one for obtaining fluorescent and another for obtaining phase contrast images), an additional step was performed where images were aligned to facilitate proper overlay between images. This was followed by a selection procedure of trajectories. The extracted data could be used among others to study the mean square displacement (MSD) and diffusion coefficient of phages, as well as, the reversible binding distribution, dwell time and area, and directionality of movement. Lastly, trajectories could be subjected to a step-finding algorithm to study on-cell motion in detail, providing information on the nature of movement. For discrete movement, step sizes and stepping dwell times can be retrieved. For this latter step in the workflow, we performed in parallel a second, more detailed, analysis on the cell motion to examine the degree of cell motion at sub-pixel level.

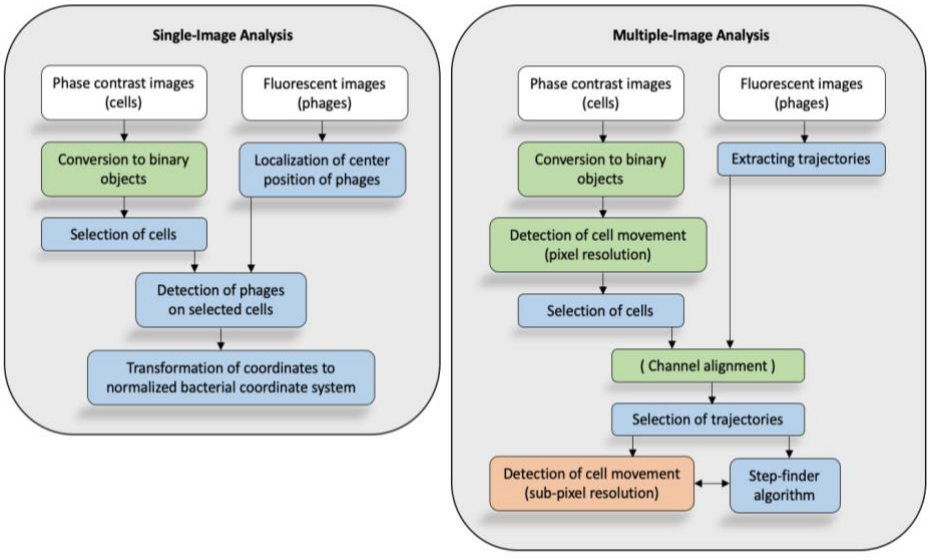

Figure 2.27: Image processing workflow for single- and multiple image analysis. The following workflows were used to extract data for obtaining and studying the binding distribution (single-image analysis) and dynamical interaction between phage and cell (multiple-image analysis). Each block in the scheme presents a step where data was processed, with the colors indicating the used image analysis software. Colors green, blue, and orange present Fiji, Matlab, and Python, respectively.

2.6.3 Single-image analysis

We set up a workflow to analyze the phage binding distribution that contained the following steps: i) binarization and selection of cells, ii) center detection of phages, and

iii) transformation of the cell and phage coordinates to a normalized bacterial coordinate system. In the next paragraphs, each of these steps will be elaborated.

2.6.3.1 Binarization and selection of cells

Phase contrast images of cells were loaded in Fiji and processed by a macro containing the following procedures to extract the contour of cells. First, contrast enhancement was applied by saturating the pixels with 0.03%, followed by a Gaussian blur, with a sigma of 2, to smooth the outline of the cell. The last step was to binarize the image using the Yen threshold function [48]. Due to thresholding, the binary image of the bacterium was slightly smaller than that of the raw image. Therefore, an extra pixel was added to the outline of the binary object using the function dilate.

This was followed by a selection procedure to define the cells that could be used for further analysis. Therefore, binary images were loaded into Matlab and binary image objects were detected using the function regionprops. An automatic selection procedure was applied to the designated valid objects using the following criteria: minimum object area, maximum object area, minimum solidity of the object, and minimum eccentricity of the binary object. Here the first two criteria were set at 20000 and 80000 nm^2 and used to discard to small and to large objects (e.g. noise and clusters of bacteria), respectively. The minimum solidity was defined as the area divided by the convex area of a binary object. This threshold was

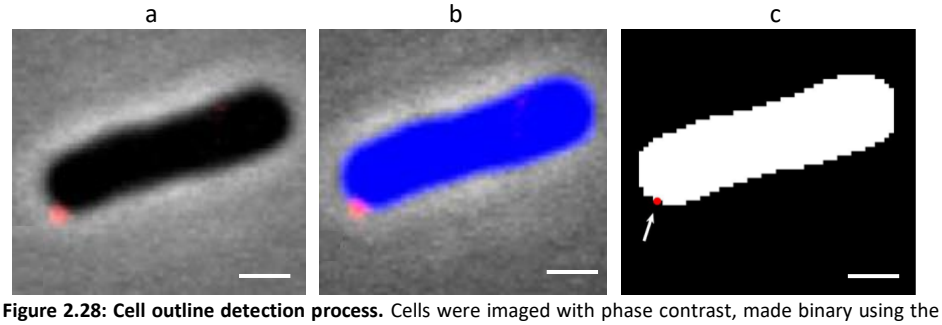

Figure 2.28: Cell outline detection process. Cells were imaged with phase contrast, made binary using the Yen thresholding method in Fiji, and loaded into Matlab for further analysis. **a,** Original phase contrast image with a single *E. coli* B cell (black elongated object) overlaid with corresponding fluorescent image visualizing an irreversibly bound T4 phage (red dot). **b,** Binarized cell (blue) overlaid with original image depicted in a. **c,** Binarized image was loaded into matlab and the image object (cell) was detected (white objects) and characterized. In parallel the center position of irreversibly bound phage was determined (red dot indicated with white arrow). Scale bar presents 1 µm.

set at 0.9 and used to discard clustering or dividing bacteria. The last criteria, the eccentricity (*e*) of the binary object, was defined by equation 2.2,

$$e = \sqrt{1 - \frac{b^2}{a^2}}, \qquad \text{Equation 2.2}$$

and describes the ratio between *a* the long and *b* short axis of an ellipsoid object. A value of 0 and 1 for *e* represents a circle and line segment, respectively. Since *E. coli* cells are rod-shaped, the eccentricity of the binary object was set to 0.7. This threshold was used to discard binary detected objects that were too round. The round shape of these objects often indicated that the detected bacteria were larger than the minimum required object area but still too small resulting in poor detection of the cellular poles.

After the automatic selection procedure (Figure **2.29**), images with selected objects were manually inspected, and if required, objects were discarded manually, i.e. dividing or moving cells (in case of time-lapse imaging cells were subjected to cell movement analysis, section 2.6.4.4).

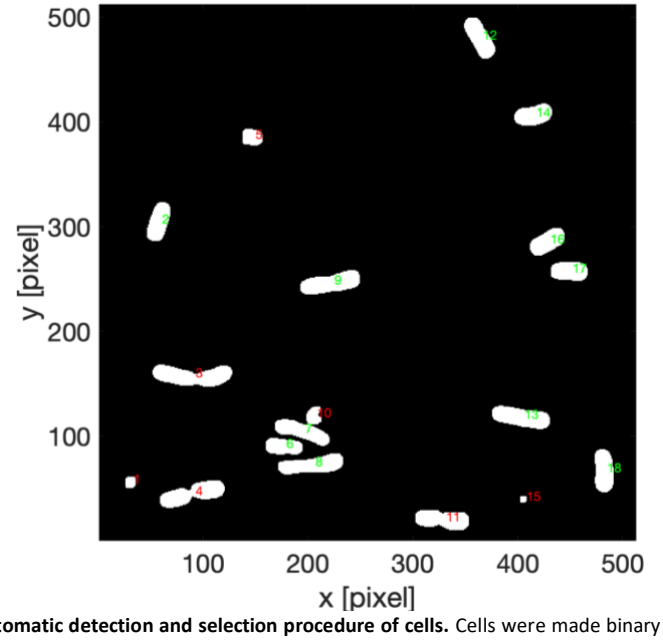

Figure 2.29: Automatic detection and selection procedure of cells. Cells were made binary (white objects) and selected automatically by thresholding the objects based on minimal and maximal area, minimum solidity, and minimum eccentricity. Cells could also be discarded manually, by deselecting the binary object. Selected and discarded objects received green and red numbers, respectively.

2.6.3.2 Detection of center position of fluorescent phages

Next, we determined the position of phages. Therefore, fluorescent images were loaded into Matlab (Figure **2.30**a). Automatic detection of phages was accomplished by the following steps. First, the image was exposed to a bandpass filter using the function bpass [49] to reduce the noise within the images (Figure **2.30**b). Secondly, each phage was detected using the function pkfind (Figure **2.30**c). This function identifies the center position of individual phages at pixel level accuracy. Here an intensity threshold of 0.15 was used to turn the image binary and identify individual phages. When two intensity peaks laid in too close proximity (>880 nm), only the peak with the highest intensity remained for analyses. Lastly, the function cntrd (Figure **2.30**d) was used to accurately detect the center position of each phage of the previously identified phages with sub-

pixel level accuracy. From each of these phages the centroid was determined by calculating the weighted average over a region with diameter of 720 nm.

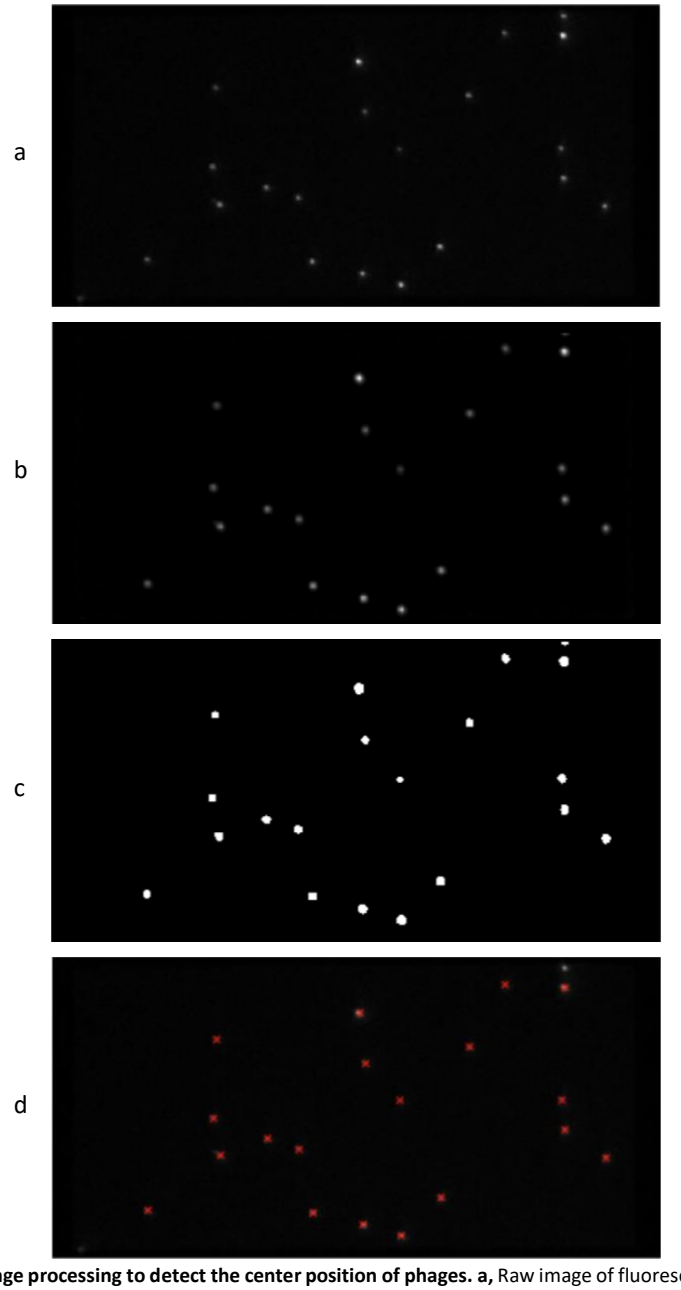

Figure 2.30: Image processing to detect the center position of phages. a, Raw image of fluorescently labeled phage T4 obtained with fluorescent microscopy in HILO mode. The following steps (b-d) were applied to determine the center position of phages. **b,** Image noise reduction using a bandpass filter. **c,** Detection of local intensity peaks. **d,** Sub-pixel detection of peak positions of phage T4 (red crosses).

2.6.3.2 Transformation of the cell and phage coordinates to a normalized bacterial coordinate system

Lastly, automatic detection of phage positions on the cell surface of selected cells was determined. First, the outlines of bacterial cells were obtained with the Matlab function bwboundaries, followed by acquiring their corresponding centroid coordinates, as well as, orientation angles using the Matlab function regionprops.

$$\vec{r} = \begin{pmatrix} x \\ y \end{pmatrix}$$ Equation 2.3

Here, we applied, using equation 2.4, a translational transformation.

$$\vec{r'} = \vec{r} - \vec{r}_{centroid},$$ Equation 2.4

This was used to define the centroid coordinates as the new origin of the coordinate system (Figure **2.31**a). This step was followed by a rotational transformation, using equation 2.5.

$$\vec{r}_{rot} = \begin{pmatrix} X_{L,rot} \\ X_{S,rot} \end{pmatrix} = M_{rot} \cdot \vec{r'} = \begin{pmatrix} cos(\theta) & sin(\theta) \\ -sin(\theta) & cos(\theta) \end{pmatrix} \begin{pmatrix} x' \\ y' \end{pmatrix},$$ Equation 2.5

where rotation matrix M_{rot} defined the rotation matrix, θ correspond to the counterclockwise rotation angle, and $X_{L,rot}$ and $X_{S,rot}$ defined to the long and short axis of the bacterium (Figure **2.31**b), respectively. Next, the coordinates of the bacterium were normalized using equation 2.6.

$$\vec{r}_{norm} = \begin{pmatrix} \frac{X_{L,rot}}{L/2} \\ \frac{X_{S,rot}}{W/2} \end{pmatrix},$$ Equation 2.6

where L and W defined the length and width, corresponding to the outer bacterium boundary points in $X_{L,rot}$ and $X_{S,rot}$ direction (Figure **2.31**c). The last step involved a second translational transformation, using equation 2.7. This was used to re-center the bacterium in case of a small offset that might have occurred in the first translational transformation step (Figure **2.31**d).

$$\vec{r'}_{norm} = \vec{r}_{norm} - \vec{r}_{center} = \begin{pmatrix} X_L \\ X_S \end{pmatrix}$$ Equation 2.7

The corresponding phage centers were normalized accordingly (Figure **2.32**). Phages detected within a region of 80 nm (corresponds to 1 pixel) from the boundary of a selected binary object (i.e. cell) were included in the analysis for the following reason. The center of the phage was determined by the peak of the fluorescent intensity, which was directly correlated to the number of fluorescent labels. We expected that the

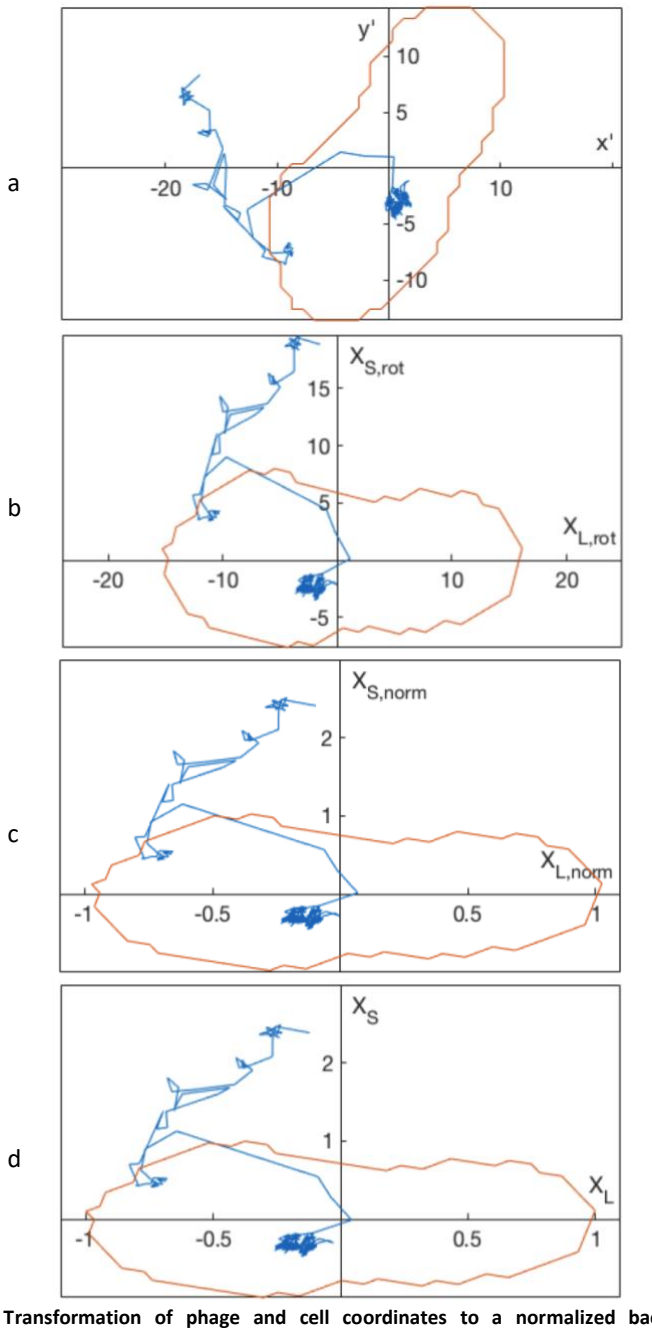

Figure 2.31: Transformation of phage and cell coordinates to a normalized bacterial coordinate representation. The following steps (a-d) were applied to enable comparison of the position of phages on cells. **a,** Translational transformation on a phage trajectory and corresponding cell in pixel. **b,** Rotational transformation on phage trajectory and corresponding cell in pixel. **c,** Conversion to a normalized bacterial coordinate representation. **d,** Second translation to correct for a small offset within the normalized bacterial coordinate representation. Phage trajectory and cell outline were presented as blue and orange lines, respectively.

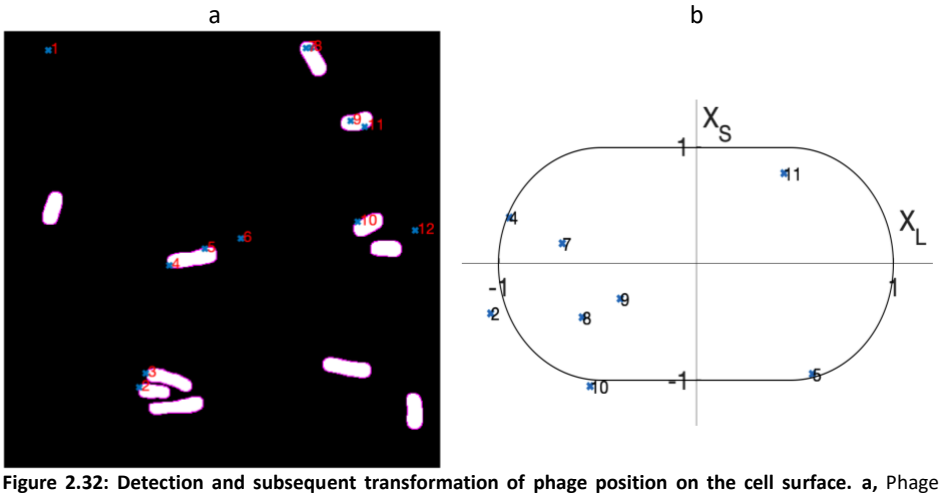

Figure 2.32: Detection and subsequent transformation of phage position on the cell surface. a, Phage positions (blue crosses) were overlaid with the corresponding image containing selected cells (white binary objects). **b,** Detected phage positions on the cell, or maximally 80 nm from the cell boundary (pink contour around white binary object), were included and transformed with respect to normalized bacterial coordinates. With X_L and X_S presenting the long and short axis of a normalized bacterial cell, respectively.

density of labels was not uniformly distributed across the phage, but rather concentrated at the phage capsid. This was based on the surface area and the number of surface exposed lysines on the capsid compared to other regions of the phage (Figure **2.9**). Therefore, we estimated that the center of fluorescent intensity was located somewhere between the middle point of the phage and that of the capsid, which was approximately between 117 and 170 nm for an irreversibly bound T4 phage orientated perpendicular to the cell surface.

Overall, this single-image analysis procedure formed the basic workflow for extracting bacterial and phage coordinates from phase contrast and fluorescent images, respectively. This workflow was determined to be sufficient for the analysis and comparison of binding distributions and applied on phage T4 in Chapter 3.

2.6.4 Multiple-image analysis

In addition to the single-image analysis workflow, we also set-up a framework for processing data for multiple-image analysis. This was used to analyze phage-host interactions, including binding dynamics and detailed on-cell motion. Here the following steps were applied: i) extracting and selecting phage trajectories, ii) channel alignment, iii) step-detection, and iv) cell motion analysis, in addition to the binarization and selection step of cells that has already been described in section 2.6.3. In the next paragraphs, each of these steps will be elaborated.

2.6.4.1 Single-particle trajectories of phages

The first step in the multiple-image analysis workflow extracted phage trajectories from the microscopy movies. This was achieved by using an open source Fiji plugin developed for (semi-) automatic tracking of single-particles (TrackMate [50]). TrackMate extracts the phage trajectories from the corresponding movies by detecting and connecting

consecutive phage centers in each frame over time (Figure **2.33**). Briefly, we analyzed our images using the built-in LoG detector, which used a plain Laplacian of Gaussian filter on the image that was based on calculations in Fourier space. This detector setting was found optimal for our chosen spot size, which was roughly between 5-15 pixels in diameter depending on the pixel size of the used microscope set-up. Bright round objects were detected for each consecutive image. Background noise was filtered out using a threshold on the spot intensity. When the number of detected spots were above a million, an extra filter, referred to as quality filter - an arbitrary measure of the likelihood of each spot to be relevant, was applied to ensure the performance of the calculations. Detected particles were linked using a build-in linking tool with the following thresholds: i) linking max distance, the maximal allowed distance between consecutive frames to link two phage foci. We approximated this distance based on a rough estimation. Here we approximate the volume of a T4 phage as a spherical particle with radius ~55 nm. The corresponding diffusion coefficient was calculated with the Stokes-Einstein equation:

$$D = \frac{K_B T}{6\pi\eta r}, \qquad \text{Equation 2.8}$$

where K_B presented the Boltzmann constant, T the temperature in Kelvin, η the solvent viscosity, and r the radius of the diffusing particle. Using Equation 2.8 led to a D of ~3.85 $\mu m^2/s$. The root-mean-squared displacement (x) that this fictive T4 phage particle traveled by freely diffusing in one dimension along one axis after elapsed time t, can be estimated by the following equation:

$$x = \sqrt{2Dt} \qquad \text{Equation 2.9}$$

This resulted in an estimate of 400 nm for the distance traveled by a freely diffusing T4 phage particle between two consecutive time points (imaged at 50 Hz), when projected on one axis. This value gave an estimation of the distance a particle could travel. To make sure particles that travelled more than this estimated distance were also included, we decided to set the max linking distance at three times the estimated distance (1200 nm). ii) gap-closing max distance, which defined the maximal distance for gap-closing after the foci vanished for a couple of frames (occurred when the particle diffused out of the focal plane). iii) Gap-closing max frame gap, which defined the maximal frame interval between two foci to be bridged. Based on visual inspection we set the latter two threshold values around 1200 nm and decreased the values when the number of particles within the field of view increased to prevent linking of two distinct particles. Hereafter, we applied a filter on the obtained trajectories, selecting for tracks with a minimum of 25 points. From each selected trajectory, the position in time was calculated and stored in a coordinate array, with *x*, *y*, *t* columns, and subsequently saved in an .XML file.

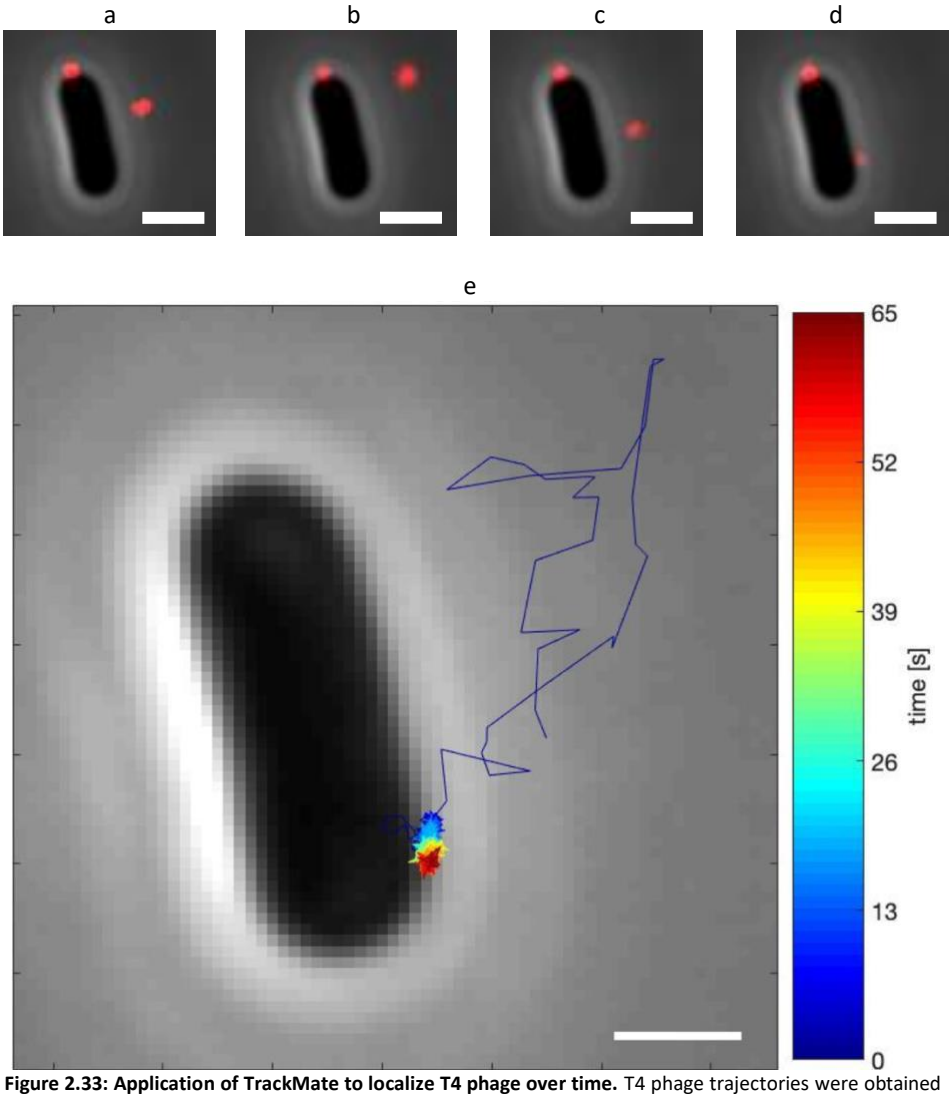

Figure 2.33: Application of TrackMate to localize T4 phage over time. T4 phage trajectories were obtained with TrackMate, by detecting and connecting corresponding phage positions in each consecutive frame. **a-d,** Snapshots of the position of T4 phage particles (red foci) over time, with 0.4 second increments between images. **e,** Trackmate generated the trajectory after position localization in each consecutive frame. Color gradient indicates time, starting in blue and ending in red. Scale bar presents 1 µm.

After retrieving the trajectories from TrackMate, a selection procedure was performed in which tracks that could not be used for analysis were discarded. This selection procedure was performed using Matlab. Therefore, coordinates of phage trajectories were loaded into Matlab using the function importTrackMateTracks. This resulted in a Matlab formatted cell structure and increased the speed with which data could be analyzed in the following steps. If required, images of bacterial cells were aligned with respect to the images with phage trajectories, as described in section 2.6.4.1, and overlaid with the corresponding trajectories for enhancement of visual assessment of

the selection procedure (Figure **2.34**). Trajectories were subjected to the following set of criteria. i) Trajectories that where on the edge and disappeared outside the field of view were automatically discarded using the function edgeDiscard. ii) Trajectories that overlapped with a minimum of three other tracks at the same pixel were automatically discarded using the function overlapDiscard. This was mainly observed for bound phages with a low fluorescence intensity (i.e. due to bleaching of the fluorophores, or out of focus particles – glass bound), resulting in poor detection and linkage that leads to too many short trajectories of the same phage particle. Lastly, trajectories were evaluated through visual inspection, where trajectories with the following features were manually discarded: interacting or bound to the glass substrate, present on moving or poorly defined bacteria (see section 2.6.4.4 for detection of moving bacteria and section 2.6.3.1 automatic detection and selection procedure of cells), or artifacts due to erroneous linking of particles in TrackMate (i.e. between two too closely neighboring particles). Taken together, these steps produced a set of trajectories that were used for further analysis.

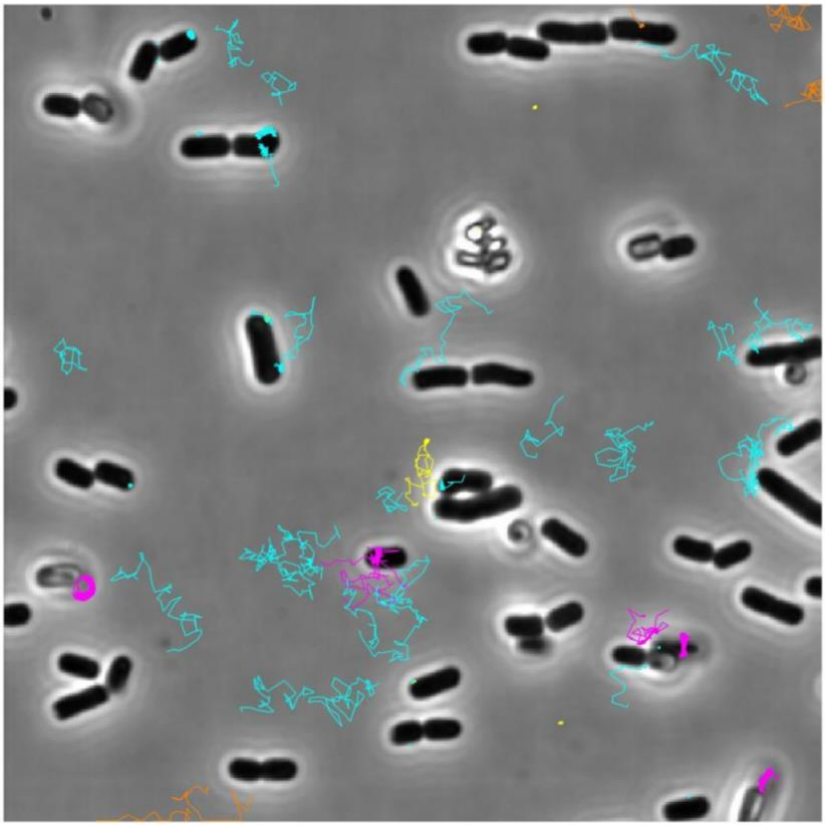

Figure 2.34: Example overview of phage trajectories after selection procedure. Phage trajectories were subjected a selection criteria for discarding and color coding accordingly. The cyan colored trajectories were used for further analysis, while the orange, yellow, and magenta trajectories that met the selection criteria were discarded, presenting on edge, glass-interaction, or overlapping trajectories, respectively.

2.6.4.2 Channel alignment

Imaging of phage trajectories was performed with two different microscope set-ups, an Olympus inverted microscope (IX81) and a Nikon inverted microscope (Ti2-E), respectively. For the latter one, two separate cameras were used, one for imaging phase contrast (bacterial cells) and another for imaging fluorescence (fluorescently labeled phages). Images obtained by these two cameras differ in the number of pixels and pixel size, preventing direct overlay of the two image channels. To align the two image channels the following procedures were required: resizing, transformation of the images, and cropping. We chose to transform the phase contrast channel with respect to the fluorescent channel, to leave the obtained data of the phage trajectories unchanged. First the phase contrast images were downscaled by a factor 0.40 to reflect the pixel size of the fluorescent channel. Secondly, we transformed the image. These transformation coordinates were acquired by alignment of images containing fiduciary markers (200 nm fluorescent TetraSpeck beads) taken prior to the start of each day of experiments. Therefore, phase contrast images of beads were first pre-processed before the algorithm for detection of the alignment coordinates could be applied. Phase contrast images with fiduciary bead markers were stacked, followed by a summation of the stack to obtain an image containing background distortions, and subsequent subtraction of the background from each obtained image within the stack. Next, the phase contrast images of the beads were inverted to obtain a similar intensity profile as the subsequent fluorescent images of the beads (high intensity of the beads with a low intensity background), followed by downscaling of the image as described earlier. Next, the coordinates to align the two channels were obtained by the use of a plugin of Fiji, referred to as descriptor-based registration (2d/3d) [51]. Briefly, this algorithm identifies the center of each bead with subpixel accuracy using a difference of Gaussian filter [52]. Then, the position of each bead was compared to all its neighboring beads creating a unique constellation which was used to identify the matching bead-pairs between the phase contrast and fluorescent image. The subsequent coordinates of matching bead-pairs were used to transform all phase contrast images depicting cells that were obtained within the same day of experiments. Since the number of pixels between the two channels was different, resulting in areas containing information of only one image channel, the last step in the process of alignment involved cropping of the image. Here the images were cropped to a size containing data from both channels. This framework was also used to align the phase contrast images to the largely reduced image field of the fluorescent images taken at higher frame rates.

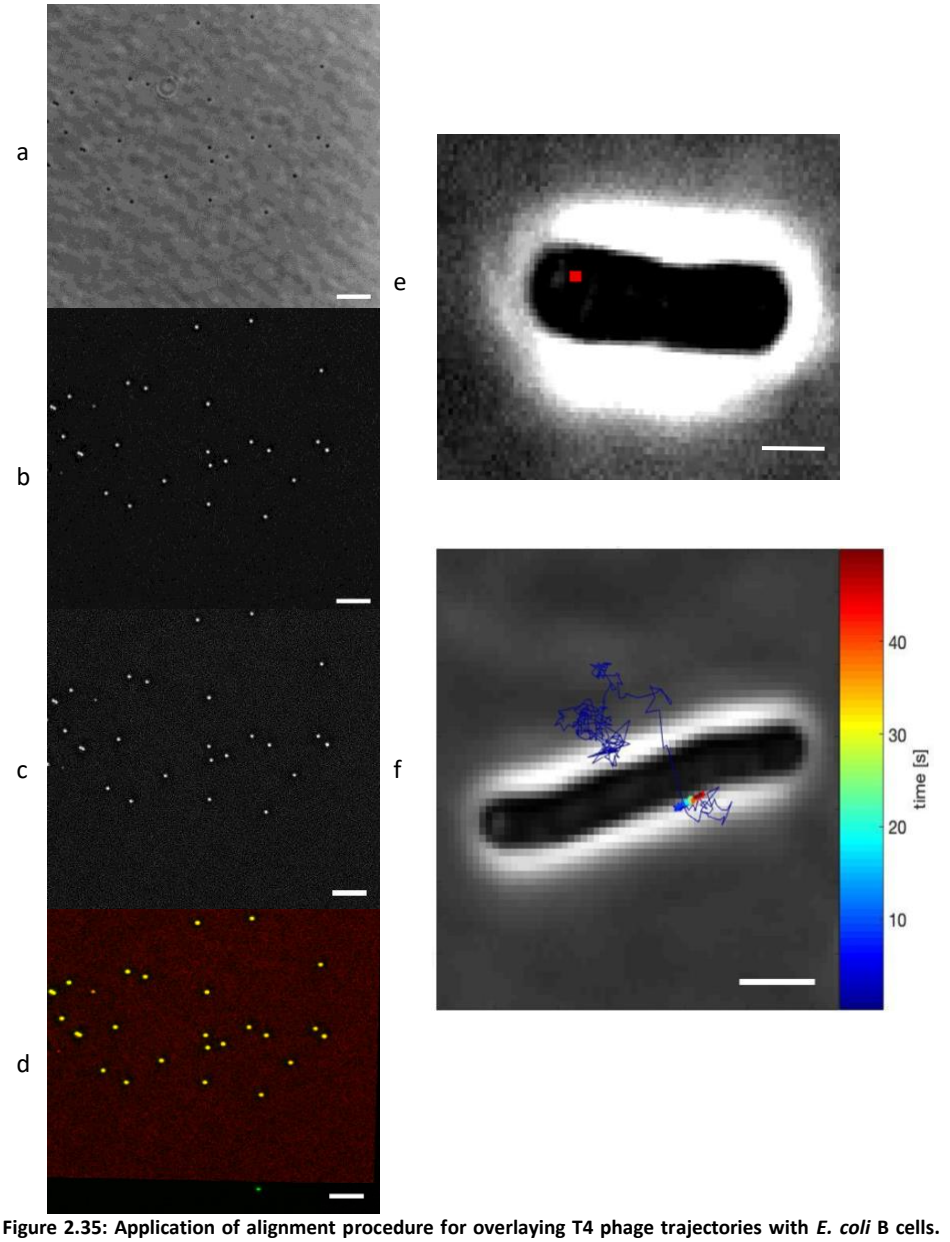

Figure 2.35: Application of alignment procedure for overlaying T4 phage trajectories with *E. coli* B cells. Phase contrast images of cells were aligned with respect to fluorescent images depicting phages. Subsequent coordinates for transformation of the phase contrast images were obtained by alignment of TetraSpeck beads (imaged in both channels) using a plugin of Fiji with the following steps (b-d). **a,** Original phase contrast image with fixated 200 nm TetraSpeck beads. **b,** Intensity profile of phase contrast image was inverted. **c,** Phase contrast image was downscaled with respect to the fluorescent image. **d,** Center position of beads in the phase contrast image (red) were determined and subsequently aligned with corresponding bead pairs in the fluorescent image (green). These alignment coordinates were used to overlay images of cells with **e.** image of a phage (red dot) or **f,** movie of a phage (time colored trajectory). Scale bar of a-d and e-f represents 5 and 1 µm, respectively.

2.6.4.3 Stepfinder

We used a previously reported step finding algorithm, first described by Kerssemakers *et a*l. [53] and later refined by Loeff *et al.* [54], referred to as Stepfinder, to examine the on-cell behavior of phages on discrete stepwise motion. This Stepfinder algorithm was based on chi-squared (X^2) minimization, dividing the trajectory in two subsets at the location that provided the largest reduction in X^2. This is then followed by finding the next best partition event, generating an additional third subset. This iterative process continues until the set number of iterations is reached. Contrary to other step finding algorithms, this algorithm has been shown to handle heterogeneous data sets with variable step sizes and duration embedded with noise. Kerssemakers *et a*l. and Loeff *et al.* described that this algorithm was capable of detecting steps that were well distinguishable from noise within the data, as well as, that their algorithm could differentiate between step-like and non-step like displacements (i.e. gradual change in displacement without an instant statistical significant transition) [53, 54].

Most step-finding algorithms fail to detect or misinterpret steps when the step sizes or dwell times become too small and therefore indistinguishable from each other or from background noise. To assess how well Stepfinder deals i) with small step sizes and short dwell times, and ii) a broad variation of step sizes and dwell times, we tested its performance. We assessed its performance as described in the Methods (section 2.8.10) for the number of iterations and acceptance threshold, by defining the percentage of accurately detected steps, as well as, the number of errors (misinterpreted steps). Here, an accurately detected step was defined as a detected step within a window of 3 frames of the actual step. First, the performance was tested against a range of step sizes, extending from 0.2 to 1.0 pixels, with a decreasing lower limit on the range of step sizes. Results showed that the performance improved with an increasing step size (Supplementary figure **2.5**). A 95% accuracy of detected steps was reached for a step size of 0.2 pixel, indicating that very small step sizes below 0.2 pixel might be missed. In a similar fashion, we tested the performance of Stepfinder against a variety of dwell times, ranging from 10 to 100 frames, with a decreasing lower limit on the range of dwell times. Similar to the results of step size, the same positive trend, but to a lesser extent, was observed for step detection with a decreasing lower limit on the range of dwell times (Supplementary figure **2.6**). Here a 95% accuracy of the steps was reached with dwell time of 30 frames, indicating that step sizes with a duration below 30 frames might be missed. Lastly, we tested the overall performance of step detection on simulated data containing both varying step sizes (uniform distribution between 0.1 and 1 pixel) and dwell times (uniform distribution between 10 and 100 frames). Stepfinder detected 92.56% of the steps accurately, with 16.9 and 26.9 mean false positives and negatives out of the 359.5 ± 2.9 simulated steps (mean $\pm$ SD) (n = 10), respectively. Overall, we found that Stepfinder performed well with step sizes larger than 0.2 pixel and dwell times of at least 30 frames within the expected noise levels of the experimental data. Obtained step size distributions with values of steps below 0.2 pixel and 30 frames should be interpreted with caution in respect to the larger uncertainty.

As proof of principle, we applied the Stepfinder to a section of a phage trajectory that was defined to be on-cell. The example trajectory analyzed by Stepfinder can be found in Figure **2.36**, indicating the presence of step-like behavior in both *x* and

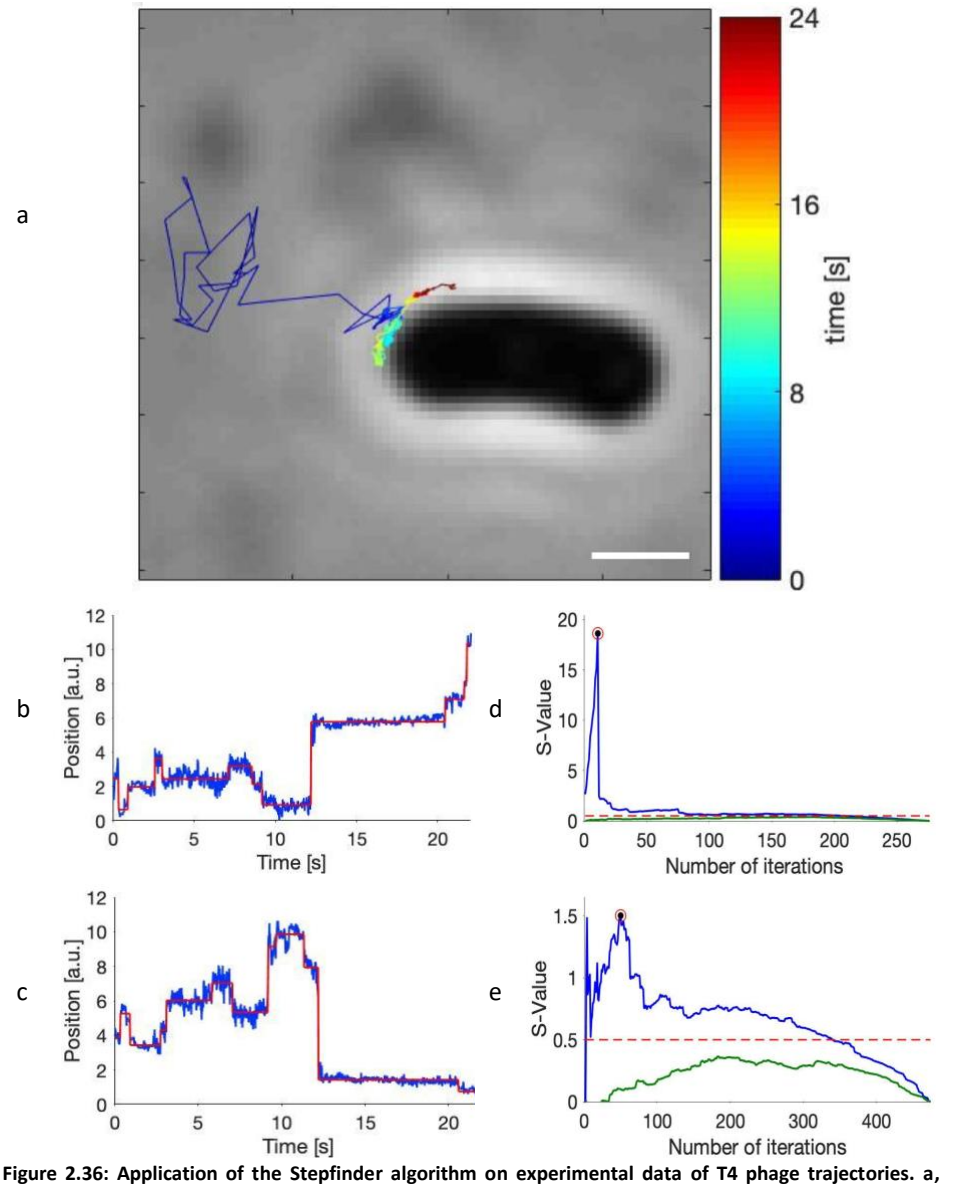

Figure 2.36: Application of the Stepfinder algorithm on experimental data of T4 phage trajectories. a, Trajectory of an interacting T4 phage with its host *E. coli* B. Color gradient indicates time, starting in blue and ending in red. **b-c,** Steps were fitted by the Stepfinder on the one-dimensional position, x- and y-axe, of T4 phage trajectory at the host cell surface over time. Blue and red lines indicate the experimental data and most optimal fit, respectively. **d-e,** Results of S-curves after two rounds of fitting on the experimental data, where the blue line presents the first and green the second round of fitting. Red dashed line presents the set value of the threshold, which in this example was not met by the global maximum of the S-curve of the second round and therefore not included within the analysis. Black dot with a red circle indicates the optimum number of iterations.

y direction with steps of varying length and duration. For this particular trajectory, a clear optimum of the S-curve was found for steps taken on the x-axis (Figure **2.36**d). This

in contrast to the rough S-curve (see Methods section 2.8.10) and therefore less clear optimum for the detected steps on the y-axis (Figure **2.36**e). For both curves the second fit did not reach the within this example set acceptance threshold of 0.5 and were therefore not accepted. This method will be used in Chapter 4 to study step-like behavior of phage T4 on *E. coli* B.

2.6.4.4 Cell movement analysis

To study and interpret phage trajectories at the cellular surface, the bacterium needs to be immobile. The flow cell was optimized in such a way that the majority of the cell population was immobilized to the substrate. However, a small fraction of cells was only partially bound to the substrate, resulting in rotational movement. We developed two methods for detecting cell movement. One was based on visual assessment of movement with pixel level accuracy and used to filter out cells displaying large movements in the first round of data analysis. The second method involved quantifying the more 'subtle' movements of a cell, as well as, drift within the image plane, at sub-pixel level accuracy. This was used to assess how well the cell was immobilized to the substrate before analyzing detailed on-cell motion of phages with the step-finder algorithm.

For the first analysis, cells within each frame of the phase contrast images were binarized, as described in section 2.6.3. After this, a stack summation was performed with color coding that allowed for easy identification of cell movement by visual assessment (Figure **2.37**). Color coding worked as follows, if the area of the binary object was present in all frames (summed fraction of 1) it was colored green, indicating that the area did not move. Any deviation, caused by cell motion or drift, resulted in a summed fraction <1 and was marked with the color red. This method indicated cell movement with single pixel level accuracy and was used to quickly scan for large

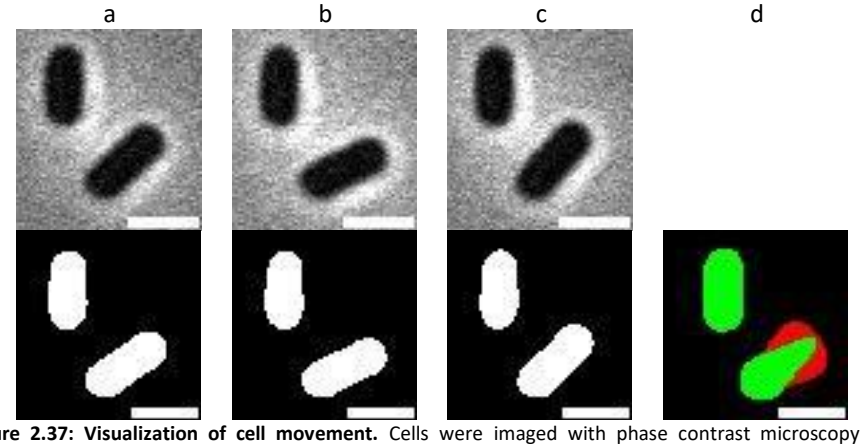

Figure 2.37: Visualization of cell movement. Cells were imaged with phase contrast microscopy and subsequently checked for movement. Each frame (**a-c**, top) was made binary (**a-c**, bottom). A summation of the stack was performed and color coding was used to visualize movement of the cells in the binary image (**d**, bottom). Green and red indicated immobilized and moving areas, respectively. Scale bar presents 2 µm.

rotational movement of cells or translational movement caused by drift within the image plane. Cells showing movement or images showing drift were discarded from the data set.

A second, more accurate cell movement analysis was used to examine very small movements of cells that could not be detected with the detection method described above. We implemented this method on a small number of focal cells for which we also analyzed trajectories of phages that interacted with it. The following framework was used to analyze the rotational movement of the cell or translational movement of the image plane (drift) with sub-pixel level accuracy. Images were pre-processed by first cropping the field of view to a size corresponding to a single cell (Figure **2.38**a). To accurately detect the edge of the cell and subsequent cell movement we smoothed the image by first applying a Gaussian filter with sigma 1, which reduced the noise level within the image. We then followed by a cubic interpolation, to obtain an image with a high-pixel density by estimating intermediate points between the obtained existing points. This increased the information related to the particle's morphology and enabled the positioning of four well-defined cross-sections. These were placed at the following positions, one over the long axis, and three over the short axis of the cell (Figure **2.38**b). These cross-sections were determined automatically by first turning the image binary using the Otsu's method [55], where after the long axis of the bacterium was defined by the open source Python package skimage [56] designed for image processing. Here the binary objects were first labeled, followed by defining the image objects properties using the function regionprops. The cross-sections along the short axis of the cell were defined by lines perpendicular to the long ax of the cell. The first cross section was set at the midpoint of the cell, with the two remaining cross-sections on the left and right cellular pole fixed with a relative distance, halfway between the pole and mid-cell. The mid-point of the bacterium within each of the cross-sections was determined by fitting the following equation:

$$f(x) = e^{\left(\frac{x-\mu}{2\sigma}\right)^n}, \qquad \text{Equation 2.10}$$

to the intensity profile (Figure **2.38**c) of the bacterium. With *f(x)* the intensity function, *x* the coordinate along the slice, σ the width of the bacterium, and μ the mid-point of the bacterium. The *n* was set to either 4 or 6, based on the highest obtained quality of the fit (R^2). To define the region of the bacterium on which this function was fitted, the intensity profile along the cross-section was divided by two. The maximal intensity point within each of these regions was determined and set as the outer boundaries of the intensity profile, essentially discarding the area outside the cell. Next, we applied a transformation on the intensity values by subtracting the highest measured intensity value (*I*) from each of the remaining pixels within the cross-section, followed by Inversion:

$$I' = max(I) - I \qquad \text{Equation 2.11}$$

Lastly, the intensity profile was normalized to 1 (Figure **2.38**d), based on the maximal detected Intensity value:

$$I'' = \frac{I'}{max\ (I')} \qquad \text{Equation 2.12}$$

As proof of concept, we analyzed the movement of various cells that had shown interaction with phages. These cells were deemed immobile by the previously described cell-movement detection algorithm that detected large movements beyond the size of a pixel. Figure **2.39** shows an exemplary result of three analyzed cross-sections along one of the short-axis, each of a different cell, that were analyzed with the sub-pixel cell-movement detection algorithm. Images of cells were taken at 50 fps for a time of 4 to 10 seconds. The mid-point position of the bacterium in each cross-section was determined for all available time points, as described in the previous section. The data was fitted by a linear line, where the corresponding slope indicated the amount of translational motion caused by directional translational movement

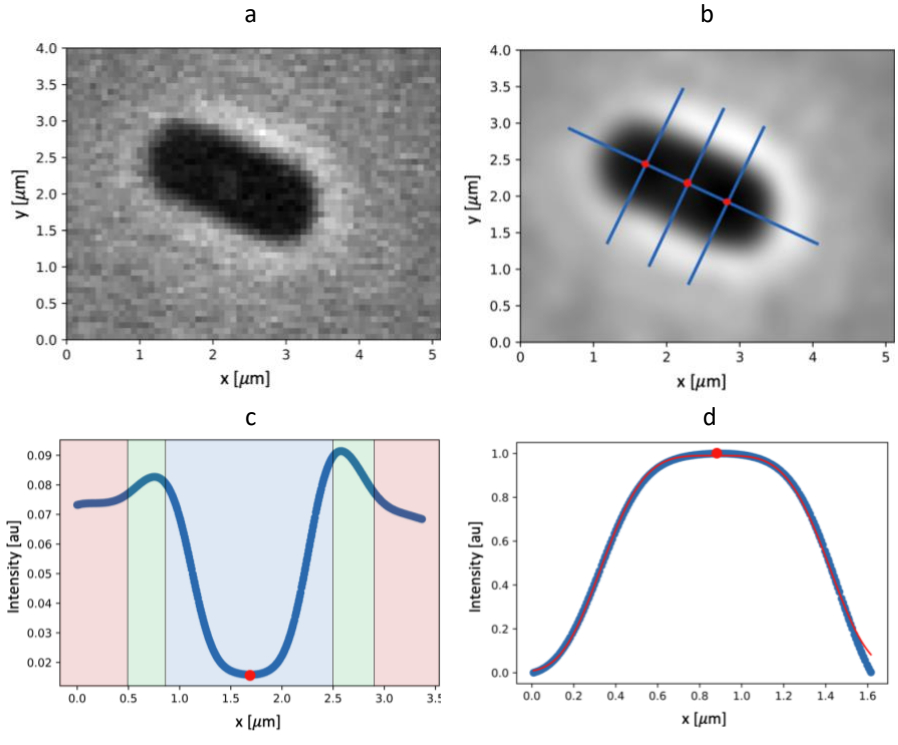

Figure 2.38: Application of cell-movement detection algorithm on experimental data. a, Phase contrast image of *E. coli* B cell. **b,** Pre-processed (Gaussian filter and interpolation) phase contrast image with four cross-sections (blue lines) and the corresponding midpoints of the bacterium within each cross-section (red dots). **c,** Intensity profile of one of the cross-sections along the short axis of the cell with the red dot presenting the midpoint position of the bacterium along the corresponding cross-section. Red, green, and blue areas indicate the region of the background, bright flare around the bacterium, and the bacterium, respectively. **d,** Normalized intensity profile of the bacterium (blue line) of the blue area indicated in c fitted by equation (2.10-2.12, red line) to determine the midpoint position of the bacterium (red dot).

a

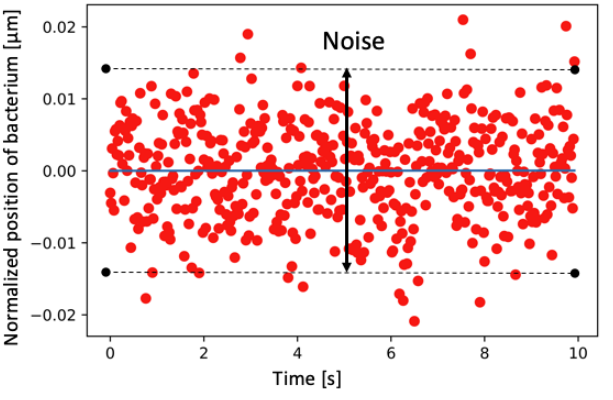

b

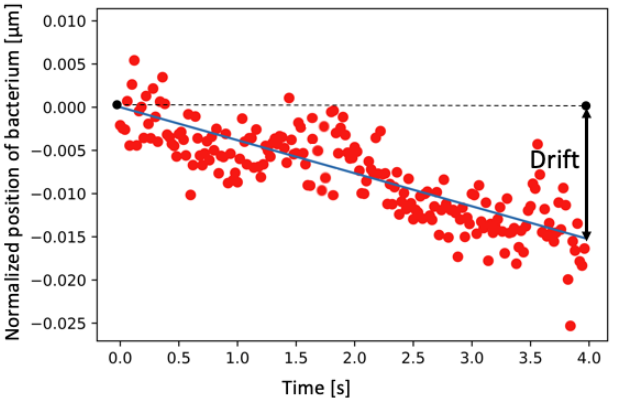

c

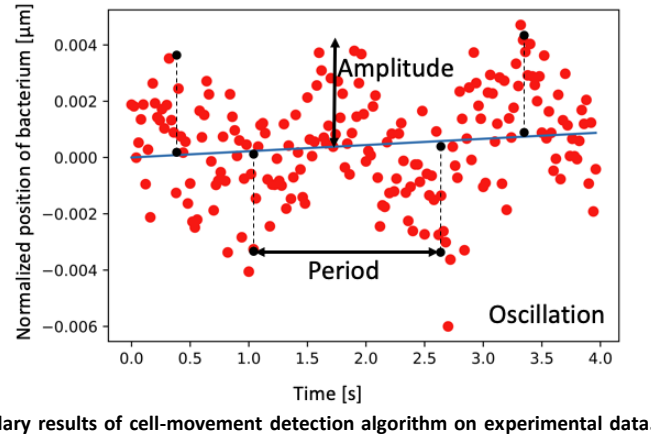

Figure 2.39: Exemplary results of cell-movement detection algorithm on experimental data. Normalized midpoint position of the bacterium as a function of delay time along a cross-section of one of the short axis. Red points present the midpoint position at each given time point determined by the cell-movement detection algorithm. Blue line presents a measure for the amount of drift within the image plane, determined by fitting a straight line to the experimental data points and extracting the corresponding slope as measure. **a,** Example of an immobilized cell – no movement. Bacterium remains at a given location ± noise fluctuations. **b,** Translational movement – drift of the image plane. Midpoint position of the bacterium moves with a certain speed in a given direction. **c,** Rotational movement – oscillation of the cell. Cell 'wiggles' with a certain amplitude and period.

(drift) within the image plane. Results indicated that the amount of drift present in an image was well detected by this method. Figure **2.39**a shows an example of a well immobilized cell with no apparent image drift. This while, Figure **2.39**b shows an example of detected drift at a speed of a couple of nm s^{-1}. Cells were also assessed for any signs in rotational movement, that was caused either by a poorly immobilized cell or by noise fluctuations that arose from the microscope stage set-up. This movement was indicated by a pattern resembling a sinus function, with the amplitude presenting the amount of rotational movement and the period indicating the speed at which this rotational movement took place (Figure **2.39**c).

Overall, this method was capable of detecting the amount of translational and rotational cell movement at sub-pixel level. In some occasions, the cross-section that was fitted along the long-axis of the cell experienced some intensity fluctuations, most likely caused by a change in density within the cell (e.g. presence of compact regions of DNA or position across the cell body were cell division takes place), affecting the quality of fitting. However, the reduction in the quality of the fit by this type of intensity fluctuation did not affect the quantification of the cell movement, as the used function remains accurate in the detection of the cell wall boundaries and therefore the midpoint position of the cell within the given cross-section.

2.7 Discussion and conclusion

To study the phage target-finding process at single-particle level, phages were fluorescently labeled and imaged with fluorescent microscopy in HILO mode and cells were imaged with phase contrast microscopy, resulting in images with gray-values that contain information on the phage and host cell positions in two-dimensional space (*x* and *y*). We developed a framework in which these fluorescent and phase contrast images could be processed, such that in-depth analysis of phage-host interactions can be studied as described in the following chapters. This involved several steps that were split in two distinct workflows, one for single- (static) and the other for multiple-image (dynamic) analysis. Both processes essentially focused on extracting phage and bacterial coordinates. The workflow consisted out of already available software programs, plugins, packages, and functions, that were adapted and tuned to form a semi-automatic framework in which images could be processed.

It has been established that single-particle tracking software platforms are often specialized in tracking unique aspects of the particle (i.e. shape and/or type of motion) within specific imaging conditions (i.e. SNR and/or density of particles), making the accuracy of tracking inherently dependent on the used parameters and preventing a universal tracking tool [57]. We chose the automated computational platform Trackmate to obtain trajectories within the multiple-image analysis workflow. Trackmate is an open source tool that has a user- and developer-friendly interface. Besides, it has been widely accepted and validated to detect, track and link, and analyze trajectories within the science community [50]. Its overall performance on detecting and linking particles in imaging conditions similar to our experimental data (high SNR and low particle density) has been previously documented as good, belonging to the

top 3 when previously compared to a total of 14 methods [57]. Another tracking software platform, based on probabilistic data association [58], showed similar performance to Trackmate, with small differences in tracking accuracy with regard to different particle and imaging conditions [57]. Contrarily to other methods, Trackmate has been generalized and can be applied on data without prior knowledge or assumptions regarding the underlying physical motion or the biological significance of events. This provides several advantages over other available algorithms, one of them is the capability to deal well with tracking different diffusive regimes (i.e. Brownian, directed, subdiffusive, constrained motion, or a combination thereof) which we expect to be present in our data (at least a free and bound state of phage particles). Further, the algorithm is an extension of Fiji and results can be imported and analyzed by Matlab. This limits the number of different software programs used within our framework, as both were already used for pre-processing images in other steps, and aids the opportunity to automatize single or even multiple steps within the workflow. A common problem among single-particle tracking algorithms, including that of TrackMate, are mistakes during the detection process, caused by e.g. particles diffusing in and out of focus, bleaching of the particles over time and particles that were too close to each other (merging). This has a considerable impact on the linking process. Trackmate provides the opportunity to decrease the number of these mistakes by allowing manual inspection and adjustment of each step by adding parameters along the way to assess and guarantee the accuracy of the processed results. In addition, obtained trajectories can be manually curated by linking and delinking detected points within and between single-trajectories. However, this is and currently remains a labor-intensive process and has therefore not been applied within this thesis. Overall, we found that this software tool was capable of pre-process fluorescent images of labeled T4 phages that were obtained by fluorescent microscopy in HILO mode. Positions of T4 phages were detected and subsequently linked over time to form single-phage trajectories that can be further analyzed to study the physical characteristics of phages as described in Chapter 4.

A study by Rothenberg *et al.* revealed that phage λ performed some kind of on-cell motion during which the phage explores the cell surface prior to its decision to irreversibly bind [1]. Hu *et al.* corroborated this idea and suggested, based on static EM snapshots, that phage T7 explored the cell surface via a tethered walk between alternating TF-receptor interactions [59]. Comparable observations of structural conformation were found for phage T4, implying that if there was such on-cell motion it was most likely governed by the same underlying mechanism [5]. Such a tethered walk most likely represented itself in discrete step-like behavior. This type of behavior could be detected in the trajectories obtained by our experimental set-up and analyzed with a step-finder algorithm. Even though there are multiple step detection algorithms available today [53, 60-68], none has been shown to be applicable to all types of data. The method of choice depends strongly on the type of signal and the knowledge of the underlying mechanism, which may rely on input of certain parameters, i.e. stepping number, stepping directionality, stepping duration, stepping sizes, or time between the consecutive steps. Since, the exact underlying mechanism of phage on-cell motion was unknown, the number of usable step-finding algorithms that could be used to examine trajectories on the presence of such discrete steps was limited. In addition, T4 phages

have multiple TFs, giving rise to a large and almost continuous variation in possible step-sizes. We chose to use the step-finding algorithm Stepfinder [54], as it was found to be a robust method with high success rate that performed well with variations among data acquisition, stepping rates, and varying amounts of Gaussian noise [69]. Even so, several caveats should be taken into account when analyzing phage trajectories with Stepfinder, or any other step-finding algorithm for that matter. The acquired data of phage movement at the cell surface contained information on the location of the phage in only two dimensions (x and y), as our current microscope set-up currently lacks the ability to provide information on the location on the z-axis (third dimension). The number of dimensions was compromised even further when analyzing the acquired data, as the algorithm analyzed the steps within phage trajectories in only one dimension (x or y). This in combination with the fact that phages most likely show no directed motion in only one dimension, as well as, small step sizes and steps short in duration within simulated data showed a higher occurrence to be missed or misinterpreted, the analysis will deviate in the actual number of detected steps and will skew the distribution of sizes and duration of steps. Nevertheless, analyzing phage trajectories with this method will provide new insights with regard to the nature of on-cell motion, and give a clear impression on the order of steps that take place and their appurtenant distributions of step sizes and duration. This paves the way for understanding the underlying mechanism behind the search process of phages and provides estimations on distributions that can be used to establish a theoretical model.

Further, we developed a cell-movement detection algorithm that can be used to check for any rotational and translational movement of the cell at sub-pixel level. With this method, we detected movement along four mid-point positions across the cell, covering the detection of motion in both x and y. The number of detection points can easily be increased by the addition of the number of cross-sections, increasing the certainty and sensitivity with which movement can be detected across the cell body. Compared to some of the other available cell outline detection methods [70-75], our method currently lacks the possibility of cell-movement analysis on cells with curved shapes, as well as, it is not always capable, depending on how well the cell edge was distinguished, of analyzing cell-motion of single cells within a tightly formed cluster or cell division process. To increase the number of morphological different cells that we can analyze, we could either make use of already available platforms developed for obtaining cell contours, i.e. MicrobeJ [74], or develop our method further by implementing a similar approach for determining the long axis of these cells. Even though some of these methods were capable of tracking the position of the cell over time [70-74], they were focused on tracking the mid-position of the particle (distance from origin), which only provided information on the distance, velocity and type of displacement. In contrast, our method was based on tracking the displacement of several points along the cell body providing quantitative information on the amount of rotational movement, which was to our knowledge, not obtained by any of the other available methods. However, due to the fact that our method relays on determining the midpoint position of a cell based on the set-slices within the first frame, large rotational movements (> 1 pixel), were not accurately detected as the cell body no longer aligned with the set cross-sections (the actual slice would no longer be perpendicular to the slice on the long-axis), leading to an underestimation of the

amount of movement. This was not considered a problem within our workflow, as the other cell movement analyses, which was performed before analyzing the trajectories, already filtered out all cells with large movements (>1 pixel). In addition, the underestimation of values for large movements did not impact our conclusion with regard to cell immobilization.

Taken together, the semi-automatic workflow demonstrated the extraction of phage position and trajectories, cell outlines, as well as, the analyses of cell movement. This framework provides all necessary steps to pre-process microscopy images and facilitate the analysis of studying phage-host interactions at single-particle level, which will be used when investigating the irreversible binding distribution of phage T4 in Chapter 3 and on-cell dynamics of phage T4 in Chapter 4 and R2-type pyocins in Chapter 5.

2.8 Material & methods

2.8.1 Bacterial strains, bacteriophage and pyocin growth conditions

Escherichia coli B (ATCC 11303) was used as host indicator strain of T4 phage ATCC 11303. *E. coli* was grown in Lysogeny broth (LB) (Sigma) supplemented with 10 mM $CaCl_2$ and 10 mM $MgSO_4$ at 37 °C and 250 rpm to early exponential phase (OD_{600} 0.1) and infected with T4 at MOI 0.5 and grown until lysis occurred (~3 hours). A final concentration of 2.5 % chloroform was added to lyse all the cells. The suspension was centrifuged for 20 min at 18000 g and filtered through a 0.22 μm filter (SFCA, Minisart NML, Satorius). 1 μg ml^{-1} RNase and DNase was added to the phage suspension and incubated for 30 min at RT, followed by PEG precipitation, using a final concentration of 1 M NaCl and 16.66 mM PEG-6000 (Sigma). Sample perpetrate was incubated overnight at 4 °C on a rocking plate, followed by centrifugation at 11,000 g for 1 hour at 4 °C. Sample was placed on ice in tilted position for 15 minutes, followed by resuspension of the pellet in MB (20mM Tris-HCl, 100mM NaCl and 10mM $MgSO_4$) in $1/100^{th}$ of the initial sample volume. Phage extraction and purification was performed using a CsCl density gradient (with the following densities: 1.33, 1.45, 1.50, 1.70) and centrifuged at 28.000 g for 3 hours at 4 °C, followed by dialysis (7 k cutoff, Thermo Fisher) in MB and stored at 4 °C until use. Purity was checked with negative stain EM and the activity and concentration was confirmed with a spot assay.

P. aeruginosa strains PAO1, R2-type pyocin producing strain, and 13s, pyocin R2 indicator strain, were kindly provided by AvidBiotics Corporation [30] and grown on tryptic soy broth at 37 °C and 250 rpm. Pyocins were obtained by PAO1 strain induction in G medium [76] with 50 μg/ml gentamicin. We used the protocol described by Williams *et al.* [30], which describes the following: Overnight culture of PAO1 was diluted 1:100 in G medium supplemented with 50 μg/ml gentamicin. Cells were continued to grow at 225 rpm and 37 °C till an OD_{600} of 0.25 was reached. Mytomycin C was added at a final concentration of 3 μg/ml and growth was continued for an additional 2.5 hours. A final concentration of 2 U/ml DNase I (Invitrogen) was added and incubated for 30 min. The sample was centrifugation at 17,000 x g for 1 h to remove cell debris. Next, saturated amounts of ammonium sulfate (4 M) were added to the pyocin supernatant at a rate of 1 ml/min. During this time the solution was continuous homogenized and kept at 4 °C until a final concentration of 1.6 M ammonium sulfate was reached. Here after, the suspension remained at 4 °C overnight. Next, the suspension was pelleted at 17,000 x g for 1 h at 4 °C, followed by resuspension of the pellet in TN50 buffer in $1/10^{th}$ of the original culture volume. This was followed by a second centrifugation step at 58,000 x g for 1 h at 4 °C and resuspension of the pellet in TN50 buffer in $1/20^{th}$ of the original culture volume and stored at 4 °C until further use. Purity was checked with negative stain EM and the activity and indication of the concentration was confirmed with a bactericidal droplet assay.

2.8.2 Transmission Electron microscopy

Intactness of the particles and purity of the sample was determined by visualization using negative stain transmission electron microscopy (TEM). 3 μl of sample was placed on a glow-discharged coper film 400 mesh EM grid (Aurion) for 1 minute, followed by blotting and washing the grid three times with a few μl of MiliQ. Sample was stained with 3 μl 1-2% uranyl acetate for 1 minute, followed by a last round of blotting. Samples where imaged at JEOL JEM-1400plus TEM, with an acceleration voltage of 120 kV and EDS detector.

2.8.3 Activity assay – spot assay

Activity and concentration was confirmed with a spot assay using a double layered agar technique [77]. Phage T4 and pyocin R2 were serially diluted tenfold and fivefold in MB and TN50, respectively. 10 μl of aliquots were spotted onto a double-layered agar plate containing the target indicator strain, *E. coli* B and *P. aeruginosa* 13s for T4 and R2, respectively. Plates were dried and incubated overnight at 37 °C. Activity was confirmed as a distinct clear 'killing'-zone on the bacterial lawn. Concentration of phages (phage forming units (PFU)/ml) was determined by counting individual plaques at the higher dilution factors.

2.8.4 Adsorption assay

Adsorption rate constant (k) and efficiency (ε) were determined by an adsorption assay. Purified T4 phage was incubated with ~10^7 CFU/ml exponentially growing, OD_{600} of 0.3, *E. coli* B cells at an MOI of approximately 0.1-1 at RT for a defined amount of time, followed by removing cell bound phages using a 0.2 μm syringe filter. Free phage lysate was serially diluted and spotted on a double layer agar plate containing exponentially growing *E. coli* B cells and incubated overnight at 37 °C. Individual plaques were counted at the higher dilution factors and used to calculate the free phage concentration in PFU/ml over time. Adsorption model, describing the adsorption kinetics of T4 phage to *Escherichia coli* system over time [43], was fitted to the experimentally obtained results to extract the binding efficiency and rate.

2.8.5 Fluorescent labeling

Fluorescent labeling of T4 phage and R2-type pyocins was accomplished by the following protocol. Purified T4 phages and R2-type pyocins were concentrated and washed with an amicon ultra-0.5 centrifugal filter unit (100 kDa cutoff, Millipore) in PBS (sigma) supplemented with freshly made 0.1 M sodium bicarbonate. Followed by fluorescent labeling with a final concentration of 0.05 mg ml^{-1} (10 mM) Alexa Fluor™ 647 or 488 NHS-Ester (Thermo Fisher), unless stated otherwise, for at least 3 hours at RT on a rocking plate and washed with an amicon ultra-0.5 centrifugal filter unit (100 kD, Millipore) in MB for phages and TN50 for pyocins and stored at 4 °C until use. In case of genome staining, T4 phage was labeled with a final concentration of 50 μM SYTOX green, unless stated otherwise, for 3 hours at RT on a rocking plate, followed by washing with an amicon ultra-0.5 centrifugal filter unit in MB.

Labeling of cells was reached by the following method. After growing *E. coli* B and 13s cells to the exponential state, cells were stained with a final concentration of 18 μM DAPI for 20 minutes at RT, followed by centrifuging 5 minutes at 2000 rpm and resuspension in interaction medium in 1/10th of the original volume.

2.8.6 Flow cell

Flow cell was assembled by the following procedure. Glass coverslips (22x40 mm, No. 1.5, VWR) were extensively cleaned with 2% Hellmanex III (Hellma GmbH). Slides were incubated for 30 minutes with 0.1% poly-L-Lysine (sigma), unless stated otherwise, were, after washing extensively with MiliQ, dried with nitrogen and stored in a box until further use. Six holes of approximately 0.1 mm were drilled in glass slides (76x26x1 mm, Fisher Scientific) at the beginning and end of each chamber to form an in- and outlet for the sample and buffers. Slides were extensively cleaned with MiliQ and ethanol. Three chambers of the following dimensions: 3.3 cm in length and 0.2 cm in width, were laser-cut in double adhesive tape where it served as a spacer between the coated coverslip and glass slide to form a flow cell. Press-fit tubing connectors (Grace Bio-labs) were placed on pre-drilled holes on top of the glass slide to which tubing (0.55 mm inner diameter, 1.07 mm outer diameter, Microbore PRFE Tubing) was connected.

Experimental infection set-up was prepared in the following way. Cells used in the experimental set-up were grown in LB to early exponential phase (OD_{600} 0.3), concentrated 10x, unless stated otherwise, by centrifugation of 1 min at 14,000 g and resuspended in M9 medium (Sigma) in 1/10th of the original volume. 10 μl of cell suspension was added to the flow cell and left for attachment to the poly-L-lysine pre-coated coverslip for 10 minutes, unless stated otherwise. Excess cells and poorly immobilized cells were removed by washing the chamber with 150 μl interaction media at 175 μl min^{-1}, unless stated otherwise, using a syringe dispenser.

2.8.7 Microscopy

Image acquisition was performed with one of the following three microscope set-ups: Olympus inverted microscope (IX81) with a widefield illumination system. Fluorescence excitation was provided by a high-power Andor AMH-200-F6S lamp. As detection device, we used an EM-CCD (Andor Luca R) containing a chip size of 1004x1025 pixels and a resolution of 79 nm/pixel. A UPlanFLN objective was used with a 100x magnification, numerical aperture of 1.3 and a working distance 0.2mm. Andor IQ3 was used as control and acquisition software. The Electron-Multiplying (EM) gain varied between 100 and 200. Excitation and emission filter 387/11 and 447/60 (Filter cube reference: DAPI-1160B-OMF-ZERO) was used for imaging with fluorophore DAPI, 628/40 and 692/40 (Filter cube reference: Cy5-4040B-OMF-ZERO) for imaging fluorophore Alexa647, and 500/24 and 542/27 (YFP-2427B-OMF-ZERO) for imaging fluorophore SYTOX green.

Olympus inverted microscope (IX81) with a TIRF illumination system: Fluorescence excitation of fluorophore Alexa480 and Alexa647 was provided by an Olympus CW laser at 488 and 640nm with a maximum output power of 150 and 100mW, respectively. As

detection device, we used an EM-CCD (Andor iXon X3 DU897) containing a chip size of 512x512 pixels with a resolution of 80 nm/pixel. A UPlanFLN objective was used with magnification 100x, numerical aperture 1.3 and working distance 0.2mm. The Electron-Multiplying (EM) gain was set to 200 unless stated otherwise. A 0.6 ND filter was used to reduce overexposure. Emission filter 524/29 or 630/92 (FF01-630/92) was used. Fluorescent imaging was performed in HILO mode.

Nikon inverted microscope (Ti2-E) with a TIRF illumination system (Gataca iLAS2): Fluorescence excitation of fluorophore Alexa480 was provided by an Olympus CW laser at 488 nm with a maximum output power of 150mW. The detection device was a dual set-up with an EM-CCD (Andor iXon Ultra 897) with a chip size of 1004x1025 pixels for the fluorescent channel and an EM-CCD (Retiga R1) with a chip size of 1376x1024 pixels for the phase contrast channel with a resolution of 161 and 63.5 nm/pixel, respectively. A Nikon Apo TIRF objective was used with magnification 100x, numerical aperture 1.49 and working distance 0.12 mm. Emission filter 525/50 was used. Fluorescent imaging was performed in HILO mode.

2.8.9 Dynamic light scattering

Hydrodynamic radius and polydispersity was determined by DLS using DynaPro NanoStar. Each measurement represents the average of 20 acquisitions performed at RT.

2.8.10 Stepfinder

In the following section, we briefly summarize the method Stepfinder, developed and described in detail by Kerssemakers *et a*l. [53] and Loeff *et al.* [54]. Since endless partition events leads to 'overfitting', resulting in the fitting of 'false positive' steps within the noise of the data, an optimum number of iterations that is being used for this analysis has to be defined. Within Stepfinder this optimum is defined by the global maximum of the so-called 'S-curve' plotted as quality of the fit as function of the number of iterations. Here, the performance of this fit was quantitatively established by the ratio between X^2 obtained by the 'secondary' fit and that of the first fit, providing a so-called 'S'-value. Here the 'secondary' fit presents a second-best fit that has been applied within the existing plateau of the first fit [53, 54]. The larger the difference in ratio between the X^2 of the fits, the higher the S-value and the more likely it presents the real number of detected steps. In other words, the optimum ratio defined the point where the number of detected steps approximated the number of steps within the experimental data. This, while the number of partition events before (underfitting of the number of detected steps – when the fit was not close enough to the actual number of steps) and after (overfitting of the number of detected steps – algorithm fitted the data to closely, mistaking noise for steps) the optimum value of the S-curve resulted in a reduced difference in X^2. If steps differ more than an order of magnitude in size or duration, a second distinct peak within the S-curve could occur with a lower optimum than the global detected optimum. However, note that in a continuous population of step sizes and/or duration, no such peaks will occur. The occurrence of a second peak was assessed by a so-called 'second run' that performed

another fit on data from which the defined steps in the first fit have been extracted [54]. If the global maximum of that second peak reached above the set acceptance threshold of the user, the steps found within that fit were included within the analysis. Stepfinder has two parameters, number of iterations and acceptance threshold, that can be tuned for the sensitivity towards the detection of steps. These values were ideally set just beyond the optimal S-value, as recommended by Kerssemakers *et al.* [53] and Loeff *et al*. [54]. To evaluate the set values for our experimental set-up, we assessed the performance of Stepfinder on the detection of steps within simulated data by varying the values of these parameters. Most elegant would be to make use of know experimental distributions within the simulated data. However, these were unknown. Therefore, we assessed the performance of these parameters with regard to step detection with simulated data that contained a large range of possible experimental step values. We used simulated data that contained a variety of step sizes - the shift in distance between two center positions, and dwell times – the time it remains within the current center position (Supplementary figure **2.4**). These were both drawn from a uniform distribution, with step sizes ranging between 0.2 and 1.0 pixel and dwell times ranging from 10 to 100 frames. This, while the step duration – the time it takes to move to a new center point, and the amount of background noise (σ) (Supplementary figure **2.4**) were kept constant. Here the former was set at 1 frame, presenting instantaneous steps, while the latter was defined as Gaussian distribution with μ = 0.15. This value was based on the local standard deviation (in pixels) of several trajectories in our experimental data that were, based on visual assessment, devoid of steps. We examined the performance of each of these parameters individually by assessing the percentage of average true positives, and number of false positives and negatives over 10 simulated trajectories with each a total length of 20000 frames. This later value was based on the maximum duration of trajectories within our obtained experimental data set. To define the most optimal number of iterations for analyzing the experimental data, we varied the number of iterations from 100 up to 20000 and assessed when the percentage of accurately detected steps was most optimal with the minimum number of errors. These results revealed that the maximum performance was reached between a value of 1000 and 5000 iterations (Supplementary table 2.1). Since increasing the number of iterations even further did not affect the outcome, any number of iterations that was $\geq 1/4^{th}$ of the number of frames within a movie was sufficient to access this type of data. To minimize the calculation time and increase the performance for analysis of longer movies, we decided to set the value of iterations equal to $1/4^{th}$ of the number of frames within a movie. Next we examined the acceptance threshold in a similar fashion, by varying the values from 0.1 to 1.0. Results showed no effect of the tested acceptance threshold values on the performance (Supplementary table **2.2**), indicating that any value within this tested range sufficed. We decided to set this value at 0.15, previously used by Kerssemakers *et al.* [53].

2.9 Supplementary

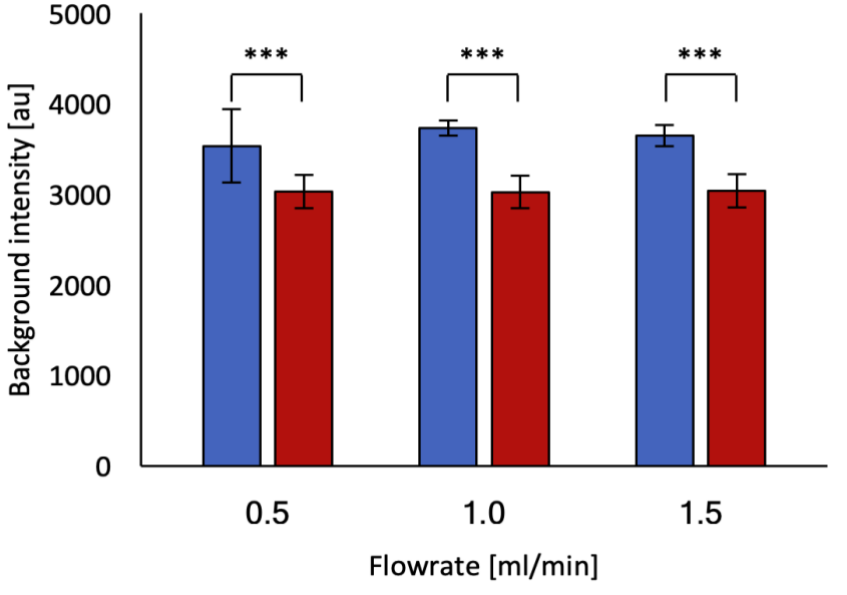

Supplementary figure 2.1: Effect of flow rate on background intensity in flow cell. *E. coli* B cells were attached to a flow cell and background intensity was measured before and after washing the flow cell at different rates. Blue and red bars represent before and after washing the flow cell, respectively. Error bars indicate standard deviation. Asterisks above brackets indicate statistical significance (***: $p < 0.001$), see text for statistics.

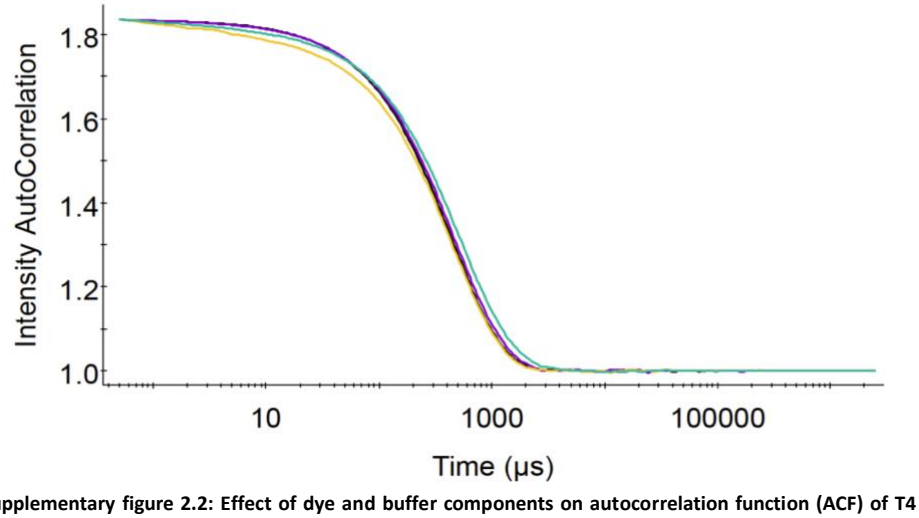

Supplementary figure 2.2: Effect of dye and buffer components on autocorrelation function (ACF) of T4 phage. The autocorrelation curve of T4 phage samples measured with DLS in the presence of different medium components, with T4 in M9 + indole (yellow line), T4 in M9 (black line), T4 in M9 + L-tryptophan (purple line), and Alexa647-labeled T4 in M9 (cyan line).

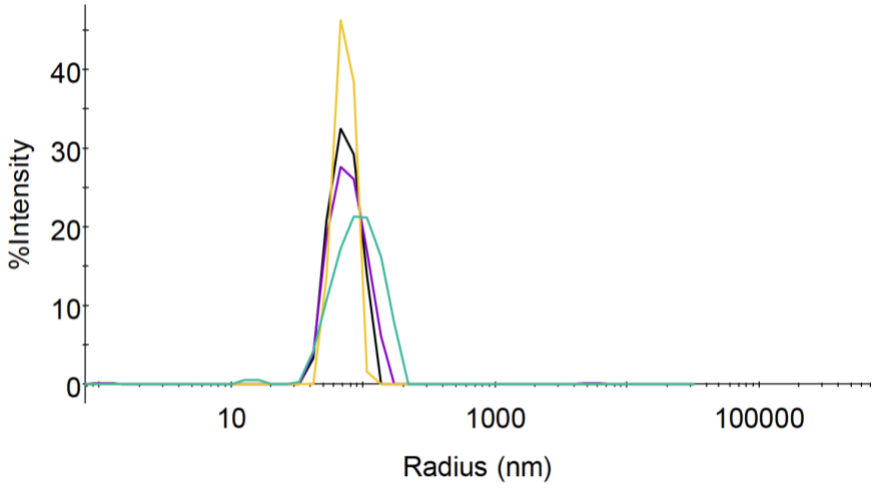

Supplementary figure 2.3: Effect of dye and buffer components on the intensity weighted particle size distribution of T4 phage. Particle size distribution obtained from the measured intensity correlation function of the following measured samples: T4 in M9 + indole (yellow line), T4 in M9 (black line), T4 in M9 + L-tryptophan (purple line), labeled T4 in M9 (cyan line).

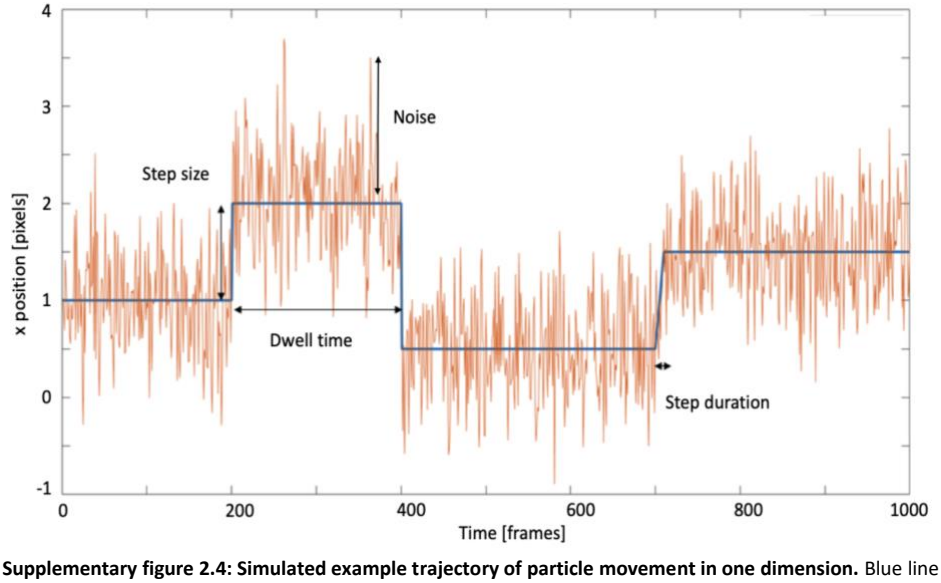

Supplementary figure 2.4: Simulated example trajectory of particle movement in one dimension. Blue line represents the actual movement of the particle in one dimension. Red line indicates the detected movement embedded within noise. Step sizes and dwell times used within this example trajectory were drawn from a uniform distribution with a fixed minimum and maximum value. Step duration and noise level were fixated with a single value.

Supplementary table 2.1: Effect of number of iterations on performance of Stepfinder

Number of iterations	Mean true positives (%)	Mean false positives	Mean false negatives
100	10.50	1	321.9
500	88.67	11.5	40.8
1000	93.18	16.4	24.5
5000	94.54	19.1	19.7
10000	94.54	19.1	19.7
20000	94.54	19.1	19.7

Supplementary table 2.2: Effect of acceptance threshold on performance of Stepfinder

Acceptance threshold	Mean true positives (%)	Mean false positives	Mean false negatives
0.1	94.54	19.1	19.7
0.3	94.54	19.1	19.7
0.5	94.54	19.1	19.7
0.8	94.54	19.1	19.7
1.0	94.54	19.1	19.7

a

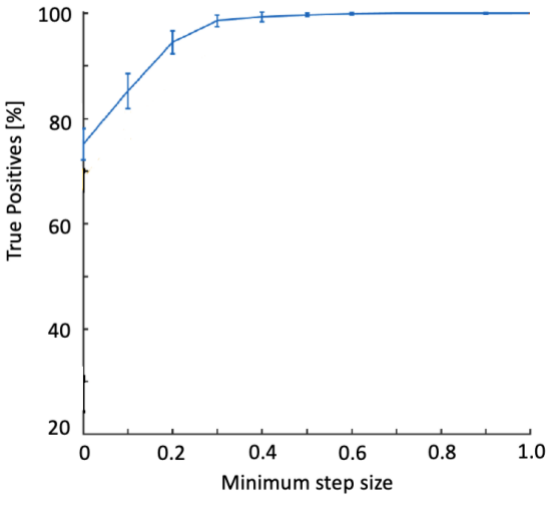

b

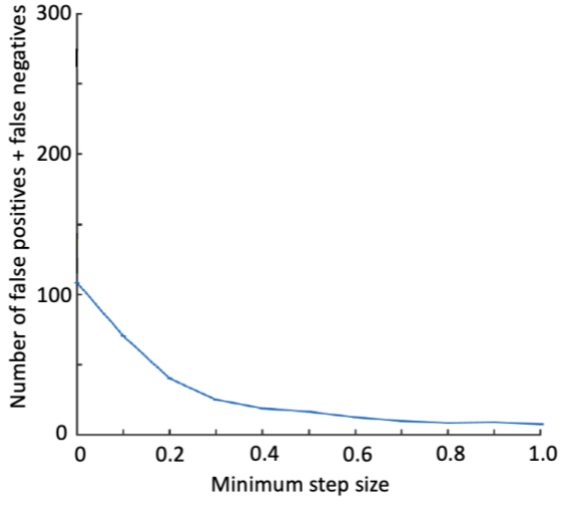

Supplementary figure 2.5: Effect of step size distribution on performance Stepfinder. Stepfinder was subjected to simulated data trajectories of 20000 frames and its performance on step detection was tested for varying step size distributions with 359.5 ± 2.9 steps (Mean ± SD, *n* = 10 simulated trajectories). **a,** Percentage of detected true positives for step size distributions with a minimum dwell time cut-off. **b,** Total number of errors (false positives + false negatives) that occurred per tested minimum step size distribution. The step sizes were drawn from a uniform distribution ranging from the minimum tested value up to 1.0 pixel. Other parameters and variables had the following settings: dwell times were drawn from a uniform distribution ranging from 10 to 100 frames, step duration was set to 1 frame, σ was 0.15, number of iterations was set at 10000, acceptance threshold at 0.15.

a

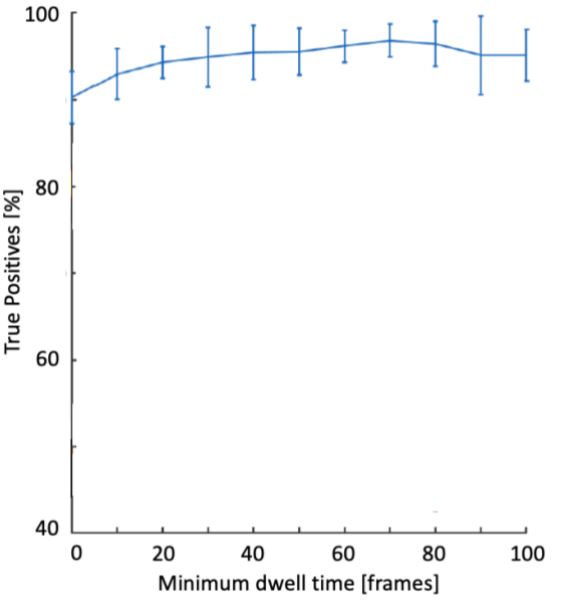

b

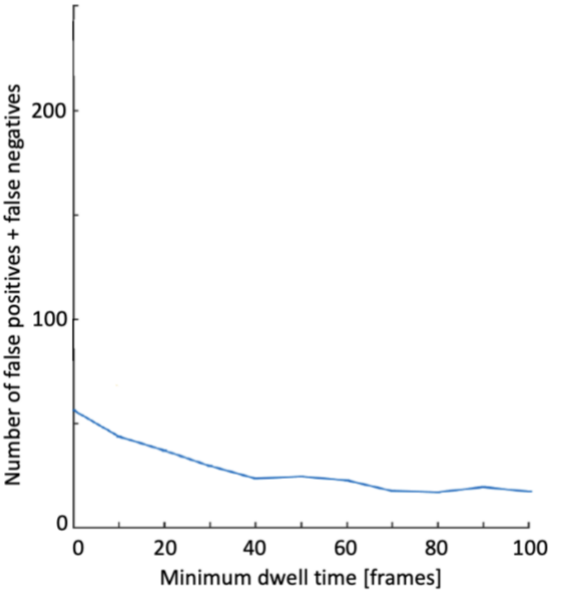

Supplementary figure 2.6: Effect of dwell time distribution on performance Stepfinder. Stepfinder was subjected to simulated data trajectories of 20000 frames and its performance on step detection was tested for varying minimal dwell time distributions (*n* = 10 simulated trajectories). **a,** Percentage of detected true positives for dwell time distributions with a minimum dwell time cut-off. **b,** Total number of errors (false positives + false negatives) that occurred per tested minimum dwell time distribution. The dwell times were drawn from a uniform distribution ranging from the minimum tested value up to 100 frames. Other parameters and variables had the following settings: Step sizes were drawn from a uniform distribution ranging from 0.1 to 1.0 pixel, step duration was set to 1 frame, σ was 0.15, number of iterations was set at 10000, acceptance threshold at 0.15.

References

[1] E. Rothenberg, L.A. Sepulveda, S.O. Skinner, L. Zeng, P.R. Selvin, I. Golding, Single-virus tracking reveals a spatial receptor-dependent search mechanism, Biophys J 100(12) (2011) 2875-82.
[2] D. Mazia, G. Schatten, W. Sale, Adhesion of cells to surfaces coated with polylysine. Applications to electron microscopy, J Cell Biol 66(1) (1975) 198-200.
[3] T.F. Anderson, Electron microscopy of phages in: J. Cairns, G.S. Stent, J.D. Watson (Eds.), Phage and the Origins of Molecular Biology, Cold Spring Harbor Laboratory Press,, NY, USA, 1992, pp. 63-78.
[4] E.S. Miller, E. Kutter, G. Mosig, F. Arisaka, T. Kunisawa, W. Ruger, Bacteriophage T4 genome, Microbiol Mol Biol Rev 67(1) (2003) 86-156, table of contents.
[5] B. Hu, W. Margolin, I.J. Molineux, J. Liu, Structural remodeling of bacteriophage T4 and host membranes during infection initiation, Proc Natl Acad Sci U S A 112(35) (2015) E4919-28.
[6] V.A. Kostyuchenko, P.G. Leiman, P.R. Chipman, S. Kanamaru, M.J. van Raaij, F. Arisaka, V.V. Mesyanzhinov, M.G. Rossmann, Three-dimensional structure of bacteriophage T4 baseplate, Nat Struct Biol 10(9) (2003) 688-93.
[7] A. Fokine, P.R. Chipman, P.G. Leiman, V.V. Mesyanzhinov, V.B. Rao, M.G. Rossmann, Molecular architecture of the prolate head of bacteriophage T4, Proc Natl Acad Sci U S A 101(16) (2004) 6003-8.
[8] P.G. Leiman, P.R. Chipman, V.A. Kostyuchenko, V.V. Mesyanzhinov, M.G. Rossmann, Three-dimensional rearrangement of proteins in the tail of bacteriophage T4 on infection of its host, Cell 118(4) (2004) 419-29.
[9] A. Washizaki, T. Yonesaki, Y. Otsuka, Characterization of the interactions between Escherichia coli receptors, LPS and OmpC, and bacteriophage T4 long tail fibers, Microbiologyopen 5(6) (2016) 1003-1015.
[10] R. Edgar, A. Rokney, M. Feeney, S. Semsey, M. Kessel, M.B. Goldberg, S. Adhya, A.B. Oppenheim, Bacteriophage infection is targeted to cellular poles, Mol Microbiol 68(5) (2008) 1107-16.
[11] H. Strahl, L.W. Hamoen, Membrane potential is important for bacterial cell division, Proc Natl Acad Sci U S A 107(27) (2010) 12281-6.
[12] T. Katsu, T. Tsuchiya, Y. Fujita, Dissipation of membrane potential of Escherichia coli cells induced by macromolecular polylysine, Biochem Biophys Res Commun 122(1) (1984) 401-6.
[13] K. Colville, N. Tompkins, A.D. Rutenberg, M.H. Jericho, Effects of poly(L-lysine) substrates on attached Escherichia coli bacteria, Langmuir 26(4) (2010) 2639-44.
[14] J.H. Wilson, R.B. Luftig, W.B. Wood, Interaction of bacteriophage T4 tail fiber components with a lipopolysaccharide fraction from Escherichia coli, J Mol Biol 51(2) (1970) 423-34.
[15] D. Van Valen, D. Wu, Y.J. Chen, H. Tuson, P. Wiggins, R. Phillips, A single-molecule Hershey-Chase experiment, Curr Biol 22(14) (2012) 1339-43.
[16] L. Zeng, S.O. Skinner, C. Zong, J. Sippy, M. Feiss, I. Golding, Decision making at a subcellular level determines the outcome of bacteriophage infection, Cell 141(4) (2010) 682-91.
[17] L. Jakutyte, C. Baptista, C. Sao-Jose, R. Daugelavicius, R. Carballido-Lopez, P. Tavares, Bacteriophage infection in rod-shaped gram-positive bacteria: evidence for a

preferential polar route for phage SPP1 entry in Bacillus subtilis, J Bacteriol 193(18) (2011) 4893-903.
[18] M.M. Doolittle, J.J. Cooney, D.E. Caldwell, Tracing the interaction of bacteriophage with bacterial biofilms using fluorescent and chromogenic probes, J Ind Microbiol 16(6) (1996) 331-41.
[19] J. Kim, M. Adhikari, S. Dhamane, A.E. Hagstrom, K. Kourentzi, U. Strych, R.C. Willson, J.C. Conrad, Detection of viruses by counting single fluorescent genetically biotinylated reporter immunophage using a lateral flow assay, ACS Appl Mater Interfaces 7(4) (2015) 2891-8.
[20] K. Li, Y. Chen, S. Li, H.G. Nguyen, Z. Niu, S. You, C.M. Mello, X. Lu, Q. Wang, Chemical modification of M13 bacteriophage and its application in cancer cell imaging, Bioconjug Chem 21(7) (2010) 1369-77.
[21] R. Edgar, M. McKinstry, J. Hwang, A.B. Oppenheim, R.A. Fekete, G. Giulian, C. Merril, K. Nagashima, S. Adhya, High-sensitivity bacterial detection using biotin-tagged phage and quantum-dot nanocomplexes, Proc Natl Acad Sci U S A 103(13) (2006) 4841-5.
[22] P.A. Mosier-Boss, S.H. Lieberman, J.M. Andrews, F.L. Rohwer, L.E. Wegley, M. Breitbart, Use of fluorescently labeled phage in the detection and identification of bacterial species, Appl Spectrosc 57(9) (2003) 1138-44.
[23] P.B. Yim, M.L. Clarke, M. McKinstry, S.H. De Paoli Lacerda, L.F. Pease, 3rd, M.A. Dobrovolskaia, H. Kang, T.D. Read, S. Sozhamannan, J. Hwang, Quantitative characterization of quantum dot-labeled lambda phage for Escherichia coli detection, Biotechnol Bioeng 104(6) (2009) 1059-67.
[24] Z. Kazmierczak, A. Piotrowicz, B. Owczarek, K. Hodyra, P. Miernikiewicz, D. Lecion, M. Harhala, A. Gorski, K. Dabrowska, Molecular imaging of T4 phage in mammalian tissues and cells, Bacteriophage 4(1) (2014) e28364.
[25] J.J. Barr, R. Auro, M. Furlan, K.L. Whiteson, M.L. Erb, J. Pogliano, A. Stotland, R. Wolkowicz, A.S. Cutting, K.S. Doran, P. Salamon, M. Youle, F. Rohwer, Bacteriophage adhering to mucus provide a non-host-derived immunity, Proc Natl Acad Sci U S A 110(26) (2013) 10771-6.
[26] K. Chen, L.P. Yap, R. Park, X. Hui, K. Wu, D. Fan, X. Chen, P.S. Conti, A Cy5.5-labeled phage-displayed peptide probe for near-infrared fluorescence imaging of tumor vasculature in living mice, Amino Acids 42(4) (2012) 1329-37.
[27] NHS ester modifications, Integrated DNA Technologies, Inc.
[28] L. Patsenker, A. Tatarets, O. Kolosova, O. Obukhova, Y. Povrozin, I. Fedyunyayeva, I. Yermolenko, E. Terpetschnig, Fluorescent probes and labels for biomedical applications, Ann N Y Acad Sci 1130 (2008) 179-87.
[29] A. Gohler, S. Andre, H. Kaltner, M. Sauer, H.J. Gabius, S. Doose, Hydrodynamic properties of human adhesion/growth-regulatory galectins studied by fluorescence correlation spectroscopy, Biophys J 98(12) (2010) 3044-53.
[30] S.R. Williams, D. Gebhart, D.W. Martin, D. Scholl, Retargeting R-type pyocins to generate novel bactericidal protein complexes, Appl Environ Microbiol 74(12) (2008) 3868-76.
[31] Y. Choi, H. Shin, J.H. Lee, S. Ryu, Identification and characterization of a novel flagellum-dependent Salmonella-infecting bacteriophage, iEPS5, Appl Environ Microbiol 79(16) (2013) 4829-37.

[32] S. Thakur, D.I. Cattoni, M. Nollmann, The fluorescence properties and binding mechanism of SYTOX green, a bright, low photo-damage DNA intercalating agent, Eur Biophys J 44(5) (2015) 337-48.
[33] M.B. Johnson, A.K. Criss, Fluorescence microscopy methods for determining the viability of bacteria in association with mammalian cells, J Vis Exp (79) (2013).
[34] S. Bakshi, H. Choi, N. Rangarajan, K.J. Barns, B.P. Bratton, J.C. Weisshaar, Nonperturbative imaging of nucleoid morphology in live bacterial cells during an antimicrobial peptide attack, Appl Environ Microbiol 80(16) (2014) 4977-86.
[35] B. Szermer-Olearnik, M. Drab, M. Makosa, M. Zembala, J. Barbasz, K. Dabrowska, J. Boratynski, Aggregation/dispersion transitions of T4 phage triggered by environmental ion availability, J Nanobiotechnology 15(1) (2017) 32.
[36] E. Kellenberger, A. Bolle, E. Boydelatour, R.H. Epstein, N.C. Franklin, N.K. Jerne, A. Reale Scafati, J. Sechaud, Functions and Properties Related to the Tail Fibers of Bacteriophage T4, Virology 26 (1965) 419-40.
[37] R.I. Gamow, L.M. Kozloff, Chemically induced cofactor requirement for bacteriopage T4D, J Virol 2(5) (1968) 480-7.
[38] M. Delbruck, Biochemical mutants of bacterial viruses, J Bacteriol 56(1) (1948) 1-16.
[39] T.F. Anderson, The role of tryptophane in the adsorption of two bacterial viruses on their host, E. coli, Journal of Cellular and Comparative Physiology 25(1) (1945) 17-26.
[40] G.S. Stent, E.L. Wollman, Studies on activation of T4 bacteriophage by cofactor. II. The mechanism of activation, Biochim Biophys Acta 6(2) (1950) 307-16.
[41] S. Brenner, S.P. Champe, G. Streisinger, L. Barnett, On the interaction of adsorption cofactors with bacteriophages T2 and T4, Virology 17 (1962) 30-9.
[42] D.J. Cummings, Sedimentation and Biological Properties of T-Phages of Escherichia Coli, Virology 23 (1964) 408-18.
[43] Z.J. Storms, E. Arsenault, D. Sauvageau, D.G. Cooper, Bacteriophage adsorption efficiency and its effect on amplification, Bioprocess Biosyst Eng 33(7) (2010) 823-31.
[44] G.S. Stent, E.L. Wollman, On the two step nature of bacteriophage absorption, Biochim Biophys Acta 8(3) (1952) 260-9.
[45] T.F. Anderson, The Activation of the Bacterial Virus T4 by l-Tryptophan, J Bacteriol 55(5) (1948) 637-49.
[46] T. Gao, C.D. Blanchette, W. He, F. Bourguet, S. Ly, F. Katzen, W.A. Kudlicki, P.T. Henderson, T.A. Laurence, T. Huser, M.A. Coleman, Characterizing diffusion dynamics of a membrane protein associated with nanolipoproteins using fluorescence correlation spectroscopy, Protein Sci 20(2) (2011) 437-47.
[47] M. Tokunaga, N. Imamoto, K. Sakata-Sogawa, Highly inclined thin illumination enables clear single-molecule imaging in cells, Nat Methods 5(2) (2008) 159-61.
[48] J.C. Yen, F.J. Chang, S. Chang, A new criterion for automatic multilevel thresholding, IEEE Trans Image Process 4(3) (1995) 370-8.
[49] D. Blair, E. Dufresne, The Matlab Particle Tracking Code Repository. <http://site.physics.georgetown.edu/matlab/>, 2008).
[50] J.Y. Tinevez, N. Perry, J. Schindelin, G.M. Hoopes, G.D. Reynolds, E. Laplantine, S.Y. Bednarek, S.L. Shorte, K.W. Eliceiri, TrackMate: An open and extensible platform for single-particle tracking, Methods 115 (2017) 80-90.

[51] S. Preibisch, S. Saalfeld, J. Schindelin, P. Tomancak, Software for bead-based registration of selective plane illumination microscopy data, Nat Methods 7(6) (2010) 418-9.
[52] T. Lindeberg, Scale-Space Theory: A Basic Tool for Analysing Structures at Different Scales, J. of Applied Statistics 21(2) (1994) 224-270.
[53] J.W. Kerssemakers, E.L. Munteanu, L. Laan, T.L. Noetzel, M.E. Janson, M. Dogterom, Assembly dynamics of microtubules at molecular resolution, Nature 442(7103) (2006) 709-12.
[54] L. Loeff, J.W. Kerssemakers, C. Joo, C. Dekker, A fast and automated step detection method for analysing single-molecule trajectories, 2017.
[55] N. Otsu, A Threshold Selection Method from Gray-Level Histograms, IEEE Transactions on Systems, Man, and Cybernetics 9(1) (1979) 62-66.
[56] S. van der Walt, J.L. Schonberger, J. Nunez-Iglesias, F. Boulogne, J.D. Warner, N. Yager, E. Gouillart, T. Yu, c. scikit-image, scikit-image: image processing in Python, PeerJ 2 (2014) e453.
[57] N. Chenouard, I. Smal, F. de Chaumont, M. Maska, I.F. Sbalzarini, Y. Gong, J. Cardinale, C. Carthel, S. Coraluppi, M. Winter, A.R. Cohen, W.J. Godinez, K. Rohr, Y. Kalaidzidis, L. Liang, J. Duncan, H. Shen, Y. Xu, K.E. Magnusson, J. Jalden, H.M. Blau, P. Paul-Gilloteaux, P. Roudot, C. Kervrann, F. Waharte, J.Y. Tinevez, S.L. Shorte, J. Willemse, K. Celler, G.P. van Wezel, H.W. Dan, Y.S. Tsai, C. Ortiz de Solorzano, J.C. Olivo-Marin, E. Meijering, Objective comparison of particle tracking methods, Nat Methods 11(3) (2014) 281-9.
[58] W.J. Godinez, K. Rohr, Tracking multiple particles in fluorescence time-lapse microscopy images via probabilistic data association, IEEE Trans Med Imaging 34(2) (2015) 415-32.
[59] B. Hu, W. Margolin, I.J. Molineux, J. Liu, The bacteriophage t7 virion undergoes extensive structural remodeling during infection, Science 339(6119) (2013) 576-9.
[60] S.C. Kuo, J. Gelles, E. Steuer, M.P. Sheetz, A model for kinesin movement from nanometer-level movements of kinesin and cytoplasmic dynein and force measurements, J Cell Sci Suppl 14 (1991) 135-8.
[61] S.M. Block, C.L. Asbury, J.W. Shaevitz, M.J. Lang, Probing the kinesin reaction cycle with a 2D optical force clamp, Proc Natl Acad Sci U S A 100(5) (2003) 2351-6.
[62] B.M. Sadler, A. Swami, Analysis of multiscale products for step detection and estimation, IEEE Transactions on Information Theory 45(3) (2006) 1043-1051.
[63] S.G. Arunajadai, W. Cheng, Step detection in single-molecule real time trajectories embedded in correlated noise, PLoS One 8(3) (2013) e59279.
[64] B. Kalafut, K. Visscher, An objective, model-independent method for detection of non-uniform steps in noisy signals, Computer Physics Communications 179(10) (2008) 716-723.
[65] N.J. Carter, R.A. Cross, Mechanics of the kinesin step, Nature 435(7040) (2005) 308-12.
[66] J. Opfer, K.E. Gottschalk, Identifying discrete states of a biological system using a novel step detection algorithm, PLoS One 7(11) (2012) e45896.
[67] V. Levi, V.I. Gelfand, A.S. Serpinskaya, E. Gratton, Melanosomes transported by myosin-V in Xenopus melanophores perform slow 35 nm steps, Biophys J 90(1) (2006) L07-9.

[68] L.S. Milescu, A. Yildiz, P.R. Selvin, F. Sachs, Maximum likelihood estimation of molecular motor kinetics from staircase dwell-time sequences, Biophys J 91(4) (2006) 1156-68.
[69] B.C. Carter, M. Vershinin, S.P. Gross, A comparison of step-detection methods: how well can you do?, Biophys J 94(1) (2008) 306-19.
[70] J.M. Guberman, A. Fay, J. Dworkin, N.S. Wingreen, Z. Gitai, PSICIC: noise and asymmetry in bacterial division revealed by computational image analysis at sub-pixel resolution, PLoS Comput Biol 4(11) (2008) e1000233.
[71] A. Paintdakhi, B. Parry, M. Campos, I. Irnov, J. Elf, I. Surovtsev, C. Jacobs-Wagner, Oufti: an integrated software package for high-accuracy, high-throughput quantitative microscopy analysis, Mol Microbiol 99(4) (2016) 767-77.
[72] O. Sliusarenko, J. Heinritz, T. Emonet, C. Jacobs-Wagner, High-throughput, subpixel precision analysis of bacterial morphogenesis and intracellular spatio-temporal dynamics, Mol Microbiol 80(3) (2011) 612-27.
[73] I. Mekterovic, D. Mekterovic, Z. Maglica, BactImAS: a platform for processing and analysis of bacterial time-lapse microscopy movies, BMC Bioinformatics 15 (2014) 251.
[74] A. Ducret, E.M. Quardokus, Y.V. Brun, MicrobeJ, a tool for high throughput bacterial cell detection and quantitative analysis, Nat Microbiol 1(7) (2016) 16077.
[75] N.O. Vischer, J. Verheul, M. Postma, B. van den Berg van Saparoea, E. Galli, P. Natale, K. Gerdes, J. Luirink, W. Vollmer, M. Vicente, T. den Blaauwen, Cell age dependent concentration of Escherichia coli divisome proteins analyzed with ImageJ and ObjectJ, Front Microbiol 6 (2015) 586.
[76] K. Ikeda, F. Egami, Receptor substance for pyocin R. I. Partial purification and chemical properties, J Biochem 65(4) (1969) 603-9.
[77] B. Szermer-Olearnik, M. Sochocka, K. Zwolinska, J. Ciekot, A. Czarny, J. Szydzik, K. Kowalski, J. Boratynski, Comparison of microbiological and physicochemical methods for enumeration of microorganisms, Postepy Hig Med Dosw (Online) 68 (2014) 1392-6.
[78] U. Bachrach, A. Friedmann, Practical procedures for the purification of bacterial viruses, Appl Microbiol 22(4) (1971) 706-15.

2

3

Irreversible binding distribution of phage T4 on *Escherichia coli* B is targeted towards the cellular poles

Lisa L. Dreesens, Igor Rutka, Marie-Eve Aubin-Tam, Hubertus J. E. Beaumont

Binding to the correct host is the first step in the infection process of a phage. T4 phages and several of its *Escherichia coli* strains have been used as a model to understand the underlying mechanisms of myoviridae-phage host targeting. It has been shown that phage T4 can infect *E. coli* of different strains using the specific sugars moieties of the lipopolysaccharide (LPS) receptors (*E. coli* B). When these specific moieties cannot be reached by the long tail fibers (LTFs) for the initial interaction, the presence of a second receptor, outer membrane protein C (OmpC), can facilitate the irreversible binding (*E. coli* K-12). Examination of the spatial distribution of T4 irreversible binding has been examined for the two-receptor system and revealed a preference to the cell poles. However, this has not been studied for a single LPS receptor system. This can shed light on the role of protein receptors in determining polar preference and provides a point of reference for the study of directional biases in on-cell dynamics (Chapter 4). In this chapter, we study the spatial distribution of irreversibly bound T4 phages on *E. coli* B. We used HILO microscopy to observe the irreversible binding distribution of fluorescently labeled T4 phages on its host cell *E. coli* B in two different media (LB and M9). The latter is relevant because much of the previous work on phage T4 was carried out in LB medium while our single-particle measurements will be performed in M9. We found that T4 phages preferentially bind to the old polar regions of *E. coli* B cells in a manner that was not differentially affected by M9 vs. LB medium. Comparison to literature on the distribution of phage T4 on *E. coli* cells to which it binds using both LPS and a protein receptor reveals that the receptor spectrum appears to play a role in the binding distribution. This indicates a possible role of the diversity, distribution and density of cellular receptors in the phage decision-making process that governs host discrimination and commitment to irreversible binding. These results are a first step towards understanding the mechanism and key-factors that play a role in the target-finding process of the T4 phages.

3.1 Introduction

Bacteriophages are viruses that infect and kill bacteria. The first step of this viral infection cycle is the attachment to the host. Initial attachment of the phage to a host is governed by specific interactions between host cell receptors and the distal end of the long tail-fibers (LTFs), tail-spikes or central tail spike of the phage, which can act as the receptor-binding proteins (RBPs) and enable host-cell discrimination by binding specifically to host receptor proteins [1]. Phage receptors include a range of structures on the bacterial outer membrane that comprise proteins, liposaccharides (LPS), or teichoic acids.

Attachment of the phage to the host follows two steps: reversible and irreversible binding. The process of irreversible binding and initiation of infection for the class of myoviridae has been best characterized for T4, a frequently used model phage, which infects *Escherichia* and *Shigella* strains [2, 3]. Compared to most other phages within this class, T4 has, besides the long tail-fibers (LTFs), an additional set of short tail-fibers (STFs) that plays a role in the binding process. During reversible binding, T4 interacts with at least one of its LTF to the host, keeping the phage tethered to its surface. Binding of a second LTF will allow the phage to orient its baseplate perpendicular to the cell surface [4]. In this stage, the phage can still detach from a cell when contact between LTF and receptor is lost. It is believed that when at least three out of six LTFs are bound to the specific LPS sugar moieties Glc I or Glc I-Glc II, a conformational change takes place within the baseplate, resulting in the release of the STFs that can bind to LPS [4-7]. Binding of the STFs brings the phage closer to the surface and triggers further conformational changes in the baseplate. At this stage the phage is irreversibly bound [4-7]. This is a cue for the second stage of the infection process: sheath contraction and piercing of the membrane to eject the DNA into the host and start replication.

For several tailed phages (λ, SPP1, 80, T4, P1, KVP40, T7 and A1122) across three phage families (*shipho-, myo-, podoviridae*) of the class *Caudovirales*, that all have distinct cellular receptors, it has been reported that the irreversible binding locations of the phages on the cell are biased to the cellular poles at a low MOI (≤ 1) [8-11]. In addition, it has been reported that for phage SPP1, DNA injection and replication have a higher chance of succeeding at these polar regions [10]. So, not only does irreversible binding seem to happen more frequently at the polar regions, also successful infection and propagation is more likely to occur within these regions. Phage T4 has even been shown to make use of two kinds of receptors to facilitate irreversible binding, LPS and OmpC, depending on the receptor spectrum available on the host strains. For example, T4 has been shown to infect *E. coli* B strains by facilitating irreversible binding between the LTFs and specific sugar moieties on the LPS. However, some *E. coli* strains (i.e. K-12) have a branched LPS, preventing direct contact between the LTFs and specific moieties within the LPS chain and only facilitating weak reversible interaction. Phage T4 has circumvented this problem and extended its host range, by reorganizing and facilitating irreversible binding with a second receptor, OmpC [12, 13]. The later infection process still requires LPS to facilitate weak reversible interaction, as well as, binding of the STFs to the bacterial surface, but in an OmpC dependent mater [12]. Studying and comparing the binding distributions of phage T4 to both strains would provide insights on the

possible effect and contribution of receptor spectrum on the biased binding distribution to the cellular poles.

The factors that cause the observed spatial bias in commitment to irreversible binding, which have a substantial effect on the final position of binding to the host, and with that, play an important role in the critical steps of adsorption, receptor binding, and breaching of the cell envelope, remain largely elusive. Revealing them will improve our basic understanding of the biology of phages, and will help us reverse engineer the underlying mechanisms involved in the phage adsorption process and the decision-making event of the phage to bind irreversibly. Furthermore, mapping the sensitivity of the binding distribution towards certain factors will aid the therapeutic applications of phages through genetic engineering or synthetic biology.

One of these potential key-factors driving the binding distribution is the receptor distribution and density across the cell surface. Receptor LamB was shown to be distributed in a helical pattern on the surface of *E. coli*, forming receptor rich regions, with the highest concentration found at the cellular poles [11]. Phage λ (*Siphoviridea*), that uses this receptor, has been demonstrated to make first contact with *E. coli* cells at random locations, drift towards LamB-rich regions and subsequently move over these helical patterns towards the cellular poles causing preferential binding at this location [11]. Investigating the effect of a shift in receptor distribution, e.g. either by changing the receptor spectrum (i.e. the type of receptors available on different suitable host cells) or by manipulating receptor density, can provide insight into its role in shaping the binding distribution. We accomplished this by expanding the measured binding distribution of T4 with strain *E. coli* B. This strain differed from the previously documented distribution of T4 on K-12 in structure of the host cell receptor LPS (unbranched, exposing the specific sugar moieties Glc I or Glc I-Glc II required for irreversible binding), in addition to the lack of OmpC on the outer surface (Supplementary 3.5.1), resulting in a OmpC independent irreversible binding process [12].

In addition to the above-mentioned host-cell parameters, environmental factors have also been shown to affect phage-host interactions and might impact the irreversible binding distribution. These factors include among others, temperature, pH, ion concentrations, and organic co-factors that can have a significant impact on adsorption kinetics. For example, changes in temperature have shown to play a role in binding rate and DNA ejection time for phages that require the presence of two receptors to facilitate binding [14, 15]. In addition, it has been shown that a certain range of pH [16], heat [17], or cationic detergent [18] triggers sheath contraction. Further, mono- and divalent cations can facilitate electrostatic interaction, which have shown to play an important role in the first stage of binding [14, 15, 19-21], orientating the phage in a favorable position relative to the cell surface, enhancing the chance for LTF-receptor interaction [15]. Lastly, it has been found that some phages require small organic co-factor molecules for binding. For example, T4 has been shown to be dependent on the co-factor L-tryptophan, governing LTF deployment [22] and affecting the adsorption efficiency [23, 24]. It is possible that some of these environmental

factors (i.e. temperature, ion concentration, or co-factors) facilitate a faster binding event between the LTFs and host receptors, and thereby potentially influence the irreversible binding distribution among hosts. The role of environmental factors is of additional interest because our single particle protocol to study phage-host interactions makes use of M9 medium while most phage T4 studies have been performed in highly auto fluorescent LB medium. Therefore, we compared the binding distribution of T4 to *E. coli* B in LB and M9 medium, which differ among others, in ion and L-tryptophan concentration.

Here we analyze the effects of receptor spectrum and environment on the distribution of irreversible phage binding. In particular, we report the binding distribution of phage T4 on *E. coli* B cells (single receptor system) in LB and M9 media and compare this to the previously published distribution of T4 on *E coli* K12 (two receptors system).

3.2 Results

Previous studies revealed that several phages bind irreversibly with a higher frequency to polar regions of a cell [8-11]. We were interested if this was shared by phage T4 when making use of the single receptor system, by examining the spatial distribution of irreversibly bound T4 phages on host strain *E. coli* B using solely the host receptor LPS (Supplementary 3.5.1). This was the basis for further investigation to examine whether there was an effect of a shift in medium composition and receptor distribution on the irreversible binding distribution of T4. Therefore, we first investigated the binding location of T4 phages on *E. coli* B in LB medium, and subsequently, examined the effect of medium by comparing the observed binding distribution in LB, which is a nutrient-rich medium, to the one obtained in M9, a nutrient-poor medium. This was also used to assess the use of M9 medium to study dynamical phage-host interactions at single-particle level (Chapter 4). Secondly, we investigated the effect of host-receptors used to commit to irreversible binding on the binding distribution. For this, we compared a shift in receptor spectrum by investigating the binding of T4 to two strains of *E. coli* (B and K-12). It is known that phage T4 binds to *E. coli* B *via* LPS molecules, while it binds to *E. coli* K-12 *via* both OmpC and branched LPS [12]. The latter was previously studied by Edgar *et al.* [8].

To establish and detect the irreversible binding position of T4 phages on *E. coli* B cells in two different media compositions, we used an adaptation of the method described by Edgar *et al.* [8]. We fluorescently labeled the phages with Alexa488, *via* a chemical conjugation as described in chapter 2 section 2.4.1. Fluorescently labeled phages were incubated with a liquid culture of exponentially growing *E. coli* B cells at an MOI < 1 in the specified interaction medium. After a 5-minute incubation period, cells with irreversibly bound phages were collected by centrifugation and inserted into the flow cell, as described in chapter 2 section 2.2.1. Fluorescent T4 phages and hosts were detected using fluorescence microscopy in HILO-mode and phase contrast microscopy (Figure **3.1**), respectively. The position of the phage on the cell was quantified as described in chapter 2 section 2.6. We analyzed the irreversible binding position of a phage across the long axis (X_L) of a cell. This distribution was normalized and made

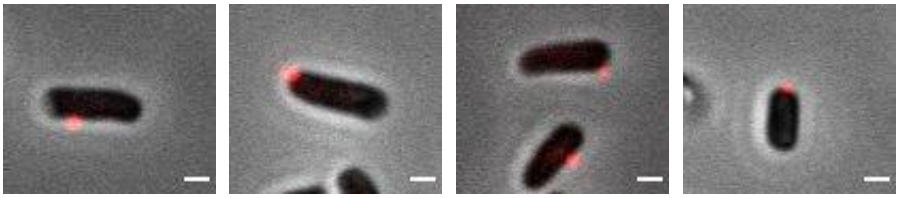

Figure 3.1: Micrographs of irreversibly bound T4 phages in LB medium. Overlay between fluorescent micrograph, showing fluorescently labeled T4 phages (red foci), and phase contrast micrograph, showing their host *E. coli* B. Images were obtained with an exposure time of 100 ms, EM gain of 200, and laser intensity of 180 µW. Scale bar represents 1 µm.

absolute, with the mid and pole region of the cell defined as 0 and 1, respectively. The obtained location data was divided into 5 bins along X_L, in which the bins comprised an equal surface area. No correction was required for the polar bins, as the surface area (*S*) per unit on X_L is identical for the hemispherical pole bin and a bin comprising a cylindrical region of an equal radius (*r*) on this basis of approximation by a geometric model (supplementary 3.5.2) with equation [25]:

$$S = 2rh \qquad \text{Equation 3.1}$$

The frequency of phage observation was normalized to the total number of observations. The results for T4 phages binding to *E. coli* B in LB medium showed that 41% of all bacterial cells had a bound T4 phage (*n* = 1241, from 4 independent experiments), confirming a MOI < 1. The fraction of phages bound to old polar regions (the rounded ends of a rod-shaped cell that were assigned as the outer bins) of the cell in LB medium was 0.35. This was more than twice the number of phages bound to an average surface section of the remaining part of the cell. To express the degree of polar bias, we define a polarity index: normalized, ln-transformed ratio of polar versus non-polar bound phages. This value indicates the strength for preference of irreversible binding towards the poles with: 1 a very strong polar preference, 0 no preference (uniform distribution), and -1 a preference towards the mid- cell region. Here the polarity index is 0.19 ± 0.07 (Mean ± SD) (*n* = 4).

Secondly we tested if this distribution changed when phages were allowed to bind in a different medium: M9. Compared to LB, this medium differs mainly in the following manner: lack of the amino acid L-tryptophan and higher ion concentration. Both L-tryptophan and a high ion concentration have shown to play an important role in the binding kinetics and binding efficiency of phage T4 [23]. The former, has been shown to act as co-factor in LTF deployment, playing an important role in both the binding rate and efficiency (fraction of phage that adsorbs irreversible to the host) [21-23, 26-28]. While the latter plays an important role after LTF deployment, promoting the collision efficiency between LTFs and receptor. Here the highly polar side chains of L-tryptophan attract ions, resulting in the furnishing of LTFs with positive ions. The electrostatic forces between LTFs and host cell surface allows the phage to orientate in a favorable position increasing the chance to bind a host receptor [15]. We found that the fraction of phages bound to old polar regions of the cell was 0.29, with a polarity index of 0.11 ± 0.05 (Mean ± SD) (*n* = 5). Similar to the observed distribution in LB, we found that also

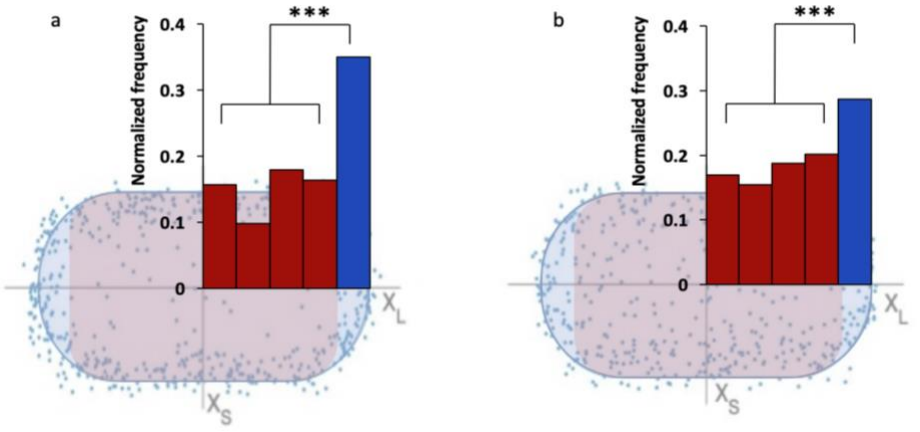

Figure 3.2: Irreversible binding distribution of phage T4 in LB and M9 media. Histogram with irreversible binding distribution of T4 phages on *E. coli* B cells. Frequency was normalized in absolute values along the long axis of cells (X_L). Binding occurred either in **a**, LB medium (N = 580) or **b,** in M9 medium (N = 512). Red and blue bars indicated the mid and pole region of cells, respectively. Asterisks above brackets indicated significance of effect of region on the cell (***: p < 0.001; see text for statistical analysis).

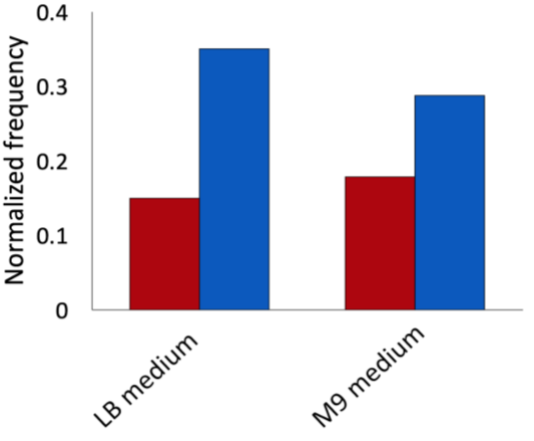

Figure 3.3: Ratio irreversible binding position of phage T4 along the cell in different media composites. Normalized binding ratio of T4 phages on *E. coli* B cells in LB and M9 medium. Red and blue bars present the normalized ratio between binding to mid and pole region of a cell, respectively.

in M9, phages were more likely to bind to the polar regions of the cell (Bonferroni corrected X^2 goodness fit; n = 512, p < 0.001; Figure 3.2b). Here, also no detectable statistically significant deviation was found between experiments (Bonferroni corrected X^2 test of independence; n = 5, p < .1; Supplementary 3.5.3), indicating that the obtained means of each individual experiment were most likely drawn from the same population distribution. Next, we tested whether there was an effect of the medium on the biased binding to the old poles. To this end we tested the obtained binding distribution of T4 on *E. coli* B in M9 medium against the null hypothesis of a binding distribution not deviating from that of LB. No detectable statistically significant deviation was found

between the binding distribution of M9 compared to that of LB after Bonferroni correction (Figure **3.3**), showing no detectable effect of medium composition on the irreversible binding distribution.

Lastly, we examined if there was an effect of host-receptor on the binding distribution. Therefore, we compared the frequency of polar binding (i.e. old pole and new pole at mid cell region) of T4 to host strain *E. coli* B in LB against the previously documented distribution of T4 on strain K-12 in LB described by Edgar *et al.* [8]. Results revealed a statistically significant deviation between irreversible binding to the polar regions of strain K-12 and B, (Bonferroni corrected X^2 goodness fit; n = 1160, p < 0.001). This demonstrated that T4 was more likely to bind irreversibly to the polar regions on K-12, a strain expressing the host-receptor OmpC and a branched version of LPS.

3.3 Discussion and conclusion

Phage adsorption is the first maneuver, in a series of crucial steps, in the phage infection process. So far, the molecular details behind the initial interaction between phage and host cell that lead to irreversible phage attachment remain largely unknown. One aspect of this is the location of the irreversible binding site on the cell. While the global phage binding distribution over the cell has been studied for a range of different phages, insight into the more 'subtle' effects of the type and number of different receptors and the environment is lacking. These factors might play an important role as they reflect the outcome of the dynamical interactions that govern host selection and infection kinetics. To address this, we examined the distribution of fluorescent T4 phages on *E. coli* B, infection which requires only a single type of receptor (LPS), and compared this to the distribution on *E. coli* K-12 cells, for which infection depends on both LPS receptor and protein receptor (OmpC).

We found that phage T4 has a bias towards irreversible binding at the polar regions of *E. coli* B cells. This bias was not affected by a switch of interaction medium from LB to M9, a finding that indicates that we can meaningfully compare single particle-level observations made in M9 medium (Chapters 4) with the body of observations made previously in LB medium for dynamics that underpin polar bias. Comparison of the irreversible binding distribution of T4 on *E. coli* B to that previously documented for *E. coli* K-12, showed a shift in the degree of binding that is biased to the cell poles. Based on these findings, we conclude that phage T4 preferentially binds to the polar regions of a cell in a manner that is not differentially affected by LB vs. M9 medium. In addition, these findings strongly indicate that the degree of binding to the cellular poles, which is needed for infection of the host cell, is sensitive to the receptor spectrum.

We found that T4 phages bind preferentially to the polar regions of *E. coli* B cells. Since irreversible binding requires specific interaction with the cellular receptors, a likely explanation for preferential binding to the polar regions of a cell is that it is correlated to the receptor density and distribution. So far, little is known about the density and distribution of host receptor LPS at the bacterial cell surface. A study by Ghosh and Young found that LPS was non-uniformly distributed on *E. coli* 2334, with an angle and

pitch in a helical pattern similar to that found for several Omp's [29]. Most importantly, they seemed, even though not quantified, to observe slightly higher LPS densities at the cellular poles. Despite the fact that this study was performed on a strain of *E. coli* that was not strain *B*, it is likely that this LPS distribution is shared by all strains. If this is indeed the case, one possible cause for the observed polar bias is that the slightly higher concentration of LPS at the polar regions of the cell results in an increased probability of adsorption and subsequent local commitment to irreversible binding. Overall, the observed distribution falls in line with the general trend described in the literature of pole-biased irreversible binding for many different classes of phages using a variety of receptors [8-11]. So far, only one exception has been documented, podophage Sf6, which showed preferential binding to the mid cell region [30]. The observed polar binding might suggest that, in addition to the high polar receptor density, tethered on-cell walking in combination with receptor distribution and/or geometrical considerations related to the cell shape cause phages to preferentially move towards the poles. Overall, these findings indicate that the receptor spectrum needed for infection and/or the receptor distribution are factors that shape irreversible binding distribution of phages on their host. Future experiments, involving labeling of LPS, can examine whether there is a correlation between the density of LPS at the surface of *E. coli* B cells and the phage T4 binding distribution.

Besides the specific phage-receptor interaction, environmental factors have also been shown to affect the binding kinetics of phages [23]. Some of these environmental factors impacted the dynamics of the phage adsorption process, and in this way, might affect the binding distribution. Despite the detected impact of a change in medium (LB versus M9) on bulk kinetics (i.e. binding efficiency (Chapter 2, section 2.4.4), no detectable effect was found on the irreversible binding distribution. This suggests that the reversible binding distribution was already targeted towards the cellular poles, and that environmental factors (i.e. L-tryptophan) that alter on-cell tethered walking dynamics do not influence the outcome of irreversible binding position. Two studies that have documented the reversible binding positions of phages showed contradicting conclusions: phage SPP1 was directly targeted at the cellular poles [10], while phage λ first interacted with the cell at a random location before moving towards the poles for irreversible binding [11]. For this reason, it remains difficult to draw conclusions on the dynamics of reversible binding and their effects on the irreversible binding distribution of phage T4 on the basis of the static data presented in this chapter. It might even be that, depending on the phage and sensitivity to certain environmental factors, different interaction modes are being used. Future experiments that examine the reversible binding distribution and/or dynamics preceding irreversible binding at the single particle level, optionally combined with modification of environmental factors, can shed more light on its impact on the irreversible binding distribution of phages.

Further, our work showed that it is very likely that there is a distinct effect of receptor spectrum on the preference of binding to the polar regions of bacterial cells. Phage T4 binds with a higher degree to the cellular poles of K-12 compared to *E. coli* B. The experimental conditions between obtaining the binding distribution of T4 on *E. coli*

B and that of T4 on K-12, previously reported by Edgar *et al.* [8], were similar, with the exception of the fluorescent label, namely Qdot655 versus organic dye Alexa488. However, the chemical conjugation method used for dye attachment was the same (NHS-ester). Therefore, the difference observed between the distributions for the two strains most likely result from the difference in receptors used by T4 for infection. Overall, these findings strongly indicate an effect of receptor spectrum on binding distribution. However, direct comparison within the same environment is needed. Given the robustness of the polar bias degree to medium observed within our experiments, it is unlikely that subtle experimental differences or differences in physiological state of the host cell between experiments can cause the large difference. It does have to be noted that previously documented phage P1, A1122, and T7, all using host-receptor LPS for irreversible binding, showed a stronger preferential polar binding than what we observed for phage T4 on *E. coli* B. However, the degree of polar binding of these phages was still lower than what was documented for T4 on K-12 [8].

The differences between the distributions of the protein receptors used for irreversible binding to K-12 (OmpC) and the LPS receptors used for this purpose on strain *B* allows us to speculate about a possible mechanism for the observed differences in polar bias. Omp's such as OmpC are, in contrast to LPS, generally inserted in the outer membrane at the future pole at mid-cell region, where they clustered together in islands, forming a helical pattern across the cell resulting in receptor rich regions. These Omp island are mainly displaced by means of cell growth to the old poles for long term retention [31-33]. This in contrast with LPS, which is inserted in the outer membrane uniformly across the cell body, forming a helical pattern with a similar angle and pitch to that observed for Omp's, where they remain immobilized. Further, it was estimated that the average density of OmpC receptors in the outer membrane is approximately 10-fold lower (10^5 molecules [34]) than that of LPS [13], making it possible that irreversible phage binding to OmpC requires dense receptor-rich regions, i.e. the poles. This in contrast with the density of LPS across the cell, which is, with estimated numbers of 10^6 molecules, relatively high [13]. The presumably stronger non-uniform distribution of OmpC in combination with the lower density across the cell, relative to that of LPS, is a likely explanation for the observed difference in the degree of polar binding between the two strains.

Overall, these results strongly suggest a key-role of receptor spectrum on the degree of polarity of the irreversible binding distribution, which is most likely correlated to the receptor distribution and density. Binding to the polar regions of a cell might provide a competitive advantage regarding downstream infection processes. For example, phage SPP1 has been shown to have a higher success rate of DNA injection and replication at the cellular poles [10]. This might be related to the fact that these polar regions are largely devoid of chromosomal DNA, resulting in a less crowded environment. In addition, it has been shown that phage λ needs the protein ManY for its infection cycle, which was shown to concentrate mainly near the cellular poles [8]. It could be that phages exploit these cues of receptor distribution to find the most optimal target location for infection. Although this is an enticing possibility, direct experimental evidence demonstrating such an advantage is still lacking.

Taken together, our findings show that phage T4, like many other phages, has a preference for binding irreversibly to the cellular poles. We demonstrated that the degree of polar binding is likely to be receptor-spectrum and/or receptor-distribution dependent. Even though we found no effect of a shift in medium composition, from LB to M9, on the irreversible binding distribution, we cannot exclude its effect on other steps within the adsorption process. Unraveling the effects of these factors on the binding distribution are critical not only for understanding the underlying mechanism and molecular details of phage-host interaction governing adsorption and host selection, but also to provide basic insights needed for genetic engineering of phage properties for technical and medical applications including phage therapy.

3.4 Material and methods

3.4.1 Bacterial strain, bacteriophage and growth conditions

Escherichia coli B (ATCC 11303) was used as host indicator strain of phage T4 ATCC 11303. E. coli was grown in Lysogeny broth (LB) (Sigma) supplemented with 10 mM $CaCl_2$ and 10 mM $MgSO_4$ at 37 °C and 250 rpm to early exponential phase (OD_{600} 0.1) and infected with T4 at MOI 0.5 and grown until lysis occurred (~3 hours). A final concentration of 2.5 % chloroform was added to lyse all the cells. The suspension was centrifuged for 20 min at 18000 g and filtered through a 0.22 µm filter (SFCA, Minisart NML, Satorius). 1 µg ml^{-1} RNase and DNase was added to the phage suspension and incubated for 30 min at RT. Phages were extracted and purified with a CsCl density gradient (with the following densities: 1.33, 1.45, 1.50, 1.70) and centrifuged at 28.000 g for 3 h at 4 °C, followed by dialysis (7 k cutoff, Thermo Fisher) in MB (20mM Tris-HCl, 100mM NaCl and 10mM $MgSO_4$) and stored at 4 °C until use. Purity was checked with negative stain EM and the activity and concentration was confirmed with a spot assay.

Purified phages were concentrated and washed with a amicon ultra-0.5 centrifugal filter unit (100 kDa cutoff, Millipore) in PBS (sigma) supplemented with freshly made 0.1 M sodium bicarbonate. Followed by fluorescent labeling with a final concentration of 0.05 mg ml^{-1} Alexa Fluor™ 488 NHS Ester (Thermo Fisher) for at least 3 h at RT and washed with a amicon ultra-0.5 centrifugal filter unit (100 kD, Millipore) in MB and stored at 4 °C until use.

3.4.2 Microscopy

3.4.2.1 Flow cell

Glass coverslips were extensively cleaned with 2% Hellmanex III (Hellma GmbH) and pre-coated with 0.1% poly-L-Lysine (sigma). Flow cells were assembled with the use of double adhesive tape, serving as a spacer. Cells were grown in LB to early exponential phase (OD_{600} 0.3), concentrated 10x and resuspended in interaction media. Phages were incubated with cells at MOI 0.1 for 10 min. 10 µl of cell suspension was added to the perfusion chamber through a predrilled hole and left for attachment to the coverslip for 10 min. Excess cells and poorly immobilized cells were removed by washing the chamber with 150 µl interaction media at a speed of 175 µl min^{-1}.

3.4.2.2 Imaging conditions

Image acquisition was performed with an Olympus inverted microscope (IX81) with a TIRF illumination system. Fluorescence excitation of fluorophore Alexa480 was provided by an Olympus CW laser at 488 nm with a maximum output power of 150 mW. As detection device, we used an EM-CCD (Andor iXon X3 DU897) containing a chip size of 512x512 pixels with a resolution of 80 nm/pixel. A UPlanFLN objective was used with magnification 100x, numerical aperture 1.3 and working distance 0.2mm. The Electron-Multiplying (EM) gain was set to 200 and the exposure time at 100 ms. A 0.6 ND filter was used to reduce Overexposure. Emission filter 524/29 was used. Fluorescent imaging was performed in HILO mode.

3.4.2.3 Data processing and statistics

Phase contrast images, containing the bacteria, were made binary with Fiji using the following procedure. First, the contrast was enhanced by saturating 0.03% of pixel, followed by applying a Gaussian blur filter with sigma 2, and a Yen threshold method.

Using Matlab, bacteria were detected as binary objects meeting the following criteria. A minimal area of 100 and maximal area of 1000 pixel, with a minimal eccentricity of 0.7 and minimal solidity of 0.9. Manual selection was performed to discard dividing bacteria that were detected as a single object. From the fluorescent images, the center of each phage was detected as follows. First, a bandpass filter was applied using the Matlab function bpass, followed by detection of local intensity peaks with the Matlab function pkfind, and determination of the peak position with sub-pixel accuracy using the Matlab function cntrd. Detected phages were overlaid with the corresponding bacterial binary objects. Manual selection was performed to include bacteria with a single attached phage. The detected center of the phage was dependent on the density of fluorescent labels across the phage body, which was estimated to be at the center of the phage capsid. When bound irreversibly, this center can lay maximally 160 nm from the cell surface. Therefore, phages detected $\leq$ 80 nm from a binary object (cell) were included for further data analysis. To compare phage position on the cell, the coordinates were normalized in the following way. First the outline of the bacteria was obtained with the Matlab function bwboundaries, as well as the centroid coordinates and orientation angle of the bacterium with the Matlab function regionprops. A translation was performed by assigning the centroid coordinates as the new origin of the coordinate system. Secondly, a rotational transformation was performed, which aligns the long axis (length) of the bacterium with the x-as and the short axis (width) of the bacterium with the y-axe. This was followed by normalization, where the bacterial coordinates on the x- and y- axes were scaled from -1 to 1. Lastly, a second translation was performed to correct for a small offset of the initial centroid coordinates. The position of the phage was normalized accordingly. All normalized phage positions were collected and made absolute. The data was divided into 5 bins, with 1 and 0 corresponding to the pole and mid-cell, respectively. A Chi square goodness fit was performed to check for polar binding, where the pole (1 bin) vs the rest of the cell (4 bins) was tested against the expected outcome of a uniform distribution. A difference in polarity between conditions was tested with a Chi square test. Here the ratio count between a polar bin and an average bin of the non-polar region was compared.

3.5 Supplementary information

3.5.1 Signal peptide of OmpC was absent in *E. coli* B

LPS and OmpC were shown to act as receptors for phage T4 [12]. To confirm T4 solely uses LPS as receptor to bind to *E. coli* B as described previously by Wilson *et al.* [6] and Montag et al. [35], we verified whether the signal peptide of OmpC was absent from the genome, as was reported previously [12], by running a pcr (Supplementary figure 3.1) and sequencing parts of the OmpC region. We found that the signal peptide, required for transport of OmpC across the inner membrane, was indeed missing in our strain (Supplementary figure **3.2**). Sequencing the PCR product, using the primers 534 and 541 (Supplementary table 3.1) showed perfect overlap in sequence between strain *E. coli* B and BL21. This in contrast with comparing the obtained sequence of *E. coli* B with that of MG1655, where no overlap was found in the initial region up till the start of ΔOmpC region. Without this signal peptide, OmpC is not expressed on the outer surface of the membrane [36, 37]. Therefore, we assumed that within our conducted experiments T4 only used LPS as a receptor for binding on *E. coli* B.

Supplementary figure 3.1: PCR primers targeting OmpC sequence within *E. coli* strains. Different primers targeting (parts of) the OmpC sequence on the genome of *E. coli* strains. ΔOmC presents an OmpC sequence without the signal peptide part required for transport of OmpC across the plasma membrane.

Supplementary table 3.1: Primers used for sequencing OmpC.

Primer name	Sequence (5'-> 3')
525	GAAACTCAGGTTACTGACCAGCTG
529	CTACGATGTTATCAGTGTTGATGCC
530	TAAAGTACTGTCCCTCCTGGTCCCAGC
534	ATCTGGCCTACAGGTGATTAGTCTTT
541	ATCCTGGAATTTCAGACCTGCGAATGC

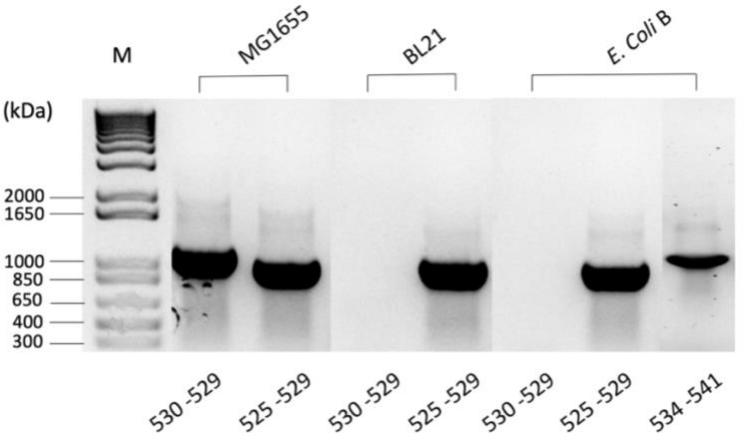

Supplementary figure 3.2: Signal peptide of OmpC was absent in *E. coli* B. Different primers targeting (parts of) the OmpC sequence on the genome of *E. coli* strains. MG1655 expresses OmpC on the outer membrane, while BL21 and *E. coli* B lack the signal peptide required for transport of OmpC across the plasma membrane. M presents the size marker for the length of PCR products. Numbers at the bottom described the used primers within the PCR product.

3.5.2 Independence of surface area across long axis of geometric model *E. coli* cells

The shape of *E. coli* cells within our set-up was approximated by a geometric model described by Weisstein [38]. This model is depicted in Supplementary figure **3.3** and consists out of two basic components, a cylindrical part with radius *R* and length *H* and two hemispherical caps with radius *R* located on either end of the cylinder. This model describes that a surface segment *S* with radius *R* and width *Δl* of the cylindrical and spherical part of the cell can both be approximated by equation 3.1.

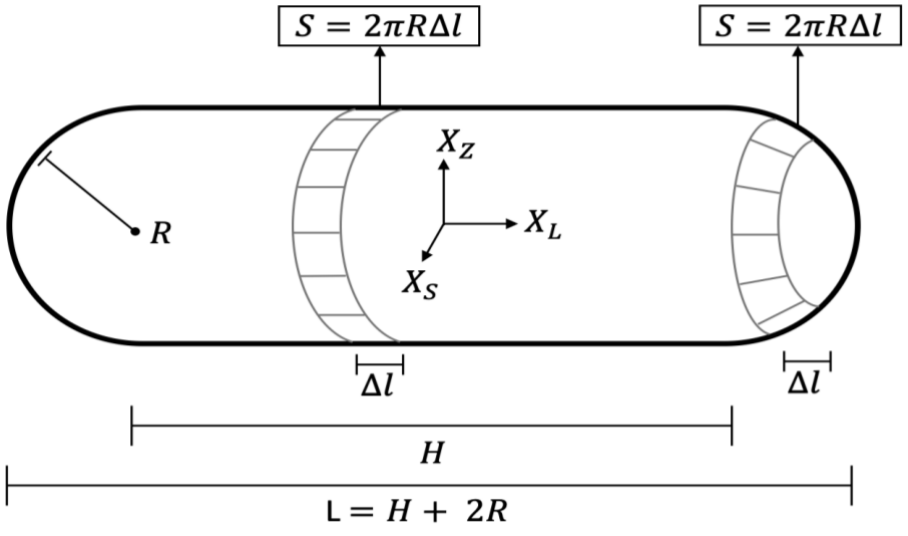

Supplementary figure 3.3: The geometric shape of *E. coli* cells were approximated by a model. This model was described by Weisstein [38] and consists of two basic components, a cylinder with radius *R* and length *H* and a hemispherical cap with radius *R* located at either end of the cylinder. Here, the center of the bacterium was defined as the origin of the coordinate system (X_L, X_S, X_Z). Using this model, the surface *S* of a segment with width *Δl* were considered similar for the spherical and cylindrical part.

During microscopy, the obtained data was projected from 3D to a 2D image plane. Due to reduction of dimensionality information across the different focal planes, z-resolution (X_Z), was lost. It has been shown that distributions can change upon the perceived angle. For example, data points that were evenly distributed across a circle showed a uniform distribution when visualized from a front angle (Supplementary figure **3.4**a), but become non-uniformly, with more points at the edge relative to the center, when visualized from the top (Supplementary figure **3.4**b).

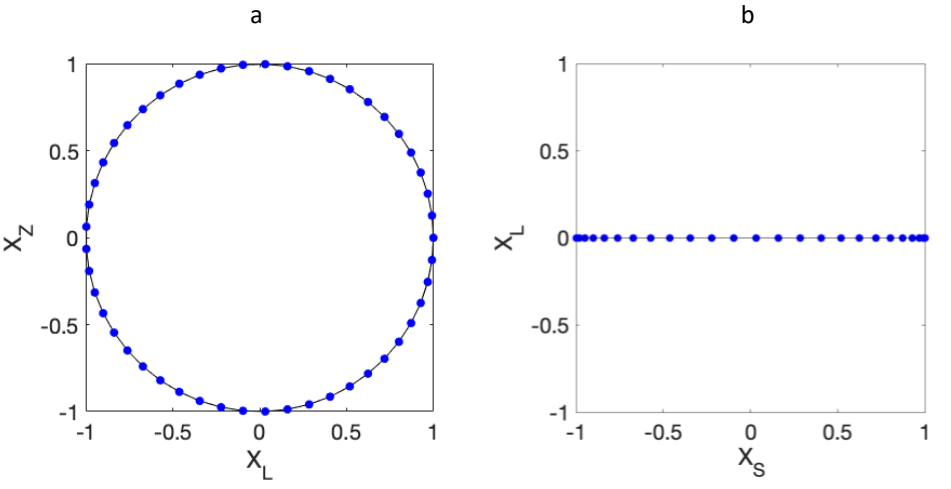

Supplementary figure 3.4: Effect of distribution of points along a circle on perceived views from different angles. Points were simulated, with evenly distributed space between them, across a circle. **a,** Front and **b**, top view of perceived distribution of points along the circle.

To test if there was an effect of reduction in dimensionality on the perceived distribution of the coordinates of the position of fluorescently labeled phages on cells, we simulated uniformly distributed random points (500) across the surface of an *E. coli* model with dimensions of ~ 3 x 1 µm [37] (Supplementary figure **3.5**). The corresponding data points were projected on a 2D plane, equivalent to the image plane. The perceived distribution across the long (X_L) and short (X_S) axis of the cells were tested against the alternative hypothesis of a non-uniform distribution. We found no effect of the reduction in dimensionality on the perceived distribution of data points across the long axis (X_L) of the cell. However, a significant effect was found for the perceived distribution across the short axis (X_S) of the cell (KS test; n = 500, p < 0.0001). These results demonstrated that only a correction was required when studying the binding distribution of T4 phages across the X_S of a cell.

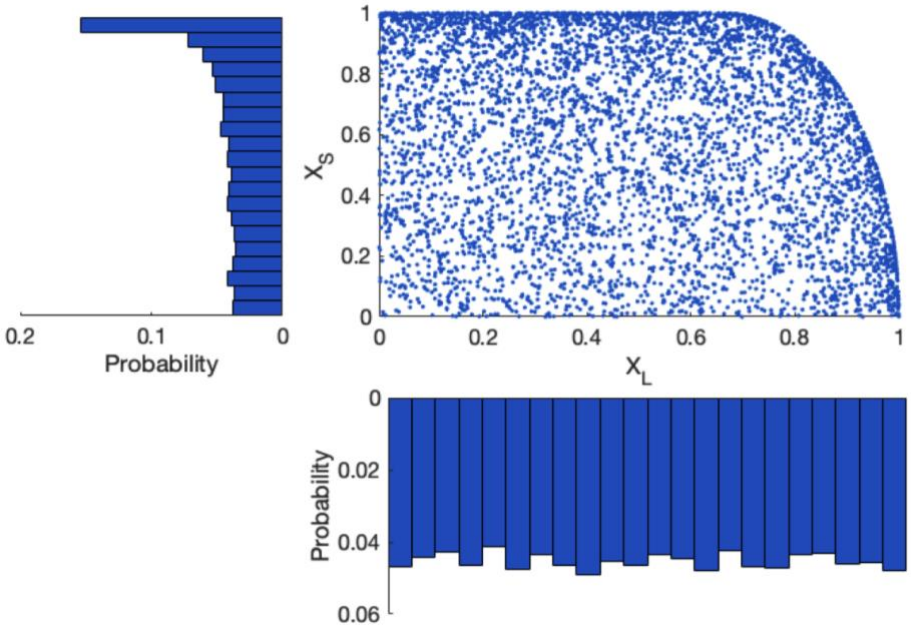

Supplementary figure 3.5: Effect of distribution of uniformly distributed random points on the surface of an *E. coli* model on perceived views from different angles. Points were simulated randomly on the surface of a modeled *E. coli* cell consisting of a cylinder with on both sides a spherical cap. Simulated points were projected on a two-dimensional plane (representing the short (X_S) and long axis (X_L) of a cell) equivalent to the image plane and subsequent coordinates were normalized to absolute values and presented in a histogram. Histograms show the corresponding distributions of normalized points along X_L and X_S.

3.5.3 Experimental variation in the binding distribution between replicate experiments

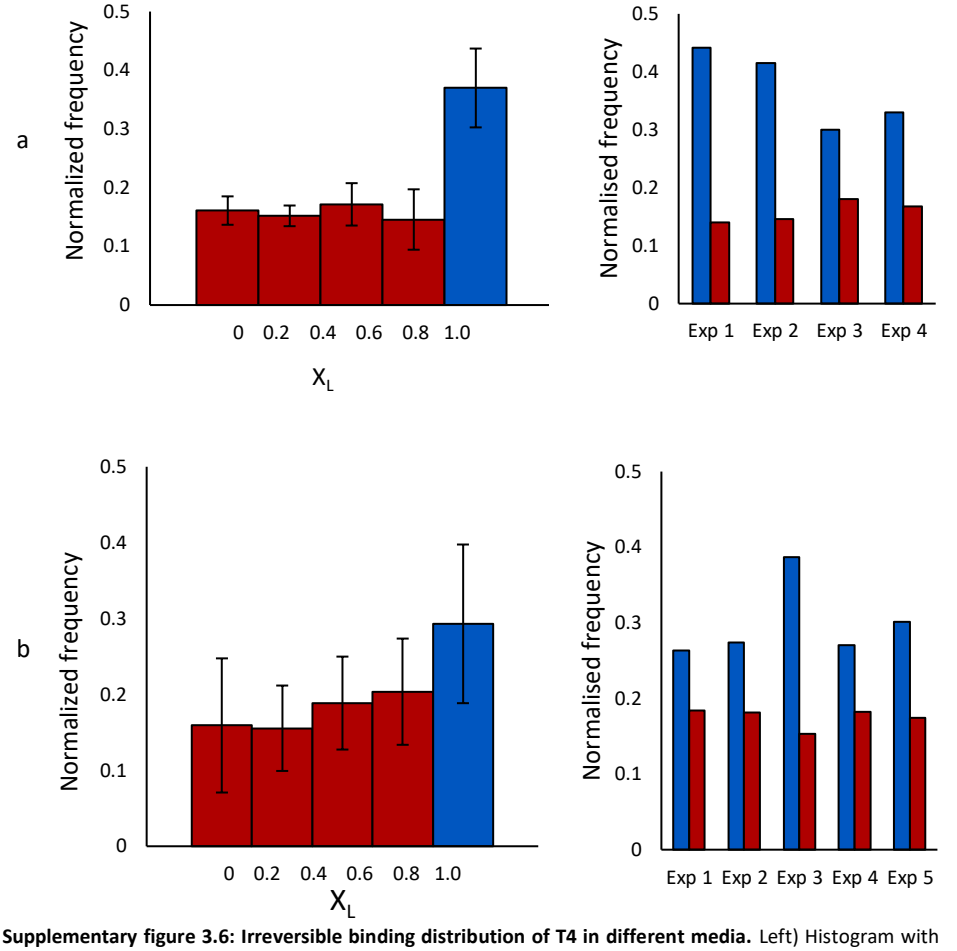

Supplementary figure 3.6: Irreversible binding distribution of T4 in different media. Left) Histogram with the mean irreversible binding distribution of T4 on *E. coli* B cells. Frequency was normalized in absolute values along the long axis of cells (X_L). Red and blue bars indicated the mid and pole region of cells, respectively. Right) Ratio irreversible binding position of phage T4 along the cell for individual experiments. Red and blue bars present the normalized ratio between binding to mid and pole region of a cell, respectively. Binding occurred either in **a,** LB medium (*N* = 580) or **b,** in M9 medium (*N* = 512). Error bars present standard deviation.

References

[1] F.L. Nobrega, M. Vlot, P.A. de Jonge, L.L. Dreesens, H.J.E. Beaumont, R. Lavigne, B.E. Dutilh, S.J.J. Brouns, Targeting mechanisms of tailed bacteriophages, Nat Rev Microbiol 16(12) (2018) 760-773.

[2] E.M. Miller, W.F. Goebel, Studies on bacteriophage; the relationship between the somatic antigens of Shigella sonnei and their susceptibilitv to bacterial viruses, J Exp Med 90(3) (1949) 255-65.

[3] M.A. Jesaitis, W.F. Goebel, The interaction between T4 phage and the specific lipocarbohydrate of Phase II Sh. sonnei, Cold Spring Harb Symp Quant Biol 18 (1953) 205-8.

[4] B. Hu, W. Margolin, I.J. Molineux, J. Liu, Structural remodeling of bacteriophage T4 and host membranes during infection initiation, Proc Natl Acad Sci U S A 112(35) (2015) E4919-28.

[5] L.D. Simon, T.F. Anderson, The infection of Escherichia coli by T2 and T4 bacteriophages as seen in the electron microscope. I. Attachment and penetration, Virology 32(2) (1967) 279-97.

[6] J.H. Wilson, R.B. Luftig, W.B. Wood, Interaction of bacteriophage T4 tail fiber components with a lipopolysaccharide fraction from Escherichia coli, J Mol Biol 51(2) (1970) 423-34.

[7] J.T. Crawford, E.B. Goldberg, The function of tail fibers in triggering baseplate expansion of bacteriophage T4, J Mol Biol 139(4) (1980) 679-90.

[8] R. Edgar, A. Rokney, M. Feeney, S. Semsey, M. Kessel, M.B. Goldberg, S. Adhya, A.B. Oppenheim, Bacteriophage infection is targeted to cellular poles, Mol Microbiol 68(5) (2008) 1107-16.

[9] L. Jakutyte, C. Baptista, C. Sao-Jose, R. Daugelavicius, R. Carballido-Lopez, P. Tavares, Bacteriophage infection in rod-shaped gram-positive bacteria: evidence for a preferential polar route for phage SPP1 entry in Bacillus subtilis, J Bacteriol 193(18) (2011) 4893-903.

[10] L. Zeng, S.O. Skinner, C. Zong, J. Sippy, M. Feiss, I. Golding, Decision making at a subcellular level determines the outcome of bacteriophage infection, Cell 141(4) (2010) 682-91.

[11] E. Rothenberg, L.A. Sepulveda, S.O. Skinner, L. Zeng, P.R. Selvin, I. Golding, Single-virus tracking reveals a spatial receptor-dependent search mechanism, Biophys J 100(12) (2011) 2875-82.

[12] A. Washizaki, T. Yonesaki, Y. Otsuka, Characterization of the interactions between Escherichia coli receptors, LPS and OmpC, and bacteriophage T4 long tail fibers, Microbiologyopen 5(6) (2016) 1003-1015.

[13] M.Z. Islam, A. Fokine, M. Mahalingam, Z. Zhang, C. Garcia-Doval, M.J. van Raaij, M.G. Rossmann, V.B. Rao, Molecular anatomy of the receptor binding module of a bacteriophage long tail fiber, PLoS Pathog 15(12) (2019) e1008193.

[14] R. Moldovan, E. Chapman-McQuiston, X.L. Wu, On kinetics of phage adsorption, Biophys J 93(1) (2007) 303-15.

[15] T.T. Puck, A. Garen, J. Cline, The mechanism of virus attachment to host cells. I. The role of ions in the primary reaction, J Exp Med 93(1) (1951) 65-88.

[16] D.H. Coombs, F. Arisaka, T4 tail structure and function, in: J.D. Karam (Ed.), Molecular Biology of Bacteriophage T4, American Society for Microbiology, Washington, D.C., 1994, pp. 259-281.
[17] F. Arisaka, J. Engel, H. Klump, Contraction and dissociation of the bacteriophage T4 tail sheath induced by heat and urea, Prog Clin Biol Res 64 (1981) 365-79.
[18] C.M. To, E. Kellenberger, A. Eisenstark, Disassembly of T-even bacteriophage into structural parts and subunits, J Mol Biol 46(3) (1969) 493-511.
[19] P. Horacek, V. Zarybnicky, J. Roubal, J. Turkova, M. Dobisova, Influence of NaCl, KCl and MgSO4 concentration on total and irreversible adsorption of T2r phage on isolated cell walls, Folia Microbiol (Praha) 15(4) (1970) 282-7.
[20] A.D. Hershey, G.M. Kalmanson, J. Bronfenbrenner, Coordinate Effects of Electrolyte and Antibody on the Infectivity of Bacteriophage, J Immunol 48(4) (1944) 221-239.
[21] D.J. Cummings, Sedimentation and Biological Properties of T-Phages of Escherichia Coli, Virology 23 (1964) 408-18.
[22] E. Kellenberger, A. Bolle, E. Boydelatour, R.H. Epstein, N.C. Franklin, N.K. Jerne, A. Reale Scafati, J. Sechaud, Functions and Properties Related to the Tail Fibers of Bacteriophage T4, Virology 26 (1965) 419-40.
[23] Z.J. Storms, E. Arsenault, D. Sauvageau, D.G. Cooper, Bacteriophage adsorption efficiency and its effect on amplification, Bioprocess Biosyst Eng 33(7) (2010) 823-31.
[24] T.F. Anderson, Cold Spring Harbor Symp. Quant. Biol. 11 (1945) 1-13.
[25] E.W. Weisstein, Surface Area. http://mthworld.wolfram.com/SurfaceArea.html.
[26] T.F. Anderson, The role of tryptophane in the adsorption of two bacterial viruses on their host, E. coli, Journal of Cellular and Comparative Physiology 25(1) (1945) 17-26.
[27] S. Brenner, S.P. Champe, G. Streisinger, L. Barnett, On the interaction of adsorption cofactors with bacteriophages T2 and T4, Virology 17 (1962) 30-9.
[28] G.S. Stent, E.L. Wollman, Studies on activation of T4 bacteriophage by cofactor. II. The mechanism of activation, Biochim Biophys Acta 6(2) (1950) 307-16.
[29] A.S. Ghosh, K.D. Young, Helical disposition of proteins and lipopolysaccharide in the outer membrane of Escherichia coli, J Bacteriol 187(6) (2005) 1913-22.
[30] K.N. Parent, M.L. Erb, G. Cardone, K. Nguyen, E.B. Gilcrease, N.B. Porcek, J. Pogliano, T.S. Baker, S.R. Casjens, OmpA and OmpC are critical host factors for bacteriophage Sf6 entry in Shigella, Mol Microbiol 92(1) (2014) 47-60.
[31] T.S. Ursell, E.H. Trepagnier, K.C. Huang, J.A. Theriot, Analysis of surface protein expression reveals the growth pattern of the gram-negative outer membrane, PLoS Comput Biol 8(9) (2012) e1002680.
[32] H. Wang, N.S. Wingreen, R. Mukhopadhyay, Self-organized periodicity of protein clusters in growing bacteria, Phys Rev Lett 101(21) (2008) 218101.
[33] P. Rassam, N.A. Copeland, O. Birkholz, C. Toth, M. Chavent, A.L. Duncan, S.J. Cross, N.G. Housden, R. Kaminska, U. Seger, D.M. Quinn, T.J. Garrod, M.S. Sansom, J. Piehler, C.G. Baumann, C. Kleanthous, Supramolecular assemblies underpin turnover of outer membrane proteins in bacteria, Nature 523(7560) (2015) 333-6.
[34] B. Hu, W. Margolin, I.J. Molineux, J. Liu, The bacteriophage t7 virion undergoes extensive structural remodeling during infection, Science 339(6119) (2013) 576-9.

[35] D. Montag, S. Hashemolhosseini, U. Henning, Receptor-recognizing proteins of T-even type bacteriophages. The receptor-recognizing area of proteins 37 of phages T4 Tula and Tulb, J Mol Biol 216(2) (1990) 327-34.
[36] T. Mizuno, M.Y. Chou, M. Inouye, A comparative study on the genes for three porins of the Escherichia coli outer membrane. DNA sequence of the osmoregulated ompC gene, J Biol Chem 258(11) (1983) 6932-40.
[37] G. Reshes, S. Vanounou, I. Fishov, M. Feingold, Cell shape dynamics in Escherichia coli, Biophys J 94(1) (2008) 251-64.
[38] E.W. Weisstein, Zone. https://mathworld.wolfram.com/Zone.html.

4

Long-range discrete on/near-cell motion of labeled bacteriophage T4

Lisa L. Dreesens, Wouter Liefting, Marie-Eve Aubin-Tam, Hubertus J. E. Beaumont

Bacteriophages must infect suitable bacterial host to reproduce and survive. The events between the first contact of a phage with a bacterial cell and commitment to irreversible binding and infection are critical to the ability of phages to discriminate between hosts. The vast majority of the mechanistic insight into this process comes from measurements in bulk and static EM images, none of which shed direct light on the nanoscopic on-cell dynamics of phages. However, the static EM images did indicate that phages might be capable of performing a tethered-walk on the surface, allowing the phage to explore the cell surface before commitment to irreversible binding and infection. The only single-particle level study performed thus far showed on-cell interactions with spatial focusing features, indicating a phage-host receptor specific mechanism by which phages move over the cell to reach its final destination the cellular pole. This strengthens the idea that phages perform a tethered-walk on the cell surface. However, the temporal resolution in this study was too low to investigate the characteristics of the on-cell dynamics in more detail. Here we investigate the dynamical interactions between fluorescently labeled T4 phage and its host *Escherichia coli* B via trajectories extracted from images with high spatial and temporal resolution obtained with single-particle fluorescent microscopy in HILO mode. Our results provide the first concrete evidence that other phages, i.e. T4 phage, show long-range motion on/near the cell surface and that this occurred in a discrete step-wise manner trough repeated shifts in mean tethering point positions via tethered-walking and/or hopping. This provides a proof-of-concept that this method is capable of analyzing these characteristics (i.e. step sizes, step durations and stepping dwell times) of the observed discrete long-range on/near-cell motion. However, our current analysis of the data cannot yet conclusively distinguish between hopping and tethered walking or accurate step-size distributions due to analysis of data in only one dimension. Together, these findings demonstrate that this method allows direct study of the phage-cell interactions that govern host discrimination at nanoscale resolution and provide the first direct evidence of step-wise on/near-cell walking.

4.1 Introduction

Phages are viruses that infect and kill bacteria to produce and release progeny. The 'decision' of infecting a cell relies on the specific interactions between long tail fibers (LTFs) and host receptors, allowing phages to discriminate between hosts. Elucidating the nanoscopic dynamics between initial contact of phage and the critical moment of commitment to irreversible binding and infection of the host are still poorly understood. Resolving this is essential to grasp how these molecular nanomachines work and can enable engineering them for applications such as altering the host range of phages in order to combat antibiotic resistant bacteria.

The factors that govern LTF binding and commitment to infection have been well studied for myoviridae phage T4. Islam *et al.* studied T4 phages and developed extensive genetic and biochemical analyses, binding assays, as well as, a near atomic structural model of T4 phage which together revealed the presence of multiple binding sites at the distal pole of the LTF [1]. This allows T4 to bind to two structurally different host receptors, namely outer membrane protein C (OmpC) and lipopolysaccharide (LPS) [1], facilitating efficient infection of *E. coli* strains B and K-12 [2] with high specificity. The majority of the work by Washizaki *et al.* examined interactions between T4 and two *E. coli* strains, K-12 and *B,* strains that differ in terms of LPS structure and presence of OmpC [2]. Strain B lacks OmpC and T4 binding on this strain is facilitated by LPS. Contrastingly, binding to strain K-12 cannot occur through LPS alone [2]. This is a result of a branched LPS structure that prevents binding of the LTFs to the designated sugar moieties, most likely due to steric hindrance, making the binding to K-12 OmpC dependent [2].

Most of what is known about the binding kinetics and on-cell behavior of phage T4 stems from bulk kinetics experiments that show that the adsorption of phage T4 occurs highly efficiently. In the presence of high host cell concentrations, the free phage fraction rapidly decays over time at a rate that reaches the theoretical limit determined by diffusion models [3]. This has led to the idea that each encounter with a host leads essentially to irreversible binding [4, 5].

The main configurational states of T4 that occur during the binding process have been studied by cryo-electron tomography (cryo-EM). The images revealed valuable insight into the different intermediate states and corresponding structural changes during the target-finding and infection process of tailed phages. The work by Hu *et al*. uncovered that LTFs are in a dynamic equilibrium oscillating up and down between retracted and extended states, allowing interaction with the cell at any given time [6, 7]. Even though, binding of a single LTF was found to be the minimal requirement to promote baseplate reconfiguration and initialization of tail contraction in phage T4, it requires binding of multiple LTFs to properly orient the baseplate perpendicular to the surface [6-8]. On average, binding of three LTFs were found enough to destabilize the baseplate of phage T4 resulting in conformational changes, releasing the short tail fibers (STFs) [6]. Binding of at least one STF brought the phage closer to the surface and was proposed to prohibit any further movement of the phage, triggering the next conformational change within the baseplate [6]. This second cue leads to sheath contraction, allowing the inner tube to puncture the cell envelope. Once penetrated, the last trigger for DNA ejection is initiated.

Even though these studies provided detailed information on the nature of phage-host interaction and revealed which conformational changes facilitate this process, the dynamic interactions that govern the critical events between first-contact and irreversible commitment to infection still remain largely unresolved. This requires a dynamical understanding of the mechanisms of the target-finding and 'decision making' processes that phages execute on and/or near the cell surface.

More recent studies by Storms *et al.* [9-11] and Moldovan *et al.* [12] suggested, based on results from bulk kinetic experiments and a model that made use of first-order rate equations, that the binding process can be explained by a two-stages process, reversible and irreversible binding. Here the initial state is dictated by reversible binding behavior, where the phage is bound to the cell via non-specific interaction or attachment of least one LTF to a host receptor that can, through unbinding of LTFs, detach and return back to solution. This in contrast with the second stage, which follows upon the initial stage of reversible binding to the host. Here multiple LTFs and/or STFs are bound to host receptors, triggering the required conformational change for cell envelope penetration, resulting in an irreversible transition. This latter step was found to occur predominantly at the cellular poles [13-16], including T4 phage infecting *E. coli* strain B (Chapter 3) and K-12 [13]. Interestingly, it was found that the initial point of contact (i.e. reversible binding state) occurred randomly at the cell body [14, 16]. This raises the question of how phages explore the cell and find the target location that facilitates irreversible binding.

Two possible scenarios by which the phage could move locations are: i) repeated binding through random collisions with the cell and unbinding (i.e., hopping), where detachment takes place if such favorable binding location was not reached, or ii) continually tethered on-cell motion. The latter mechanism of host exploration is consistent with EM images that reveal phages bound to the cell-surface with variable numbers of TFs [6, 7]. Based on this, cell exploration has been hypothesized to occur via TF-mediated random tethered-walks over the cell surface. Here, continuous binding and unbinding of individual LTFs to nearby receptors result in the repositioning of the phage and could theoretically facilitate movement of the phage at the bacterial surface. Such tethered walks have been shown to work for molecular spiders theoretically [17] and for DNAzyme spiders experimentally [18-20]. This would require a strong binding interaction between the TF and receptor to keep the phage docked at the cell surface, but weak enough to not constrain its movement. Secondly, it demands the receptor concentration to be high enough to facilitate such "walk". Lastly, the tail-fibers need to be highly dynamic and capable to act as a pivot to allow the phage to easily bind to nearby receptors. These criteria are met for the T4-*E. coli* B model system [1, 7, 16, 21, 22]. However, direct evidence of either these on/near-cell dynamics at the single particle level that reveal discrete step-like motion of a phage particle on or near the cell surface are still missing.

So far, the nanoscopic target-finding and 'decision-making' dynamics of phages remain largely unexplored. At present, the only study that examined single phage particle dynamics in real-time is work by Rothenberg *et al.*, which tracked interactions between

single λ phages and their host over time using fluorescence microscopy [16]. They confirmed that reversible binding occurred randomly on the cell surface, while irreversible binding took place predominantly at the cellular poles. Interestingly they observed an apparent mode of on/near-cell motion after first-contact with the cell, during which the phage stayed either on or very close to the cell surface. Once at the cell surface, λ appeared to perform a random walk that ended in specific LamB receptor-rich regions on the cell surface. This involved a unique spatial focusing process that was found to be receptor-concentration driven. The highest receptor concentration was found at the cellular poles and most likely explained the on-cell motion observed for phage λ. These dynamic data provide the first insight into the way in which phages localize from a random position towards the final destination at the cellular poles. However, their evidence is based on the presence of a lower diffusion coefficient when on/near the cell surface but lacks direct observation of series of discreate tethering points with the cell surface. Currently this is the deepest understanding at nanoscopic level behind the dynamical behavior of the target search process and commitment to infection.

In spite of the insights generated by Rothenberg *et al*. [16] and in addition to the lack of direct evidence of discrete tethered steps or hops, there are still many open questions regarding the on/near-cell dynamics of phages and how these bring about accurate host-cell discrimination and efficient initiation of infection. For example, how universal is this behavior among phages? Do phages explore the cell by repeatedly binding and unbinding (bouncing/hopping) the cell, do they perform a tethered walk or does a combination of these two occur? How much of the phage motion can be attributed to cell motion or other artefacts? What are the kinetics of these critical interactions? How long do phages investigate a potential host cell before making a decision to irreversibly bind or move on? Do they ever detach after irreversible binding?

In this chapter, we shed new light on these questions using the method described in chapter 2. We address the question whether this method is sufficient to track the initial interaction dynamics between T4 phage and host. Further, whether T4 phage shows similar long-range on-cell motion and if this motion occurs in a continuous or discrete fashion. If T4 shows long-range on-cell motion, what is the range of dwell times and step sizes. We used the optimized single-particle tracking method (described in chapter 2) to characterize different motion regimes of phage T4 corresponding to the different stages of the adsorption/commitment process. Further, the rate of dynamics combined with a higher temporal resolution has been used to investigate the detailed structures observed during on-cell motion. We made use of real-time tracking using fluorescent microscopy in HILO mode to obtain trajectories of individual fluorescently labeled T4 phages on metabolic active *E. coli* B host cells with high spatial (nanometer) and temporal (millisecond) resolution to gain knowledge on the reversible binding dynamics. Together, these results demonstrate that this method has a spatial and temporal resolution that is sufficient to track T4 phage-host dynamics at the single particle level and can reveal discrete on/near-cell motion of phage T4 at nanoscale level, paving the way toward a more detailed understanding of the critical on-cell dynamics that govern host discrimination.

4.2 Results

To study the dynamic interactions between single T4 phages and their host cells that give rise to cell-type specific commitment (irreversible binding) and sheath contraction, we applied the experimental methods and data analysis workflow described in Chapter 2. Briefly, fluorescently labeled phages were added to a flow cell containing immobilized *E. coli* B cells grown to the exponential growth phase. The position of labeled phages was tracked by means of video fluorescence microscopy in HILO mode combined with particle tracking analysis of the obtained movies using the TrackMate algorithm in Fiji and trajectory analysis with the MATLAB @msdanalyzer package [23]. Trajectories were further analyzed using the step finding algorithm Stepfinder [24, 25]. Together, this pipeline provided quantitative insight into the off- and on-cell dynamics of phage T4. In particular, this chapter describes results on the differently observed motion regimes corresponding to different stages of the target search process and detailed characterization of on-cell interactions shedding light on the mechanism behind host exploration and decision making process.

4.2.1 Classification of phage trajectories

After obtaining trajectories from movies using TrackMate and applying the selection procedure to remove inaccurate trajectories as described in Chapter 2 section 2.6.4.1, we were left with 673 phage trajectories that showed different characteristics with respect to interaction with the cell. Approximately half of the phage trajectories showed no interaction with a cell, while the other half did interact for at least a fraction of the trajectory.

To study the interaction dynamics between phage and cell we needed to separate the interacting from non-interacting trajectories. Qualitatively we noticed that the frame-to-frame displacement (FTF displacement) values of a phage particle between two consecutive time points were smaller when the trajectory overlapped with a cell (Figure ***4.1***), i.e. the time the phage co-localized with the binary object after conversion of the phase contrast image and defining cells as binary objects.

Small FTF displacement values are expected for phage particles that become constrained in their motion due to interactions with a cell. Larger FTF displacement values are expected for phages diffusing freely in solution (no cell-interaction), where diffusion is governed only by the temperature, the viscosity of the fluid, and the hydrodynamic radius of the particle. To assess whether the mean FTF displacement of a trajectory could serve as a measure suitable to distinguish trajectories that interacted with a cell from those that remained in the bulk liquid, we calculated the mean FTF displacement of each trajectory and assessed whether the resulting distribution showed the presence of two peaks reflecting the two groups (i.e. *interacting* and *free* trajectories). The resulting histogram indeed showed two distinct peaks (Figure ***4.2***), one at low and another at high mean FTF displacement values (0.15 and 0.37 µm, respectively), indicating slow and fast displacement regimes. The peak at the higher mean FTF displacement value appeared to follow a Gaussian distribution. In order to obtain a FTF-displacement value threshold from the data that could be used to classify trajectories into *interacting* and *free* categories, we fitted a Gaussian to the high-FTF

displacement peak and placed a threshold before the start of the first bin located within this fit at the lower left tail (208 nm).

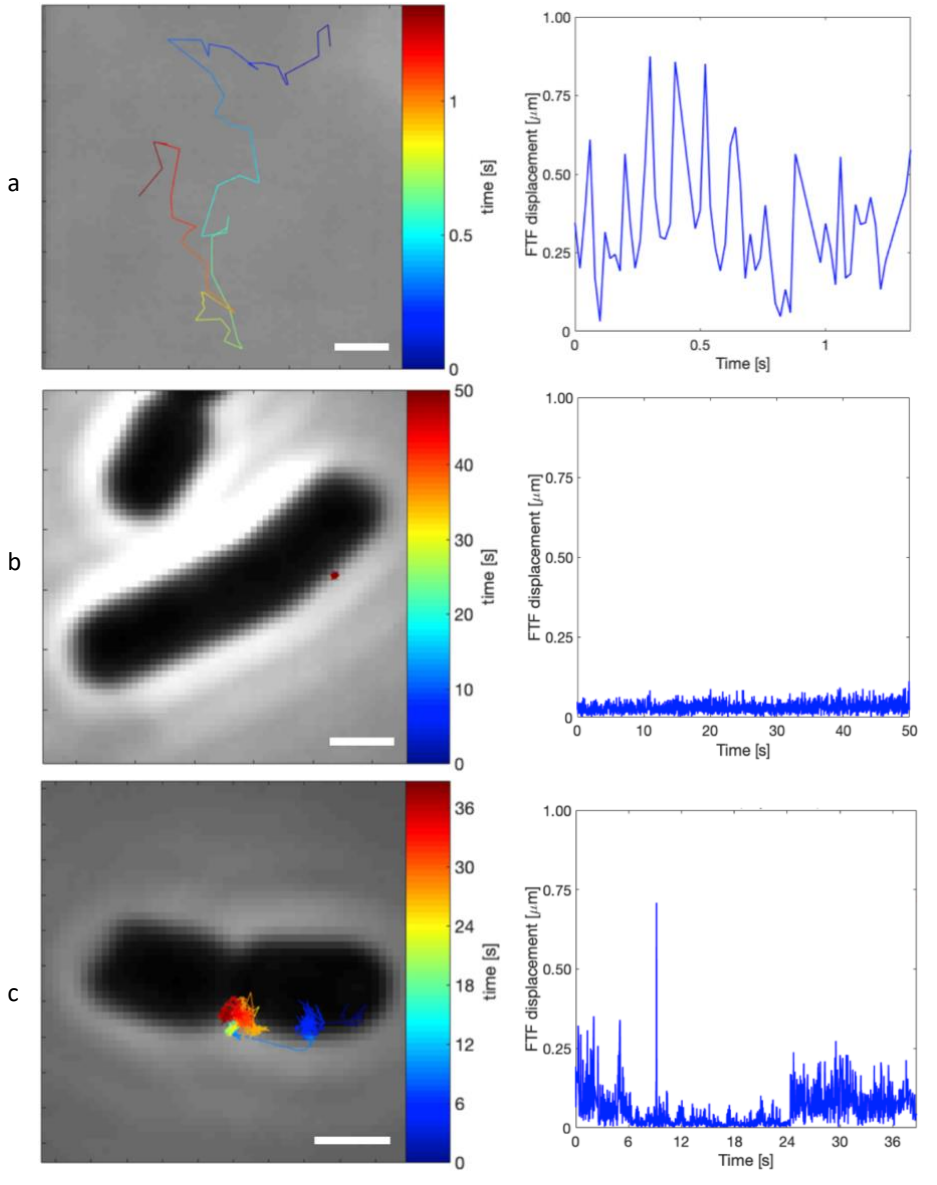

Figure 4.1 Single-phage trajectories in flow cells containing fixed cells. Examples of different types of trajectories with respect to interaction with a cell. Left windows: overview of the trajectory with color indicating time and a phase-contrast image. Right windows: frame-to-frame displacement between consecutive frames at increasing time points in the corresponding trajectories. **a,** Phage free in solution. **b,** Apparent irreversibly bound (and potentially contracted) phage to a cell. **c,** Apparent reversibly bound phage interacting with a host cell. Scale bar represents 1 µm.

Manual examination of trajectories from each of the two peaks revealed that the left peak, was predominantly (fraction of 0.25 of the trajectories) associated with particles that co-localized with cells at one or more points in the trajectory. Trajectories in the right peak predominantly (fraction of 0.75 of the trajectories) contained particles that did not overlap with the cell at any point in time. This classification was relatively accurate as only approximately 1% of the obtained trajectories were deemed misclassified upon visual inspection. These classification artefacts usually involved phage particles that were found to spend the majority of the time free in solution but did interact with a cell near the end of a movie, or phage particles that showed cell interaction within the first few frames of a movie before detachment and spending the remaining major fraction of time free in solution. Given that these trajectories had a mean FTF displacement beyond that of the set threshold for classifying *interacting* trajectories, but did show interaction with a cell, we manually assigned these trajectories to the *interacting* category. Based on these observations, we conclude that the two peaks in the FTF-displacement histogram represent *free* and *interacting* phage particles (*i.e.* off- and on-cell dynamics). The so obtained classification of trajectories enables more specific analyses of the behavior of free phages and of phages interacting with the cell, allowing us to, for example, study dwell time, interaction area, regime of motion, information that in turn allows us to explore the mechanism behind phage-host dynamics in detail.

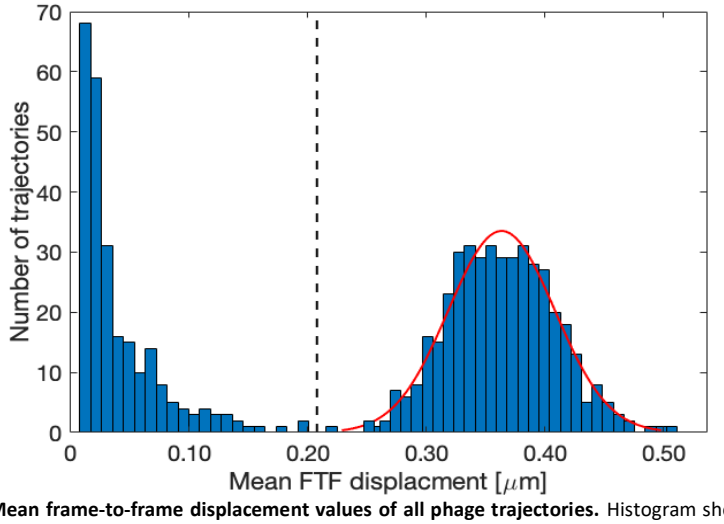

Figure 4.2 Mean frame-to-frame displacement values of all phage trajectories. Histogram showing mean FTF displacement values for each individual trajectory. Red line indicates a fit of a Gaussian function. Black dashed line presents the set threshold that we defined to separate interacting from non-interacting trajectories.

Interestingly, we noticed that the group of *interacting* phage particles comprised a diverse range of trajectories that seemed to differ in terms of their net displacement (i.e. Euclidean distance travelled during the trajectory time-window relative to a fixed point) and contour length of the trajectory (Figure ***4.1***b and c). In addition, qualitative inspection of on-cell interactions already indicated that *interacting* trajectories

included both reversibly bound, as well as, irreversibly bound phages (Figure ***4.1***b and c). However, the low peak in the FTF distribution did not contain obvious sub-peaks corresponding to reversibly- and irreversibly bound phages. To further examine if the low FTF displacement trajectories comprised distinct subgroups we used an alternative metric that is discussed below.

If we assume that phages that are irreversibly bound to a cell (i.e contracted) are constrained in their motion due to multiple long and/or short tail fibers that are interacting with their receptors and/or insertion of the tube in the cell envelope, then we would expect their maximal displacement values to be low compared to those of phages that are reversibly bound to the cell. The logic behind this is because reversibly bound phages are not interacting with their STF or contracted and only bound with one or multiple LTFs. The latter situation would, at least occasionally, be capable of FTF displacements larger than those of irreversibly bound phages, which can only move around their fixed anchoring point. Following this logic, reversibly bound phages would have larger maximal FTF displacement values than irreversibly bound phages. To examine whether such a difference in maximal FTF displacement existed among the low FTF displacement trajectories, we examined the distribution of the maximal FTF displacement over all trajectories in the category *interacting*. The resulting distribution seemed to be consistent with the presence of two underlying distributions: one sharp peak at very low values and a unimodal distribution comprising a broad range with slightly higher displacement values. Based on visual assessment of trajectories and the maximal FTF distribution values, we placed an arbitrary threshold just after the first sharp peak in the distribution at 144 nm (Figure ***4.3***).

Next, we manually examined the trajectories from each of the two resulting groups of trajectories. This qualitatively revealed that, the left peak (0.46 of trajectories) contained predominantly particles that were bound to the cell and remained positioned within a confined circular area with a relatively small diameter (Figure ***4.1***b). We referred to this subcategory of *interacting* trajectories as *irreversibly-bound* trajectories. In contrast, the right peak (Figure ***4.3***) comprised mostly particles of which a segment of the trajectory was free in solution or particles that displayed long periods of on-cell displacement over a relatively large distance (compared to *irreversible-bound* phages). The area covered by the latter group of particles exceeded the radii observed for the previously mentioned *irreversibly-bound* trajectories (Figure ***4.1***c). We will refer to this subcategory of *interacting trajectories* as *free/bound.* Note that, as there was considerable overlap between the two so defined subclasses of *interacting* phage trajectories, the used threshold resulted in some misclassification. To improve this for further analysis, we manually assessed, based on qualitatively assessing the trajectory path, the phages assigned to the group *irreversibly-bound*. We assessed whether these trajectory paths co-localized with the cell during the entire movie and/or if they changed apparent position in time (shift of mean position in time, no circular pattern). For example, this could occur when imaging of the trajectory started almost directly after attachment or stopped directly after detachment with the cell (≥ 1 frame in which the phage was free in diffusion). Other examples that could lead to misclassification were among others caused by very slow movement of position in time or a short

distance shift in position to for example a neighboring cell showed comparable max FTF displacement values as was observed for phages classified as *irreversibly-bound*. Most of these misclassifications, approximately 0.01 of tracks, occurred around the set threshold value. For each of the given classes we fitted a Gaussian distribution to the data based on the mean and with of each distribution (Figure ***4.3***). This fits showed that the chosen set-threshold was nicely defined at the intersection of the two distributions.

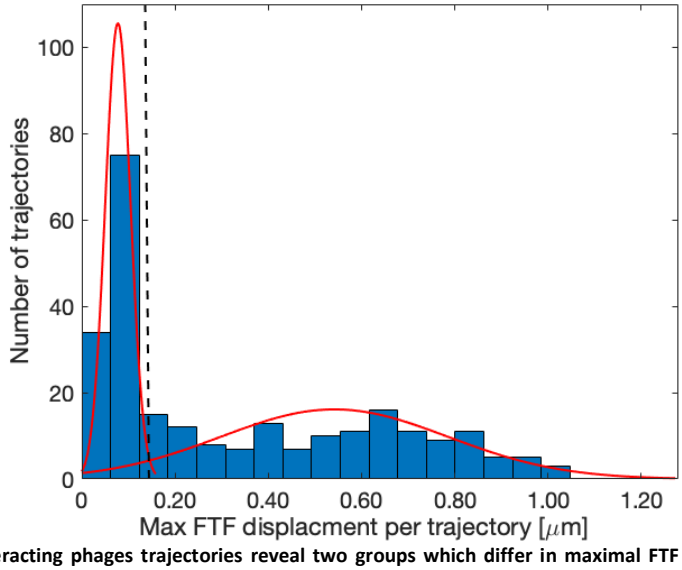

Figure 4.3 Interacting phages trajectories reveal two groups which differ in maximal FTF displacement values. Histogram showing max. FTF displacement values for each individual trajectory within the group 'interacting' trajectories. Red lines present fits of Gaussian distribution. Black dashed line presents the set threshold that was used to separate the *irreversibly-bound* trajectories from *interacting* trajectories *free/bound.*

Within the subcategory of *free/bound* trajectories, we observed phages that collided with the cell and remained attached within a confined area around the point of first-contact during the remainder of the movie (Figure ***4.4***a). It is likely that these phage trajectories represent phages that transition from free diffusion in bulk liquid to irreversibly bound almost directly after first contact. We also observed the opposite for a few trajectories. Here, phages were bound to a cell for a prolonged period of time and remained within the same area of relatively small diameter, qualitatively resembling movement of *irreversible-bound* phages. However, these phages displayed sudden detachment (Figure ***4.4***b). These detachments showed no prior increase in FTF displacement values, indicating that this proceeds via either the dissociation of a single/very weak bond or a fast unbinding event beyond the temporal resolution of the currently used microscope set-up. Unbinding might occur as a result of reversible interaction with the surface and/or, if a particle was irreversibly bound, might represent failed tube injection events during which the force exerted by sheath contraction causes TF-receptor interactions to be broken, possible caused by steric hindrance of the dye. We will refer to these and the previously mentioned trajectories as subclass *single binding/unbinding event.*

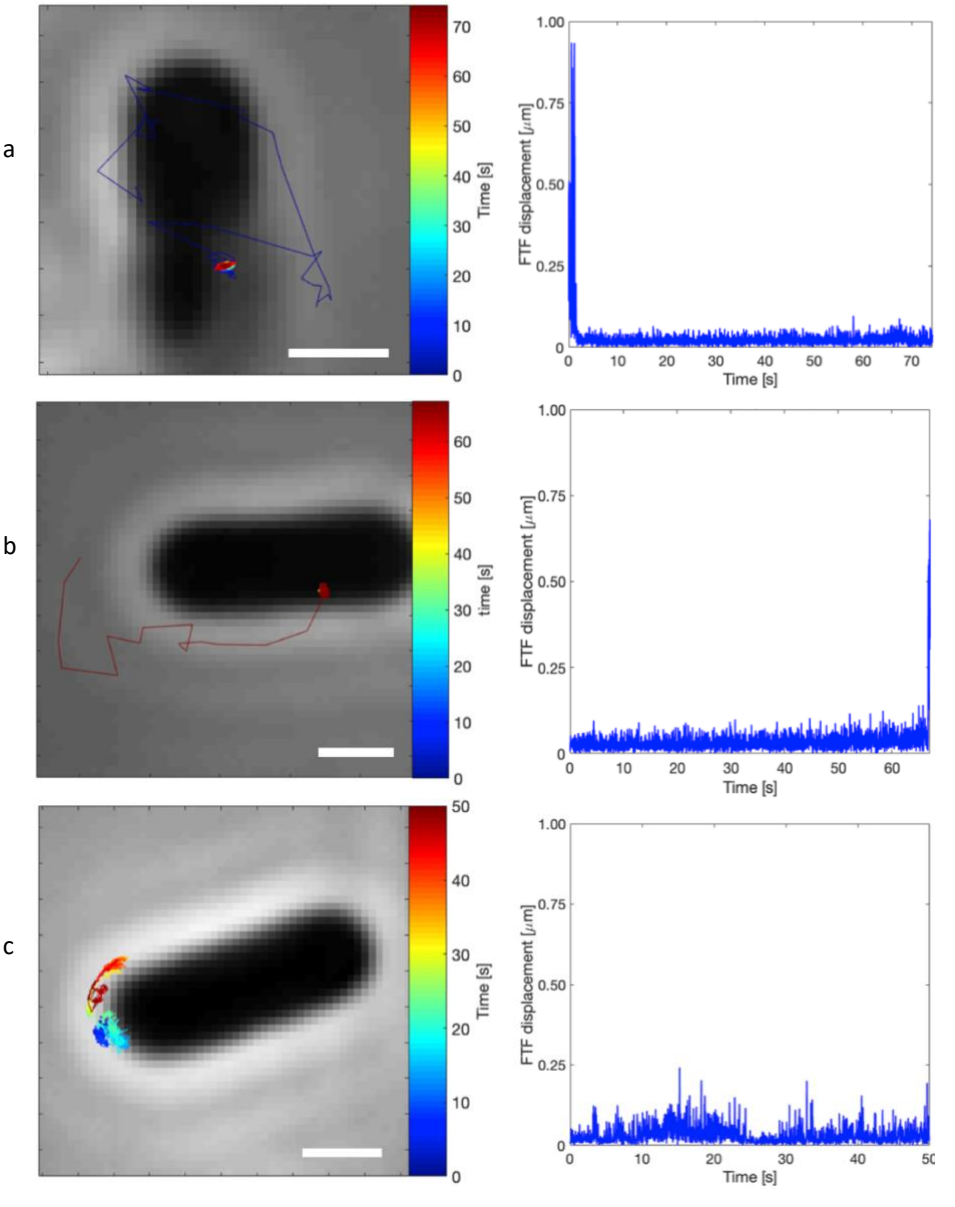
a
b
c
Time [s]
time [s]
FTF displacement [μm]
Time [s]

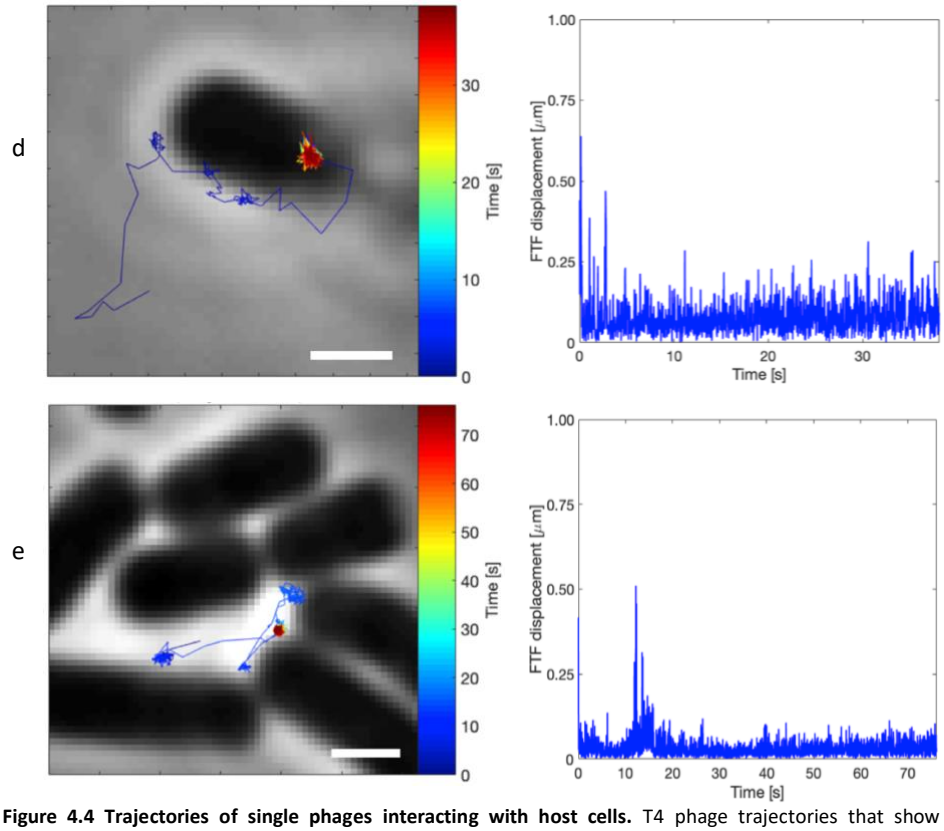

Figure 4.4 Trajectories of single phages interacting with host cells. T4 phage trajectories that show interaction with its host *E. coli* B differ in terms of their net displacement and duration of interaction. Images on the left side provides an overview of the phage trajectory and host, with color indicating time overlaid on a phage contrast image of the cell. Images on the right side shows the corresponding FTF displacement graph as a function of time. **a,** Phage trajectory that starts free in solution and upon encounter with its host interacts and binds, where it remains constrained within a confined region, indicated by the reduced and low FTF displacement. **b,** Phage trajectory showing detachment after a prolonged interaction period within a confined region of the cell, indicated by the increased FTF displacement. **c,** Phage trajectory spanning a large interaction area at the cell surface. **d,** Phage trajectory showing several rebinding events. Here the phage shortly interacts with the cell, followed by detachment and subsequent attachment within another region of the cell. **e,** Phage trajectory showing attachment and detachment events between different cells. Scale bar represents 1 μm.

In contrast to the rapid and tight binding upon first interaction observed in some *free/bound* trajectories, we also observed trajectories that showed a kind of hopping behavior consisting of (repeated) reversible binding (indicated by the reduced FTF displacement) and detachment of the particle (based on large FTF displacement). In some of these trajectories, we observed detachment from the cell into the medium followed by rapid re-binding at another location on the same cell (Figure ***4.4***d) or neighboring cell (Figure ***4.4***e), which we will refer to as *hopping*. In general, the reversible interactions in these trajectories were short in duration (between tenths of a second up to a few seconds compared to the remaining fraction of *free/bound* trajectories). Next to relatively short hopping interactions, we also observed phage trajectories that, upon collision with the cell, showed prolonged apparent near/on-cell

diffusion during which the phage covered a relatively large area of the cell surface while not displaying obvious detachment events detectable by eye in the FTF-displacement signal or co-localization in the microscopy images (Figure ***4.4***c). We will refer to this subclass as *near/on-cell diffusion.*

The size of the area that the phages with trajectories in the *free/bound* subcategory covered while interacting with the cell surface varied substantially and in the case of apparent near/on-cell diffusion sometimes exceeded the area that can be reached by a phage that is constantly attached at a single mean tethering point. That is to say, these phages covered an area that cannot be reached by phages attached with a single LTF throughout the interaction (Figure ***4.4***c). This indicated that changes in the mean tethering position must occur during the interaction in order to explain the large area in combination with the absence of detachment events. In addition, this would require the phage to traverse on or very near to the cell surface.

In summary, we defined the classification of phages based on the following structure (Supplementary figure ***4.1***): from all selected trajectories that went into the analysis pipeline, trajectories were first separated based the presence or absence of interaction with a cell defined by a threshold for mean FTF displacements. This separation gave two classes, namely phages remaining free in solution – *free* (Figure ***4.1***a), and phages interacting with a cell both in a reversible and irreversible way - *interacting*. Next, for the interacting trajectories, we made a distinction, based on the maximal FTF displacement, resulting in the separation of phages in two subclasses, those that were *irreversibly-bound* (phages that remained attached to a cell and stayed within the same location/mean tethering position for the duration of the movie; Figure ***4.1***b) and phages that were *free/bound* consisting of trajectories that showed either a type of reversible behavior (movement of the phage over the cell surface or detachment from the cell) or the presence of two types of motion behaviors in one trajectory (e.g. a phage initially free in solution followed by interaction with a cell). From those within subclass *free/bound* we observed several types of interactions which led to another layer of classification, those interacting with a cell with a *single binding/unbinding event* that during interaction with a cell remained within a fairly confined circular area not extending the reach of a phage tethered to a single LTF (Figure ***4.4***a and b), those showing repeated attachment and detachment during which the phage moved briefly free in diffusion – *hopping* (Figure ***4.4***d), and those showing *near/on-cell diffusion* where the phage apparent position moved over time of which some occurred beyond the reach of what could be explained by a phage tethered with a single LTF to a location on the cell surface (Figure ***4.4***c).

4.2.1.1 Isolation of on-cell interaction segments

A considerable number of *free/bound* trajectories appeared to contain both intervals in which the phage interacted with the cell, as well as, intervals in which the phage was undergoing free diffusion. In order to be able to considerer these two modes independently in our further analyses, we segmented interacting trajectories in intervals during which the particle interacted with the cell (i.e. on-cell segments) and intervals during which the cell was free in solution (i.e. off-cell segments). The purpose

of this segmentation was to enable specific examination of *reversible* and *irreversible* on-cell dynamics, and of the behavior of *free* trajectories. To achieve this segmentation of interacting trajectories, we made use of the fact that the FTF displacement values decreased during periods of cell interaction. Based on this fact, we set out to define a set threshold below which we could meaningfully consider a particle to no longer be free in solution. To define such a threshold, we modelled the displacement expected for a phage particle during the initial stage of attachment – a tethered phage bound with a single LTF to the surface. In this model, we made the following assumptions: the displacement of a labeled phage particle was, due to the density of the labeling across the phage, tracked by following the center point position of the capsid (Supplementary figure ***4.2***a). When such a labeled phage particle is tethered with a single LTF to the surface, its center-point could be localized in a hemispherical region above the surface with radius 300 nm (Supplementary figure ***4.2***b). This is a conservative estimate, as i) the sheath, baseplate, and TF were also tagged by fluorescent labels, and ii) we assumed the LTF were rigid and completely stretched. Lastly, the displacement of this tethered particle was random, with an inverse relationship between distance and probability:

$$P\ (x) \propto \frac{1}{x}, \qquad \text{Equation 4.1}$$

i.e. the path a particle would travel with twice the length has half the probability. The simulated displacements of the particle in the hemisphere (3D) was projected on a 2D surface to match the data acquisition of our experimental set-up. Next, we calculated the Euclidean distance between two consecutive time points to obtain 1D data position data similar to that which we experimentally obtained and used to calculate the FTF displacement values (Supplementary figure ***4.2***b). The obtained distribution of this tethered particle was compared to that obtained for phages characterized as *free*. We smoothed our data points to obtain a more conservative mean value for phages tethered to a single TF and phages free in solution, giving the fact that the FTF displacement values were reduced during cell interaction, leading to a more accurate representation of the given FTF displacements values for both groups. Smoothing of the data points was achieved by applying a sliding window of three frames. As a consequence, the high-frequency noise fluctuations within the obtained dataset for *free* phage trajectories, that were caused by the microscope set-up were reduced. The resulting distributions were used to derive a threshold with which we assessed whether the average value for multiple FTF displacements of a tethered phage at a given time point was distinct from that of *free* phages. Based on this threshold, we identified likely attachment and detachment points (i.e. defining the on-cell segment).

The distribution of the modelled FTF displacement of a tethered phage resulted in a Gaussian distribution that showed considerable overlap with the experimentally obtained distribution for phages *free* in solution (Supplementary figure ***4.2***c). This was to be expected, given the large radius in which the phage can move while still tethered to a single TF and the non-zero probability of the occurrence of multiple relatively small FTF displacements in free-phage trajectories. Consequently, this implies that any

possible threshold would result in a number of misclassified on/off-cell transitions, which should be taken into account during downstream analysis. Since we were equally interested in determining both the point of attachment and detachment, we placed the threshold at the crossing of the two Gaussian distributions at 272 nm, which is expected to give almost an equal value in terms of the ratio false positives/negatives for on- and off-cell segments. Plotting the cumulative distribution function for both distributions revealed that this threshold might miss the detection of 0.21 interacting segments, while giving a false positive 0.29 times of the cases (Supplementary figure ***4.2***d).

Misclassification, due to the set threshold and/or smoothing of data points, might lead to a lack of detection of very short moments and/or small displacement of particles that were briefly in free diffusion (i.e. segment of off-cell displacement between two sequential on-cell segments). The opposite holds true as well, for very short cell interactions (e.g. a short moment of interaction with the cell between two longer off-cell periods in which the particle was free in diffusion). In addition, very weak but continuous interactions between phage and cell might be detected as several on- and off-events (when the FTF displacement values fluctuate within a range below and beyond the set threshold – right end-tail of distribution of tethered phage). Lastly, attachments or detachments near the start or end of a movie (i.e. within the first or last frames of a movie) might be missed, as well as, detection of attachment and detachment might be a few (maximal of three frames) too early or late. However, we assumed that the number of false positives in both detected on- and off-cell events were minimal and occurred in equal numbers. Despite the fact that the threshold resembled an imperfect boundary, leading most likely to some degree of misclassification, the identified on-cell segments (*n* = 218) provided the opportunity to study for the first time the more detailed structures of phage movement at the cell surface. In spite of these limitations, classification of the so obtained threshold allowed us to identify intervals during which the dynamics of the phage particles were almost completely governed by continuous or at least very frequent interactions with the cell.

4.2.2 Mean Square displacement analysis

Next, we characterized the motion regime of the different classes of phage trajectories defined above using mean square displacement (MSD) analysis. For each individual trajectory, the MSD was calculated as a function of the delay time. This was used to examine what type of diffusion best described each trajectory, as well as, to estimate the diffusion coefficient *D* for fluorescently labeled freely diffusing T4 phage particles under our experimental conditions.

To characterize the type of diffusion for each of the categories, the exponent α was determined for each trajectory within the group by fitting the following equation to the data:

$$log(MSD) = \alpha\ log(\tau) + C, \qquad \text{Equation 4.2}$$

Alpha reflects the slope of the relationship between MSD and the delay time τ, starting at offset *C*. To prevent the large relative standard deviation of the MSD at larger delay

values from decreasing the accuracy of the estimated α value (due to large fluctuations caused by the reduced number of data points at high delay values), we used only the first 25% of the delay values for the fitting procedure, as was recommended by [26, 27]. The trajectories classified as *free* in solution exhibited a mean exponent α of 1.00 ± 0.21 (mean ± SD, *n* =421), with an average trajectory duration of 0.88 s. The fit had an R^2 of 0.961 ± 0.058 (mean ± SD), indicating that the average MSD curve was well approximated by a straight line. The values of α for individual trajectories followed a normal distribution (Supplementary figure ***4.3***) with a mean that did not deviate significantly from α = 1 (Figure ***4.5***a). This result indicated that phages *free* in solution exhibited normal (Fickian) diffusion, which is consistent with free diffusion in bulk. This was corroborated by an analysis of the velocity, in which we checked whether the observed displacements in two orthogonal direction (i.e. instantaneous velocity, as our displacements were computed over varying frame intervals) were uncorrelated. In case of Brownian motion, the displacement in the x and y direction should be symmetrical and centered at 0. Our results showed this with close approximation, with mean values of -0.17 ± 14.50 and 0.20 ± 14.37 µm/s (mean ± SD, *n* = 421) for x and y, respectively (Supplementary figure ***4.4***). This revealed that the displacement in two dimensions was indeed uncorrelated. Taken together, this analysis led us to conclude that the labeled phage particles displayed pure Brownian motion, a requirement for comparison of our single particle data to published results obtained from measurements in bulk.

We calculated the weighted mean MSD (mMSD) over multiple trajectories, where the weighting was performed according to the number of averaged data points per time-delay value in individual curves. This was used to obtain the diffusion coefficient (*D*) of free phages by fitting a straight line to the initial part, first 15%, of the log(mMSD) as a function of log(τ) (Figure ***4.5***b). Using only the initial part of the curve led to a more accurate estimation of D, as this prevented the inclusion of the relatively large standard deviation of the mMSD caused by the reduced number of data points at high delay values, and therefore decreased uncertainty at large time lags, as recommended by [26, 27]. The resulting diffusion coefficient was 2.56 $\mu m^2/s$ with a 95% confidence interval of 2.53 - 2.59 $\mu m^2/s$ (*n* = 421). To confirm that this diffusion coefficient represented single labeled T4 particles, we calculated the radius of a spherical particle that displays the same diffusion coefficient and compared this to the size of a T4 phage. This resulted in a spherical particle with a radius of 85 nm, a value that is in close agreement with the size of labeled T4 particles that we obtained by dynamic light scattering (78.7 ± 0.8 nm (Mean ± SD), Chapter 2 section 2.4.4). Even though T4 phage particles have a more ellipsoid shape, the indicative estimated size was relatively close to that for T4 phage particles observed by EM with LTF in the retracted position (dimensions of head and sheath: 115x85 and 98x22 nm), confirming the single-particle state of intact labeled T4 phages (not clustered or degraded). Taken together, these results corroborate the validity of our measurement techniques and analyses, and demonstrated that labeled T4 phages within our flow cell behaved as separate particles that undergo normal diffusion.

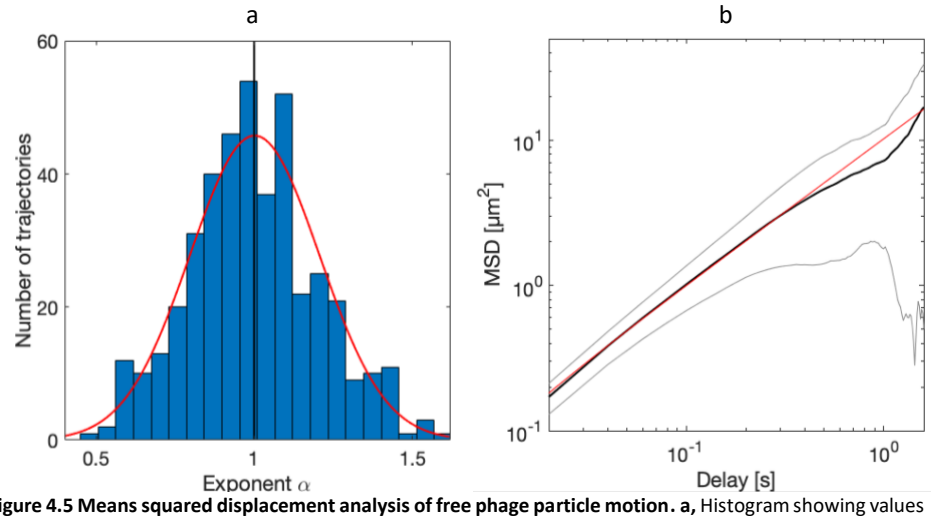

Figure 4.5 Means squared displacement analysis of free phage particle motion. a, Histogram showing values for exponent α for each individual trajectory that were obtained by a linear fit on the first 25% of the log-log MSD curve as a function of delay time. The red curve presents fit for normal distribution with sigma 1.00 and mu 0.21. The black line presents the mean value of exponent α. **b,** Diffusion coefficient estimation by means of a linear weighted fit (red line) on the first 15% of the weighted average of the MSD curve (black line). Area between the grey lines represent the weighted standard deviation over all individual MSD curves.

4

Very different values for the α exponent (fitting of exponential function to the MSD as function of τ) and offset *C* (intersection with the y-axis) were observed for phages classified as *irreversibly-bound*. Phages in this group had an α exponent of 0.14 ± 0.09 (mean ± SD, *n* = 120; Figure ***4.6***a), indicating that their motion was indeed constrained. Based on the intercept of the mMSD with the y-axis at t = 0.02 s, it can be estimated that, given the assumption these particles showed symmetric constrained diffusion, these particles remained within a position that matches to a circular area of 463 nm^2. In order to investigate if they indeed remained in a confined area, we measured the area in which *irreversibly-bound* particles were constrained by calculating the area within the convex hull for each trajectory. This showed that these particles were indeed confined and remained within a confined region of 104.14 ± 54.35 nm^2 (Mean ± SD, *n* = 120; Supplementary figure ***4.5***). This value was relatively close to previous estimated value based on the offset *C*. Even though these values differed slightly in terms of their obtained values, both results show that these particles were constrained in their motion and remained within a small confined region, corroborating our earlier conclusion that they were most likely irreversibly bound to the cell.

For on-cell segments of trajectories that we classified as *free/bound*, we obtained an average dwell time of 15.47 ± 22.19 s (Mean ± SD, *n* = 140; Figure ***4.7***a). It has to be noted that the majority of these interactions were short in duration (< 3 seconds). During these interaction intervals, the phages moved within an area of 1198 ± 1174 nm^2 (Mean ± SD, *n* = 140; Figure ***4.7***b), which was significantly larger than the dwell area found for phages classified as *irreversibly-bound* (Mann-Whitney U test; $p < 0.0001$, *n* = 322). Next, we examined the type of motion for the *free/bound* segments in a similar fashion as described earlier for phages categorized as *free* or *irreversibly-bound.* To

obtain a reliable value for exponent α, we only included interaction segments with a duration ≥ 0.5 second, an interval similar to that over which the α exponent was calculated for phage trajectories classified as *free*. This analysis yielded an α exponent of 0.40 ± 0.27 (mean ± SD, *n* =165; Figure ***4.6***a), demonstrating that the motion regime of phages that were classified as *free/bound* behaved sub-diffusive. The distribution of

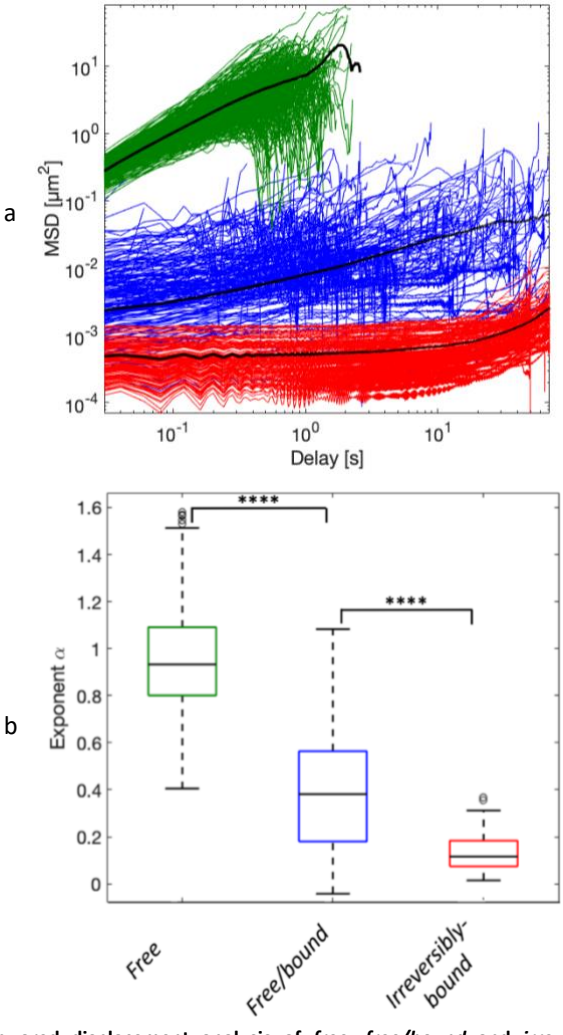

Figure 4.6 Means squared displacement analysis of *free*, *free/bound* and *irreversibly-bound* phage trajectories. a, Log-log plot of the calculated MSD as function of delay time for individual T4 phage trajectories assigned to one of three categories: *free* trajectories (green), *free/bound* trajectories (blue), and *irreversibly-bound* trajectories (red). Black lines present mean MSD of each group. **b,** Boxplot showing exponent α for each category. Values were determined by fitting a line to the first 25% of each individual phage trajectory. For the group interacting with cell, only on-cell segments with a duration of ≥ 0.5 second were included. The box and corresponding black line presents the 25th and 75th percentiles and median, respectively. Error bars indicate the most extreme data points that were within a range of 1.5 times the values of those within the interquartile range (data points within the bottom and top of box). Data points extending beyond the 1.5 times the interquartile range were marked by black circles (o).

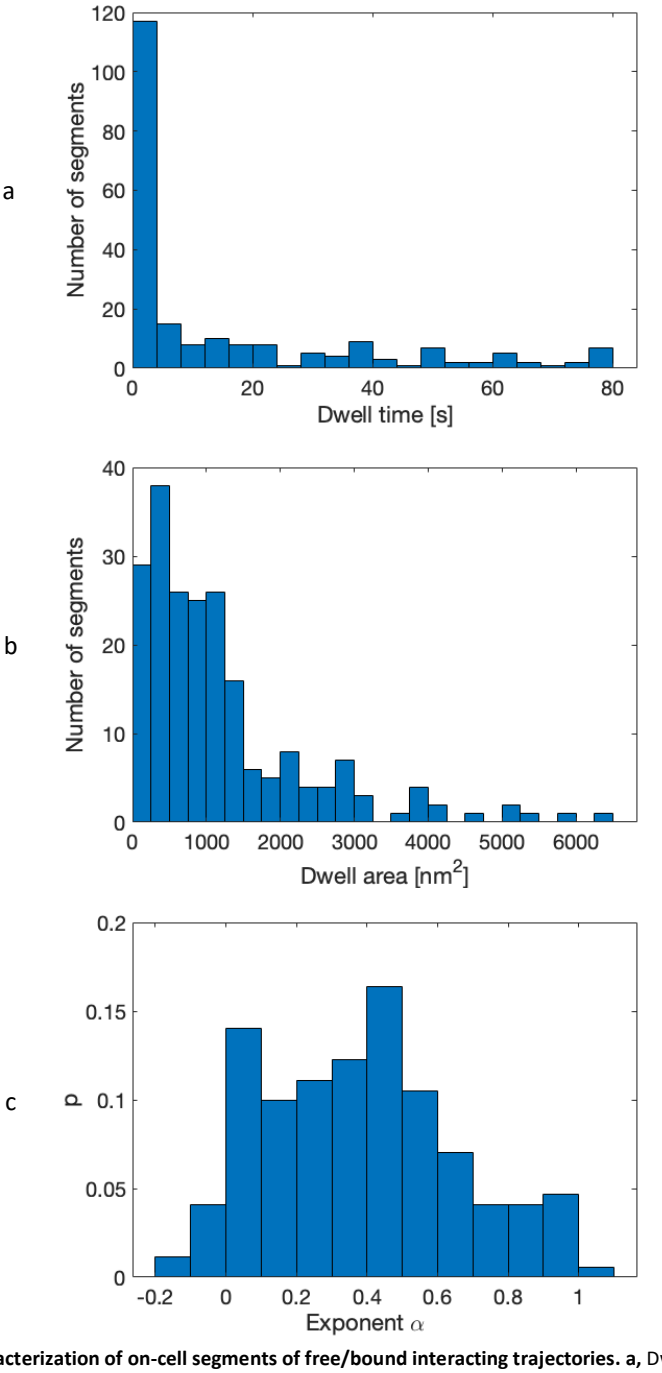

Figure 4.7 Characterization of on-cell segments of free/bound interacting trajectories. a, Dwell time and **b,** dwell area of segments that were obtained by calculating the duration and surface area within the convex hull for each segment of individual trajectories identified as *free/bound*. **c,** Histogram showing values for exponent α for each individual trajectory segment that were obtained by a linear fit on the first 25% of the log-log MSD curve as a function of delay time.

α exponents obtained for individual *free/bound* segments was found to be significantly different from those observed for *free* (Mann-Whitney U test; $p < 0.0001$, $n = 586$; Figure ***4.6***b) and *irreversibly-bound* trajectories (Mann-Whitney U test; $p < 0.0001$, $n = 271$; Figure ***4.6***b). However, the range of obtained α exponent values was very broad, reaching from low values equivalent to those found for *irreversibly-bound,* up to high values equivalent to those found for trajectories classified as *free.* We observed that the on-cell segments that were associated with lower α exponent values stemmed from trajectories that either seemed to bind directly upon impact (Figure ***4.4***a) or detached after prolonged confined interaction (Figure ***4.4***b). The remaining, larger fraction of on-cell segments had α exponent values in the midrange (0.2-0.8). These values were mainly associated with trajectories that showed 'hops' (i.e. short interaction moments with the cell separated by parts free in diffusion (Figure ***4.4***d and e)) or trajectories that lacked obvious hops but covered a large area on the cell (Figure ***4.7***c).

4.2.3 Characterization of on-cell displacement

Interestingly, within a large fraction of T4 phage trajectories ($n = 93$) in the class *free/bound* we observed two apparently different types of on-cell motion: confined diffusion on a short time scale and an apparently unconstrained diffusive motion of which the effect is visible on a longer time scale (Figure ***4.8***a). The occurrence of the unconstrained motion was further substantiated by the fact that the data set contained a number of on-cell trajectories ($n = 33$) that covered an area that not only extended beyond the range of an *irreversibly-bound* phage (radius of ~10 nm), but also exceeded the theoretical area a phage can cover when tethered with a single LTF to a single point on the cell surface (radius of ~300 nm) (Figure ***4.8***a). This indicated that, during the on-cell segment of these trajectories, the phages interacted with the cell at multiple sites on the surface (i.e. the mean tethering point of the phage on the surface changed). To study the nature of these on-cell dynamics in more detail, we obtained additional data with higher temporal resolution (imaged at 200 fps). This yielded trajectories that showed on-cell interaction but did not display constrained diffusion around a single tethering point ($n = 20$) as observed for *irreversibly-bound* phages. These on-cell dynamics were similar to what was previously observed for trajectories imaged at 50 fps.

To examine whether the observed on-cell motion was caused by movement of the phage relative to the cell or due to an artefact, we tested if they could be explained by one or combination of the following alternatives: i) image drift, ii) noise caused by the microscope set-up (noise at the limit of our ability to detect the position of the cell; which is a composite of microscope vibrations, camera detector noise and noise added during downstream analysis), or iii) cell movement (i.e. clear visible displacement of the mean position of the cell for a period of time, e.g. could give rise to oscillating behavior – 'wiggling' of the cell, due to poor immobilization of the cell to the substrate). These observations together might explain the observed on-cell motion in the trajectories, where the first could result in apparently unconstrained diffusive behavior, while the latter two could result in fast-confined motion that was visible on the short-time-scale period. To assess whether one of these alternative mechanisms could explain the

observed on-cell movement, we quantitatively analyzed cells on which phage trajectory data had been collected with the cell-motion algorithm described in Chapter 2, section 2.6.4.3. Briefly, we tracked the mid-point position of four cross-sections (three on the short and one on the long axis) per cell over time, which allowed us to quantitatively analyze the amount of i) translational motion (i.e. drift), ii) subtle rotational motion (i.e. cell movement), and iii) noise (i.e. phase shifts of areas outside the focal plane giving rise to out-of-focus blur and optical phase contrast artifacts e.g. halos and shade-off contrast patterns, causing variations in the intensity gradient impairing uncertainty in the quantification of intensity and therefore position of a particle [28]). We analyzed cells of eleven representative trajectories (n = 7 at 50 fps and n = 4 at 200 fps). Phage trajectories on all of these focal trajectories exceeded the theoretical area accessible by a phage tethered to a single point on the cell surface (diameter of 600 nm), did not have a problematic number of frames in which the phage location could not be determined and, most importantly, were present at the cell surface of cells of which the outline could reliably be detected by the cell-motion algorithm (i.e. not on the edge of the field of view and preferentially not clustered or within cell division).

The cell-motion analysis showed that translational motion (microscope stage drift) occurred at rates of 2.97 $\pm$ 2.21 and 3.54 $\pm$ 2.85 nm s^{-1} (mean $\pm$ SD) in x (n = 10) and y (n = 9), respectively. We approximated the rate of the apparently unconstrained component of the on-cell motion of trajectories by measuring the maximal distance between two points on a convex hull drawn around the outer edges of the on-cell trajectory segment in one dimension (x or y) and dividing it by the duration of the on-cell segment. The so estimated rate was conservative, as the estimated distance was, due to measurements across a straight line in the longest direction of only one dimension, most likely shorter than the total distance travelled by the phage and therefore an underestimation of the actual speed. This resulted in an average speed of the apparently unconstrained on-cell motion at 30 $\pm$ 18 nm s^{-1} (mean $\pm$ SD, n = 10), which was significantly larger than thee measured rate of stage drift (Mann-Whitney U test; n = 20, p < 0.0001). The low rate of drift was corroborated by the lack of detectable lateral motion for *irreversibly-bound* phages fortuitously present within the same field of view for one of the 200 fps trajectories (Figure ***4.8***a). Based on this, we conclude that drift did not explain the observed slow on-cell motion of the phages.

The cell-motion analysis did not detect rotational and/or other types of oscillatory motion in the six cells associated with the on-cell trajectories imaged at 50 fps. For the cells on which the higher frame rate trajectories had been imaged, we did observe rotational oscillating movement. However, the maximal deviation from the mean midpoint position of these oscillations did not exceed 12 nm and the average period was 7 seconds. These values are, respectively, small and extremely slow compared to our conservative estimate of the speed of the slow component of the on-cell phage motion and therefore deemed negligible.

Lastly, we assessed the noise level of the microscope set-up and therefore lower detection limit. We found that the midpoint position of the focal cells (n = 10) that were free of large rotational and/or oscillatory motions can sporadically fluctuate from frame to frame with a mean value always remaining <13 nm. We detected a maximal frame to frame value that reached 25 nm from the average mid-point position. These noise fluctuations, or extremely rapid but confined motions, most likely are part

of the observed motion of the phage. However, the detected noise level cannot exclusively account for the observed constrained motion of phages visible at short timescale. These constrained motions might be a combination of both noise caused by the microscope set-up, noise added by the downstream analysis of tracking the phage position, and noise caused by thermal fluctuation (i.e. collision of water molecules against the phage capsid). The detected noise level for the apparent microscope set-up can be neglected for the observed large apparently unconstrained motion of phages that occurred at longer timescales.

Overall, these results show that the apparently unconstrained diffusive motion component of the on-cell trajectory cannot be explained by drift, cell motion, or measurement noise. We conclude that this component in the trajectories of phages in the reversibly bound category must therefore have originated from interaction dynamics between the phage and the host cell's surface.

4.2.4 Mechanism behind on-cell motion

Next, we consider the mechanism that underlies the long-distance motion of reversibly bound phages. We consider the following possible mechanisms and combinations thereof:

i) *Receptor diffusion*: On-cell diffusion mediated by diffusion of the receptors in the cell envelop.

ii) *Non-specific hopping/rolling*: On-surface hopping/rolling mediated by electrostatic or van der Waals forces.

iii) *LTF hopping*: On-surface hopping mediated by specific LTF-receptor interactions.

iv) *LTF walking*: On-surface walking mediated by dynamic specific binding and unbinding of LTFs to receptors and a minimum of one LTF bound at any point in time.

First, we investigated if the long-distance diffusive movement could be explained by receptor diffusion across the surface. This explanation is rejected by observations of Ghosh and Young, which revealed that the host-cell receptors (LPS) showed no movement on the timescale of minutes (imaged at 5 s/frame for a minimum of 5 minutes), which was neglectable compared to the speed with which phages displayed long-distance motion on-cells (30 ± 18 nm s^{-1} (mean $\pm$ SD, $n = 10$) [22, 29]).

Next, we investigated if non-specific phage-host interactions could explain the extent of the observed on-cell displacement. We found that these interactions between phage and host need to be specific to facilitate irreversible binding, as we observed no irreversible interaction between T4 phages and *E. coli* K-12 ΔOmpCΔLPS host cells lacking the receptor in bulk (Supplementary figure **4.6**). This indicates that the strength of any other interaction that could occur was not strong enough to facilitate irreversible binding. During on-cell displacement the phage interacts with the cell for a prolonged time, during which the interaction needs to be strong enough to keep the phage

tethered to the cell surface, hinting towards the necessity of requiring specific phage-receptor interaction for reversible binding. We examined if this was the case by tracking phage-host interactions in the absence of receptors at the level of individual labeled T4 phages and *E. coli* cells that lacked LPS and the OmpC receptors (imaged at 50 fps). This sheds light on the extent to which on-cell dynamics depend on LTF-receptor interactions. From the approximately 300 phage trajectories obtained from eleven movies, imaged under the same experimental conditions as those for phages interacting with *E. coli* B, we only observed two phage trajectories that, by eye, appeared to interact with a host for a duration that lasted no longer than 2 seconds. These numbers are extremely small compared to the phages interacting with *E. coli* B in the presence of a receptor (260 out of 636 trajectories, with a minimal interaction time of 0.5 seconds). Overall, this experiment showed that in the absence of a receptor less than 1% of phages were capable of interacting with the cell via non-specific interaction. From all isolated on-cell interaction segments, 59% had an interaction duration longer than 2 seconds. Given the chance that non-specific host interaction occurred at these given time-scales is extremely low, which led us to conclude that host receptors were not only required for irreversible interaction but also needed to explain the extended and prolonged on-cell displacement observed for reversible interaction on cells with host receptor. This was further strengthened by the fact that the phage capsid and sheath were negatively charged, while the distal end of the LTF was neutrally charged, causing repulsion between capsid and cell surface, while the TF should be able to interact more easily with the cell. In addition, the fluorescent label was negatively charged, making the phage surface even more repulsive towards the cell surface, further lessening the scope for non-specific interactions based on electrostatic interactions. Also, phages have been shown not to interact strongly with any other component of cell other than LPS [30]. Based on these considerations, we conclude that the long-distance on-cell motion cannot be explained fully by non-specific hopping/rolling and depends predominantly on specific TF-receptor interactions that provide the necessary interaction strength to keep the phage tethered at the cell surface.

This leaves LTF-mediated hopping or LTF-mediated walking as two possible predominant mechanisms that could underpin the long-range on-cell motion we observed. LTF hopping would involve movement of the phage over the cell surface by repeated attach- and detachment events to the cell. Here, the phage remains reversibly bound within a confined region for a period of time and periodically detaches while remaining in close proximity of the cell to subsequently at a nearby but different point on the surface. This in contrast with TF-mediated walking, which we define as movement of the phage on the cell while remaining in contact with the cell at all times with at least a single TF. During walking, the phage moves on the surface due to dissociation of individual TFs from their receptor and re-binding to a different nearby receptor. For such a tethered-walk to occur, both the initial and final energy barriers to dissociate from or bind irreversibly to a cell must be relatively high, while the energy barrier of the intermediate state - reversible behavior, i.e. a tethered walk, needs to be relatively low (Supplementary figure ***4.7***). The estimated dissociation constant between T4 LTF and host receptor LPS from *E. coli* strain B has shown to be strong [21], indicating

that the energy difference between a phage free in solution and a phage bound with a single LTF is high, satisfying the first required criterion. To reach irreversible binding we assume the phage requires a large transition energy, one that is high enough to entail the necessary conformational changes in the baseplate, satisfying the second criterion. The presence of high energy barriers for dissociation and sheath contraction results in an in-between phase in which the phage could potentially walk. The third requirement depends on the slope of the energy function in the intermediate region, defined by the energy difference between two different states (initial contact and irreversible binding), dictating the speed with which the final state is reached and therefore influences the traveled distance of a tethered-walk. We could imagine that the tension stored in the TF counteracts some of the steepness of the slope due to the high binding energy, resulting in a moderate slope. Together these properties could in principle facilitate walking behavior, with high stepping rates and distance traveled, as well as, a long time on the cell before either dissociation or commitment to infection.

An important similarity between the higher-order pattern of motion of both mechanisms is the possibility that they produce steps in the trajectories we captured. The reason for this is because both involve temporal changes in mean tethering position of the phage relative to the cell surface. In the case of hopping, mean tether-point shifts occur by a departure into the bulk liquid followed by rebinding at a different mean tethering-point on the cell. In the case of walking, this involves random LTF un/re-binding events that alter the mean tethering-point on the surface. Depending on the rates of these events, the resulting shifts in mean tethering-point and our ability to capture events at these temporal and spatial scales, our data might contain step-like signals that separate periods of phage-diffusion around a mean tethering-point followed by abrupt changes in this mean tethering-point.

To assess whether the observed on-cell motion data contained such detectable shifts in tethering position we quantitatively analyzed the previous selection of focal on-cell segments (n = 6 and n = 4 for trajectories imaged at 50 and 200 fps, respectively) with the step finding algorithm Stepfinder [24, 25]. Stepfinder detects changes in displacement (i.e. steps) across one dimension (i.e. movements in x and y where therefore analyzed separately) by chi-square minimization and performs a quality check on the detected steps by applying a counter fit to the remaining plateaus (described in more detail in Chapter 2 section 2.6.4.3). Results obtained by Stepfinder showed the presence of 'step-like' behavior, with an average of 100 and a minimum of 12 detected steps (i.e. shifts in tethering position), in all tested on-cell segments. Figure ***4.8*** shows an example of such analyzed trajectory, containing 132 detected steps across X_L of the cell. These steps were also found in on-cell segments of trajectories located at mid-cell surface (data not shown; Supplementary figure **4.8**), where there was no possible interference between phage and substrate that could have resulted in these observed discrete movements. Given the apparent contribution of the observed sudden hops/steps to the long-distance motion of the phages on cells — the phages appear to only be moving around a fixed tethering point in the vast majority of periods between steps/hops — it seems that discrete hopping/stepping is the most parsimonious explanations for the long-distance on-cell phage motion that was observed.

As a first step toward distinguishing between these two explanations, we asked whether the observations match the theoretical expectations for hopping or walking by assessing: i) number of consecutive steps, ii) step size distributions: the distance between two mean tethering positions, iii) dwell time distribution: the time it diffuses around a single mean tether point, and iv) step duration distribution: the time it takes to move between mean tether points. For the number of consecutive steps, we can argue that a tethered-walk can produce an infinite number of consecutive steps while the probability of large *n* hops will asymptotically reach zero. In case of step-sizes, the displacement of hopping can reach infinite sizes, while the maximal step size of a tethered-walk is set by the tip-to-tip distance between two-opposite LTFs (approximately 180 nm). Given the lack of mechanistic insight into the underlying processes, we do not define expectations for the two modes of long-distance near/on-cell motion; however, the dwell-time distribution does provide valuable insight into the phenomena observed. Lastly, a tethered-walk could produce infinite step-durations, while for a hopping phage the duration is limited by the distance of the step and the speed with which a phage displaces in free diffusion.

To identify step-like displacements in the data, we fitted discrete steps to the data in Stepfinder. This identified a substantial number of candidate steps (67, 131, 23, 12, 43, 48, 22, 35, 23, and 73; mean of steps over *x* and *y* dimension) in each of the ten focal on-cell segments that were larger than the conservative threshold of 50 nm. These results suggest that, if hopping was the main mechanism causing the long-distance on-cell motion, it involved many relatively small hops. This reduces the probability that every shift in position can be explained solely by hopping. The obtained step-sizes ranged from 2 to 525 nm (Figure ***4.9***a), with 42% of detected step-sizes having a value above the conservative threshold of 50 nm (i.e. 975 steps) and less than 1% having a value above 180 nm (i.e. 22 steps), the maximal stepping distance for a tethered-walk. This indicated that the vast majority could be explained by the tethered walk model. However, some steps were larger, indicating that hopping or rotation of a tethered phage also occurred. Here rotation was defined as a phage tethered with a single TF to the surface while the body of the phage rotates within a hemispherical cap during which the phage (i.e. center position of capsid) can travel a maximal theoretical distance of 600 nm (Supplementary figure ***4.2***). As for the detected steps, we observed dwell times that ranged from values equal to the imaging rate up to almost 10 seconds (Figure ***4.9***b), indicating a large variety of interaction times and emphasizing the strength of the specific interaction between TF and receptor, lasting far beyond the durations observed in the absence of receptor. Lastly, we considered the step-duration by analyzing the time it takes for the phage to move from one to another tethering point. Analyzing the step duration of all steps detected over two trajectories, one taken at 50 fps and another at 200 fps with 55 and 87 detected steps in one dimension respectively, showed that all shifts in tethering position had occurred at a rate equal or faster than the imaging rate (i.e. temporal resolution). A hopping phage that moves with the speed of free diffusion travels on average, depending on the frame rate (200 and 50 fps), a distance of 100 to 160 nm within a single frame, respectively, which is well within the observed range of step sizes. Taken together, these results do not allow us to exclude either of the two hypotheses.

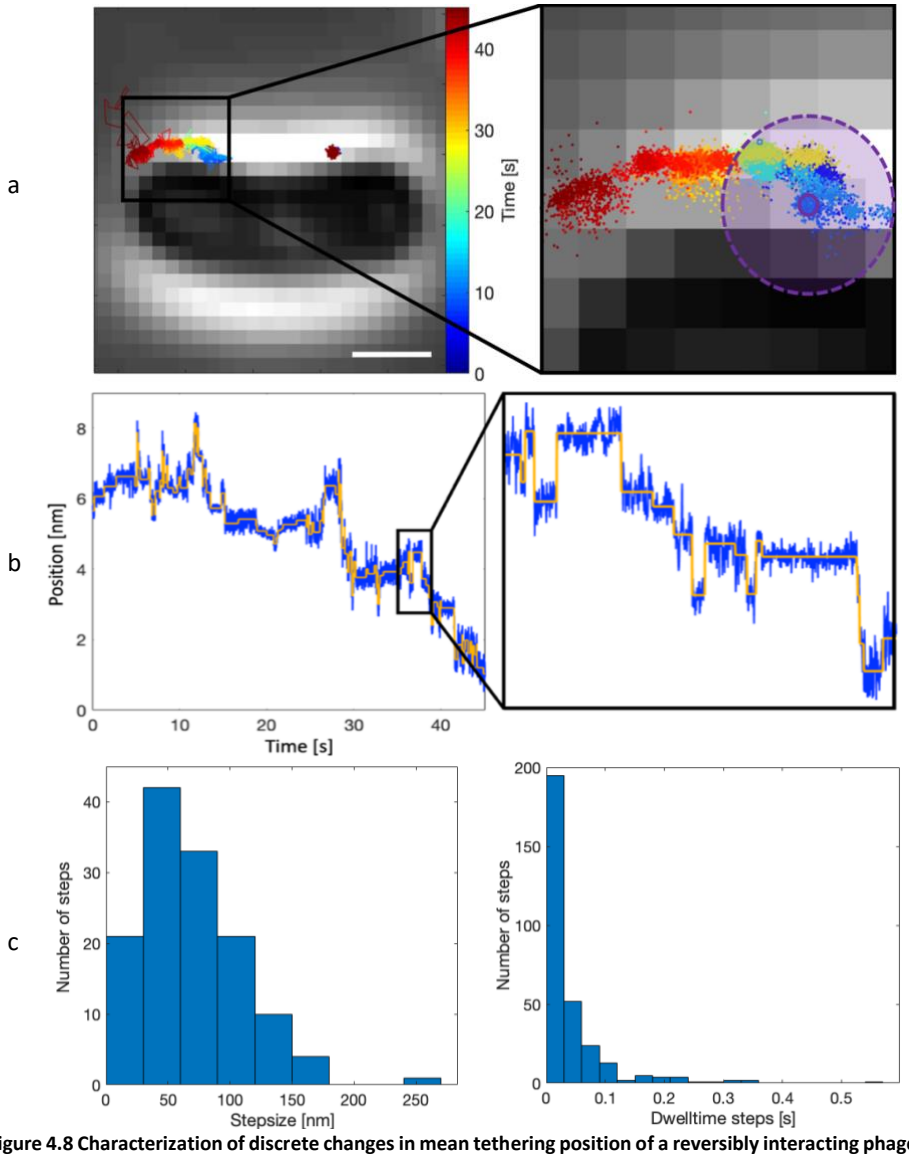

Figure 4.8 Characterization of discrete changes in mean tethering position of a reversibly interacting phage. **a,** Left window: overview trajectory, with color indicating time and phase-contrast image showing the target cell. Right window: magnification of on-cell part of trajectory. Here the small purple circle presents a reference indication of the interaction area of a phage classified as *irreversibly-bound* and the big dashed purple circle presents the maximal theoretical area in which a phage tethered to a single-LTF can move. **b,** Left window: Fit performed by Stepfinder to detect discrete changes in position, with the blue line presenting the experimentally obtained position in one-dimension (x-coordinates) as function of time (data obtained at 200 Hz) and yellow line the fit performed by Stepfinder. Right window: magnification of a small area showing the finer details of the experimentally obtained data and corresponding fit. **c,** Left window: histogram showing obtained step size values of steps that were detected by Stepfinder. Right window: histogram showing obtained dwell time values of the steps that were detected by Stepfinder. Scale bar represents 1 µm.

Owing to time constraints, we did not analyze the data beyond this point. However, additional analyses that could shed more light on the nanoscopic details of the observed on/near-cell walking/hopping are possible. One way in which this could be approached involves quantitatively estimating the likelihood of each of the two explanations using mathematical models or simulations. Below, we briefly outline how this could be done.

An initial model for the hopping explanation could be based on the work described by Lagerholm and Thompson [31]. They propose a simple model that describes the probability that a rebinding event between ligand and receptor at the same cell can occur within a given time and distance. Even though the phage-host binding is, with six independent LTF that can bind/unbind each to a receptor, more complex than that of a ligand-receptor, it can be used to obtain an initial estimate of the probability of such a re-binding event. This rebinding model is mainly shaped by the following parameters: kinetic association and dissociation rate constants, total density of the surface receptors, and diffusion coefficient. The former could be obtained from experimental data or from literature. For the number of host receptors an estimated value based on literature can be used [1, 22]. While the latter has already been experimentally obtained, and described in section 4.2.2. Together, these can be plugged in the model to assess how well they describe the experimentally obtained data by assessing how likely it is to observe *n* consecutive rebinding steps with the experimentally obtained dwell time and step size distributions.

An initial start to derive a model for tethered-walking could be based on the following assumptions: i) detected shifts in position are due to association or dissociation events between LTFs and host receptors. Here association/dissociation constant values of TF-receptor interaction can be obtained or estimated based on literature [9, 21]. ii) Each of the six LTFs acts independent. iii) The receptor concentration at the cell surface is dense enough to assume that the phage can move on-cell to any given direction. v) The binding position of the TF to the host receptor as function of the distance from the baseplate can be approximated by a quadratic energy landscape, where the energy between each LTF-receptor interaction can be modelled like a spring with a spring constant. iv) Association/dissociation of individual TFs leads to repositioning of the baseplate. Due to the labeling method, we track the movement of the capsid, consequently there is a lag time between the actual shift in position and subsequent slower movement of the phage capsid. When these assumptions are plugged in a model it produces random walks at a surface (Supplementary figure **4.9**a), that when including an amount of distortions/noise (i.e. random movements of the viral capsid), qualitatively represents the experimentally obtained trajectories (Supplementary figure **4.9**b and c). This model needs some further improvements, where insights could be gained by investigating so-called molecular spider walker models [17], but does provide a basic model against which the experimental data could be tested.

Due to time constraints, we did not take this further. However, testing the experimentally obtained distributions (number of consecutive steps, step sizes, dwell times, step durations) against those obtained by the two models would be a next step in testing how likely these underlying mechanisms explain the experimental data.

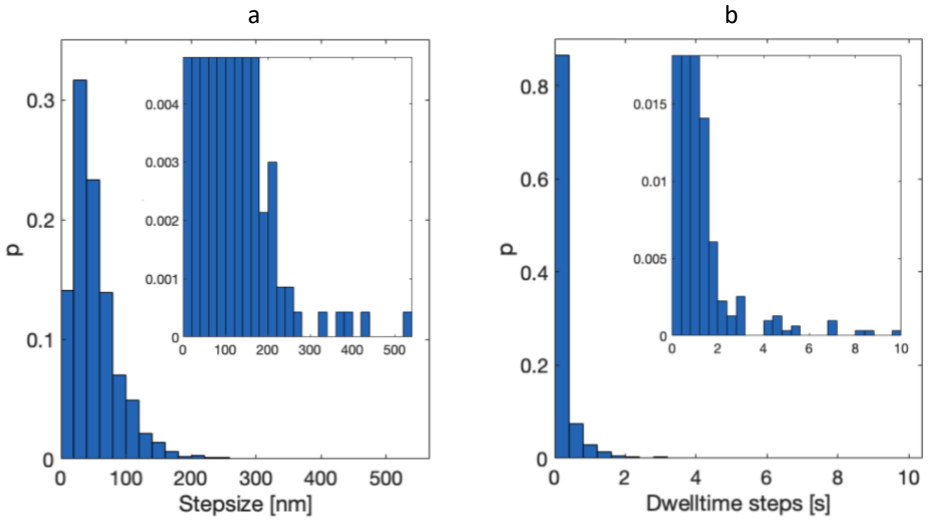

Figure 4.9 Characterization of discrete movements in on-cell position. a, Step size and **b,** dwell time values of steps detected by Stepfinder, insert shows magnification in y-axis.

4.3 Discussion and conclusion

Phages are specialized 'parasites', capable of discriminating between hosts with high specificity. How phages, which act as colloidal particles subjected to Brownian motion, localize and infect suitable host cells with near 100% efficiency remains unknown. These events between first contact between phage and cell and commitment to irreversible binding and infection are critical to the ability of phages to discriminate between hosts and reproduce efficiently. Mechanistic insight into this process is almost completely limited to measurements from bulk experiments and static images of phage particles interacting with the cell [6, 7, 9-11, 13, 14]. Static EM images indicate that LTF binding dynamics could allow phages to perform a tethered-walk on the surface before commitment to irreversible binding and infection [6, 7]. However, these images lack information on the dynamics and do not demonstrate that this occurs [6]. The sole study that looked at dynamic phage behavior on cells in real time and at single-phage level is work by Rothenberg *et al*. on phage lambda. Their data indicates that lambda moves over and/or near the cell surface of *E. coli* via receptor-rich regions towards the cellular poles where irreversible binding takes place [16]. This conclusion was based on (i) the decreased diffusion coefficient and (ii) the occurrence of spatial focussing toward receptor rich regions. However, it remained unclear whether phage lambda moved on or near the surface and in a continuous fashion — 'bouncing' on the surface — or in a discrete manner where the particle resides for a short period at a single tethering point between steps. Currently, their data has shown qualitatively no evidence of the presence of shifts in mean tether-point positions [16]. Also, they provided no insight on the size/length of surface area explored by the phage or the upper limits of steps/hop sizes and range of stepping dwell times.

With the aim of shedding some more light on these questions and to explore on-cell dynamics in a different phage, we performed experiments with labeled T4 phages and host *E. coli* B with high temporal resolution (50 and 200 Hz). Similar to what was observed by Rothenberg *et at.* for phage lambda, we observe three distinct stages for the target-search process: free in diffusion, on-cell motion and irreversibly bound, which were consistent with the observations documented for phage lambda [16]. In addition, long-term interaction occurred for both phages trough specific interaction between TFs and receptors, as in the absence of receptors no prolonged interaction was observed. We also observed the intermediate class of dynamics during which the phage appeared to move on or near the cell surface in a long-range motion that reached beyond that of a phage tethered to a single point. We observed the first direct evidence of long-range motion of phage on cell along a trajectory that involved multiple tether-points. Here, T4 phage showed clear evidence of step-wise shifts in mean tether-point positions along the long-range on/near-cell trajectories. This in contrast to phage lambda that qualitatively revealed no indication of these step-wise shifts in mean tether-point position during long-range on/near-cell motion other than the shift in position captured by the camera at a given moment in time. In other words, at their given temporal resolution, which was 0.66 times lower than the minimal temporal resolution used in our experiments, phage lambda has qualitatively not been shown to reside at a mean-tether point position during the long-range on/near-cell motion at the cell surface. With their temporal resolution of 33 Hz, phage lambda rather seems to move in a more continuous fashion at the cell surface [16]. In our case, the observed discrete motions for phage T4 showed two types of on/near-cell motion that occurred simultaneously at two different timescales: a fast-confined motion (short timescale) and an apparently unconstrained diffusive motion (longer timescale). Thus, while evidence for interactions between phage lambda and its host were inferred from the reduced diffusion coefficient, our data demonstrates step-wise physical interactions between phage and cell directly by revealing a large number of consecutive shifts in mean tethering position.

It is important to note that the study by Rothenberg *et al.* did not perform controls to address artefacts caused by cell-movement. This makes it impossible to accurately examine the dynamics of on-cell motion. Within our method we incorporated a cell-movement analysis in which we examined the extend of artefacts created in the on-cell movements of the phage by cells that might have been poorly attached to the glass substrate. Here we showed that the on/near-cell movement of phage T4 was not caused due to movement of the cell, as this was deemed neglectable compared to the extent of long-range on/near-cell movement of the phage.

The observed long-distance discrete on-cell motion shows that phage T4, and possibly other phages by extension, is in principle capable of performing near/on-cell 2D walks. It is important to consider the possibility that discrete on-cell movement could be an artefact of the covalently bound fluorescent dye. Even though the dye does not bind directly to the given location of the part of the LTF that binds to the LPS receptor, it has the potential to bind to a nearby position and in this way, might induce steric hindrance. We have already observed that labeling effects the capability to bind irreversibly within a 15-minute time window (chapter 2 section 2.4.4). Therefore, this steric hindrance could potentially also affect the reversible binding process. A possible

scenario would be that the binding between TF and receptor is strong enough to keep the phage tethered to the cell surface, but due to steric hindrance too weak to induce conformational changes required to bind irreversibly, resulting in dye induced on-cell movement. However, this seems unlikely, as this would suggest that the mechanism for on-cell movement arises from the exact positioning of the dye label on the LTFs (i.e. within this exact conformation the binding energy to promote walking is optimal). In addition, even if we were to assume that this dye effect does cause discrete motion in our experiment, it implies that the binding is tunable and therefore might be within a regime compatible with long-distance discrete on/near-cell motion when T4 — or other phages — interacts with another hosts or under different environmental conditions. Thus, our findings suggest that near/on-cell 'hopping/walking' is likely to also occur for unlabeled T4 phages under some conditions. Labeling could also promote non-specific interaction resulting in the observed prolonged on-cell interaction. However, this latter seems improbable, as we observed that, in the absence of a host receptor, there is no prolonged interaction detectable between labeled phage and cell surface. Whether dye induced steric hindrance leads to this near/on-cell motion behavior could be investigated by analyzing phage trajectories of T4 phages that have been labeled via the use of a different strategy that cannot induce any steric hindrance between LTF and receptor, i.e. labeling of the genome (chapter 2 section 2.4.3) or labeling the capsid trough a modification [32]. In order to use these alternative labeling methods, one of the points that needs to be examined is whether the signal-to-noise ratio of the fluorescent phage over time can be tracked long enough with the same temporal resolution before visualization of the particle is lost due to bleaching of the dye molecules. Given the fact that phage lambda [16] that was only labeled at the capsid also showed long-range on-cell motion lends further support to the assumption that our observation of discrete near/on-cell motion was not caused solely by the non-specific label.

Medium composition might also have a potential effect on the extend of on-cell motion. In chapter 2 we showed that the presence of L-tryptophan has a large effect on extension of LTFs and affects directly the binding efficiency. Therefore, it could be that when all LTFs are in extended position, the chance of binding a host receptor and committing directly to infection is high. This would result in a decreased on-cell distance traveled by the phage. Within our set-up we made use of M9 medium, which lacks the co-factor molecule L-trypthophan, resulting on average in 1-2 TFs being in the extended position [33], which potentially aids the 'hopping/walking' behavior due to the limited number of available LTF in extended position. It would be interesting to test this hypothesis, by obtaining trajectories in M9 medium supplemented with a saturated concentration of L-tryptophan with respect to their effects on LTF deployment state to observe whether this effects the travelled long-range on-cell motion.

If we assume that on/near-cell exploration is a realistic possibility for T4 and perhaps other phages, then this has implications for our understanding of nanoscopic mechanisms that govern (i) the adsorption kinetics, (ii) the capacity of phages to distinguish between candidate host cells and (iii) receptor 'searching' by phages that use multiple receptors (e.g., T4 on *E.* coli K12 bind irreversibly by binding to LPS in an OmpC dependent maner). (i) Near/on-cell motion has shown to be an important part of the binding process and should be taken into consideration when modeling

adsorption kinetics. (ii) Near/on-cell motion, during which the phage 'explores' the cell surface, is a different way of sampling the surface to discriminate hosts compared to colliding with the cell and sample if enough LTFs can bind to initiate commitment to infection. In the former scenario, initial binding to a single receptor can still lead to irreversible binding if the required number of receptors are within the 'walking'-range compared to the latter scenario, which can only bind upon collision with the cell when enough receptors are within immediate vicinity of the phage LTFs. In other words, the mean number of LTFs that has to attach to host receptors upon initial binding is lower in the former scenario compared to the latter to reach the state of irreversible binding. (iii) Near/on-cell motion could possibly provide an advantage for phages to reach the final destination via a 2D near/on-cell walk.

Our findings are consistent and lend direct support for, the commonly held notion that phages are capable of performing tethered walks on the cell surface, which so far had only been based on EM images showing phages bound with different numbers of TFs [6, 7]. However, it is also possible that the shifts in mean tethering points involved long series of consecutive hops or a combination of tethered steps and small hops. Another possible explanation for the observed discrete shifts not mentioned before could be a combination of the mechanism described above, where hopping and/or stepping resulted in a shift in tether-point position, combined with discrete non-isotropic diffusion around the tethering points. By non-isotropic, we refer to diffusion within multiple constrained areas while the phage is tethered via nonspecific interactions at a single main tethering point. However, considering the relatively well supported assumption outlined in the result section that states that nonspecific interactions are too weak to cause constrained diffusion, it follows that this latter explanation, which would also depend on such nonspecific interactions, is equally unlikely. For this reason, we have not explored this explanation beyond this point. Given that it seems unlikely that the phage moves near the cell by repeated detaches and attachment to a nearby position for the large number of steps within trajectories that we have observed, but reversible behavior with detachment from the cell back into solution is observed regularly, tethered walking and tethered walking in combination with an occasional hopping seem both very likely. The next step would be to test the experimental data against a model for hopping, walking and a combination of the two to test how likely the mechanisms can be explained by each of these models.

Step sizes and dwell times observed for T4 near/on-cell motion showed a large heterogeneity. This was also noted by the relatively low peak of the obtained S-curves (curve showing ratio of best fit and counter fit) within Stepfinder. This is most likely caused by the large variety of potential step sizes that the phage can take, as the phage can set a step in any direction within a given range that is linked to the number and position of remaining bound LTFs. This also results in a large range of dwell times. In addition, the size of the actual steps (displacement of baseplate relative to the cell) is obscured by the fact that steps of phages are extracted in one-dimension while the phage moves in three-dimensional space providing only an estimate of actual step size taken. Further, extensive non-specific labeling of the phage results in tracking of the phage capsid that drags behind the movement of the phage baseplate. This in combination with tail-tube capsid complex being an object prone to Brownian motion results in capsid oscillation obscuring the actual steps with even an even more noisy

signal. Given these facts: the large variety of potential step sizes, detection of the steps in only one-dimension and noise obscuring accurate detection of displacement of baseplate position makes it currently impossible to obtain accurate step sizes. Therefore, the obtained step size distribution provides only a range of representative step sizes which can still generate new insights and can be used to develop and improve the accuracy of theoretical models.

Besides the observed discrete on-cell motion, phage T4 also showed to reside on average longer on-cell compared to phage lambda before detachment from the surface into the bulk liquid occurred. This could be due to the increased number of available receptors for phage T4 (100-fold difference) [1, 34, 35]. The time the phage remains at the cell surface most likely increases with increasing chance for a LTF to bind a nearby receptor. Further, if the local receptor density is high, the phage will remain tethered to a local mean position for a longer time, which might explain the discrete shifts in position not present/visible at the given time-scale for phage lambda.

Further, observations of on-cell movement for phage lambda have revealed gradual localization to the cellular poles where irreversible binding takes place. Here the phage is guided via the receptor distribution (helical pattern) and receptor concentration gradient (highest at the cellular poles). The LPS receptor for phage T4 on *E. coli* B is most likely spatially organized in a similar fashion as host receptor LamB for phage lambda, albeit the concentration gradient across the cell might be less distinctive (mid cell compared to cellular poles) [22]. Whether T4 phage also lands randomly at the cell surface and moves along these receptor-rich regions towards the cellular poles for irreversible binding in a similar fashion as observed for phage lambda, or that the majority of T4 phages commit to infect the cellular poles due to a higher chance of binding irreversibly when landing directly at the cellular poles compared to mid-cell (more detachment takes place) as observed for phage SPP1 [14], still needs to be investigated. With the currently available data the directionality of on-cell motion and number and fraction of attach- and detachments per cell segment can be obtained, which together can provide an answer on this question.

Taken together, we interpret our data as providing the first direct evidence of T4 phage long-range motion near and/or on the cell surface by discrete steps and/or hops that that cause repeated shifts in mean tethering point location. In addition, we provide an upper limit of step-duration times and a range of step sizes. Further, we reported a dwell-time distribution for mean tether point positions that contains information that can shed light on the underlying kinetics of the process. These findings represent a step forward towards understanding the mechanisms underlying phage-cell interactions. The on-cell motion we observerd could play a role in phage ecology if it has a positve impact on fitness by dimensionally reducing the search for the final receptor and/or optimal location on the cell surface.

4.4 Acknowledgement

The authors thank Wouter Duverger and Dr. Martin Depken for the discussion and first developments on a theoretical model of T4 phage on-cell tethered-walking and Jeremie Capoulade for the technical support of the microscopy work.

4.5 Experimental procedures

4.5.1 Strains, media, and growth conditions

Escherichia coli B (ATCC 11303) was used as host indicator strain of phage T4 ATCC 11303. E. coli was grown in Lysogeny broth (LB) (Sigma) supplemented with 10 mM $CaCl_2$ and 10 mM $MgSO_4$ at 37 °C and 250 rpm to early exponential phase (OD_{600} 0.1) and infected with T4 at MOI 0.5 and grown until lysis occurred (~3 hours). A final concentration of 2.5 % chloroform was added to lyse all the cells. The suspension was centrifuged for 20 min at 18000 g and filtered through a 0.22 μm filter (SFCA, Minisart NML, Satorius) and saved at 4 °C until further use.

4.5.2 Phage purification, activity, and labeling

The following steps were applied to purify the phage suspension. 1 μg ml^{-1} RNase and DNase was added to the phage suspension and incubated for 30 min at RT. Phages were extracted and purified with a CsCl density gradient (with the following densities: 1.33, 1.45, 1.50, 1.70) and centrifuged at 28.000 g for 3 h at 4 °C, followed by dialysis (7 k cutoff, Thermo Fisher) in MB (20mM Tris-HCl, 100mM NaCl and 10mM $MgSO_4$) and stored at 4 °C until use.

Impurity and fraction of contracted particles was determined by visualization of negative stain transmission electron microscopy (TEM). 3 μl of sample was placed on a glow-discharged coper EM grid with a 400 Mesh Carbon film (Aurion) for 3 minutes, followed by blotting and washing the grid three times with 5 μL MiliQ, and staining the sample 1 min with 3 μl 1-2% uranyl acetate, followed by a last round of blotting. Samples were imaged at JEOL JEM-1400plus TEM, with an acceleration voltage of 120 kV and EDS detector.

Purified phages were concentrated and washed with an amicon ultra-0.5 centrifugal filter unit (100 kDa cutoff, Millipore) in PBS (sigma) supplemented with freshly made 0.1 M sodium bicarbonate. Followed by fluorescent labeling with a final concentration of 0.05 mg ml^{-1} Alexa Fluor™ 488 NHS Ester (Thermo Fisher) for at least 3 h at RT and washed with a amicon ultra-0.5 centrifugal filter unit (100 kD, Millipore) in MB and stored at 4 °C until use.

Activity and concentration of the purified labeled phage suspension was confirmed with a spot assay. The phage sample was serially diluted in tenfold in MB and 10 μl aliquots were placed onto a double-layered agar plate containing the target indicator strain *Escherichia coli* B and incubated overnight at 37 °C. Activity was confirmed as a distinct clear 'killing'-zone on the bacterial lawn and concentration was determined by counting single plaques visible at spots with higher dilutions.

4.5.3 Microscopy

4.5.3.1 Flow cell

Glass coverslips were extensively cleaned with 2% Hellmanex III (Hellma GmbH) and pre-coated with 0.1% poly-L-Lysine (sigma). Flow cells were assembled with the use of double adhesive tape, serving as a spacer. Cells were grown in LB to early exponential phase (OD_{600} 0.3), concentrated 10x and resuspended in interaction media. 10 μl of cell

suspension was added to the perfusion chamber through a predrilled hole and left for attachment to the coverslip for 10 min. Excess cells and poorly immobilized cells were removed by washing the chamber with 150 µl interaction media at a speed of 175 µl min^{-1}. Tracking of T4 phage particles in real-time was performed by adding labeled phages to a flow cell containing immobilized *Escherichia coli* B cells at an MOI ≥ 1.

4.5.3.2 Imaging conditions

Image acquisition at low frame rate (50 fps) was performed with an Olympus inverted microscope (IX81) with a TIRF illumination system. Fluorescence excitation of fluorophore Alexa480 was provided by an Olympus CW laser at 488 nm with a maximum output power of 150 mW. As detection device, we used an EM-CCD (Andor iXon X3 DU897) containing a chip size of 512x512 pixels with a resolution of 80 nm/pixel. The Electron-Multiplying (EM) gain was set to 200. A 0.6 ND filter was used to reduce Overexposure. Emission filter 524/29 was used. Fluorescent imaging was performed in HILO mode. A UPlanFLN objective was used with magnification 100x, numerical aperture 1.3 and working distance 0.2mm. 500 images of the phase contrast and 2000 or 4000 images of the fluorescent channel were taken with an exposure time of 100ms and 20 ms, respectively. The laser intensity was set approximately at 100-200 μW.

Image acquisition at a high frame rate (200 fps) was performed with a Nikon inverted microscope (Ti2-E) with a TIRF illumination system (Gataca iLAS2). Fluorescence excitation of fluorophore Alexa480 was provided by an Olympus CW laser at 488 nm with a maximum output power of 150mW. The detection device was a dual set-up with an EM-CCD (Andor iXon Ultra 897) with a chip size of 1004x1025 pixels for the fluorescent channel and an EM-CCD (Retiga R1) with a chip size of 1376x1024 pixels for the phase contrast channel with a resolution of 161 and 63.5 nm/pixel, respectively. A Nikon Apo TIRF objective was used with magnification 100x, numerical aperture 1.49 and working distance 0.12 mm. Emission filter 525/50 was used. Fluorescent imaging was performed in HILO mode. To obtain phage trajectories, 2000 images were taken at an exposure time of 4 ms and a laser intensity of 198 μW. This while for detecting cell movement, 200 images were taken with phase contrast microscopy with an exposure time of 100 ms.

4.5.3.3 Data processing and statistics

4.5.3.3.1 Alignment of fluorescent and phase contrast images taken at high frame rate

Images of 200 nm TetraSpeck™ beads (Invitrogen) were taken in both the fluorescent and phase contrast channel prior to high frame rate movies obtained by the Nikon inverted microscope (Ti2-E). These images were used to determine the alignment coordinates for proper overlay between the phase contrast channel (cells) and the fluorescent channel (phage trajectories). Background subtraction and inversion was applied on bead images taken with the phase contrast channel, followed by downscaling of the image to 0.39 of its original size. Then alignment coordinates for overlaying the phase contrast with the fluorescent channel were obtained by the

descriptor-based registration (2d/3d) plugin of Fiji [36]. These coordinates were used for alignment of all pre-processed (downscaled) phase contrast images of cells. This was followed by cropping the PC images to the same size as the fluorescent image.

4.5.3.3.2 Cell outline

Phase contrast images, containing the bacteria, were made binary with ImageJ using the following procedure. First, the contrast was enhanced by saturating 0.03% of pixel, followed by applying a Gaussian blur filter with sigma 2, and a Yen threshold method. Using Matlab, bacteria were detected as binary objects meeting the following criteria. A minimal area of 100 and maximal area of 1000 pixel, with a minimal eccentricity of 0.7 and minimal solidity of 0.9

4.5.3.3.3 Cell movement analysis

Analysis of cell movement was performed by converting each phase contrast image to a binary image as described in Chapter 2 (section 2.6.4.4). A stack summation was performed with color coding indicating movement of the cell at pixel level accuracy and was used to quickly scan for large rotational or translational movement of cells. Cells containing phage trajectory segments that were subjected to Stepfinder were analyzed by a second cell movement analysis algorithm, also described in Chapter 2 (section 2.6.4.4). Here the midpoint of a cross-section along the long axis, as well as the midpoint of three cross-sections along the short axis (covering the middle of cell and both polar regions of the cell), were tracked and compared per frame to assess smaller rotational and translational movement of the cell with subpixel level accuracy.

4.5.3.3.4 Phage trajectories

Phage trajectories were obtained by a plugin of ImageJ, referred to as Trackmate [23], and downstream analysis of trajectories were performed with Matlab using @msdanalyzer, as was described briefly in chapter 2.

4.5.3.3.5 Stepfinder

Step finder algorithm Stepfinder, described by kerssemakers *et al.* [24] and Loef *et al.* [25] and described in Chapter 2 (section 2.6.4.3), was used to analyze discrete movements within on-cell segments of phage trajectories.

4.6 Supplementary

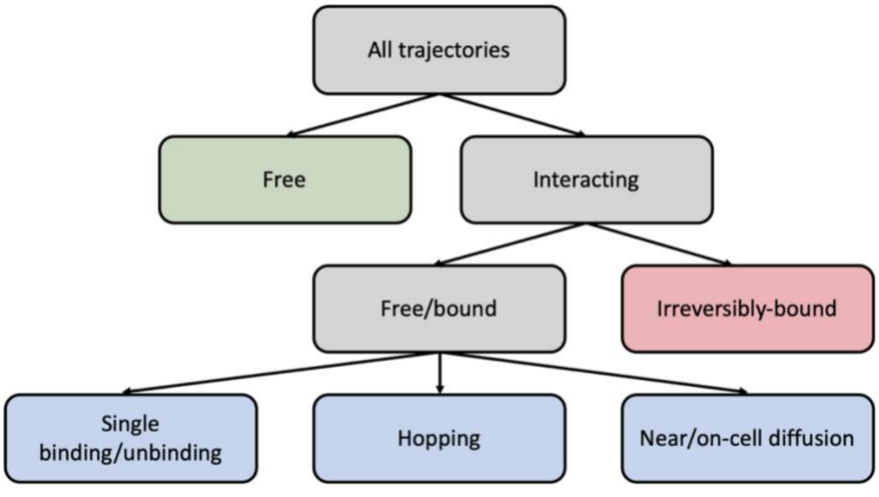

Supplementary figure 4.1 Classification of trajectories.

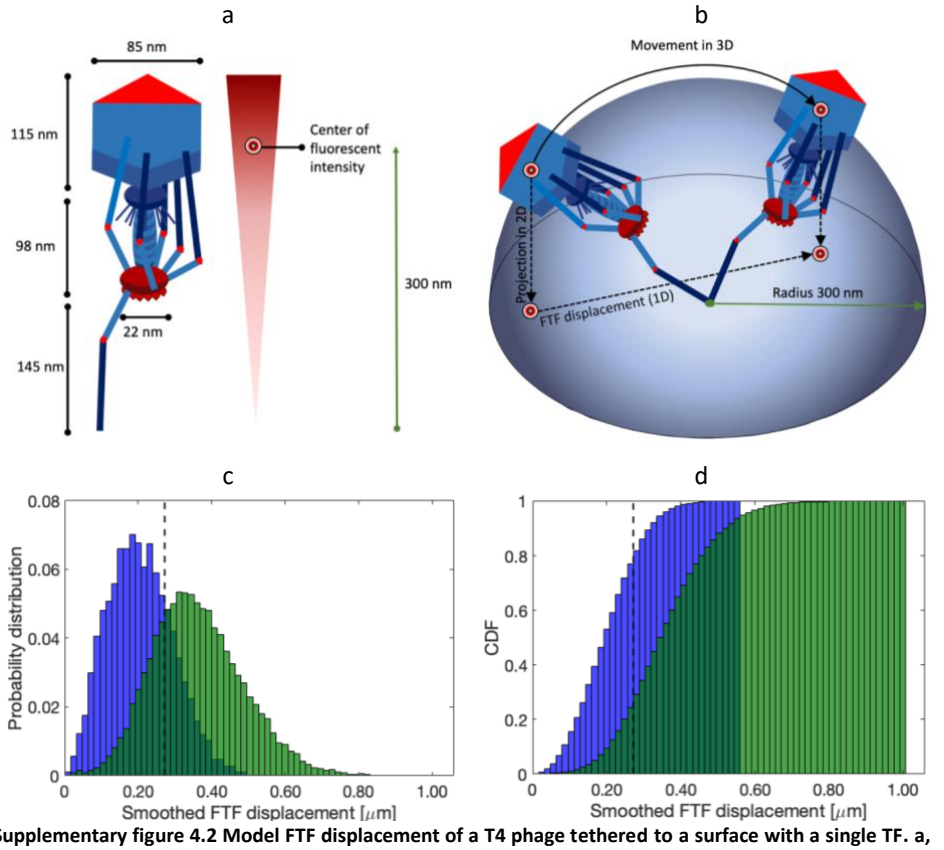

Supplementary figure 4.2 Model FTF displacement of a T4 phage tethered to a surface with a single TF. a, Dimensions of T4 phage components and fluorescence intensity across T4 phage based on density of labels. **b,** Range in which a fluorescently labeled T4 phage particle can be detected when tethered to a location on the surface with a single TF. **c** and **d**, Probability distribution and CDF distribution of smoothed FTF displacements of a modelled T4 phage particle that is tethered to a surface with a single TF versus T4 phages free in solution. To obtain a representative distribution of FTF displacement values for a tethered T4 phage particle, we simulated 100 trajectories with a total length of 1e4 points. Dashed line presents the set threshold used to separate tethered from free phages.

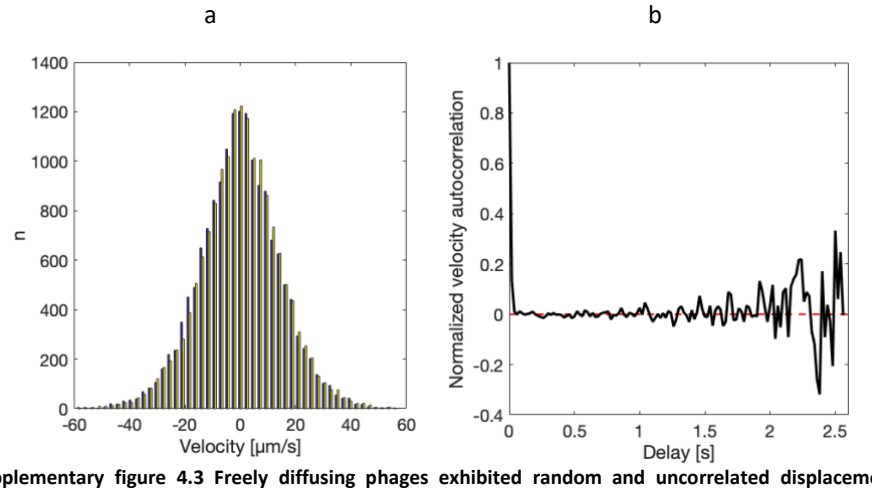

Supplementary figure 4.3 Freely diffusing phages exhibited random and uncorrelated displacement. Velocity analysis distribution for all individual trajectories classified within the group *free*. **a,** Symmetric instantaneous velocity distribution graph, showed x and y displacements with mean values centered around 0. Yellow and purple bars presented x and y displacement, respectively. **b,** Normalized velocity autocorrelation, showed, with the exception of $\Delta t = 0$, a mean value centered around 0 during the course of time.

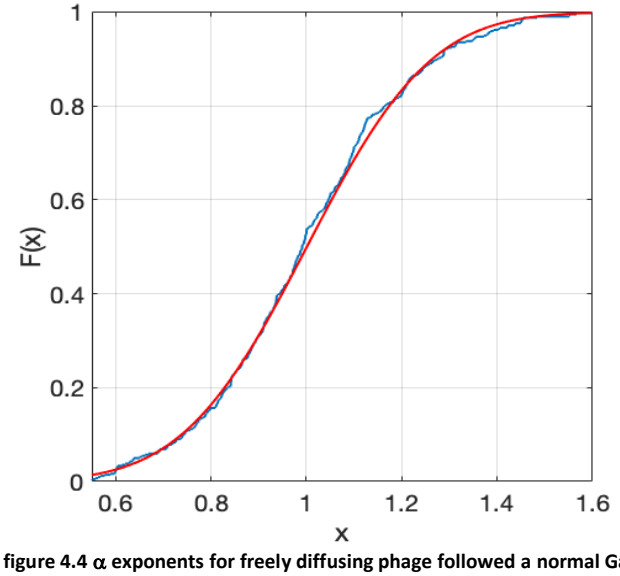

Supplementary figure 4.4 α exponents for freely diffusing phage followed a normal Gaussian distribution. α exponents were obtained from a linear fit on the first 15% of each individual trajectory curve in a log-log plot of MSD as a function of delay time. The cumulative distribution function (CDF) was used to calculate the cumulative probability for every given x-value. The obtained empirical CDF was tested, using a Kolmogorov-Smirnov test, against the null-hypothesis of a standard normal CDF. Results showed no significant deviation, demonstrating that the data followed a standard Gaussian distribution. Blue and red curves presented the empirical CDF and standard normal CDF with mu 1.00 and sigma 0.21, respectively.

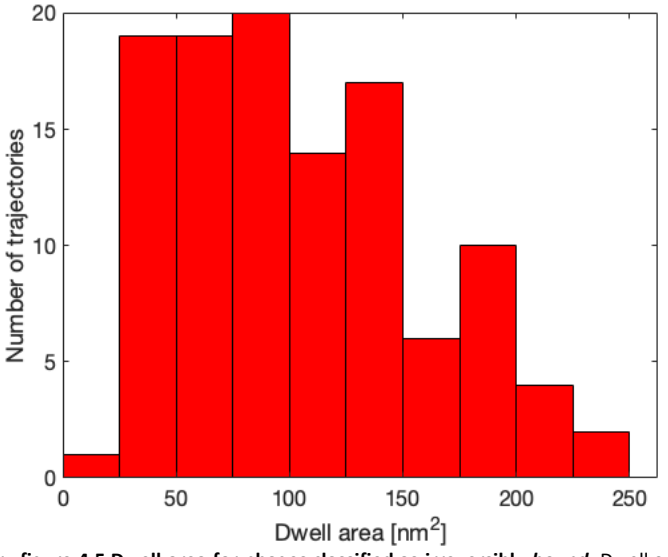

Supplementary figure 4.5 Dwell area for phages classified as irreversibly-*bound*. Dwell area was obtained by calculating the surface area within the convex hull for each individual trajectory classified within this group.

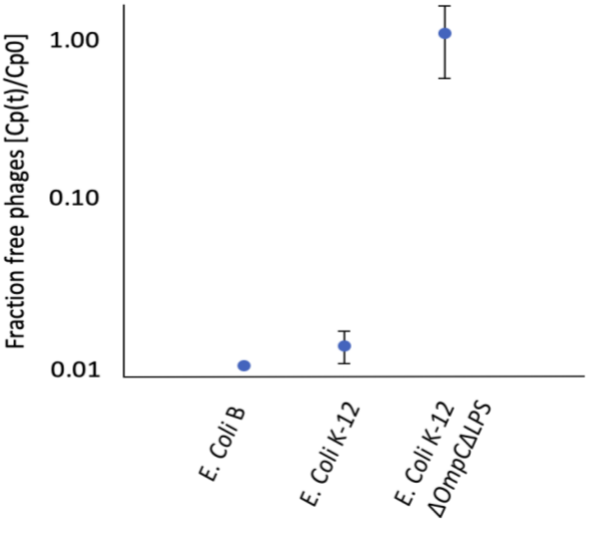

Supplementary figure 4.6 Effect of presence of host receptor on binding efficiency phage T4. Phages were incubated with one of the following host in LB medium: *E. coli* B (host receptor: LPS), *E. coli* K-12 (host receptor OmpC in combination with LPS), and *E. coli* K-12 ΔOmpCΔLPS (lacking host receptors). After 15-minute incubation with one of the host, the remaining fraction that was still free in solution was measured using a spot assay. Every tested strain represents 5 or 6 replicas.

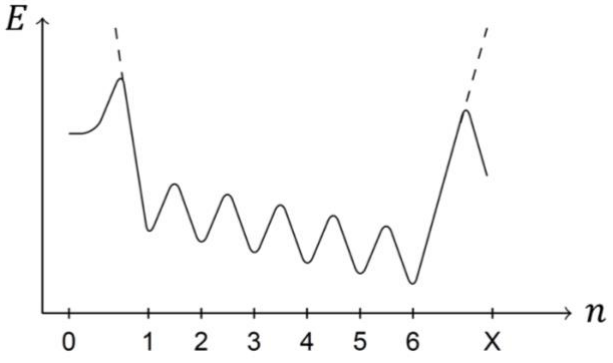

Supplementary figure 4.7 Representation of a hypothetical energy landscape for phage performing a tethered-walk. For a tethered-walk to occur (dashed line), the initial and final energy barrier to detach from the cell and commitment to infection need to be high (n = 0 and n = X, respectively), while the intermediate energy barrier need to be low with a moderate slope.

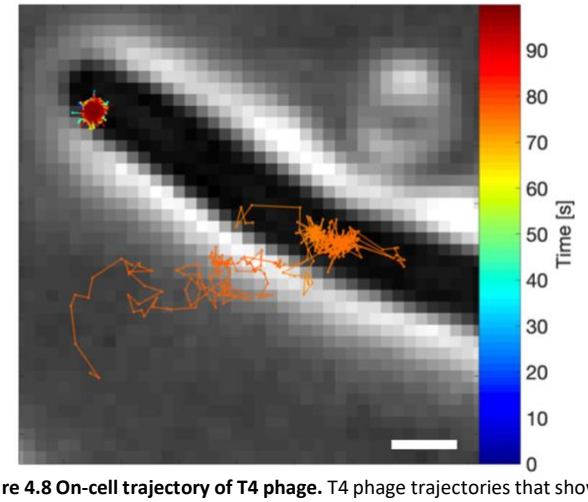

Supplementary figure 4.8 On-cell trajectory of T4 phage. T4 phage trajectories that showed interaction with its host *E. coli* B. One of the trajectories is classified as *irreversibly-bound* (location at left upper corner) and the other is reversibly bound (*free/bound*, location at the middle of image). Colors indicate time, starting in blue and ending in red. Scale bar represents 1 µm.

a

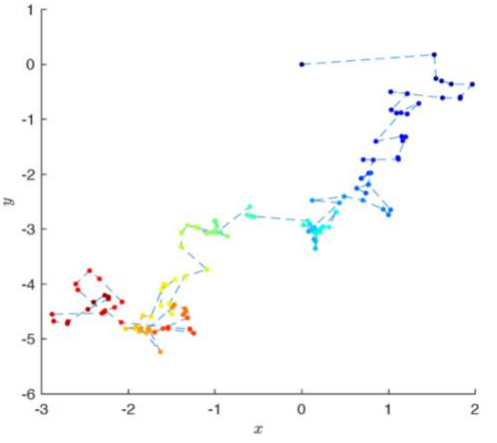

b

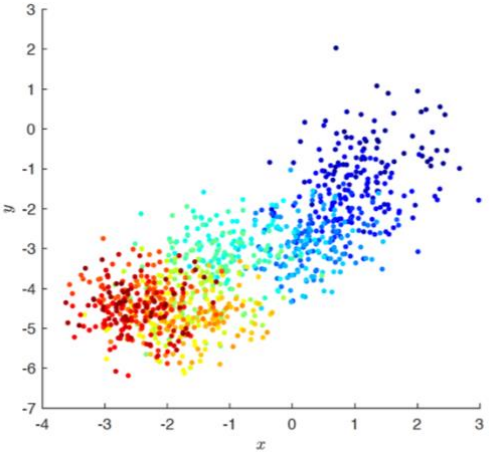

c

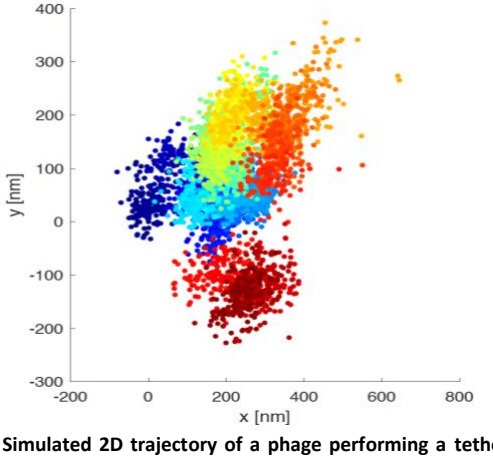

Supplementary figure 4.9 Simulated 2D trajectory of a phage performing a tethered-walk. a, Simulated trajectory of a tethered-walk. **b,** The same trajectory embedded in noise (i.e. random movements of the viral capsid). **c**, Experimentally obtained trajectory resembling the simulated trajectory qualitatively. Colors indicate time, starting in blue and ending in red.

References

[1] M.Z. Islam, A. Fokine, M. Mahalingam, Z. Zhang, C. Garcia-Doval, M.J. van Raaij, M.G. Rossmann, V.B. Rao, Molecular anatomy of the receptor binding module of a bacteriophage long tail fiber, PLoS Pathog 15(12) (2019) e1008193.
[2] A. Washizaki, T. Yonesaki, Y. Otsuka, Characterization of the interactions between Escherichia coli receptors, LPS and OmpC, and bacteriophage T4 long tail fibers, Microbiologyopen 5(6) (2016) 1003-1015.
[3] H.C. Berg, E.M. Purcell, Physics of chemoreception, Biophys J 20(2) (1977) 193-219.
[4] D. Bryan, A. El-Shibiny, Z. Hobbs, J. Porter, E.M. Kutter, Bacteriophage T4 Infection of Stationary Phase E. coli: Life after Log from a Phage Perspective, Front Microbiol 7 (2016) 1391.
[5] M. Schwartz, The adsorption of coliphage lambda to its host: effect of variations in the surface density of receptor and in phage-receptor affinity, J Mol Biol 103(3) (1976) 521-36.
[6] B. Hu, W. Margolin, I.J. Molineux, J. Liu, Structural remodeling of bacteriophage T4 and host membranes during infection initiation, Proc Natl Acad Sci U S A 112(35) (2015) E4919-28.
[7] B. Hu, W. Margolin, I.J. Molineux, J. Liu, The bacteriophage t7 virion undergoes extensive structural remodeling during infection, Science 339(6119) (2013) 576-9.
[8] X. Liu, Q. Zhang, K. Murata, M.L. Baker, M.B. Sullivan, C. Fu, M.T. Dougherty, M.F. Schmid, M.S. Osburne, S.W. Chisholm, W. Chiu, Structural changes in a marine podovirus associated with release of its genome into Prochlorococcus, Nat Struct Mol Biol 17(7) (2010) 830-6.
[9] Z.J. Storms, E. Arsenault, D. Sauvageau, D.G. Cooper, Bacteriophage adsorption efficiency and its effect on amplification, Bioprocess Biosyst Eng 33(7) (2010) 823-31.
[10] Z.J. Storms, L. Smith, D. Sauvageau, D.G. Cooper, Modeling bacteriophage attachment using adsorption efficiency, Biochemical Engineering Journal 64(15) (2012) 22-29.
[11] Z.J. Storms, D. Sauvageau, Modeling tailed bacteriophage adsorption: Insight into mechanisms, Virology 485 (2015) 355-62.
[12] R. Moldovan, E. Chapman-McQuiston, X.L. Wu, On kinetics of phage adsorption, Biophys J 93(1) (2007) 303-15.
[13] R. Edgar, A. Rokney, M. Feeney, S. Semsey, M. Kessel, M.B. Goldberg, S. Adhya, A.B. Oppenheim, Bacteriophage infection is targeted to cellular poles, Mol Microbiol 68(5) (2008) 1107-16.
[14] L. Jakutyte, C. Baptista, C. Sao-Jose, R. Daugelavicius, R. Carballido-Lopez, P. Tavares, Bacteriophage infection in rod-shaped gram-positive bacteria: evidence for a preferential polar route for phage SPP1 entry in Bacillus subtilis, J Bacteriol 193(18) (2011) 4893-903.
[15] L. Zeng, S.O. Skinner, C. Zong, J. Sippy, M. Feiss, I. Golding, Decision making at a subcellular level determines the outcome of bacteriophage infection, Cell 141(4) (2010) 682-91.
[16] E. Rothenberg, L.A. Sepulveda, S.O. Skinner, L. Zeng, P.R. Selvin, I. Golding, Single-virus tracking reveals a spatial receptor-dependent search mechanism, Biophys J 100(12) (2011) 2875-82.

[17] P.H.E. Hamming, N.J. Overeem, J. Huskens, Influenza as a molecular walker, Chem Sci 11(1) (2020) 27-36.
[18] R. Pei, S.K. Taylor, D. Stefanovic, S. Rudchenko, T.E. Mitchell, M.N. Stojanovic, Behavior of polycatalytic assemblies in a substrate-displaying matrix, J Am Chem Soc 128(39) (2006) 12693-9.
[19] K. Lund, A.J. Manzo, N. Dabby, N. Michelotti, A. Johnson-Buck, J. Nangreave, S. Taylor, R. Pei, M.N. Stojanovic, N.G. Walter, E. Winfree, H. Yan, Molecular robots guided by prescriptive landscapes, Nature 465(7295) (2010) 206-10.
[20] Y. Tian, Y. He, Y. Chen, P. Yin, C. Mao, A DNAzyme that walks processively and autonomously along a one-dimensional track, Angew Chem Int Ed Engl 44(28) (2005) 4355-8.
[21] E. Brzozowska, A. Lesniewski, S. Sek, R. Wieneke, R. Tampe, S. Gorska, M. Jonsson-Niedziolka, J. Niedziolka-Jonsson, Interactions of bacteriophage T4 adhesin with selected lipopolysaccharides studied using atomic force microscopy, Sci Rep 8(1) (2018) 10935.
[22] A.S. Ghosh, K.D. Young, Helical disposition of proteins and lipopolysaccharide in the outer membrane of Escherichia coli, J Bacteriol 187(6) (2005) 1913-22.
[23] J.Y. Tinevez, N. Perry, J. Schindelin, G.M. Hoopes, G.D. Reynolds, E. Laplantine, S.Y. Bednarek, S.L. Shorte, K.W. Eliceiri, TrackMate: An open and extensible platform for single-particle tracking, Methods 115 (2017) 80-90.
[24] J.W. Kerssemakers, E.L. Munteanu, L. Laan, T.L. Noetzel, M.E. Janson, M. Dogterom, Assembly dynamics of microtubules at molecular resolution, Nature 442(7103) (2006) 709-12.
[25] L. Loeff, J.W. Kerssemakers, C. Joo, C. Dekker, A fast and automated step detection method for analysing single-molecule trajectories, Technische Universiteit Delft, Delft, 2017.
[26] M.J. Saxton, Modeling 2D and 3D diffusion, Methods Mol Biol 400 (2007) 295-321.
[27] X. Michalet, Mean square displacement analysis of single-particle trajectories with localization error: Brownian motion in an isotropic medium, Phys Rev E Stat Nonlin Soft Matter Phys 82(4 Pt 1) (2010) 041914.
[28] R. Polic, Phase-contrast microscopy principle and applications in Materials sciences, 2020.
[29] C. Kleanthous, P. Rassam, C.G. Baumann, Protein-protein interactions and the spatiotemporal dynamics of bacterial outer membrane proteins, Curr Opin Struct Biol 35 (2015) 109-15.
[30] J.H. Wilson, R.B. Luftig, W.B. Wood, Interaction of bacteriophage T4 tail fiber components with a lipopolysaccharide fraction from Escherichia coli, J Mol Biol 51(2) (1970) 423-34.
[31] B.C. Lagerholm, N.L. Thompson, Theory for ligand rebinding at cell membrane surfaces, Biophys J 74(3) (1998) 1215-28.
[32] Z. Kazmierczak, A. Piotrowicz, B. Owczarek, K. Hodyra, P. Miernikiewicz, D. Lecion, M. Harhala, A. Gorski, K. Dabrowska, Molecular imaging of T4 phage in mammalian tissues and cells, Bacteriophage 4(1) (2014) e28364.
[33] E. Kellenberger, A. Bolle, E. Boydelatour, R.H. Epstein, N.C. Franklin, N.K. Jerne, A. Reale Scafati, J. Sechaud, Functions and Properties Related to the Tail Fibers of Bacteriophage T4, Virology 26 (1965) 419-40.

[34] K.A. Gibbs, D.D. Isaac, J. Xu, R.W. Hendrix, T.J. Silhavy, J.A. Theriot, Complex spatial distribution and dynamics of an abundant Escherichia coli outer membrane protein, LamB, Mol Microbiol 53(6) (2004) 1771-83.
[35] F.C. Neidhardt, J.L. Ingraham, K.B. Low, B. Magasanik, M. Schaechter, H.E. Umbarger, Escherichia coli and Salmonella typhimurium: Cellular and Molecular biology. , 2nd ed., American Society for Microbiology, Washington, DC, 1987.
[36] S. Preibisch, S. Saalfeld, J. Schindelin, P. Tomancak, Software for bead-based registration of selective plane illumination microscopy data, Nat Methods 7(6) (2010) 418-9.

5

Single-particle dynamics of R2-type Pyocins

Lisa L. Dreesens, Aishwarya Karthikeyan, Marie-Eve Aubin-Tam, Hubertus J. E. Beaumont

R2-type pyocins are bacteriocins that show both morphological, structural, and genetic similarities with phages. Pyocins are encoded on the genome of some bacterial species, which use them to kill competing bacterial cells by dissipation of their electrochemical membrane potential. They represent a promising candidate for use as alternative antimicrobial agent. However, single-particle and single-cell insight into the mechanism and dynamics of this attack and killing process is lacking. Here we demonstrate a method for real time tracking of single pyocin particles and their effect on membrane potential at the single cell level. The results show that this approach has the potential to uncover the nanoscopic events that govern interaction of pyocin with their target cells and link them to a vital physiological parameter.

5.1 Introduction

In 1952, bacteria that produce high-molecular-weight bactericidal compounds were discovered [1]. It took another 10 years before Kageyama & Egami began investigating these structures in more detail, laying the fundamental groundwork that led, among other things, to the characterization of the physical properties of these structures [2]. They found that the bactericidal protein particles produced by *Pseudomonas aeruginosa* were structurally and serologically similar to phages. The discovered bactericidal protein complexes, referred to as phage tail-like bacteriocins (PTLBs), can be divided into two subgroups based on their morphology: rod-like (R)-type tailocins with a straight contractile tail resembling phages from the *Myoviridae* class and flexuous rod-like (F)-type tailocins with a long flexible tail tube resembling phages of the *Siphovirdae* class [3]. Both contain a baseplate and long tail-fibers (LTFs) with receptor binding proteins (RBPs) that allow docking to their target cells.

Among *P. aeruginosa* strains, it has been estimated that at least 90% [4] encodes one or more types of pyocins that are located on a single genomic cluster and regulated by RecA [3]. PTLBs were found not to be limited to *P. aeruginosa* strains but to be widespread in both gram-positive and gram-negative bacteria, e.g. F-type monocins in *Listeria monocytogenes* [5], R-type diffocins in *Clostridium difficile* [6], R-type maltocin in *Stenotrophomonas maltophilia* [7], R-type carotovoricin in *Erwinia carotovora Er*. [8], R-type xenorhabdicin in *Xenorhabdus nematophilus* [9] and R-type vibriocins in *Vibrio* cholerae [10-12].

Their ecological role is not yet fully elucidated, but they seem to play a role in the bacterial survival within dense communities containing closely related strains [13, 14]. When competition for nutrients is strong, their expression is upregulated, giving the producer strain a competitive advantage over closely related strains [15]. The expression of these PTLBs among bacteria seems to be a stochastic process and only occurs in a small fraction of the population [16]. Since the cell has to lyse in order to release the produced PTLBs to the environment, this might be seen as a form of altruism (to protect its own kin).

Over the recent years, more similarities between PTLBs and phages have been found. Although PTLBs do not have their own genome — they are encoded within the genome of bacteria — their coding genes are found in genetic clusters that show high similarity with those encoding for phages [3, 11]. These genes include proteins that play a role in transcription, as well as, genes encoding structural components and their corresponding chaperones that will assemble new PTLBs and a lysis gene cassette that ensures the release of these new PTLBs to the environment [3]. Besides gene cluster organization, also cross-compatibility between proteins from PTLBs and closely related phages has been shown [17-19]. Sequence comparison of different R-type pyocins showed a conserved N-terminus, but a rather diverged C-terminal region of the tail-fibers. This part of the region acts as the RBP and determines the host binding interaction to different moieties of the host cell receptor LPS, establishing the host-range [13]. This allows interesting applications of pyocins: exchanging the C-terminal part of their TFs with those for other PTLBs or phages allowed engineering of their host specificity [20-22]. Starting from 1969 the antimicrobial effectivity of PTLBs was shown by rescuing chick embryos, mice and rabbits that were infected by host sensitive strains

[22-27]. In contrast to phages, PTLBs kill bacterial cells by dissipation instead of lysis, minimizing the release of endotoxins. In addition, PTLBs carry no genetic material and cannot evolve on their own and therefore have been shown to be safely administered either intraperitoneal or intravenous without harming the beneficial flora, the latter one being a common problem when treating infections with antibiotics. PTLBs have also shown to be potential candidates for industrial applications, including bacterial typing [28-34] and within food preservation and safety [5, 21].

Since genetic and structural resemblance between phages and PTLBs are high, we might assume that their mechanism of target-finding, discriminating and cell penetration must be similar too, revealing a possible universal mechanism for all contractile systems. During assembly of rod-like (R)-type tailocins energy is stored in the sheath. As was observed for phages of the *Myoviridae* class, binding of multiple TFs most likely triggers a conformational change within the baseplate, resulting in the release of the stored energy in the sheath leading to rapid sheath contraction. During this contraction, the inner tube is pushed through the cell membrane [35]. However, in addition to the obvious lack of a capsid and genome, there is a striking additional difference between PTLBs and phages, namely the charge of the amino-acids on the inside of the tail-tube [35]. This suggests that the pyocin tube has a different function than that of its phage counterparts. Phages have a net-positively charged inner tail-tube to facilitate the translocation of negatively charged DNA. In contrast, the inside of the tail-tube of R-type pyocins was found to be overall negatively charged. T4 phages that lack DNA, as well as, PS17 capsidless tail structures have shown to possess some, but to a very low extend, bactericidal activity [36]. Based on a scarce number of studies, the mechanism of action for R-type PTLBs is believed to be as follows: upon binding of enough TFs to the host cell, sheath contraction is triggered, pushing the inner tail tube through the cell membrane creating a permanent pore. Here the tail-tube acts as a proton-conducting channel facilitating the release of intracellular ions and protons, causing rapid and effective cell death by depolarization of the cytoplasmic membrane and dissipation of the ion-motive force that powers active transport and energy metabolism [37]. R-type PTLB-killing appears to be very efficient with most likely a single particle capable of killing a bacterial cell [38-40]. The mechanism of action for F-type PTLBs is not known, but scarce experimental evidence suggests a similar function. Whether this distinction in function affects other relevant processes, e.g. binding distribution or kinetics, has not yet been studied.

So far, studies have focused predominantly on the structure, phylogenetic diversity and ecology of PTLBs. Insight into the kinetics of its interaction with the cell and the resulting dynamics of killing are lacking. To exploit the promise of PTLBs as fully engineerable antibacterial agents, it is essential to open a window into the nanoscopic details that govern their behavior in real time. Here we show a proof of principle of an approach that allows the study of PTLBs-host interactions at the single-particle level and in real time using fluorescence microscopy.

5.2 Results

In the previous two chapters, we showed first insights in the search strategy of T4 phages at single-particle level. We were interested in investigating whether the observed preferential binding of phages to the cellular poles of cells was shared by protein complexes resembling phages, i.e. pyocin R2. In addition, we were interested in examining if the dynamics and search process of pyocin R2 was similar to that observed for phages. Lastly, we were interested in gaining knowledge about the depolarization process of cells by pyocin R2. Therefore, we tested i) whether the method described in Chapter 2 allowed for single particle tracking of pyocins with its host strain *P. aeruginosa* 13s, which is known to be susceptible to pyocin R2 [20], ii) optimized the concentration of a cationic membrane-permeable fluorescent dye, and iii) test whether it can be used to monitor the membrane potential of the host at single-cell level. This work yielded data on i) the static binding distribution, ii) pyocin-host interaction dynamics and iii) kinetics for pyocin induced membrane potential dissipation.

5.2.1 Pyocin R2 binding distribution

We were interested in studying the irreversible binding distribution of R2-type pyocins. Expressing and purifying active R2-type pyocins and subsequently fluorescently labeling them with Alexa647 was already successfully shown in Chapter 2, where we provided evidence that labeled pyocins were active and could be tracked over a substantial amount of time using fluorescence microscopy. To establish if this method can be used to study the irreversible binding distribution, we performed a proof of principle experiment. Here we detected the irreversible binding position of pyocin R2 on host cell strain *P. aeruginosa* 13s. Therefore, exponentially growing 13s cells were fluorescently labeled with the DNA stain DAPI, for localization of the cells. Cells were inserted into a flow cell and immobilized to the substrate as described in Chapter 2. Hereafter, fluorescently labeled pyocins were inserted in the flow cell and allowed to bind to the immobilized target cells for at least 10 minutes. Target cells with a bound pyocin were detected using fluorescence microscopy (Figure **5.1**). Pyocins bound to its host were distinguished from the ones bound to glass by their intensity profile. Due to the focal plane at mid cell, pyocins bound to glass showed a low and broad intensity profile compared to pyocins bound to target cells, as was previously shown for phages (Chapter 2 section 2.4.1).

Overall, the frequency of bound pyocin particles was low. For the few recorded observations, we determined the position of the pyocin on the long-axis of the cell manually, by measuring the distance from the center of the pyocin to the closest cell pole. The obtained distribution was normalized and made absolute, with the mid and cellular pole region of the cell defined as 0 and 1, respectively. The obtained data was divided into 5 bins, in which every bin presented an equal surface area (Chapter 3 section 3.5.2). The fraction of pyocins binding to the old polar regions (the rounded ends of a rod-shaped cell that were assigned as the outer bin) of the cell in TN50 buffer was 0.63 (Figure **5.2**). This is more than three times the number of pyocins compared to an equal cell surface area *n* of the remaining part of the cell (fraction of 0.09), giving

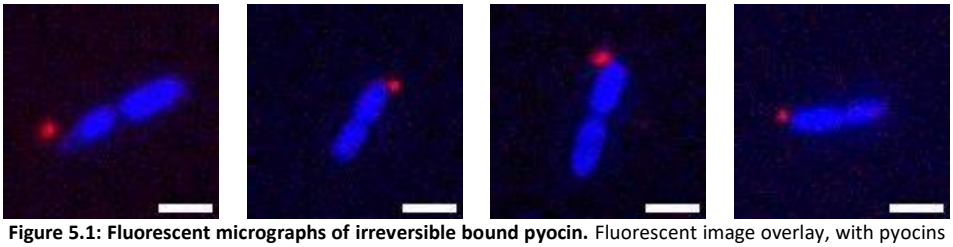

Figure 5.1: Fluorescent micrographs of irreversible bound pyocin. Fluorescent image overlay, with pyocins (red) labeled with 10 mM alexa-647 and *P. aeruginosa* 13s cells (blue) stained with DAPI. Images of pyocins were obtained with an exposure time of 100 ms, an EM gain of 100, and a laser intensity of 671 μW. Images of cells were obtained with an exposure time of 52 ms, an EM gain of 80, and a laser intensity of 346 μW. Scale bar represents 2 μM.

a polarity index of 0.41. We included the total observed counts and tested this against the null hypothesis of a uniform binding distribution. We found that the binding distribution significantly deviated from a uniform distribution (X^2 goodness fit; n = 16, p < 0.0001), showing a strong preference for binding to polar sites on the bacterial surface of *P. aeruginosa* strain 13s. Taken together, these results first of all indicate that this method can be used to study the irreversible binding distribution of R2-type pyocins and secondly the limited number of observations point towards the direction of irreversible binding position similar to phages.

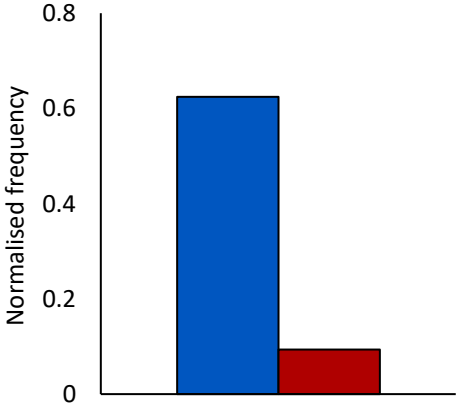

Figure 5.2: Fraction of irreversible binding position of pyocin R2. Normalized binding ratio of pyocin R2 on *P. aeruginosa* 13s cells. Red and blue bars present the ratio between the normalized binding frequency of the pole and mid region of a cell, respectively.

5.2.2 Single pyocin trajectories

Next, we collected some dynamic data as a proof of principle to show that the procedure can be used to investigate the dynamic interactions between pyocins and host over time. Therefore, we used the method and workflow described in Chapter 2. Briefly, fluorescently labeled pyocins were added to the flow cell containing immobilized *P. aeruginosa* 13s cells, and dynamic interactions were tracked by means of fluorescence microscopy in HILO mode. Pyocin trajectories were obtained by TrackMate (Fiji) [41], a single-particle tracking software package within Fiji, and track

motility was analyzed in MATLAB using the @msdanalyzer package [42]. We observed a range of pyocin trajectories (*n* = 122) with different characteristics. The majority of these pyocin trajectories were free in solution (Figure **5.3**a). However, in rare events we also observed pyocins interacting with (defined as particles that showed reduced frame-to-frame (FTF) displacements when present at the cell surface) and bound to (showing a low FTF displacement in a confined region at the cell surface during the course of the entire movie), cells of the host strain *P. aeruginosa* 13s (Figure **5.3**b and c).

These trajectories were manually classified, based on visual assessment of interaction with its host, in one of the following regimes: *free* in solution, *interacting* with host cell in a reversible manner, and *bound* to the host cell in an irreversible manner. The latter was defined as pyocins that interacted with its host in a confined spherical region throughout the course of the movie. For each individual trajectory, the mean square displacement (MSD) was calculated as a function of the delay time. We used the MSD analysis to examine the type of diffusion regime, as well as, to estimate the diffusion coefficient *D*. A clear distinction in both the α exponent (slope) and offset *C* (intersection with the y-axis) between the three classified groups was observed (Figure **5.4**).

To characterize the type of motion, the exponent α was determined for each trajectory within the classified groups by fitting a linear line with equation 5.1.

$$log(MSD) = \alpha\, log(\tau) + C \qquad \text{Equation 5.1}$$

We determined the slope of the corresponding relationship between MSD as a function of delay time τ over the first 25% of the log-log transformed curve. This to prevent the large relative standard deviation of the MSD (fluctuations caused by the reduced number of displacement points) at large time lags, as recommended by [43, 44]. The trajectories classified as free in solution exhibited a mean exponent α of 1.02 $\pm$ 0.22 (mean $\pm$ SD, *n* = 117). The fit has a R^2 of 0.941 $\pm$ 0.076 (mean $\pm$ SD), indicating that the average MSD curve was well approximated by a straight line. Variable α showed a normal distribution (Supplementary figure ***5.1***) with a mean that did not deviate significantly from α = 1 (Figure **5.5**). This result indicates that pyocins free in solution exhibit normal (Fickian) diffusion, which is consistent with free diffusion in bulk. This was corroborated by analysis of the velocity, in which we checked whether the generated displacements (i.e. instantaneous velocity, as our displacements were computed over varying frame intervals) were uncorrelated. In case of Brownian motion, both the displacement in x and y direction should be centered at 0. Indeed, our results showed this with close approximation, with mean values of - 0.08 $\pm$ 13.25 and 0.15 $\pm$ 13.43 μm/s (mean $\pm$ SD, *n* = 117) for x and y, respectively (Supplementary figure ***5.2***). This showed that the displacement was uncorrelated, indicating that pyocin particles moved randomly (displacement in both x and y were equally likely to occur), as expected for pure Brownian motion, and can therefore directly be compared to results

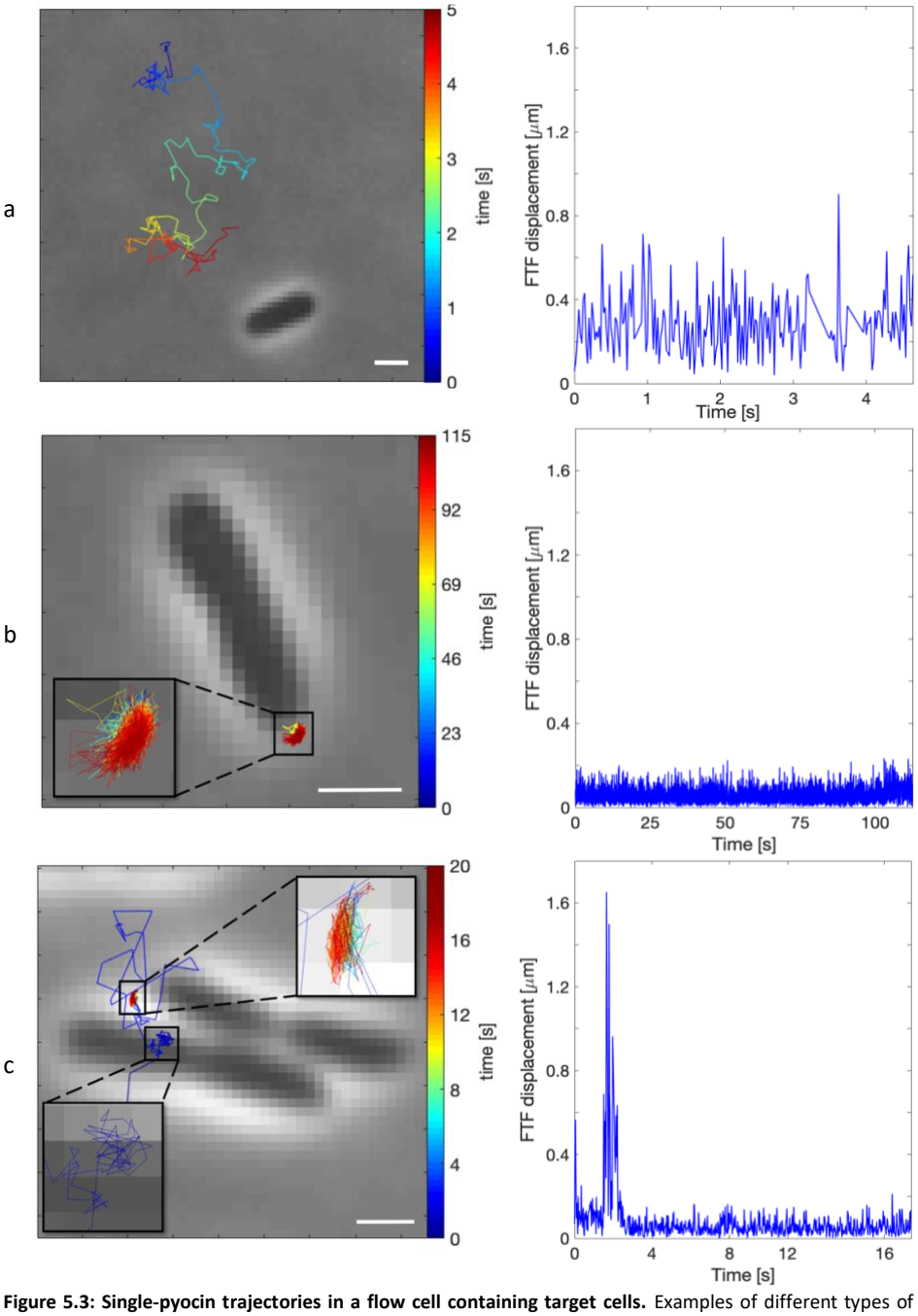

Figure 5.3: Single-pyocin trajectories in a flow cell containing target cells. Examples of different types of observed trajectories with respect to interaction with a cell. Left windows: overview of the trajectory, with color indicating time. Right window: frame-to-frame (FTF) displacement of the corresponding trajectories as a function of time. **a,** Pyocin free in solution. **b,** A irreversibly bound (and potentially contracted) pyocin to a host cell (*P. aeruginosa* 13s). **c,** A reversibly bound pyocin interacting with a host cell. Scale bar represents 1 μM.

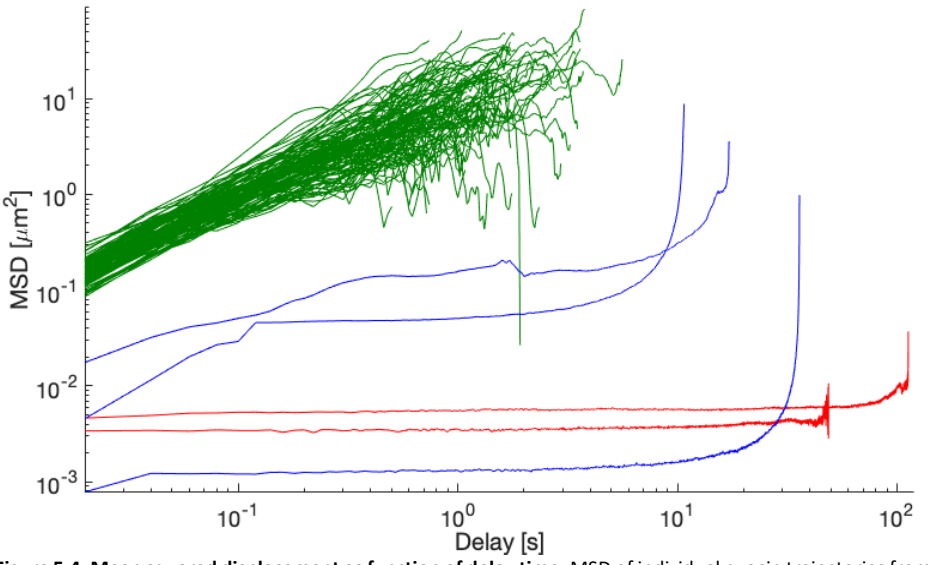

Figure 5.4: Mean squared displacement as function of delay time. MSD of individual pyocin trajectories from three classes: free, interacting, and bound trajectories color coded in green, blue, and red, respectively.

obtained in bulk. Next, the diffusion coefficient was calculated by first computing the weighted average over all MSD curves of pyocin particles free in diffusion that had an α exponent > 0.8 (giving an R^2 of 0.998), discarding particles that exhibited multiple types of diffusion (e.g. freely diffusion particles that interacted briefly with glass), giving a more realistic approximation of the diffusion coefficient of the population. Here, the weighting was performed relative to the number of averaged data points per time-delay value in individual curves. The resulting diffusion coefficient was 3.42 $\pm$ 2.45 $\mu m^2/s$ (mean $\pm$ SD, n = 90). A size indication of the particle was approximated by extracting the radius for a spherical particle for the given diffusion coefficient. This gave a radius of 63 nm, which, even though the particle has an ellipsoid shape, aligns perfect with the 60 nm radius of R2-type pyocin particles observed by EM (dimensions of sheath: 120x24 nm [35]). Taken together, these results corroborate the validity of the approach taken, demonstrating that labeled pyocins within a flow cell reveal normal diffusion, and therefore behave as expected.

In a similar fashion, we examined the type of diffusion of trajectories categorized as *interacting* (n = 3) and *bound* pyocins (n = 2). Here we found an α exponent of 0.04 (R^2 = 0.705, n = 2) for the *bound* pyocins, demonstrating constrained motility within a region with radii of ~100 and ~56 nm. These results correspond well with our visual inspection of the trajectories. In contrast, pyocins from the *interacting* category had an α exponent of 0.22 $\pm$ 0.12 (Mean $\pm$ SD, R^2 = 0.743 $\pm$ 0.029, n = 3), revealing sub-diffusive motility. However, care should be taken with regard to interpretation of these values, as these trajectories consist most likely out of at least two types of diffusive motion regimes (free and on-cell motion). To warrant the interpretation with regard to the type of on-cell diffusion these regions should be isolated from sections of the trajectory that were free in solution allowing for independent fitting of the α exponent. However, due

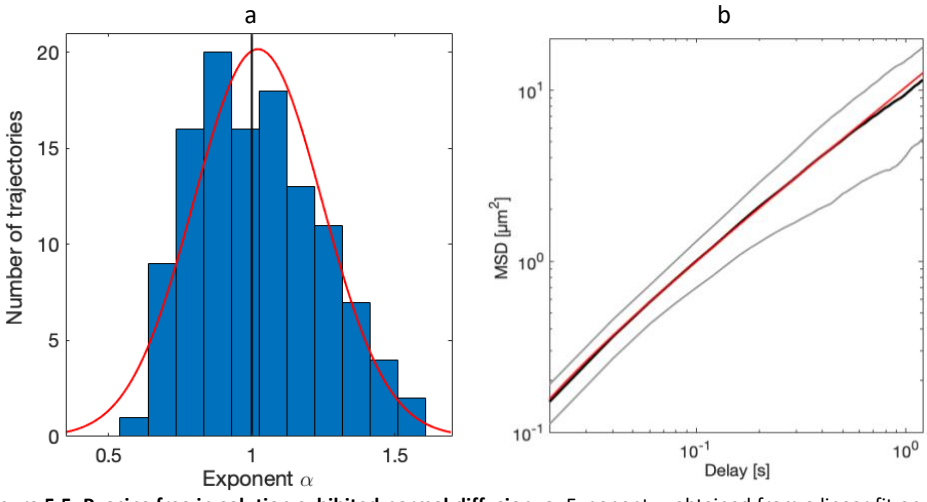

Figure 5.5: Pyocins free in solution exhibited normal diffusion. a, Exponent α obtained from a linear fit on the first 25% of each individual trajectory curve in a log-log plot of MSD as function of delay time for individual pyocin trajectories free in solution. The red curve presents fit for normal distribution. The black line presents the mean α exponent. **b,** Diffusion coefficient estimation by means of a linear weighted fit (red line) on the first 25% of the weighted average of the MSD curve (black line). Area between the gray lines represents the weighted standard deviation of all individual MSD curves.

to the limited number of interacting trajectories within the data set we decided not to proceed in this direction. The interaction regions of the trajectory presented in Figure **5.3**c, span radii of ~180 and ~100 nm, with the former representing an interaction area larger than the reach of a pyocin tethered to a single tail fiber, indicating that a mode of tethered near/on-cell motion might have occurred opposed to the alternative explanation of hopping (repeated binding and unbinding events of the pyocin from the cell surface). The latter requires several rebinding events within the same area, which was deemed to be unlikely [57, 58]. The two remaining trajectories within the *interacting* category (Supplementary figure ***5.3***) resemble more the characteristics of the *bound* pyocins as they showed prolonged cell-interaction (10.6 and 35.9 seconds) within a confined region (radius ~36 nm). However, these particles detached and therefore were classified as *interacting*. Surprisingly, they detach without showing any visible increase in movement before leaving the cell.

Overall, these first few trajectories show that this method can be extended in its use to observe and study single-pyocin behavior, opening new possibilities to gain nanoscopic insights into the target-finding and killing process of pyocins.

5.2.3 Depolarization of cells upon exposure to pyocins

Lastly, we were interested in extending the reach of this method to study the bactericidal activity process. Therefore, we i) optimized the concentration of a cationic membrane permeable fluorescent dye $DiSC_3(5)$ that can be used to follow the depolarization process of a cell, and ii) subsequently investigated whether this dye has the potential to be used to track bactericidal activity of single-pyocin R2 particles. The uptake of the dye by the cell depends on both the plasma and mitochondrial membrane potential. Hence, cell hyperpolarization results in uptake of the positively charged

cyanine dye molecules by the cell till the Nernstian equilibrium is reached, whereas depolarization results in the release of dye molecules. Therefore, the mean fluorescent intensity of the cell can be directly correlated to the intracellular dye concentration.

In order to visualize cell depolarization, we first assessed what the optimal $DiSC_3(5)$ dye concentration was for use with *E. coli* B cells with respect to cell viability and detection of changes in membrane potential in our flow cell. To this end, *E. coli* B cells were examined in the presence of three different dye concentrations: 80 μM, 400 μM, and 2 mM. This was accomplished by a 10-minute incubation of the dye with cells grown to exponential phase, followed by pelleting of the cells and resuspension in a fresh buffer to remove excessive dyes from the environment. Labeled cells were loaded into a flow cell and immobilized to the surface, as described in Chapter 2. For each condition tested, we captured at least two images and analyzed a total of 100 cells. The fluorescence intensity of a cell was quantified by analysis of the mean pixel intensity along a line following the long axis of the cell. Subsequently, we examined the signal-to-background ratio to identify the optimal dye concentration. This was achieved by dividing the obtained mean intensity of each cell by that of the corresponding background, defined as an ROI immediately adjacent to the cell. Results revealed that staining cells with both 80 and 400 μM resulted in a similar signal-to-background ratio, while a higher concentration of 2 mM dye resulted in a significant decrease of signal-to-background ratio (Bonferroni corrected Mann Whitney U test; $n = 200$, $p < 0.001$; Figure **5.6**). Since, the intensity profile of cells stained with 400 μM was higher than that for cells stained with 80 μM (Figure **5.7**), making it easier to visualize cells, we decided to continue our experiments with staining *E. coli* B cells with 400 μM $DiSC_3(5)$.

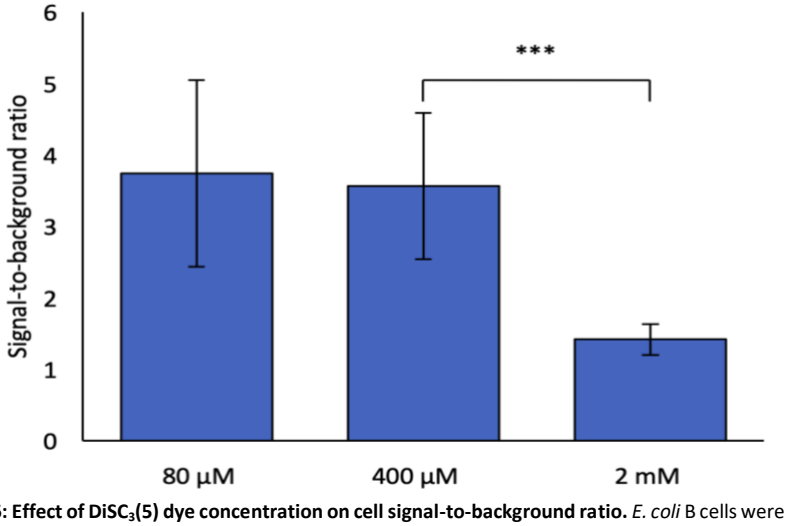

Figure 5.6: Effect of $DiSC_3(5)$ dye concentration on cell signal-to-background ratio. *E. coli* B cells were stained with three different concentrations of the membrane-potential sensitive dye $DiSC_3(5)$ and the signal-to-background ratio of individual cells were measured per tested condition. Error bars indicate standard deviation. Asterisks above brackets indicate significance of effect of dye concentration (***: $p < 0.001$).

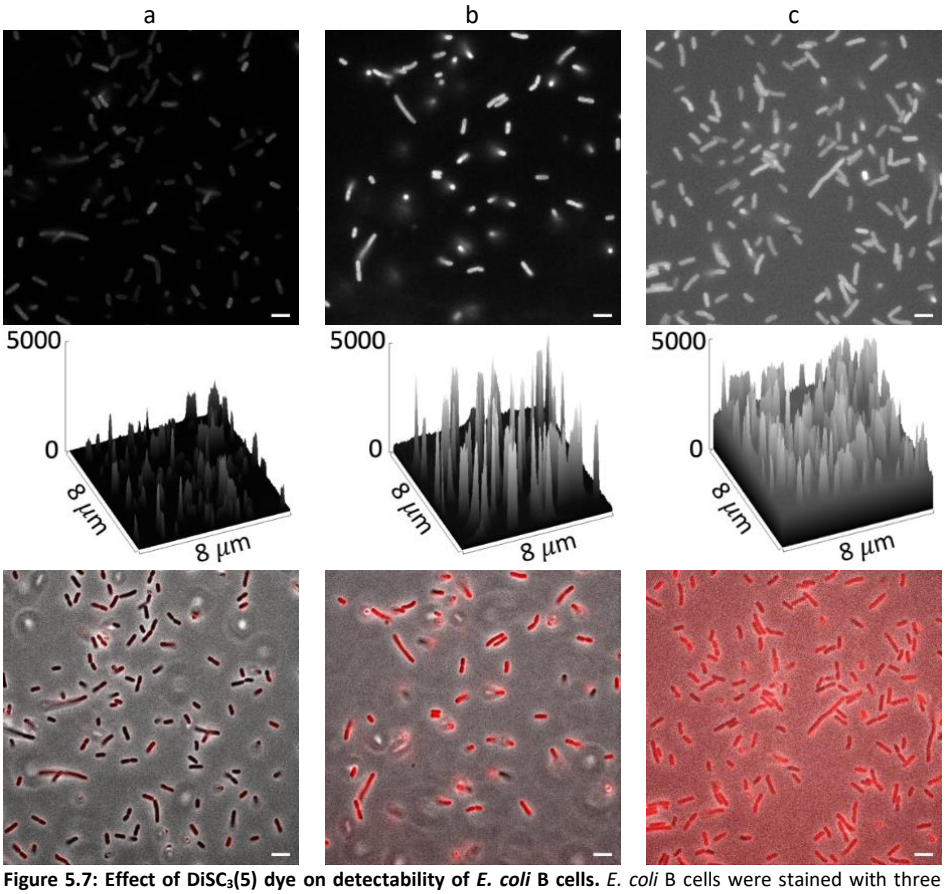

Figure 5.7: Effect of $DiSC_3(5)$ dye on detectability of *E. coli* B cells. *E. coli* B cells were stained with three different concentrations of the membrane-potential sensitive dye DiSC3(5), with **a**, 80 μM, **b,** 400 μM, **c,** 2 mM. Fluorescent images (top), their intensity profile (middle), and an overlay (bottom) between the fluorescent image and phase contrast image. Fluorescent images were taken with an exposure time of 100 ms, an EM gain of 100, and a laser intensity of 424 μW. Scale bar presents 5 μM.

The optimal dye concentration for staining cells might differ between bacterial species and strains. Since we want to study the depolarization of cells upon bactericidal activity of pyocin R2, we performed this staining experiment on the target strain of pyocins, *Pseudomonas aeruginosa* 13s. Qualitatively, we found similar results to staining *E. coli* B cells, where the highest fluorescent intensity and signal-to-background ratio was obtained for a concentration of 400 μM dye (Figure **5.8**). Taken together, these observations led us to conclude that 400 μM $DiSC_3(5)$ dye is optimal to stain the cells, independent of the tested bacterial strain.

To examine whether the presence of $DiSC_3(5)$ in the environment affects the bactericidal activity of pyocin R2, we estimated the killing efficiency using a bactericidal droplet assay. Here we mixed pyocin R2 with and without a final concentration of 10 μM $DiSC_3(5)$ dye. This was followed by a five-fold serial dilution and subsequent pipetting small droplets on an actively growing lawn of the host indicator strain

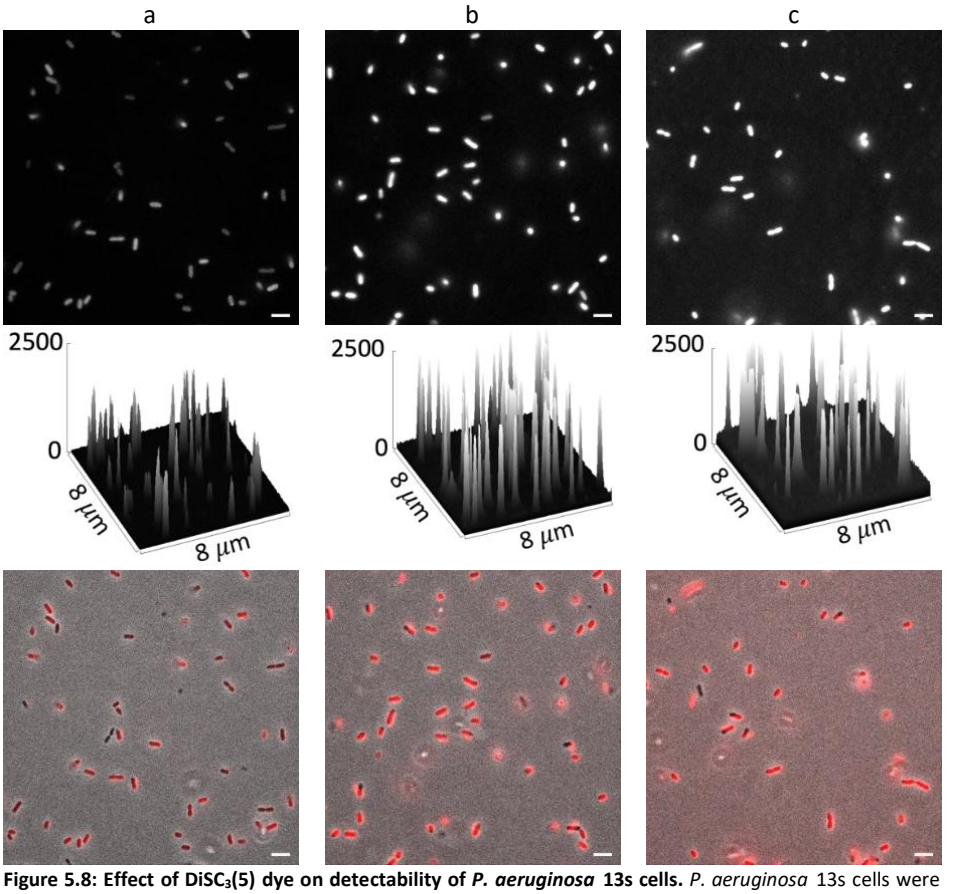

Figure 5.8: Effect of $DiSC_3(5)$ dye on detectability of *P. aeruginosa* 13s cells. *P. aeruginosa* 13s cells were stained with three different concentrations of the membrane-potential sensitive dye $DiSC_3(5)$, with **a,** 80 μM, **b,** 400 μM, **c,** 1 mM. Fluorescent images (top), their intensity profile (middle), and an overlay (bottom) between the fluorescent image and phase contrast image. Fluorescent images were taken with an exposure time of 100ms, an EM gain of 100, and a laser intensity of 424 μW. Scale bar presents 5 μM.

P. aeruginosa 13s. After overnight incubation at 37 °C, we assessed the effect of dye on the bactericidal activity by qualitatively comparing the lowest dilution factor that still showed a clearing zone. The results showed no observable difference between the bactericidal activity in presence and absence of the dye, indicating there were no large effects of the dye on pyocin mediated killing (Figure **5.9**). In addition to testing the effect of the dye on the functionality of pyocins, we also assessed the effect of the dye on the growth rate of cells. Here we observed no difference in growth rate in the presence of dye (data not shown).

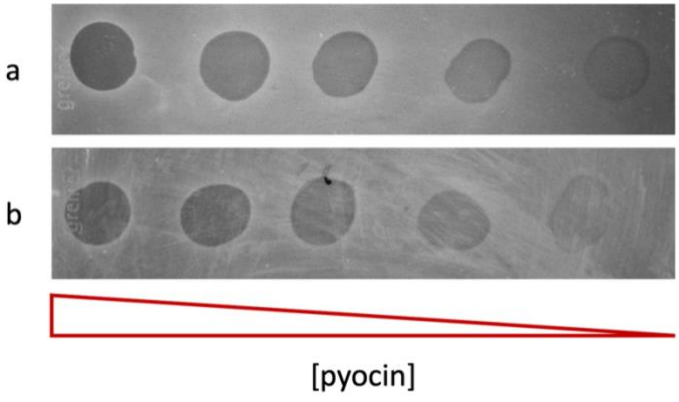

Figure 5.9: Effect of $DiSC_3(5)$ dye on bactericidal activity of R2-type pyocins. Bactericidal droplet assay showing the bactericidal activity of R2-type pyocins in five-fold serial dilution on the target indicator strain *P. aeruginosa* 13s after overnight incubation at 37 °C. **a,** Without the presence of $DiSC_3(5)$ dye. **b,** Pyocins mixed with 10 μM $DiSC_3(5)$ dye. Clearing of the bacterial lawn (dark areas) indicated cell death.

After having established the optimal dye concentration to label cells, we confirmed if this method was capable of detecting depolarization of cells. This was assessed by labeling *E. coli* B and 13s cells with 400 μM $DiSC_3(5)$ dye, immobilizing them in the flow cell, and exposing them to ethanol, which leads to rapid weakening/destruction of the membrane. Both phase contrast and fluorescent images were taken before and after insertion of ethanol in the flow cell. Phase contrast images were used to confirm the presence and position of cells, while the fluorescent image was used to assess the detection of depolarization of cells by qualitatively comparing the fluorescent intensity of cells before and after exposure to ethanol. The results showed a clear effect of ethanol on the fluorescence intensity of both *E. coli* B and *P. aeruginosa* cells, where the fluorescent intensity of cells decreased substantially and could no longer be distinguished from background signal (Figure **5.10** and Figure **5.11**, respectively). The phase contrast images still showed the presence of cells, indicating complete loss of membrane potential upon exposure to ethanol. These results demonstrate that our experimental set-up can be used to detect depolarization of cells.

Next, we tested the ability to observe depolarization of cells by the bactericidal activity of R2-type pyocins using our set-up. This was assessed by time-lapse imaging of fluorescently labeled $DiSC_3(5)$ cells immobilized to the substrate with and without the presence of pyocins (n = 3 replica experiments per tested condition). Pyocins were inserted in the flow cell by pipet, and imaging started as soon as possible, within approximately 40 seconds after their insertion. A 2-minute time interval was used between images. We quantified changes in membrane potential by examining how the normalized average fluorescence intensity of the cells (fluorescence at t divided by fluorescence at t=0) changed as a function of time in the presence and absence of pyocin particles (number of cells observed n = 178 and n = 232, respectively). We found that the average fluorescence intensity of labeled *P. aeruginosa* 13s cells over time upon exposure to pyocin R2 decreased rapidly over time (Figure **5.12**). However, we also observed a decrease in fluorescent intensity level of cells in the absence of pyocins.

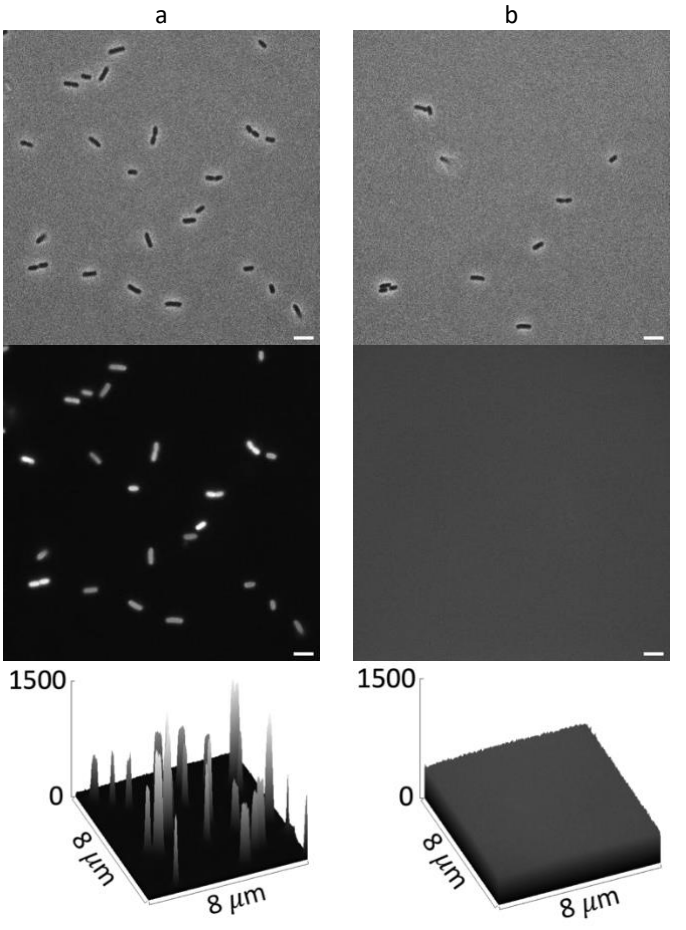

Figure 5.10: Effect of ethanol on depolarization of *E. coli* B cells. *E. coli* B cells were prestained with 400 μM depolarization dye $DiSC_3(5)$. **a,** Before and **b,** after exposure to ethanol. Phase contrast images (top), fluorescent images (middle), their intensity profile (bottom). Fluorescent images were taken with an exposure time of 100ms, an EM gain of 100, and a laser intensity of 172 μW. Scale bar presents 5 μM.

The latter could be attributed to the effect of bleaching of the accumulated dye molecules over time. To examine if there is an effect of depolarization of cells upon exposure to pyocins we compared the normalized intensity levels of the two treatments for each given time point. Results showed that the normalized fluorescence intensity in the presence of pyocins was significantly lower than that in the absence of pyocins for each given time point (Bonferroni corrected Mann-Whitney U test; $n = 337$, $p < 0.001$; Figure **5.13** and Figure **5.14**). To confirm that depolarization of cells was indeed due to the bactericidal activity of pyocins and not by the presence of other components within the buffer, we exposed the pyocin solution to fluorescently labeled *E. coli* B cells, a pyocin insensitive strain (Supplementary figure ***5.4***), and qualitatively tracked the fluorescent intensity of single cells over time. We observed a slight but no sudden drastic substantial loss of fluorescent intensity upon exposure to pyocins (Figure **5.15**). The slight loss of fluorescent intensity over time qualitatively resembled that of the

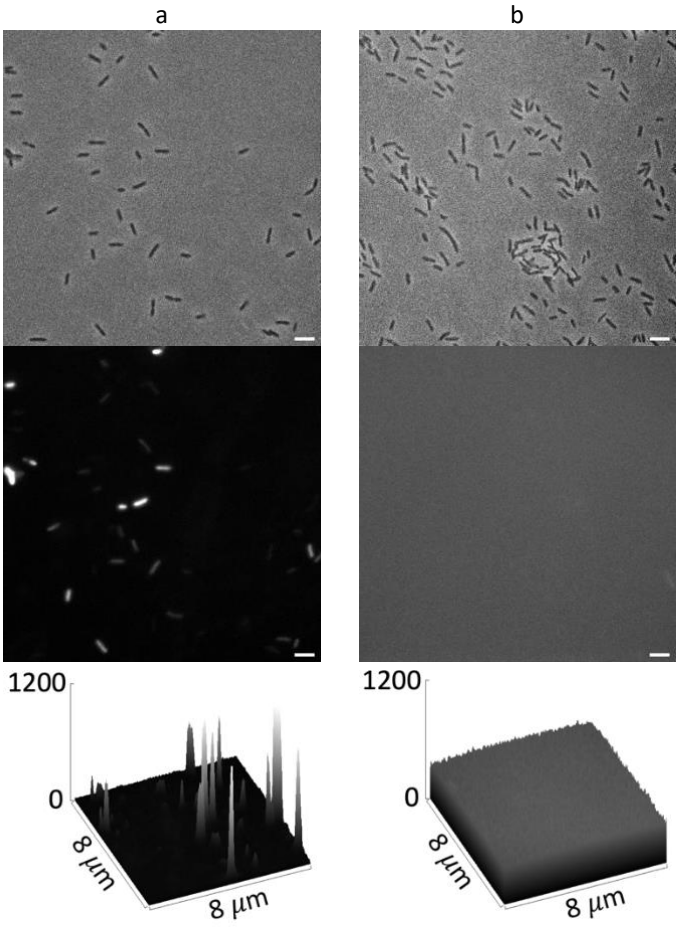

Figure 5.11: Effect of ethanol on depolarization of strain *P. aeruginosa* 13s cells. *P. aeruginosa* 13s cells were prestained with 400 μM depolarization dye $DiSC_3(5)$. **a**, Before and **b**, after exposure to ethanol. Phase contrast images (top), fluorescent images (middle), their intensity profile (bottom). Fluorescent images were taken with an exposure time of 20ms, an EM gain of 100, and a laser intensity of 172 μW. Scale bar presents 5 μM.

experiments with *P. aeruginosa* 13s cells in absence of pyocins. Even though not quantified, these observations support the fact that the loss of fluorescent signal of *P. aeruginosa* 13s cells upon exposure to pyocins was caused by depolarization of the cells as response to the bactericidal activity of pyocin R2. Overall, these results show that our experimental method is capable of detecting single-cell depolarization of pyocins. In addition, it has the potential to be used in combination with simultaneous tracking of pyocins labeled with Alexa488, which were already previously used in experiments involving tracking of the dynamical interaction described in section 5.2.2.

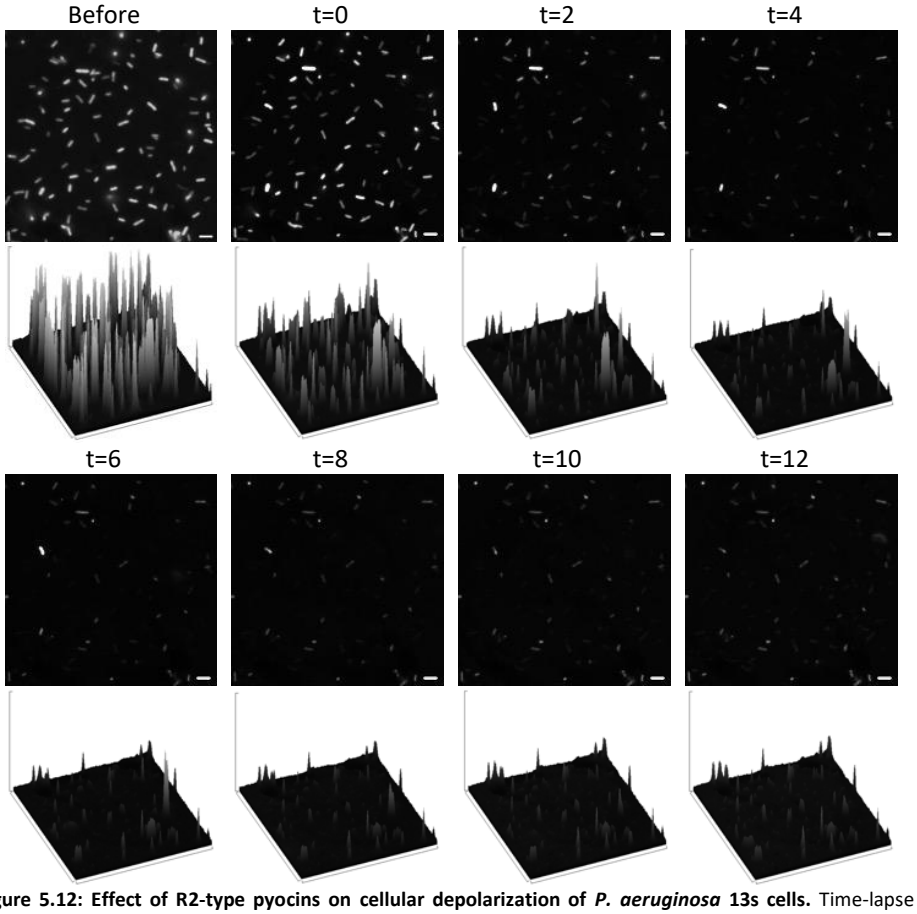

Figure 5.12: Effect of R2-type pyocins on cellular depolarization of *P. aeruginosa* 13s cells. Time-lapse images of fluorescently labeled *P. aeruginosa* 13s cells, stained with 400 μM depolarization dye $DiSC_3(5)$, exposed to pyocins. One image was taken before pyocins were inserted in the flow cell. Others were taken directly after insertion of pyocins in the flow cell, with t=0 taken as soon as possible (approximately 40 seconds after insertion). A two-minute time interval was used between images. Fluorescent images (top) and their corresponding intensity profile (bottom). Fluorescent images were taken with an exposure time of 100ms, an EM gain of 100, and a laser intensity of 172 μW. Scale bar presents 5 μM.

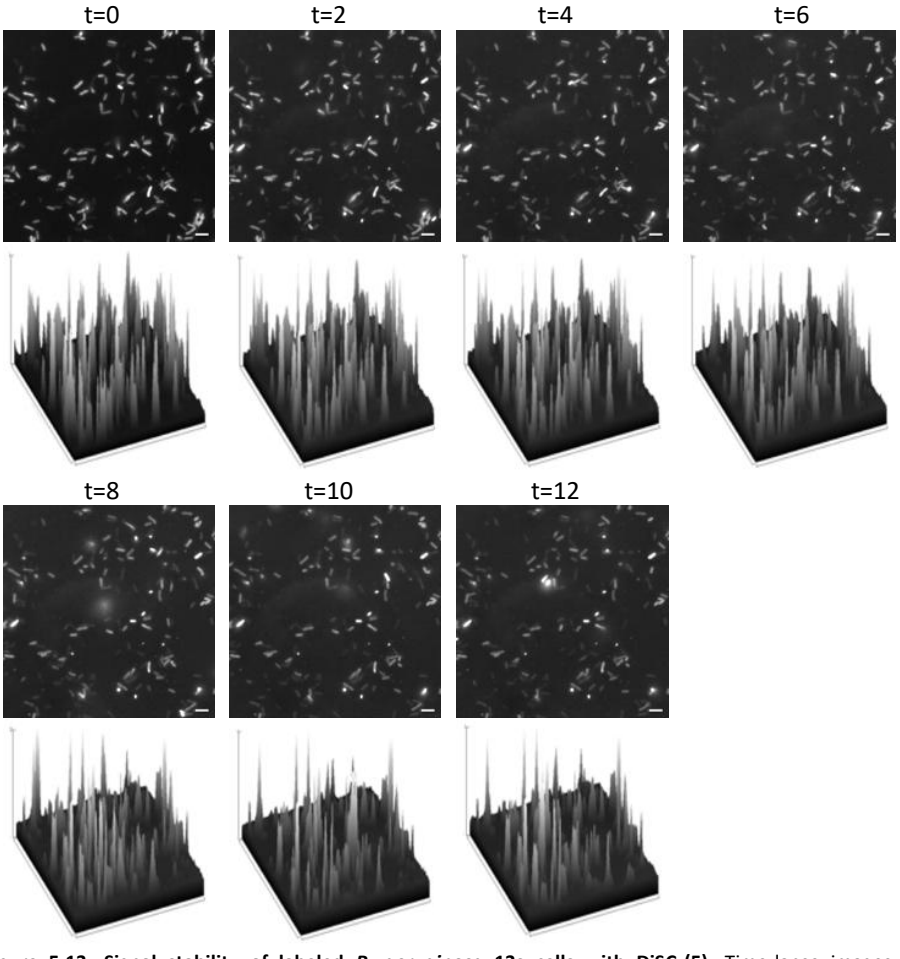

Figure 5.13: Signal stability of labeled *P. aeruginosa* 13s cells with $DiSC_3(5)$. Time-lapse images of fluorescently labeled *P. aeruginosa* 13s cells stained with 400 μM depolarization dye $DiSC_3(5)$. Images were taken every two minutes. Fluorescent images (top) and their corresponding intensity profile (bottom). Fluorescent images were taken with an exposure time of 100ms, an EM gain of 100, and a laser intensity of 172 μW. Scale bar presents 5 μM.

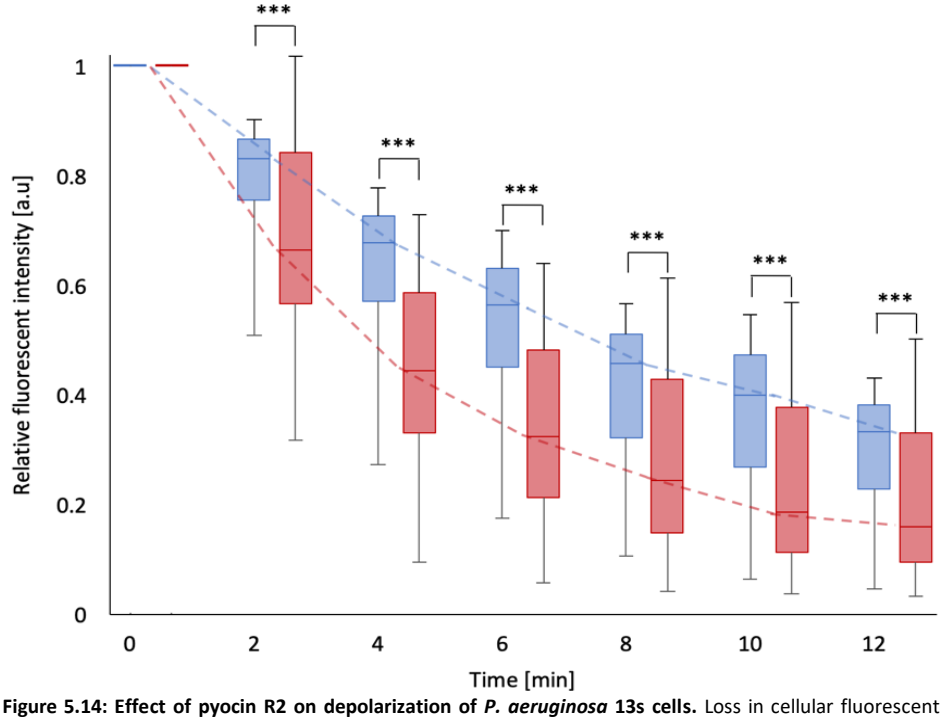

Figure 5.14: Effect of pyocin R2 on depolarization of *P. aeruginosa* 13s cells. Loss in cellular fluorescent intensity of the membrane-potential sensitive dye $DiCS_3(5)$ in *P. aeruginosa* 13s cells over time. Red and blue bars present with and without the exposure to R2-type pyocins, respectively. The relative fluorescent intensity was established by dividing the fluorescent intensity of a cell at a given time point by the initial fluorescent intensity of the corresponding cell at t=0. Dashed-line guides the eye on the relative drop in fluorescent intensity over time. Error bars indicate the minimal and maximal relative fluorescent intensity. Asterisks above brackets indicate significance of effect of depolarization (***: $p < 0.001$).

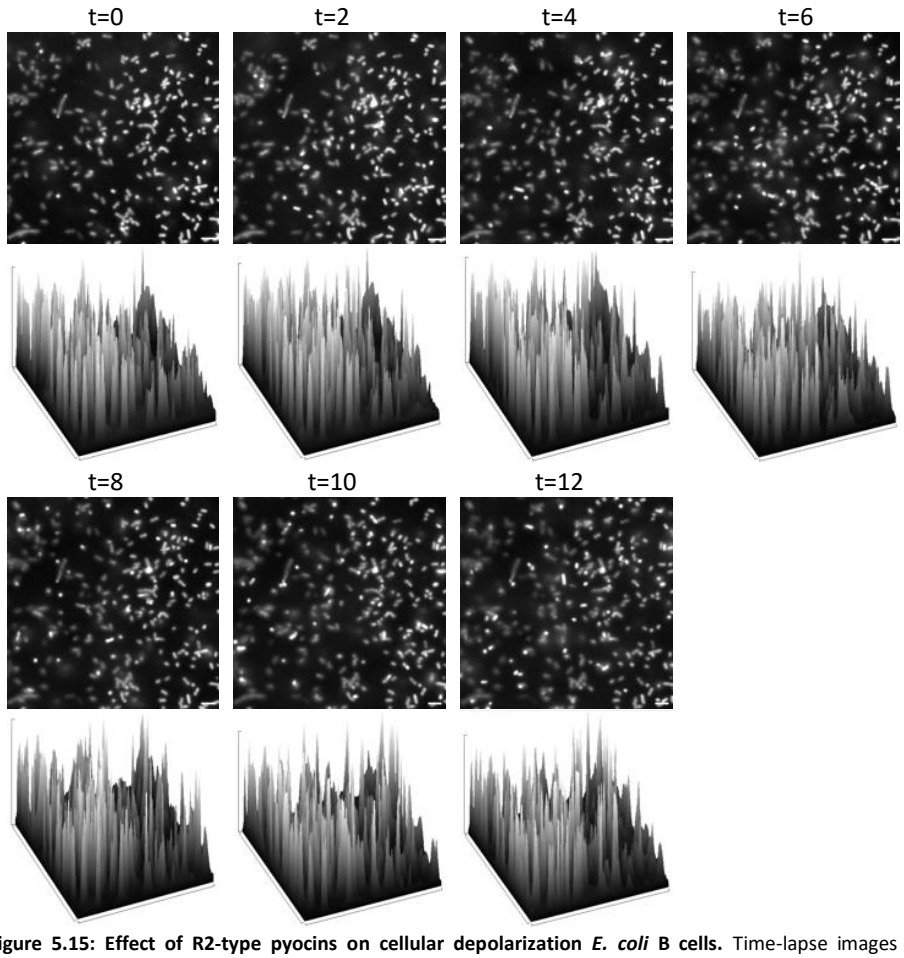

Figure 5.15: Effect of R2-type pyocins on cellular depolarization *E. coli* B cells. Time-lapse images of fluorescently labeled *E. coli* B cells, stained with 400 μM depolarization dye $DiSC_3(5)$, exposed to pyocins. Pyocins were inserted in the flow cell, where after imaging started at t=0, with two-minute time intervals between images. Fluorescent images (top) and their corresponding intensity profile (bottom). Fluorescent images were taken with an exposure time of 100ms, an EM gain of 100, and a laser intensity of 172 μW. Scale bar presents 5 μM.

5.3 Discussion and conclusion

The results on labeling and particle tracking demonstrate that our method allows study of the dynamics of pyocin-cell interactions that govern target finding, binding distributions and kinetics at the single-particle level with high temporal and spatial resolution. In addition, application of the fluorogenic membrane potential-probe $DiSC_3(5)$ allowed detection of pyocin-induced changes in membrane potential. Using these approaches we delivered the first dynamic insight into the interaction between a pyocin and its host cell at the single-particle level, and first direct demonstration of pyocin-induced depolarization of the membrane potential. Pyocin-cell interactions resembled those observed for phages. First of all, observations revealed a strong

binding distribution targeted to the cellular poles. Secondly, tracking single-pyocin dynamics showed three modes of motion also observed for phages: free in diffusion, on-cell sub-diffusive motility, and constrained 'bound' behavior.

Although our method was capable of visualizing the binding distribution and binding dynamics of pyocins, the number of interactions we observed per particle present in the flow cell was low when compared to what we observe with bacteriophages. This could be due to steric hindrance caused by the dye used to detect the pyocins and/or a suboptimal medium for pyocin adsorption (e.g. lacking a co-factor. While this had, as far as we know, a limited impact on the characterization of free pyocins in solution and the observed binding distribution — other than decreasing the likelihood of a binding event — it likely affected the cell interaction dynamics to some degree. One explanation for the low fraction of pyocin particles that interacted with the cell is that the attached dye molecules rendered them to become unstable. However, it is more likely the position and/or the number of dye molecules had an effect on the ability for the tail fibers to interact effectively with host receptors, as was previously observed for phages (Chapter 2 section 2.4.4).

We observed no large effect of the dye on the bactericidal activity of labeled pyocins, hence the capacity to bind, (Chapter 2 section 2.4.4), which on the one hand suggest that the low fraction of observed interactions was not caused by the dye. However, this should be confirmed with a quantitative bacterial survival assay (that counts the surviving cells after pre-incubation with different concentrations of R2-type pyocins) that has the sensitivity to measure at or close to single-cell killing events. On the other hand, it might point towards the lack of binding requiring components within the minimal buffer used for tracking binding interactions at single-particle level. Even though no sensitivity of medium composition towards binding kinetics has currently been documented for pyocin R2, dependency of components within the environment required for binding has been shown for an extended number of phages [45-48] and likely hold true for the similarly structured pyocins. To increase the number of binding event, as well as to limit the effect of dye on the binding properties, we recommend both the optimization of the dye concentration for labeling pyocins, limiting the impact of the effect of dye on the interaction kinetics while retaining enough labels for single-pyocin visualization over time, as well as, studying the effect of medium components on the binding efficiency to establish an ideal buffer that is compatible with fluorescence microscopy imaging.

The observed binding distribution showed a strong resemblance to that observed for phages. It has been suggested by some authors that phages localized at the cellular poles due to a higher rate of successful DNA injection and infection [49]. However, pyocins also seem to preferentially bind to the cellular poles, but do not require DNA injection to perform their function and have a positive fitness contribution on the producing strain. This supports the hypothesis that polar preference of phages and pyocins is likely to be caused by a universal mechanism that is based on TF-receptor mediated interaction and independent of DNA ejection. This idea is corroborated by the first insights in pyocin TF-receptor binding properties and transmission of signals from the TF to the baseplate destabilizing the current conformation and triggering contraction after irreversible binding of multiple TFs [50, 51].

Even though the fraction of pyocin trajectories showing interaction with the cell was very limited, one of the observed cell-interaction areas was larger than the radius that a pyocin tethered to a cell with a single tail fiber can cover, suggesting that pyocins might perform on-cell tethered walking via binding and unbinding of individual TFs. An alternative explanation would be hopping, repeated attach and detach events of the pyocin to the surface. However, this latter explanation was deemed less likely, as it has been opposed that several rebinding events within the same area were unlikely [57, 58]. Extended research, involving detailed analysis of these areas, with for example a step-finder (Chapter 2 section 2.6.4.3), will help unravel the nature of this interaction. If tethered on-cell motion occurs, it is likely that the underlying mechanism is similar to that observed for phages, which has been hypothesized to involve sequential alternating association and dissociation of TF-receptor interaction (referred to as 'walking') as a mechanism to 'explore' the cell surface for an area fit for binding.

We observed two trajectories that released from the cell surface without an increase in their diffusive motion before detachment after prolonged cell interaction within a confined area. Representing the first evidence (n =2) of reversible binding at single particle level of pyocin. We would expect this when unbinding involves step-wise release of tail-fibers as opposed to one-step release. This phenomenon has also been observed for T4 phages in Chapter 4. One possible explanation for this phenomenon could be the limitation of our optical resolution and/or method, where the detection was not sensitive enough to detect such changes in movement caused by a difference in the number of attached TFs. This could be caused by the fact that the center of intensity of the fluorescently labeled pyocin was close to the cell surface (below that of the pixel resolution). Any change in the angle of the position of pyocin relative to the cell surface will only lead to a small relative movement, which might be too low to be detected. However, an alternative explanation could be that detachment was caused by a 'failed' attempt to puncture the cell, where the force exerted caused instantaneous detachment of the pyocin.

So far, the dissipation of the membrane potential has only been studied at bulk level [37, 38]. Here we showed the possibility of studying the bactericidal activity at single-particle level, which is a first step toward combining the detection and monitoring the behavior between single pyocin and cell. Irrespective of the $DiSC_3(5)$ dye concentration and bacterial strain (*E. coli* B or *P. aeruginosa* 13s), the cell population was not uniformly stained and showed considerable variation in fluorescent intensity. Several underlying causes have been documented aiding variation in staining. Firstly, a very high concentration of dye molecules in some cells has been shown to lead to quenching of the fluorescence [52, 53], and hence the variations in fluorescent intensity. Secondly, poly-L-lysine, with which our slides were coated to facilitate cell adhesion, has been reported to be capable of partial dissipation of the membrane potential [54]. The effect of quenching might also explain the observed decrease in signal-to-noise ratio for the use of an increased dye concentration. This effect has been observed before by te Winkel *et al.* [52], who described that an increase $DiSC_3(5)$ dye concentration, as well as, a high density of cells, led to a better visual signal of labeled cells but also reduced the measurable difference in fluorescent intensity that could be correlated to the membrane potential.

Overall, the method allowed us to detect depolarization of cells in response to the presence of pyocins. Since our imaging (t=0) started tens of seconds after addition of the pyocins to the flow cell, the detected effect of the pyocins, relative to the effect of bleaching, was most likely an underestimation. This was corroborated by the drastic difference of the relatively low fluorescent intensity of the cells at t=0 compared to reference images (before) of cells without pyocins. This implies that either the bactericidal activity of pyocins was very rapid, or more likely that the concentration of pyocins was very high, giving the extreme drop of fluorescent intensity between the before and first image after insertion of pyocins in the flow cell (t=0). Future experiments should track the time between insertion of pyocins to the flow cell and the start of imaging, so the initial state of the level of fluorescent intensity (before image) can be used as a new reference point (t=0), in addition to lowering the concentration of pyocins inserted in the flow cell to increase the time resolution without intensifying the effect of bleaching. Since the cellular concentration of dye follows a Nerstian distribution, detection of fluorescence signals can be coupled to quantitative kinetic measurements. This has previously been shown by te Winkel *et al*. that used this dye for quantifying the effect of membrane-targeting antimicrobials on the membrane potential [52]. In addition, this method has shown to be compatible with simultaneous detection of $DiSC_3(5)$ and GFP [52]. As we have demonstrated that pyocins can be labeled with Alexa488 NHS-ester dyes that overlap with the spectrum of GFP, simultaneous tracking of both the target-finding and killing process of pyocins could be envisioned. This opens possibilities towards studying a direct correlation between pyocin number and cell depolarization rate. It also has the advantage that it allows for examining the effectiveness of bactericidal activity of pyocins and their heterogeneity among the population.

Taken together, our results show that the described approaches can in principle be used to simultaneously detect pyocin location and membrane potential, providing a way to gain insights into the mechanisms that underpin target-finding and killing by pyocins. As such, this approach will contribute key information for the engineering of pyocins as antibacterial agents in a more fine-tuned manner. Despite the fact that certain conditions need further optimization or testing, i.e. labeling concentration, medium composition, and further development of quantitatively measuring the membrane dissipation, we believe that this approach will likely be of great value to the study of other PTLBs. Our first insights suggested pyocins might not only bear a high resemblance to phages of the *myoviridae* class in terms of their structure, but also in terms of their interaction dynamics and binding distribution.

5.4 Experimental procedures

5.4.1 Strains, media, and growth conditions

P. aeruginosa strains PAO1 and 13S were kindly provided by AvidBiotics Corporation [20] and grown on tryptic soy broth at 37 °C and 250 rpm. *Escherichia coli* B (ATCC 11303) was grown in Lysogeny broth (LB) (Sigma) at 37 °C and 250 rpm. Pyocins were obtained by PAO1 strain induction in G medium [55] with 50 μg/ml gentamicin, as described by Williams *et al.* [20]. 13S served as target indicator strain for R2-type pyocins. TN50 buffer (10 mM Tris-HCL [pH 7.45], 50 mM NaCl) was used for pyocin storage.

5.4.2 Pyocin purification and assays

To obtain and purify R2-type pyocins, as well as, assess their concentration and viability we applied the protocol described by Williams *et al.* [20]. Here an overnight culture of PAO1 was diluted 1:100 in G medium that had been supplemented with 50 μg/ml gentamicin. Cells were continued to grow at 225 rpm and 37 °C till an OD_{600} of 0.25 was reached. Mytomycin C was added at a final concentration of 3 μg/ml and growth was continued for an additional 2.5 hours. A final concentration of 2 U/ml DNase I (Invitrogen) was added and incubated for 30 min. The sample was centrifugation at 17,000 x g for 1 h to remove cell debris. Next, saturated amounts of ammonium sulfate (4 M) were added to the pyocin supernatant at a rate of 1 ml/min. During this time the solution was continuous homogenized and kept at 4 °C until a final concentration of 1.6 M ammonium sulfate was reached. Here after, the suspension remained at 4 °C overnight. Next, the suspension was pelleted at 17,000 x g for 1 h at 4 °C, followed by resuspension of the pellet in TN50 buffer in $1/10^{th}$ of the original culture volume. This was followed by a second centrifugation step at 58,000 x g for 1 h at 4 °C and resuspension of the pellet in TN50 buffer in $1/20^{th}$ of the original culture volume and stored at 4 °C until further use.

A bactericidal droplet assay was used to confirm the activity of pyocins. Therefore, pyocin samples were serially diluted in fivefold in TN50 buffer. Aliquots of 10 μl were placed onto a double-layered agar plate containing the growing target indicator strain *P. aeruginosa* 13s. Plates were incubated overnight at 37 °C and activity was analyzed in semi-quantitative manner by assessing distinct clear 'killing'-zones on the bacterial lawn.

Impurity and fraction of contracted particles was determined by visualization of negative stain transmission electron microscopy (TEM). 3 μl of sample was placed on a glow-discharged coper EM grid with a 400 Mesh Carbon film (Aurion) for 3 minutes, followed by blotting and washing the grid three times with 5 μL MiliQ, and staining the sample 1 min with 3 μl 1-2% uranyl acetate, followed by a last round of blotting. Samples were imaged at JEOL JEM-1400plus TEM, with an acceleration voltage of 120 kV and EDS detector.

5.4.3 Fluorescent labeling and microscopy of pyocins

Pyocins were concentrated and washed with a amicon ultra-0.5 centrifugal filter unit (100 kDa cutoff, Millipore) in PBS (sigma) supplemented with freshly made 0.1 M

sodium bicarbonate. Followed by fluorescent labeling, where labeling with Alexa Fluor™ 488 NHS-Ester (Thermo Fisher) was used for tracking pyocins over time and labeling with Alexa Fluor™ 647 NHS-Ester (Thermo Fisher) was used for obtaining the static binding distribution. Labeling was performed with a final concentration of 0.05 mg ml^{-1} Alexa dye for at least 3 h at RT, followed by washing using a amicon ultra-0.5 centrifugal filter unit (100 kD, Millipore) in TN50 and stored at 4 °C until use.

For obtaining the binding distribution (static imaging), *P. aeruginosa* 13s cells were stained with DAPI at a final concentration of 18 μM.

Static images were obtained by pre-incubating labeled pyocins with *P. aeruginosa* 13s cells for 10 min, followed by adhesion to the flowcell, as has been described in chapter 2. Images were obtained with an Olympus inverted microscope (IX81) with a widefield illumination system. Fluorescence excitation was provided by a high-power Andor AMH-200-F6S lamp. As detection device, we used an EM-CCD (Andor Luca R) containing a chip size of 1004x1025 pixels and a resolution of 79 nm/pixel. A UPlanFLN objective was used with a 100x magnification, numerical aperture of 1.3 and a working distance 0.2mm. The following filter cubes were used, DAPI-1160B-OMF-ZERO for observing DAPI stained cells, and CY5-4040B-OMF-ZERO for observing ALEXA488 labeled pyocins, respectively. To image pyocins, the Electron-Multiplying (EM) gain was set to 100, the exposure time to 100 ms, and the white light bulb intensity at 424 μW, while for imaging cells a setting of 52, 80 ms and 346 μW was used, respectively.

Tracking of pyocin particles in real time was performed by adding labeled pyocins to a flow cell containing immobilized *P. aeruginosa* 13s cells, as has been described in chapter 2. Fluorescent and phase contrast images were obtained using a Nikon inverted microscope (Ti2-E) with a TIRF illumination system (Gataca iLAS2). This set-up contained an Olympus CW laser, 488 nm with a maximum output power of 150mW, for fluorescence excitation of fluorophore Alexa488. Emission filter 525/50 was used. A Nikon Apo TIRF objective was used with a 100x magnification, numerical aperture of 1.49 and working distance of 0.12 mm. The detection device was a dual set-up with an EM-CCD (Andor iXon Ultra 897) containing a chip size of 1004x1025 pixels for the fluorescent channel and an EM-CCD (Retiga R1) with a chip size of 1376x1024 pixels for the phase contrast channel. The resolution for the fluorescent and phase contrast images was 161 and 63.5 nm/pixel, respectively. Fluorescent imaging was performed in HILO mode. To image pyocins, the Electron-Multiplying (EM) gain was set to 100, the exposure time to 20 ms, and the laser intensity at 132 μW, while for imaging cells a setting of 100, 20 ms and 178 μW was used, unless stated otherwise.

5.4.4 Alignment of images and extraction of trajectories

Images of 200 nm TetraSpeck™ beads (Invitrogen) were taken in both the fluorescent and phase contrast channel. These images were used to determine the alignment coordinates for proper overlay between the phase contrast channel (cells) and the fluorescent channel (pyocin trajectories). Images of the phase contrast channel were adjusted prior to alignment. Background subtraction and inversion was applied on bead images, followed by downscaling of the image to 0.39 of its original size. Then alignment

coordinates for overlaying the phase contrast with the fluorescent channel were obtained by the descriptor-based registration (2d/3d) plugin of Fiji [56]. These coordinates were used for alignment of all pre-processed (downscaled) phase contrast images. This was followed by cropping the PC images to the same size as the fluorescent image. Pyocin trajectories were obtained by a plugin of Fiji, referred to as Trackmate [41], and downstream analysis of trajectories were performed with Matlab using @msdanalyzer, as was described briefly in chapter 2.

5.4.5 Analysis of membrane potential using fluorescent dye $DiSC_3(5)$

Dye $DiSC_3(5)$ (Sigma-Aldrich) is a voltage-sensitive dye and was used to quantitatively analyze the membrane potential of cells. Cells where grown to early-mid logarithmic phase (OD_{600} 0.3) and incubated with a final concentration of 400 μM $DiSC_3(5)$ for 10 min unless stated otherwise, followed by 1 min centrifugation at 14,000 x g and resuspended in 1/10 of the original volume with fresh medium. Cells were added to the flow cell, as was described in chapter 2.

Images of cells were made with the Olympus inverted microscope (IX81) using a widefield illumination system. System details and settings were described in section (5.4.3). The CY5-4040B-OMF-ZERO filter cube was used to detect the fluorescent signal of $DiSC_3(5)$ stained cells. Variation in the Electron-Multiplying (EM) gain, exposure time, and the laser intensity was used and stated independently in the subscription of the figures.

The fluorescent intensity of cells (uptake of $DiSC_3(5)$ dye) was quantified in the following way. First the fluorescent image was binarized in Fiji using the Otsu threshold method. In the case of time-lapse microscopy an additional check was performed for movement, as documented in Chapter 2. Data was imported and analyzed using in-house made Matlab scripts. Cells with the following criteria were selected; minimal area of 200 pixels, maximal area of 630 pixels, minimal eccentricity .7, minimal solidity .8 (area/convex area), and for time-lapse microscopy the additional criteria of being immobilized during the entire movie was taken into account. Cells on the border were excluded. Manual selecting and deselecting of cells was used when appropriate. These selected regions of interest (ROI) in the fluorescent images were saved. The mean intensity of each identified ROI per time point was measured and divided by the mean background determined by three ROIs in the first image to obtain the signal-to-background ratio. Significance in signal-to-noise ratio between different dye concentrations was tested with a Bonferroni corrected Mann-Whitney U test. For time-lapse imaging the binarized cells were linked to each other by overlaying the centroid of each identified ROI. Followed by discarding all cells with an initial fluorescent intensity below 4750 arbitrary units, as these cells show the same fluorescent intensity as depolarized cells and are therefore seen as metabolically inactive, in addition to, their lack of response to the bactericidal activity of pyocins. The relative fluorescent intensity was determined by dividing the fluorescent intensity of the cell at a certain time point by the fluorescent intensity of the cell at T=0. A Bonferroni corrected Mann-Whitney U test was used to test for significance in the drop in relative fluorescent intensity over time between cells exposed to pyocins and its control.

5.5 Supplementary information

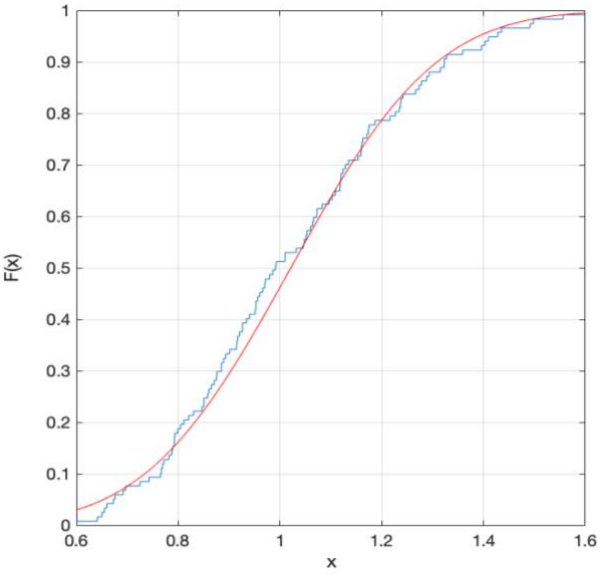

Supplementary figure 5.1: α exponents for freely diffusing pyocins followed a normal Gaussian distribution. α exponents were obtained from a linear fit on the first 25% of each individual trajectory curve in a log-log plot of MSD as a function of delay time. The cumulative distribution function (CDF) was used to calculate the cumulative probability for every given x-value. The obtained empirical CDF was tested, using a Kolmogorov-Smirnov test, against the null-hypothesis of a standard normal CDF. Results showed no significant deviation, demonstrating that the data followed a standard Gaussian distribution. Blue and red curves presented the empirical CDF and standard normal CDF with mu 1.02 and sigma 0.22, respectively.

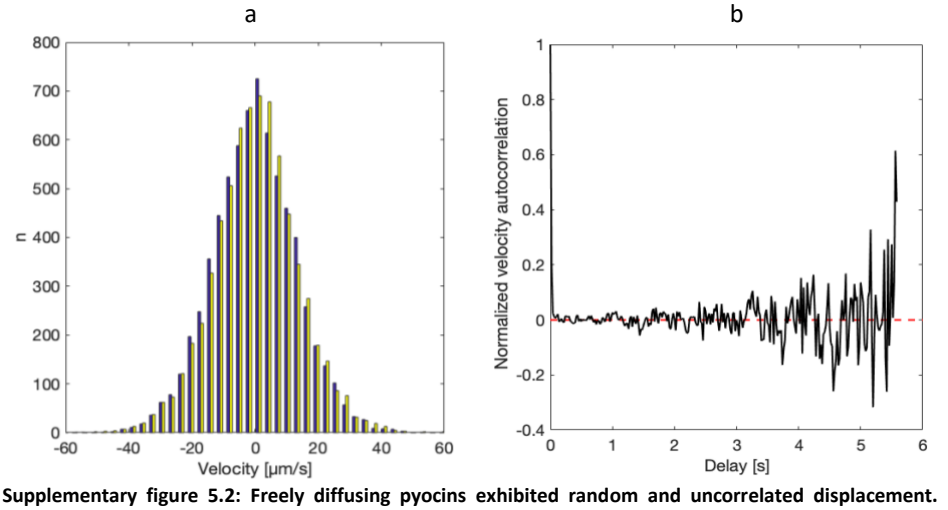

Supplementary figure 5.2: Freely diffusing pyocins exhibited random and uncorrelated displacement. Velocity analysis distribution for all individual trajectories classified within the group *free in solution*. **a,** Symmetric instantaneous velocity distribution graph, showed *x* and *y* displacements with mean values centered around 0. Yellow and purple bars presented *x* and *y* displacement, respectively. **b,** Normalized velocity autocorrelation, showed, with the exception of $\Delta t = 0$, a mean value centered around 0 during the course of time.

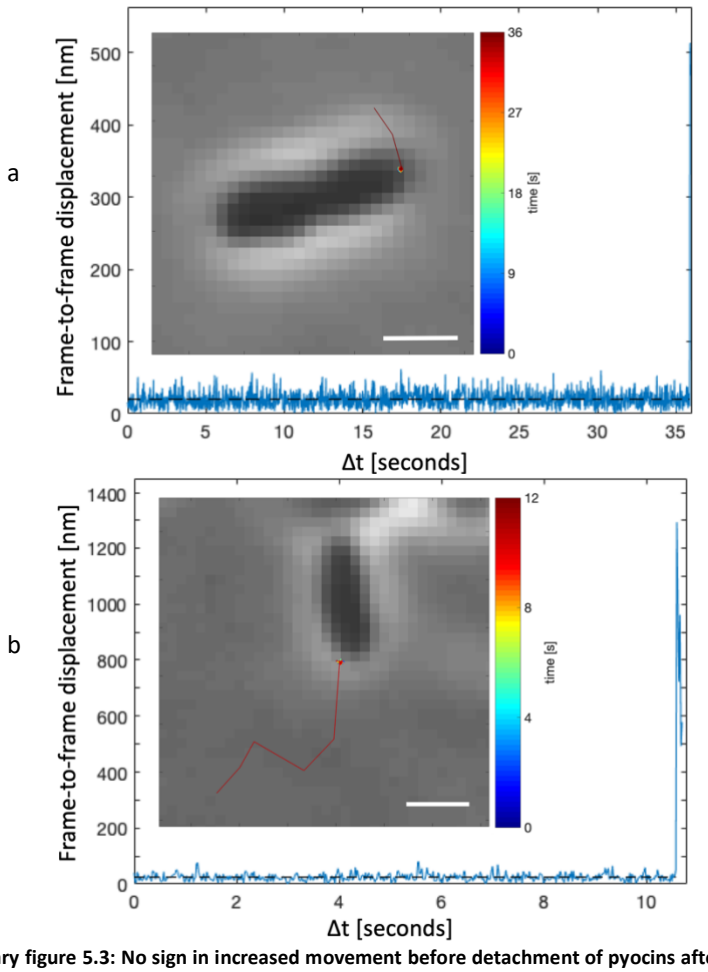

Supplementary figure 5.3: No sign in increased movement before detachment of pyocins after prolonged cell interaction. Two examples of pyocins that detached from a cell after showing prolonged interaction within a very confined region on a cell (inserts of corresponding images in graph **a** and **b**). Frame-to-frame (FTF) displacement showed no increase in size of displacement before detachment. Blue and black dotted lines present experimental data and mean FTF displacement of on-cell interaction. Scale bar represents 1 μM.

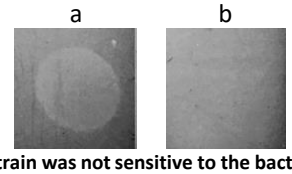

Supplementary figure 5.4: *E. coli* B strain was not sensitive to the bactericidal activity of pyocin R2. R2-type pyocins were placed as 10 μl droplets on an actively growing lawn of **a**, *P. aeruginosa* 13s and **b,** *E. coli* B strain. Clearing of the bacterial lawn (light spot) indicated cell death.

5.6 References

[1] F. Jacob, [Induced biosynthesis and mode of action of a pyocine, antibiotic produced by Pseudomonas aeruginosa], Ann Inst Pasteur (Paris) 86(2) (1954) 149-60.
[2] M. Kageyama, F. Egami, On the purification and some properties of a pyocin, a bacteriocin produced by Pseudomonas aeruginosa, Life Sci (1962) 1 (1962) 471-6.
[3] K. Nakayama, K. Takashima, H. Ishihara, T. Shinomiya, M. Kageyama, S. Kanaya, M. Ohnishi, T. Murata, H. Mori, T. Hayashi, The R-type pyocin of Pseudomonas aeruginosa is related to P2 phage, and the F-type is related to lambda phage, Mol Microbiol 38(2) (2000) 213-31.
[4] M.A. Riley, Molecular mechanisms of bacteriocin evolution, Annu Rev Genet 32 (1998) 255-78.
[5] G. Lee, U. Chakraborty, D. Gebhart, G.R. Govoni, Z.H. Zhou, D. Scholl, F-Type Bacteriocins of Listeria monocytogenes: a New Class of Phage Tail-Like Structures Reveals Broad Parallel Coevolution between Tailed Bacteriophages and High-Molecular-Weight Bacteriocins, J Bacteriol 198(20) (2016) 2784-93.
[6] D. Gebhart, S.R. Williams, K.A. Bishop-Lilly, G.R. Govoni, K.M. Willner, A. Butani, S. Sozhamannan, D. Martin, L.C. Fortier, D. Scholl, Novel high-molecular-weight, R-type bacteriocins of Clostridium difficile, J Bacteriol 194(22) (2012) 6240-7.
[7] J. Liu, P. Chen, C. Zheng, Y.P. Huang, Characterization of maltocin P28, a novel phage tail-like bacteriocin from Stenotrophomonas maltophilia, Appl Environ Microbiol 79(18) (2013) 5593-600.
[8] A.H. Nguyen, T. Tomita, M. Hirota, T. Sato, Y. Kamio, A simple purification method and morphology and component analyses for carotovoricin Er, a phage-tail-like bacteriocin from the plant pathogen Erwinia carotovora Er, Biosci Biotechnol Biochem 63(8) (1999) 1360-9.
[9] J.O. Thaler, S. Baghdiguian, N. Boemare, Purification and characterization of xenorhabdicin, a phage tail-like bacteriocin, from the lysogenic strain F1 of Xenorhabdus nematophilus, Appl Environ Microbiol 61(5) (1995) 2049-52.
[10] A. Datta, L.M. Prescott, Bacteriocin production by Vibrio cholerae. I. Effects of vibriocins on Vibrio cholerae, Indian J Med Res 57(8) (1969) 1402-8.
[11] D. Scholl, Phage Tail-Like Bacteriocins, Annu Rev Virol 4(1) (2017) 453-467.
[12] M.G.K. Ghequire, R. De Mot, The Tailocin Tale: Peeling off Phage Tails, Trends Microbiol 23(10) (2015) 587-590.
[13] T. Kohler, V. Donner, C. van Delden, Lipopolysaccharide as shield and receptor for R-pyocin-mediated killing in Pseudomonas aeruginosa, J Bacteriol 192(7) (2010) 1921-8.
[14] R.D. Waite, M.A. Curtis, Pseudomonas aeruginosa PAO1 pyocin production affects population dynamics within mixed-culture biofilms, J Bacteriol 191(4) (2009) 1349-54.
[15] S.A. Naz, N. Jabeen, M. Sohail, S.A. Rasool, Biophysicochemical characterization of Pyocin SA189 produced by Pseudomonas aeruginosa SA189, Braz J Microbiol 46(4) (2015) 1147-54.
[16] L. Turnbull, M. Toyofuku, A.L. Hynen, M. Kurosawa, G. Pessi, N.K. Petty, S.R. Osvath, G. Carcamo-Oyarce, E.S. Gloag, R. Shimoni, U. Omasits, S. Ito, X. Yap, L.G. Monahan, R. Cavaliere, C.H. Ahrens, I.G. Charles, N. Nomura, L. Eberl, C.B. Whitchurch, Explosive cell lysis as a mechanism for the biogenesis of bacterial membrane vesicles and biofilms, Nat Commun 7 (2016) 11220.

[17] T. Shinomiya, Phenotypic mixing of pyocin R2 and bacteriophage PS17 in Pseudomonas aeruginosa PAO, J Virol 49(2) (1984) 310-4.
[18] T. Hayashi, H. Matsumoto, M. Ohnishi, S. Yokota, T. Shinomiya, M. Kageyama, Y. Terawaki, Cytotoxin-converting phages, phi CTX and PS21, are R pyocin-related phages, FEMS Microbiol Lett 122(3) (1994) 239-44.
[19] T. Shinomiya, S. Ina, Genetic comparison of bacteriophage PS17 and Pseudomonas aeruginosa R-type pyocin, J Bacteriol 171(5) (1989) 2287-92.
[20] S.R. Williams, D. Gebhart, D.W. Martin, D. Scholl, Retargeting R-type pyocins to generate novel bactericidal protein complexes, Appl Environ Microbiol 74(12) (2008) 3868-76.
[21] D. Scholl, M. Cooley, S.R. Williams, D. Gebhart, D. Martin, A. Bates, R. Mandrell, An engineered R-type pyocin is a highly specific and sensitive bactericidal agent for the food-borne pathogen Escherichia coli O157:H7, Antimicrob Agents Chemother 53(7) (2009) 3074-80.
[22] D. Gebhart, S. Lok, S. Clare, M. Tomas, M. Stares, D. Scholl, C.J. Donskey, T.D. Lawley, G.R. Govoni, A modified R-type bacteriocin specifically targeting Clostridium difficile prevents colonization of mice without affecting gut microbiota diversity, mBio 6(2) (2015).
[23] T.J. Bird, H.G. Grieble, Pyocin antibiosis in chick embryos, Antimicrob Agents Chemother (Bethesda) 9 (1969) 495-8.
[24] D.J. Merrikin, C.S. Terry, Use of pyocin 78-C2 in the treatment of Pseudomonas aeruginosa infection in mice, Appl Microbiol 23(1) (1972) 164-5.
[25] H. Haas, T. Sacks, N. Saltz, Protective effect of pyocin against lethal Pseudomonas aeruginosa infections in mice, J Infect Dis 129(4) (1974) 470-2.
[26] D. Scholl, D.W. Martin, Jr., Antibacterial efficacy of R-type pyocins towards Pseudomonas aeruginosa in a murine peritonitis model, Antimicrob Agents Chemother 52(5) (2008) 1647-52.
[27] J.M. Ritchie, J.L. Greenwich, B.M. Davis, R.T. Bronson, D. Gebhart, S.R. Williams, D. Martin, D. Scholl, M.K. Waldor, An Escherichia coli O157-specific engineered pyocin prevents and ameliorates infection by E. coli O157:H7 in an animal model of diarrheal disease, Antimicrob Agents Chemother 55(12) (2011) 5469-74.
[28] R. Zink, M.J. Loessner, I. Glas, S. Scherer, Supplementary Listeria-typing with defective Listeria phage particles (monocins), Lett Appl Microbiol 19(2) (1994) 99-101.
[29] R. Zink, M.J. Loessner, S. Scherer, Characterization of cryptic prophages (monocins) in Listeria and sequence analysis of a holin/endolysin gene, Microbiology (Reading) 141 (Pt 10) (1995) 2577-84.
[30] E. Bannerman, P. Boerlin, J. Bille, Typing of Listeria monocytogenes by monocin and phage receptors, Int J Food Microbiol 31(1-3) (1996) 245-62.
[31] J.A. Fyfe, G. Harris, J.R. Govan, Revised pyocin typing method for Pseudomonas aeruginosa, J Clin Microbiol 20(1) (1984) 47-50.
[32] D. Jurado Chacon, A. Chueca Sancho, J.F. Guillen Solvas, B. Garcia-Villanova Ruiz, R. Galvez Vargas, Possibility of using purified pyocins for typing Pseudomonas aeruginosa: purification of pyocins and sensitivity of P. aeruginosa in different tests, Ann Inst Pasteur Microbiol (1985) 137A(3) (1986) 253-66.
[33] H.D. Sidberry, J.C. Sadoff, Pyocin sensitivity of Neisseria gonorrhoeae and its feasibility as an epidemiological tool, Infect Immun 15(2) (1977) 628-37.

[34] C.C. Blackwell, J.A. Law, Typing of non-serogroupable Neisseria meningitidis by means of sensitivity to R-type pyocines of Pseudomonas aeruginosa, J Infect 3(4) (1981) 370-8.
[35] P. Ge, D. Scholl, P.G. Leiman, X. Yu, J.F. Miller, Z.H. Zhou, Atomic structures of a bactericidal contractile nanotube in its pre- and postcontraction states, Nat Struct Mol Biol 22(5) (2015) 377-82.
[36] T. Shinomiya, S. Shiga, Bactericidal activity of the tail of Pseudomonas aeruginosa bacteriophage PS17, J Virol 32(3) (1979) 958-67.
[37] Y. Uratani, T. Hoshino, Pyocin R1 inhibits active transport in Pseudomonas aeruginosa and depolarizes membrane potential, J Bacteriol 157(2) (1984) 632-6.
[38] E. Strauch, H. Kaspar, C. Schaudinn, P. Dersch, K. Madela, C. Gewinner, S. Hertwig, J. Wecke, B. Appel, Characterization of enterocoliticin, a phage tail-like bacteriocin, and its effect on pathogenic Yersinia enterocolitica strains, Appl Environ Microbiol 67(12) (2001) 5634-42.
[39] B. Westling-Haggstrom, T. Elmros, S. Normark, B. Winblad, Growth pattern and cell division in Neisseria gonorrhoeae, J Bacteriol 129(1) (1977) 333-42.
[40] S.A. Morse, B.V. Jones, P.G. Lysko, Pyocin inhibition of Neisseria gonorrhoeae: mechanism of action, Antimicrob Agents Chemother 18(3) (1980) 416-23.
[41] J.Y. Tinevez, N. Perry, J. Schindelin, G.M. Hoopes, G.D. Reynolds, E. Laplantine, S.Y. Bednarek, S.L. Shorte, K.W. Eliceiri, TrackMate: An open and extensible platform for single-particle tracking, Methods 115 (2017) 80-90.
[42] N. Tarantino, J.Y. Tinevez, E.F. Crowell, B. Boisson, R. Henriques, M. Mhlanga, F. Agou, A. Israel, E. Laplantine, TNF and IL-1 exhibit distinct ubiquitin requirements for inducing NEMO-IKK supramolecular structures, J Cell Biol 204(2) (2014) 231-45.
[43] X. Michalet, Mean square displacement analysis of single-particle trajectories with localization error: Brownian motion in an isotropic medium, Phys Rev E Stat Nonlin Soft Matter Phys 82(4 Pt 1) (2010) 041914.
[44] M.J. Saxton, Modeling 2D and 3D diffusion, Methods Mol Biol 400 (2007) 295-321.
[45] R. Moldovan, E. Chapman-McQuiston, X.L. Wu, On kinetics of phage adsorption, Biophys J 93(1) (2007) 303-15.
[46] T.T. Puck, A. Garen, J. Cline, The mechanism of virus attachment to host cells. I. The role of ions in the primary reaction, J Exp Med 93(1) (1951) 65-88.
[47] P. Horacek, V. Zarybnicky, J. Roubal, J. Turkova, M. Dobisova, Influence of NaCl, KCl and MgSO4 concentration on total and irreversible adsorption of T2r phage on isolated cell walls, Folia Microbiol (Praha) 15(4) (1970) 282-7.
[48] Z.J. Storms, E. Arsenault, D. Sauvageau, D.G. Cooper, Bacteriophage adsorption efficiency and its effect on amplification, Bioprocess Biosyst Eng 33(7) (2010) 823-31.
[49] R. Edgar, A. Rokney, M. Feeney, S. Semsey, M. Kessel, M.B. Goldberg, S. Adhya, A.B. Oppenheim, Bacteriophage infection is targeted to cellular poles, Mol Microbiol 68(5) (2008) 1107-16.
[50] S.A. Buth, M.M. Shneider, D. Scholl, P.G. Leiman, Structure and Analysis of R1 and R2 Pyocin Receptor-Binding Fibers, Viruses 10(8) (2018).
[51] A.J. Salazar, M. Sherekar, J. Tsai, J.C. Sacchettini, R pyocin tail fiber structure reveals a receptor-binding domain with a lectin fold, PLoS One 14(2) (2019) e0211432.

[52] J.D. Te Winkel, D.A. Gray, K.H. Seistrup, L.W. Hamoen, H. Strahl, Analysis of Antimicrobial-Triggered Membrane Depolarization Using Voltage Sensitive Dyes, Front Cell Dev Biol 4 (2016) 29.
[53] P.J. Sims, A.S. Waggoner, C.H. Wang, J.F. Hoffman, Studies on the mechanism by which cyanine dyes measure membrane potential in red blood cells and phosphatidylcholine vesicles, Biochemistry 13(16) (1974) 3315-30.
[54] H. Strahl, L.W. Hamoen, Membrane potential is important for bacterial cell division, Proc Natl Acad Sci U S A 107(27) (2010) 12281-6.
[55] K. Ikeda, F. Egami, Receptor substance for pyocin R. I. Partial purification and chemical properties, J Biochem 65(4) (1969) 603-9.
[56] S. Preibisch, S. Saalfeld, J. Schindelin, P. Tomancak, Software for bead-based registration of selective plane illumination microscopy data, Nat Methods 7(6) (2010) 418-9.
[57] A.M. Goldfain, R.F. Garmann, Y. Jin, Y. Lahini, V.N. Manoharan, Dynamic Measurements of the Position, Orientation, and DNA Content of Individual Unlabeled Bacteriophages, J Phys Chem B 120(26) (2016) 6130-8.
[58] M. Schwartz, The adsorption of coliphage lambda to its host: effect of variations in the surface density of receptor and in phage-receptor affinity, J Mol Biol 103(3) (1976) 521-36.

6

Final remarks & Outlook

From the past to the future: Impact of phage research on society

Lisa L. Dreesens

Since the discovery of phages a century ago, phage research has played a fundamental and central role in molecular biology as we know it today and resulted, among others, in the discovery of DNA, gene regulation, transcription, expression and replication [1-4]. The impact of this first era of phage biology has also been large in terms of the establishment of molecular tools. These include among others DNA polymerases, restriction enzymes and ligases, gene-expression systems and phage display technology [2-4]. With the rise of resistance among bacteria against conventional antibiotics [5], there is an urgent need for alternatives, which has led to a second era of phage research. Current hurdles that need to be overcome are among others the basic understanding of the mechanism behind phage infection, as well as, which factors influence their behavior, purification and administer methods, narrow host spectrum, and clinical studies on the effect of phage stability, effectivity, and adverse effects on our body. New developments in the state-of-the-art of technology allow for faster and more broad screening of samples on the presence of phages, resulting in the rapid discovery of new phages and receptors [6-8], but also unravels the more detailed interactions between phage and host [7, 9-11]. With most recently a huge breakthrough with the discovery of a prokaryotic 'adaptive immune system' called CRISPR-Cas. CRISPR technology, that makes use of the CRISPR-Cas system, has great prospects as gene-editing tool and is not limited to modifying genes in bacteria [12].

With the development of single-particle fluorescence microscopy it is now possible to study the phage infection process in real-time and within an ecologically relevant environment, from finding [11] and infecting [13] a target cell up to lytic or lysogenic replication [14], providing new information on the molecular side of phage biology as we know it today. Fluorescence microscopy has undergone enormous improvements over the recent years in both spatial and temporal resolution and can now image with incredible detail, allowing us to study phage biology in more detail. Developments of this technique resulted among other in the localization and tracking of single phage-host interactions, as well as, following the DNA ejection process or genome localization within the host. For example, Rothenberg *et al.* found that phage λ co-localized with receptor rich regions and moved over this helical carpet of receptors towards the cellular pole where they were generally found to bind irreversibly and infect the cell [11]. The phenomenon of phages ending-up at the cellular poles is not limited to λ, but was also found to occur in other phages [11, 14-16]. These results are initial leads showing pieces of this large complex puzzle around the fundamentals behind the target-search process of bacteriophages. However, many unresolved questions remained: e.g. what is the mechanism behind this on-cell movement and are these universal among phages? What are key-factors influencing these interactions in terms of environment, receptors and metabolic state of the host, and phage binding proteins? And what are the accompanying trade-offs and constraints at the level of phage-host binding interactions? Answers on these questions are crucial as they form the basis of understanding the phage infection process and pave the way in phage biology to unravel their profound and important role in ecology, including that of our own gut microbiome.

Within this thesis, we focused on developing a tool that can provide answers on questions concerning the phage target finding process. Here the experimental method used by Rothenberg *et al.* and Edgar *et al*. to study the target-finding process and preferred binding location at the cell surface was used as basis [11, 15]. In Chapter 2 we described the optimization of the experimental set-up in terms of: i) increasing throughput of usable data by optimizing the adherence properties of host cells to the substrate of the flow cell, ii) setting up a general method of fluorescently labeling to study multiple phages, as well as, phage-like particles, given that the surface of these particles contained exposed lysines to which the dye binds, and iii) assembled a data analysis workflow that is capable of investigating this target-finding process of both phage and phage-like particles at a deeper level beyond that what has been studied today. Together this resulted in an improved method capable of accurate detection of phage position at the cell surface, as well as, tracking of phage, phage-like particles, and bacterial positions over time. The increased spatial and temporal resolution of our set-up allowed for tracking the nanoscale position at the microsecond timescale, increasing the information density required to study the phage-host interaction at a more detailed level which has, to our knowledge, not been reached before.

In Chapters 3, 4 and 5, we showed the first insights gained with this improved method. In Chapter 3 we revealed the irreversible binding distribution of phage T4 on *Escherichia coli* B, which showed to bind preferentially at the cellular poles. Interestingly, we found similar behavior for R2-type pyocins on *pseudomonas aeruginosa* 13s (Chapter 5). These results were in line with previous observations documented for other phages and/or hosts receptors [11, 14-16], pointing towards a general trend. Within this chapter we went beyond the observation of investigating the binding distribution of T4 phage on a new host and achieved the next step in initiating the investigation of factors that play a key-role in facilitating this interaction behavior that leads-up to this preferential irreversible binding position, i.e. environmental and host conditions. For certain of these environmental and host conditions it has been shown that they affect the infection process. For example, a switch in certain components of the medium composition, or mutations or deletions of crucial host receptors, affects the binding rate and efficiency of several phages including that of T4 [17-19]. Surprisingly, we found that switching the medium from LB to M9 played no role in the outcome of the position of irreversible binding for phage T4 on *E. coli* B. Other relevant environmental factors (i.e. temperature, co-factors, ion concentration etc.) should be tested to investigate whether these only play a role in the first stage of the phage target search and reversible binding process. This in contrast to the finding that affect the host receptor(s) used to infect, for which our results strongly indicate a significant effect on the binding distribution of T4 to *E. coli* strain B vs. K-12. Even though further research is needed to resolve what caused this shift in binding position — that is to say, assess whether the observed effect is receptor-spectrum and/or receptor-distribution dependent — this method showed the capability of investigating the effect of such factors on irreversible binding position. Mapping these factors will provide information on how phages respond to different environments and/or changes in host conditions and in which part of the infection process these factors play a role. This provides us information on how

they operate in nature and how they can be best used with regard to sensitivity and stability within applications.

Next to investigating the irreversible binding distribution, we also studied the detailed on-cell dynamics of phage T4 on *E. coli* B and pyocin R2 on *P. aeruginosa* 13s prior to irreversible binding (Chapters 4 and 5). Phages and pyocins, which are phage-like particles, perform different functions: phages target a cell for infection and self-replication, while pyocins target a cell for killing. However, phages and pyocins have shown a high degree of similarity in structure and serological cross-reactivity [20-23], and we also revealed qualitative resemblance in their target-search behavior. For both particles, we found on-cell dynamics that extended beyond what could be reached when anchored with a single tail fiber (TF) to the cell. This indicated the existence of a mechanism with which these particles can move at the cell surface, tethering the phage till either the binding location is reached, facilitating the cell penetration and DNA ejection process, or detachment takes place. We investigated this on-cell motion in more detail for phage T4. We found that the movement with which the phage moves at the cell surface occurs with discrete shifts in position. We concluded that the mechanism behind the on/near-cell exploration was most likely explained by either hopping and/or tethered-walking. These are the first detailed recordings on dynamic interaction between phage and host that gained insight behind the mechanism of on-cell motion. The former mechanism describes the phage briefly leaving, but remaining closely to the cell, binding to a nearby position. In the latter mechanism, the phage uses binding and unbinding of individual TFs to nearby receptors to drag itself to a new position. The next step within this research is to differentiate between these two mechanisms by testing a model of hopping and tethered-walking against the experimental data. Ultimately this will reveal the mechanism behind the target search and decision making process of phage T4. This information can be directly implemented to improve the simplistic models that are currently used to describe phage-host interaction dynamics at single-particle and bulk level allowing for better prediction of how these particles operate.

Once we grasp how phages operate, phage properties could be explored in more detail, e.g. mapping the sensitivity and stability towards environmental factors (enhancing or inhibiting binding and infection) or mapping the effect of TF- and or receptor mutations on interaction dynamics and binding kinetics. This line of research will allow for both a better understanding of the mechanism behind the decision-making process, how and when a phage will commit to infect a cell, at a nanoscale level, as well as, it will improve and speed-up the engineerability of these particles through genetic engineering and synthetic biology. Together these will eventually allow us to reprogram the specificity of the phage with high precision and efficiency for the use in applications. Since our labeling method was designed to be non-specific, it can also be used to study the nanoscopic details behind the target search for other phage and phage-like particles. This will provide insights in how diverse or universal the target search mechanism is. Another future direction could be to mimic a more natural environment and explore how phages cope with competition, or act in microbial communities or even biofilms. Further, our method has shown the capability to simultaneous track the search

(chapters 4 and 5) and irreversible binding (chapters 3 and 5) process with that of the DNA ejection (chapter 2) in case of phages or cell depolarization (chapter 5) in case of pyocins and would be a future direction to explore. Investigating the on-cell motion with nanoscopic detail, and investigating crucial key-factors that might play a role facilitating the binding interaction, brings us one step closer to understanding the underlying mechanism and molecular details of phage- and phage-like host interaction governing adsorption and host selection. These are first steps and an important ingredient to understand their role and impact on ecology and evolution, including their role in maintaining and structuring microbial communities, pathogenicity and transmission of virulence genes, and their influence on the nutrient cycles. In addition, new knowledge on the search and infection process will aid the exploration regarding the usage and engineerability of phages towards a wide field of applications, i.e. phage therapy, gene delivery, pathogen detection, biocontrol of biofilms and plant pathogens, surface disinfection and food biopreservation [1-4].

A hundred years ago when d'Hérelle and Twort discovered the phages, they most likely could not have imagined the importance and impact of their discovery. Without phage research, a part of the core biological principles used today in science and education, as well as, the development of these phage-based molecular tools and potential therapeutics would not exist. Given their diverse and wide-spread abundance in nature but yet understudied role in ecology, many more discoveries lie ahead, highlighting the importance of the continuation of phage research. It is unpredictable what the future will reveal, but undoubtedly it will answer many of our questions and will lead us to exciting new developments in medical, industrial and agricultural applications.

References

[1] E.C. Keen, A century of phage research: bacteriophages and the shaping of modern biology, Bioessays 37(1) (2015) 6-9.
[2] G. Ofir, R. Sorek, Contemporary Phage Biology: From Classic Models to New Insights, Cell 172(6) (2018) 1260-1270.
[3] G.P. Salmond, P.C. Fineran, A century of the phage: past, present and future, Nat Rev Microbiol 13(12) (2015) 777-86.
[4] L.K. Harada, E.C. Silva, W.F. Campos, F.S. Del Fiol, M. Vila, K. Dabrowska, V.N. Krylov, V.M. Balcao, Biotechnological applications of bacteriophages: State of the art, Microbiol Res 212-213 (2018) 38-58.
[5] G.W.H. Organization, Global action plan on antimicrobial resistance, Switzerland 2015.
[6] N.S. Olsen, N.B. Hendriksen, L.H. Hansen, W. Kot, A New High-throughput Screening (HiTS) Method for Phages – Enabling Crude Isolation and Fast Identification of Diverse Phages with Therapeutic Potential, PHAGE 1(3) (2020) 137-148.
[7] K.E. Kortright, B.K. Chan, P.E. Turner, High-throughput discovery of phage receptors using transposon insertion sequencing of bacteria, Proc Natl Acad Sci U S A 117(31) (2020) 18670-18679.
[8] S. Roux, J. Tournayre, A. Mahul, D. Debroas, F. Enault, Metavir 2: new tools for viral metagenome comparison and assembled virome analysis, BMC Bioinformatics 15 (2014) 76.
[9] E. Brzozowska, A. Lesniewski, S. Sek, R. Wieneke, R. Tampe, S. Gorska, M. Jonsson-Niedziolka, J. Niedziolka-Jonsson, Interactions of bacteriophage T4 adhesin with selected lipopolysaccharides studied using atomic force microscopy, Sci Rep 8(1) (2018) 10935.
[10] B. Hu, W. Margolin, I.J. Molineux, J. Liu, Structural remodeling of bacteriophage T4 and host membranes during infection initiation, Proc Natl Acad Sci U S A 112(35) (2015) E4919-28.
[11] E. Rothenberg, L.A. Sepulveda, S.O. Skinner, L. Zeng, P.R. Selvin, I. Golding, Single-virus tracking reveals a spatial receptor-dependent search mechanism, Biophys J 100(12) (2011) 2875-82.
[12] H. Manghwar, K. Lindsey, X. Zhang, S. Jin, CRISPR/Cas System: Recent Advances and Future Prospects for Genome Editing, Trends Plant Sci 24(12) (2019) 1102-1125.
[13] D. Van Valen, D. Wu, Y.J. Chen, H. Tuson, P. Wiggins, R. Phillips, A single-molecule Hershey-Chase experiment, Curr Biol 22(14) (2012) 1339-43.
[14] L. Zeng, S.O. Skinner, C. Zong, J. Sippy, M. Feiss, I. Golding, Decision making at a subcellular level determines the outcome of bacteriophage infection, Cell 141(4) (2010) 682-91.
[15] R. Edgar, A. Rokney, M. Feeney, S. Semsey, M. Kessel, M.B. Goldberg, S. Adhya, A.B. Oppenheim, Bacteriophage infection is targeted to cellular poles, Mol Microbiol 68(5) (2008) 1107-16.
[16] L. Jakutyte, C. Baptista, C. Sao-Jose, R. Daugelavicius, R. Carballido-Lopez, P. Tavares, Bacteriophage infection in rod-shaped gram-positive bacteria: evidence for a preferential polar route for phage SPP1 entry in Bacillus subtilis, J Bacteriol 193(18) (2011) 4893-903.

[17] A. Washizaki, T. Yonesaki, Y. Otsuka, Characterization of the interactions between Escherichia coli receptors, LPS and OmpC, and bacteriophage T4 long tail fibers, Microbiologyopen 5(6) (2016) 1003-1015.
[18] Z.J. Storms, E. Arsenault, D. Sauvageau, D.G. Cooper, Bacteriophage adsorption efficiency and its effect on amplification, Bioprocess Biosyst Eng 33(7) (2010) 823-31.
[19] Z.J. Storms, L. Smith, D. Sauvageau, D.G. Cooper, Modeling bacteriophage attachment using adsorption efficiency, Biochemical Engineering Journal 64(15) (2010) 22-29.
[20] K. Nakayama, K. Takashima, H. Ishihara, T. Shinomiya, M. Kageyama, S. Kanaya, M. Ohnishi, T. Murata, H. Mori, T. Hayashi, The R-type pyocin of Pseudomonas aeruginosa is related to P2 phage, and the F-type is related to lambda phage, Mol Microbiol 38(2) (2000) 213-31.
[21] D. Scholl, Phage Tail-Like Bacteriocins, Annu Rev Virol 4(1) (2017) 453-467.
[22] S. Kube, P. Wendler, Structural comparison of contractile nanomachines[AIMS Biophysics 2(2) (2015) 88-115.
[23] M.G.K. Ghequire, R. De Mot, The Tailocin Tale: Peeling off Phage Tails, Trends Microbiol 23(10) (2015) 587-590.

Acknowledgements

After five years, this scientific journey almost comes to its end. The last part, when you know you're almost there but you don't see the finish line yet, is the hardest part. Writing this last part of the thesis is the knowledge that I'm almost there. In these last five years, I have grown a lot, both scientifically and as a person. This achievement would not have been made possible without the support and help of family, friends and colleagues. I therefore would like to thank the people around me who had a part in the realization of my thesis and made these last five years an unforgettable time. In particular, I would like to thank the following people:

First of all, Bertus and Marie-Eve, thank you for giving me the opportunity to work on this exciting and interesting project and the continuous guidance throughout these years. You have given me a lot of freedom and support to explore my own ideas and to choose my own direction, but at the same time guided me and assessed my work critically, making sure to explore every path or every result before taking a conclusion or decision for a next step. I'm also grateful that you have led me pursue my dreams outside science. The first year of my PhD I had the crazy idea of swimming the IJsselmeer, the toughest open water swimming competition in the Netherlands. Later on, during my fourth year of my PhD I came with the next crazy proposal, but also my dream, to swim the English Channel. I'm very happy with this opportunity to combine these sport endeavors with those of my PhD.

I also want to extend my gratitude to the committee members (Prof.dr. Bernd Rieger, Prof.dr. Ariane Briegel, Prof.dr. Abram Aertsen, Prof.dr. Nynke Dekker and Dr.ir. Stan Brouns). Thank you for taking part in my thesis defense.

Mathia, Ben en Carsten als de vier musketiers van 'the executive office' heb ik samen met jullie een ontzettend leuke periode gehad. Met jullie kon ik alles delen en overal over praten, research, politiek, het leven en most importantly de liefde. Wat was dat genieten die live soap in the office elke dag. Met zak popcorn of een kop zelfgemaakte cappuccino met een stuk chocola elkaar uithoren over de nieuwe ins en outs omtrent de liefde. Ook bedankt voor al de gezellige dagelijkse wandelingen over en om het TU-terrein met een standaard stop bij de geitjes. Mathia, ik mis je ontzettend. Het is oneerlijk hoe het leven gaat en het laatste jaar was ontzettend zwaar. In mijn gedachten zal ik jou altijd bij mij dragen. Da, Magda, Pauline, Wouter, en Lennard, jullie waren geweldige office-mates over de afgelopen 5 jaar. Ik heb genoten van jullie gezelligheid en wijsheid. Erwin, jouw directheid, gezelligheid, verhalen, en humor heb ik de laatste 2 jaar wel gemist rond het lab. Bedankt voor al jouw advies en jouw sportiviteit om

samen twee keer per week buiten een lekker rondje te rennen tijdens lunchtijd. Volgens mij is het tijd om weer eens een keer samen gezellig te borrelen en bij te kletsen!

Over de jaren heen heb ik veel studenten mogen begeleiden, wat een van de leuke aspecten van mijn PhD is geweest. Ik wil jullie allen bedanken voor jullie enthousiasme en de grote bijdrage die jullie aan mijn project hebben geleverd. Ik heb erg genoten van deze leuke en leerzame tijd die we samen hebben gehad. Cleo, jij was mijn eerste student. Ambitieus als je was ben je begonnen met het optimaliseren van de flow-cell voor het nanoscopisch bestuderen van hoe fagen en pyocins hun host vinden. De optimalisatie die jij toen aan de flow-cell hebt gedaan heb ik de rest van mijn PhD gebruikt. Igor, jij hebt een fantastische rol gespeelt in het opzetten van de data-analyse. Het was geweldig om de eerste trajectorie te zien die jij uit de experimentele data hebt getoverd. Jij hebt de basis gebouwd voor het analyseren van data waar mijn thesis op gebaseerd is. Ik wil je ook bedanken voor alle tips en trainingen omtrent het rennen. Gaius, ik heb genoten van jouw humor en enthousiasme. Je hebt hele mooie stappen gezet in het project en vooruitgang geboekt in de verdere data-analyse verwerking. Lars, Burak en Aishwarya het was een genot om jullie de kneepjes van het vak te laten zien op het lab en jullie aan de slag te zien gaan met het verzamelen van experimentele data voor fagen en pyocins. Ik weet dat dit niet altijd gemakkelijk is geweest. Zoals jullie gemerkt hebben is het verzamelen van experimentele data in de biologie een kunst. Ik vind het mooi om te zien hoe jullie je hier doorheen hebben gesleept. Kyriakos, I would like to thank you for all the developments in the data analysis and the many online conversations that we had. I admire your gift to translate all the hard-core physics in easy language, so even a biologist like me can understand it. Wouter D. en Thomas, ondanks dat ik jullie niet heb begeleid hebben jullie toch een hele mooie bijdrage geleverd aan dit project. Wouter D. bedankt voor het opzetten van de eerste stappen richting een model en Thomas voor het identificeren van een step-finder voor de data-analyse. Als laatste, Wouter L. je bent dan wel begonnen als student maar je hebt snel de overstap gemaakt naar collega. Als “partner-in-crime” wil ik je niet alleen bedanken voor de mooie en gezellige tijd, maar ook voor de discussies, gedachtes en brainstormsessies omtrent de struggles van de data-analyse op fagen. We hebben samen mooie eerste stappen gezet naar het ontdekken hoe fagen over een cel bewegen.

It was fun and a great pleasure to be part of two labs. Even though I was sitting in a different office and working most of the time in a different lab I always felt welcome in the Marie-Eve group. I would like to thank all the members of Marie-Eve group for the great conversations and stories, the fun time and the nice group-outings. In particular, I want to thank Roland and Victor for his help regarding the development of the flow-cell and Andreas and Vanessa for the help regarding EM. Further, I want to thank Stan

and all the group members for taking me up in your phage group. It was really nice to have other people around me doing similar research, as well as to discuss and present my research in the group. Franklin, thank you for the discussions and for teaching me new techniques for phage research. Jeremie thank you for all the help with setting-up my method using microscopy, as well as for sharing all your thoughts on data analysis. Wiel, thank you for helping me out with the EM. Sasha, Susanne, Jan, Anke, en het BN-secretariaat bedankt voor de gezellige gesprekken en de allerhande zaken wat ervoor heeft gezorgd dat experimenten vlot uitgevoerd konden worden en alles gesmeerd liep en geregeld was op BN. BN girls, thanks for the nice evenings and diners. I will never forget our crazy 'twerk' recordings in the evening at the escalator of the Delft train station. Members of the Chirlmin and Danelon group, thanks for all the nice conversations during lunch time. Always good to have a short break from science. Further, I would like to say a big thank you to everybody here at BN that I have not yet mentioned. I made many great new friends, had many good conversations and shared lots of good memories that made my time here at BN unforgettable!

Ook buiten de research wil ik al mijn vrienden bedanken voor de support en de ontspanning naast de research. Gezellig een terrasje nemen, beuk setjes zwemmen met de club in Den haag, of gezellige triathlons en team-trainings dagjes met de Panthera's geeft mij altijd goede ontspanning en een afleiding van de dagelijkse sleur en frustraties van het werk.

Als laatste wil ik mijn familie bedanken. Dion en Dasha bedankt voor de gezellige en ontspannen dagen. Ik geniet er altijd van om samen met jullie en de hond een lekkere ronde te lopen door de bossen. Freek en Ina, bedankt voor de 'chill' tijd en de lekkere etentjes. Fijn om af en toe in corona tijd toch even het huis uit te kunnen. Mama en Papa jullie staan altijd voor mij klaar om mij te supporteren of te ondersteunen, ongeacht de situatie of uitdaging. Ik kan jullie niet genoeg bedanken voor al jullie liefde en steun! Zonder jullie had ik niet gestaan waar ik nu sta. Carsten vanaf het moment dat ik je leerde kennen tijdens het eerste jaar van mijn PhD zijn we met de dag dichter naar elkaar toe gegroeid. Je bent mijn steun en toeverlaat geworden en ik weet dat ik altijd op jou kan rekenen! Ik kan je niet genoeg bedanken voor al de support over de laatste paar jaar. Het laatste jaar was niet altijd makkelijk, maar samen slaan we er ons doorheen en kunnen we op elkaar steunen. Samen nog even aan de laatste loodjes werken van onze PhD in 'corona tijd'. Het eind is in zicht en we zijn er allentwee bijna. Ik kijk ernaar uit wat de toekomst ons gaat brengen maar ik weet zeker dat we er samen wel gaan komen. Ik hoop dat we nog vele jaren en avonturen mogen delen.

Lisa Dreesens
Rijnsburg, April 2021

Curriculum Vitae

Lisa Laura Dreesens

05-10-1991 Born in Venray, the Netherlands.

Education

2005-2009 Secondary Education
Raayland College, Venray, the Netherlands

2009-2013 B.Sc. in Applied Sciences
Fontys Hogeschool, the Netherlands

2013-2015 M.Sc. in Biomolecular Sciences
Vrije Universiteit, The Netherlands

2016-2021 Ph.D. Bionanoscience
Delft University of Technology, the Netherlands
Thesis: Illuminating the highly dynamic on-cell target search of bacteriophage and phage-like particles

Promotor: Dr. ME. Aubin-Tam
Copromotor: Dr. H.J.E. Beaumont

List of Publications

5. **L.L. Dreesens**, A. Karthikeyan, ME. Aubin-Tam, H.J.E. Beaumont, *Single-particle dynamics of R2-type pyocins*, in preparation.

4. **L.L. Dreesens**, W. Liefting, ME. Aubin-Tam, H.J.E. Beaumont, *Phage T4 explores the host cell via discrete on-cell movement***,** in preparation.

3. **L.L. Dreesens**, I. Rutka, ME. Aubin-Tam, H.J.E. Beaumont, *Irreversible binding distribution of phage T4 on E. coli B is targeted towards the cellular poles***,** in preparation.

2. **L.L. Dreesens**, W. Liefting, I. Rutka, K. Nikolaou, T. Wisse, C. Bagchus, L. Houtman, ME. Aubin-Tam, H.J.E. Beaumont, *Establishing methods to study bacteriophage/pyocin-host interactions at the single-particle level*, in preparation.

1. F.L. Nobrega, M. Vlot, P.A. de Jonge, **L.L. Dreesens,** H.J.E. Beaumont, R. Lavigne, B.E. Dutilh, & S.J.J. Brouns, (2018). Targeting mechanisms of tailed bacteriophages. *Nature Reviews Microbiology*, *16*, 760–773. https://doi.org/10.1038/s41579-018-0070-8